Development of Hydroxyapatite and Wollastonite Coatings for Orthopaedic Implant Biomedical Applications

A Thesis Submitted in Fulfilment of the Requirements for the

Degree of Master of Engineering (MEng)

Adwait Joshi

(B.Tech, M.Tech)

Supervisors

Prof. Joseph Stokes & Dr Khaled Benyounis

School of Mechanical and Manufacturing Engineering

Dublin City University, Ireland

January 2025

Declaration

I hereby certify that this material, which I now submit for assessment on the programme of study leading to the award of Master of Engineering is entirely my own work, and that I have exercised reasonable care to ensure that the work is original, and does not to the best of my knowledge breach any law of copyright, and has not been taken from the work of others save and to the extent that such work has been cited and acknowledged within the text of my work.

Signed: Adwait Joshi Student I.D. number: 16213419 Date: 03/01/2025

List of Publications

1. Joshi, A., Stokes, J., and Benyounis, K., 2019,"Development of Coated Biomedical Implant for Biomedical Applications" (poster presentation), Faculty Research Day 2019, DCU, Dublin, Ireland.

2. Joshi, A., Stokes, J., and Benyounis, K., 2023, "Wollastonite and Hydroxyapatite Use to Improve Titanium Hip Implants Quality" (graphical abstract), Faculty Research Day 2023, DCU, Dublin, Ireland.

3. Joshi, A., Stokes, J., and Benyounis, K., 2023, "Development of Orthopaedic Implants for Biomedical Applications" (Research on walls), DCU, Dublin, Ireland.

4. Sivarajan, S., Joshi, A., Palani, K., Raghupathy, P., and Stokes, J., 2022, "View of Corrosion and Wear Protection of AISI 4140 Carbon Steel Using a Laser-Modified High-Velocity Oxygen Fuel Thermal Sprayed Coatings." J. Electrochem. Sci. Eng., 12(5), pp. 865–876.

Acknowledgements

First and foremost, I would like to thank my parents for their continuous and unconditional support in my tumultuous research journey.

I would like to extend my highest sense of gratitude to my primary supervisor Prof. Joseph Stokes. His continuous advice, constructive criticism and vision during the project is highly regarded. His knowledge, guidance and ability to find the solution in the trickiest situation have made my journey fruitful. I want to thank my co-supervisor, Dr Khaled Benyounis, for his continuous attention to my research and great support, especially at the beginning of the study. I am very fortunate to work with such two dynamic, intelligent, flexible and caring supervisors throughout my research.

Regarding research, I would like to thank the lab technician Mr Liam Dominican, Mr Michael May, Mr Christopher Crouch, Mr Michael Tyrell, Dr Barry O'Connell and Ms Leah Nolan, Dr Brandon Twarley of TCD for helping me during the experimentation procedure. I would also like to thank Ms Caoimhe O'Broin for helping me procure raw research materials.

I would like to extend my gratitude to my friends and lab mates. In particular, I would like to thank my friends; Ivan Baran, Manoj Shukla, and my clients in my part-time job. I would also like to thank my DCU colleagues; Naif, Eoin, Sanjaya, Alla, Jochelle, Tina, Beth and Teerath. They kept me updated with the latest research trends and created a positive environment for research.

In terms of financial support, I am a self-funded student. I want to thank my parents for their financial assistance during the first four months of my stay. I want to thank Prof Joseph Stokes for assisting in getting the HEA COVID relief fund for the fourth and fifth years and for covering my fees over the last two years.

I want to apologise if I left someone out, because there were so many direct and indirect contributions to my research.

Table of Contents

List of Abbreviations

Ca^{2+}	Calcium ions
Si^{4+}	Silicon ions
Ti	Titanium
Zr	Zirconium
Nb	Niobium
Al	Aluminium
V	Vanadium
Fe	Iron
PHB	Polyhydroxybutyrate
PCL	Polycaprolactone
ASTM	American Society for Testing and Materials
XRD	X-Ray Diffraction
FTIR	Fourier Transform Infrared Spectroscopy
ICP-OES	Inductively Coupled Plasma Optical Emission Spectroscopy
XRF	X-ray fluorescence
TGA	Thermogravimetric Analysis
mol/L	Mole per Litre
FDA	Food and Drug Administration
SiO_2	Silicon Dioxide
Na_2O	Sodium Oxide
P_2O_5	Phosphorous Pentoxide
CaO	Calcium Oxide
CaF_2	Calcium Fluoride
MgO	Magnesium Oxide
$CaHPO_4$	Dicalcium Phosphate
PMMA	Polymethylmethacrylate
PEEK	Polyether Ether Ketone
HDPE	High Density Polyethylene

K_2O	Potassium Oxide
SBF	Simulated Body Fluid
ALP	Alkaline Phosphatase
ISO	International Standard for Organisation
mPa.s	Millipascal Second
K	Kelvin
NLPM	Normal Litres Per Minute
Na_2CO_3	Sodium Carbonate
K_2CO_3	Potassium Carbonate
SLPM	Standard Litres Per Minute
GPSS	General Purpose Simulation System
LCD	Liquid Crytal Display
LED	Light Emitting Diode
PTFE	Polytetrafluoroethylene
g/s	Gram per Second
m^3/hr	Cubic Metres per Hour
ml/min	Millilitres per Minute
g/cm^3	Gram per Cubic Centimetre

List of Figures

List of Tables

Abstract

Development of Hydroxyapatite and Wollastonite Coatings for Orthopaedic Implant Biomedical Applications

Adwait Joshi

The project aims to develop orthopaedic implants for biomedical applications. At present, millions of people suffer from hip issues; therefore, total hip replacement surgery has become more common; thus, finding a better hip implant is imperative. This study uses the titanium implant as a substrate due to its lightness, strength, durability, and biocompatibility despite its low bioactivity. Hydroxyapatite has a similar chemical composition to inorganic bone due to its bioactive nature. Biocoating fulfils both the function of bioactivity of Hydroxyapatite and the superior mechanical property of titanium. However, the major drawbacks of this Hydroxyapatite coated titanium implant are the poor mechanical properties of Hydroxyapatite and the bioinertness of the titanium. The present study intends to add Wollastonite as an additive to improve its mechanical and bioactive properties suitable for load-bearing applications.

Hydroxyapatite was initially spray-dried with the previous process parameters. Wollastonite was spray-dried with the same process parameters as Hydroxyapatite. As observed by scanning electron microscope, spray-dried Wollastonite showed acicular shape morphology, which affected its flowability. Therefore, Hydroxyapatite, Wollastonite, and Hydroxyapatite/Wollastonite composite powder were coated on the titanium substrate using a dip-immersion technique to address this issue. In the dip coating, the precursors of calcium, phosphate and silicate were used to dip coat Hydroxyapatite and Wollastonite on to a titanium substrate, respectively and Wollastonite powder in 10, 20 and 30 wt.%, respectively was added to Hydroxyapatite gel to form a Hydroxyapatite/Wollastonite composite coating. For spray coating, Hydroxyapatite, Wollastonite was spray coated onto a titanium substrate with parameters obtained from spray drying and Wollastonite was added in 20-50 wt.% to Hydroxyapatite slurry and spray coated onto a prepared titanium substrate. Overall, for dip-coated composite samples, the addition of 10 wt.% Wollastonite to composite coatings presented optimal results, whereas for spray-coated composite samples, 20 wt.% Wollastonite added to the composite coatings showed better coating cracks, porosity, microstructure results with better crystallinity. Therefore, new coating techniques requiring further research were produced as an outcome of the research.

1 Introduction

An ageing population and sedentary lifestyle have increased the need for total hip replacement. Bone and joint problems affect millions of people worldwide, and it has been observed that half of the people over 50 suffer from this problem in developed nations [1]. This problem leads to the development of total hip arthroplasty (THA). Total hip arthroplasty came into prominence in the 1960s. During that era, metal with polymer cement became standard. However, many problems were associated with this technique, such as aseptic loosening and osteolysis and the release of possible toxic monomers and local cell necrosis [2, 3]. These problems were more pronounced in younger patients, significantly when their lifespan exceeded their hip replacement surgery [4]. In the 1970s, more focus was given to biological fixation (without the use of cement), which led to the development of biocompatible materials (such as titanium, stainless steel, alumina, and zirconia) [1, 2]. This material was introduced into the body due to its biocompatibility, chemical inertness, and non-toxic reaction between the tissue and its host, thus called a bioinert material [1]. Bioinert materials do not participate in bone remanufacturing activity. There is a stress shielding effect where superior mechanical properties of biocompatible material lead them to take up all of the load, which ultimately reduces the physiological activity of transferring the load from implant material to the bone material [1, 5]. On the other hand, biometals can lead to the release of ions which forms a fibrous layer leading to inadequate fixation of the implant and bone [4].

Shortcomings of bioinert materials have led to the development of bioactive materials in the 1980s (for example, Hydroxyapatite, Wollastonite, bioglass, etc.), which incorporate bone growth on its surface, participate in the bone remanufacturing process without the formation of a fibrous layer [6]. A chemical bond develops between the biomaterial and the bone, leading to superior bioactivity and aiding in quicker bone repair and regeneration [1, 4]. The bioactive surface layer can be coated on the biocompatible substrate to combine the benefits of superior mechanical strength of the bioinert substrate and higher biological properties of the bioactive surface coatings [7]. The bioactive coating surface is then in direct contact with the bone tissue, thus promoting fast fixability at the start and long-term stability due to the bioinert substrate [8].

The thermal spray process is used due to its versatility in overcoming various difficulties within different applications [9, 10]. One method is where a thermal spray process deposits the bioactive material onto the bioinert substrate. The substrate material is thermally minimally affected compared to other coating techniques [9]. This technique has the advantages of better coating thickness and high durability [10].

Hydroxyapatite with the chemical formula [$Ca_{10}(PO)_4(OH)_6$] has a similar composition to the mineral phase of hard tissue. Biological apatite present in bone is non-stoichiometric apatite with impurities [11]. Though Hydroxyapatite forms a stable layer with the bone tissue due to its bioactivity, it has many drawbacks, which include fatigue failure, limited stability and thermal decomposition of the Hydroxyapatite coating, interfacial failure occurring when amorphous Hydroxyapatite was plasma sprayed onto a titanium substrate has poor mechanical properties due to brittleness of Hydroxyapatite [12–15]. There is continuous movement between the metal surface and HA-coating, although the HA coating bonds with the stem overtime this ultimately leads to the failure of the coating or its bond with the stem [16].

In the present study, Wollastonite will be coated onto a titanium substrate using a spray technique and a sol-gel dip-coating technique. Wollastonite can be used for hip replacement as it aids the repair of new bone but not on its own due to limited performance [17]. However, a suitable addition of Wollastonite to Hydroxyapatite could enhance the biodegradability, bioactivity and mechanical properties of Hydroxyapatite coating [18]. Most of the studies conducted have used Wollastonite as an additive material to form a biocomposite ceramic [19]. The bending strength of HA/ Wollastonite bioceramic was 98.06 MPa at 10wt.% Wollastonite and increased to 221.30 MPa in a HA/ Wollastonite bioceramic containing 90 wt.% Wollastonite [18]. Therefore, Wollastonite in this research will be added as an additive material to form a Hydroxyapatite/Wollastonite composite coating.

Similar to bio-implants, titanium substrate is used in this experiment due to its lower density, higher strength, non-toxicity and excellent corrosion resistance [20]. The major drawback of the titanium implant is the formation of the fibrous layer that might hinder

the process of bone-bonding [21]. Wollastonite is a naturally occurring material with the chemical formula of $CaSiO_3$. Its application includes construction, dental implants, and architecture as a substitute for granite and natural marble [22]. Wollastonite can be used as a reinforcing phase or as an individual material. It has biocompatibility and bioactivity similar to Hydroxyapatite with superior mechanical strength. In the form of powder or sintered material, Wollastonite can aid in the repair of damaged hard bone tissue [23].

Compared to other thermal spray techniques, the flame spray technique is cost-effective. It has a user-friendly operation with a variable flame temperature profile depending on the rate of feedstock materials and feed rate [24]. However, the flowability of Wollastonite powder is problematic; therefore, this research will try to find ways to improve flowability, to aid a spray technique to deposit this material onto titanium substrates. To date, very little research has been done on the sol-gel dip-coating of the Wollastonite on titanium substrate. The sol-gel dipping technique enhances the substrate microstructure by modifying the surface properties and improving the oxidation resistance of the substrate [25, 26]. The sol-gel technique will be used as a comparison technique to the spray process to measure their effectiveness.

1.1 Aims and Objective of the Project

- Objective 1: - To spray the Hydroxyapatite, Wollastonite and Hydroxyapatite-Wollastonite powder mixture. Hydroxyapatite was spray-dried with the process parameters obtained from previous research. Wollastonite was spray-dried with the same process parameters. The response obtained from spray drying of Hydroxyapatite and Wollastonite was optimised using the Design of Experiment. Hydroxyapatite-Wollastonite mixture powder will be spray-dried using the optimised process parameters.
- Objective 2: - To improve the flowability of the Wollastonite powder. Several attempts like spray drying, oven drying and heating to improve the flowability of the Wollastonite were unsuccessful due to its acicular shape. To support a flame spray technique, a vibrator was designed with air pressure and connected to the top of the cartridge assembly (consisting of wollastonite powder) to produce wollastonite powder that continuously flows which was not achieved.
- Objective 3: - To dip-coat the titanium substrate in solutions containing the Hydroxyapatite and Wollastonite gel. Hydroxyapatite was formed from calcium and

phosphate precursors, whereas Wollastonite was from the precursors of calcium and silicate. The present study consists of calcium nitrate tetrahydrate as a precursor of calcium, diammonium hydrogen phosphate as a phosphate precursor and tetraethyl orthosilicate as a silicate precursor. The results of dip-coated Hydroxyapatite and Wollastonite coatings on titanium substrate will be discussed. Wollastonite in the particulate form was added to the Hydroxyapatite gel to form a Hydroxyapatite/Wollastonite composite coating, and the result will be discussed in Chapter 4.

- Objective 4: To deposit an optimised mixture of Hydroxyapatite and Wollastonite obtained from the design of the experiment in Objective 1. Hydroxyapatite and Wollastonite was spray-coated with the process parameters obtained from Objective 1. Further screening of process parameters was applied for Hydroxyapatite/Wollastonite composite powder and Hydroxyapatite/Wollastonite was spray-coated with the above process parameters and optimised.

1.2 The Novelty of the Project

There are identified novelties to this research:

- Spray coating of Hydroxyapatite. Hydroxyapatite will be spray coated onto a prepared titanium substrate (at different roughness) with the process parameters obtained from spray drying of Hydroxyapatite. Not much research has been conducted on the spray coating of Hydroxyapatite on a titanium substrate.

- Addition of Wollastonite to titanium substrate. Wollastonite use as a biomaterial has not been fully explored. This research would help to explore the vast opportunity for depositing Wollastonite. Up until now, Wollastonite has only been used as a reinforcement material or filler. Its benefits as a bioceramic with superior mechanical and biomedical properties are yet to be explored thoroughly.

- Spray drying of the Hydroxyapatite-Wollastonite mixture in composite form. Very little research has been conducted to investigate the results concerning the optimum quantity of the Hydroxyapatite-Wollastonite mixture. This study helps identify the optimum quantities of Hydroxyapatite and Wollastonite with the help of the Design of the Experiments.

- Spray coating of Hydroxyapatite/Wollastonite composite powder onto a titanium substrate. Hydroxyapatite/Wollastonite mixture powder will be spray coated onto a titanium substrate using the optimised process parameters obtained from the spray drying results of the Hydroxyapatite/Wollastonite mixture powder. Very little research has been carried out regarding the chemical characterisation of the spray-coated HA/Wollastonite composite spray-coated with optimised process parameters.
- Sol-gel dip coating of Hydroxyapatite and Wollastonite separately onto a titanium substrate at different roughness. There is little published data on the dip coating of the Hydroxyapatite and Wollastonite on a substrate with different roughness. A thorough chemical investigation of the dip-coated Hydroxyapatite and Wollastonite onto a titanium substrate at different roughness will be carried out with a discussion of the results.
- Sol-gel dip coating of Hydroxyapatite/Wollastonite mixture. Initially, the prepared titanium substrates will be dipped into a Hydroxyapatite gel. The as-prepared coating would undergo post-processing to obtain a solid coating. The obtained coating would then be dipped into a Wollastonite gel and post-processed. Very little research has been carried out on the composite sol-gel dip coating of Hydroxyapatite and Wollastonite onto a prepared titanium substrate.
- Comparison of the spray-coated Hydroxyapatite, Wollastonite and Hydroxyapatite/Wollastonite composite and sol-gel dip-coated Hydroxyapatite, Wollastonite and Hydroxyapatite/Wollastonite composite on a titanium substrate. No previous studies have compared the spray techniques and dip coating techniques of Hydroxyapatite and Wollastonite onto a titanium substrate. The coatings obtained from both techniques will be compared for their microstructure point of view.

1.3 The Structure of the Report

- The first section of the thesis provides an abstract, introduction, aims and objective and novelty of the research.

- Chapter 2 details the literature under review. In this chapter, the bone description and its remodelling process are studied. Then biomaterials are described in which Hydroxyapatite and Wollastonite details are provided. Biocoatings are reviewed afterwards, followed by Hydroxyapatite biocomposite. Surface engineering is explained

to understand the behaviour of the biomaterial, followed by coating techniques of Hydroxyapatite and Wollastonite to end.

- In Chapter 3, the experimental equipment and procedures are detailed. The equipment for powder properties is explained at the start. Powder characterisation techniques such as hall flow meter and electric vibrator description follow this subsection. This subsection is followed by coating characterisation techniques such as scanning electron microscope, FTIR spectroscopy and X-ray diffractometer. This subsection is followed by substrate preparation techniques. Spray drying experiment and equipment information, along with the Design of Experiment analysis used (DOE) follows this subsection. This subsection is followed by a brief summary to improve the flowability of the Wollastonite powder. The techniques (spray-coating technique and sol-gel technique) to apply the Hydroxyapatite, Wollastonite and Hydroxyapatite/Wollastonite coating onto a titanium substrate follows this subsection.

- In Chapter 4, the results and discussion are covered for the current study. The results of the oven drying experiment, flowability results, roughness measurement of prepared substrate and morphology of both raw materials followed by spray drying results with Design of Experiment (DOE) are presented. Following that, the optimisation of the spray-dried powder is presented. The last subsection presents the results concerning the spray-coating and sol-gel dip-coating of the Hydroxyapatite, Wollastonite and Hydroxyapatite/Wollastonite powder, along with their chemical characterisation, followed by the summary of discussion.

- In Chapter 5, the conclusions and recommendations for future work resulting from the Master's study are presented.

2 Literature Review

In this chapter, a literature review is presented. This section begins with the bone, its structure, and how it remodels and remanufactures described, followed by biomaterials, classification, and their reaction with inner body tissues. In its subsection, Hydroxyapatite (HA) and Wollastonite are reviewed in detail because they are the primary raw material in this study. Then, coatings have been explained, where different types of biocoatings, which include a different combination of polymer-metal, polymer-ceramic and ceramic-metal have been demonstrated. This subsection focuses on Hydroxyapatite biocomposite in detail, followed by protective overlays and coatings, which include bond layers. Surface engineering, where the interaction of the implant material with the body environment, is then reviewed. Following that, the basics of thermal spray technology and the microstructure of the thermally spray coatings are described. Then plasma spray technology commonly used to deposit HA, has been studied in the next subsection along with its advantages and comparison with the thermal spray technology. Flame spray technology is described in the next subsection. Following that, the sol-gel dip-coating technique is explained. This section is followed by the failure of the bio coating. The last section concerns the DOE analysis used in the current study. The summary of the chapter concludes the chapter.

2.1 Bone Structure

The most prominent bones are present in the limbs and hip in a shaft form of a human. There are two types of bone tissue: compact or cortical bone and trabecular or cancellous bone [27]. In adult bone, 80% of the mass consist of cortical bone and the remaining 20% consists of trabecular bone [28]. The bone body is cylindrical, with the central cavity termed the medullary canal. The medullary canal is porous in the middle and denser in the extremities [29]. Marrow fills up the medullary canal and the spaces in the cancellous tissue [29]. Long bones are curved a bit rather than straight, which offers better strength to the bone [29]. The process of continuous regeneration and degradation of the bone is called ossification [29]. Many parts present in bone, namely the periosteum, marrow, vessels and tissues of blood etc. are illustrated in **Figure 1**.

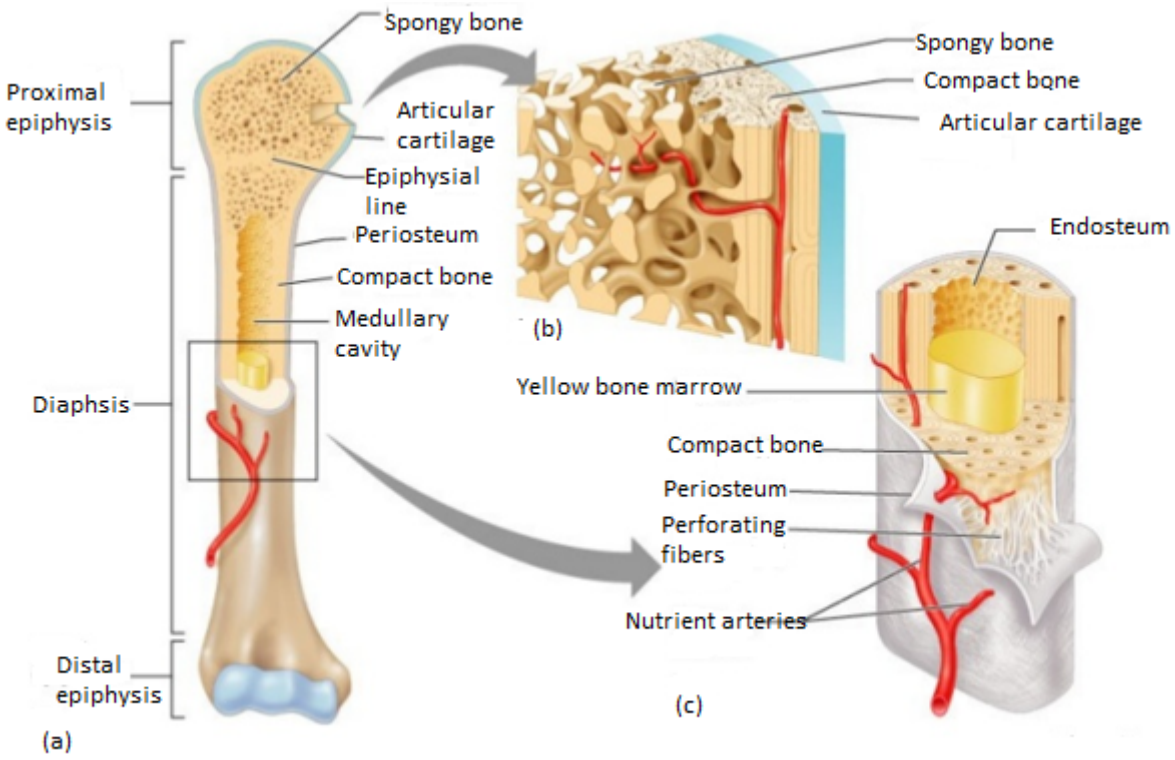

Figure 1, Structure of bone [30]

2.1.1 Bone Growth and Remodelling

Bone growth occurs by depositing the new bone lamellae onto an existing bone or a connecting tissue [31]. Osteocytes, osteoclasts and osteoblasts are the classifications of the bone cells. The osteoblasts and osteoclasts are the active adjacent sides involved in bone remodelling, and osteocytes remain stationery [31]. The bone growth is due to osteoblasts; bone degradation for regrowth is due to osteoclasts, and the matrix in which bone is grown is referred to as osteocytes [31]. Osteoblasts deposit a new bone matrix to bone width or depth [31]. This growth is called appositional growth [27]. Bone remodelling involves removing the existing bone by the osteoclasts and depositing new bone by the osteoblasts in which the newly formed spongy bone changes to compact bone, bone remodelling process involves balancing of bone formation and growth (ossification process) by osteoblasts and bone removal by osteoclasts [27].

Bone and its surrounding area consist of numerous cells. The three prominent cells are osteoblasts, osteocytes, and osteoclasts. In bone remodelling, osteoblasts are responsible for bone formation and repair. When the bone is formed, the osteoblasts get trapped in the spaces. These spaces are differentiated into cells called osteocytes. Osteoclasts are

responsible for the removal of dead bone and living bone, resulting in a process called resorption. [32]

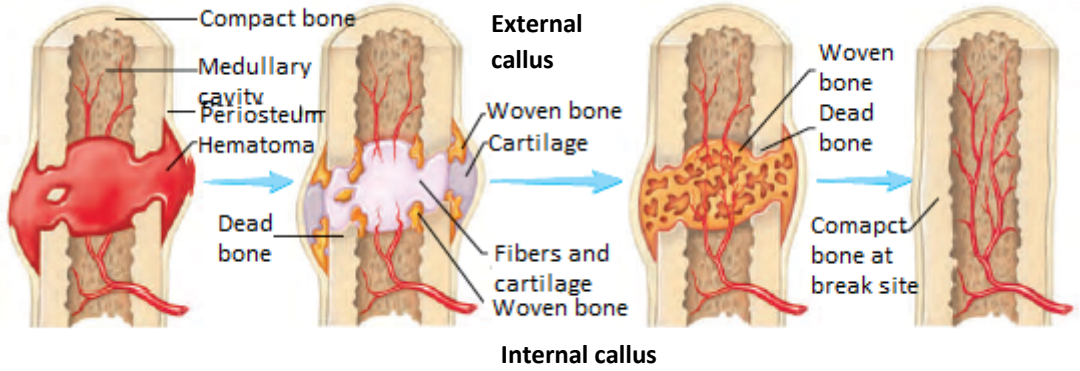

Figure 2, Bone repair [27]

2.1.2 Bone Repair

Bone repair is a step-by-step procedure, from blood to the dead bone, to woven bone to compact bone [27]. Blood released from the damaged cells leads to the formation of the hematoma—the internal callus form between the bone, and the external callus forms around the collar [27]. Woven, spongy bone replaces the internal and external callus, this compact bone replaces the woven bone, and the medullary cavity replaces the callus [27]. **Figure 2** shows the bone repair procedure.

2.1.3 Chemical Composition of Human Bone Mineral

The composition of natural bone is shown in **Figure 3**. The chemical composition of the natural bone consists of both organic and inorganic material. The organic material consists of collagen fibre and inorganic calcium and phosphate, whose chemical formula matches Hydroxyapatite [6]. As an estimate per weight, bone tissue consists of 25% water, 43% mineral, 29% collagen and 3% non-collagenous organic molecules. Bone consists of 99% calcium, and blood cells contain 1% calcium. The bone tissue consists of bone cells, minerals, and matrix [33].

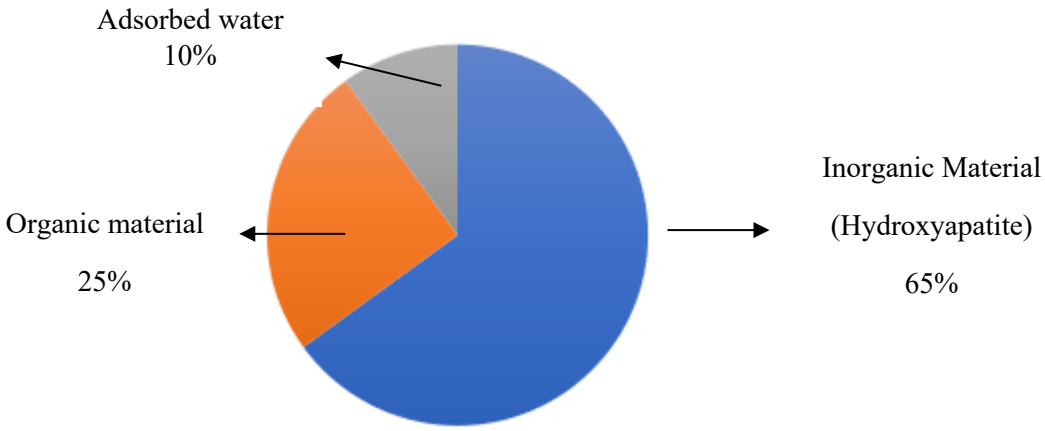

Figure 3, Composition of natural bone [34]

Bone minerals consist of biological apatite and carbonate hydroxyapatites. Carbonate hydroxyapatite dissolves very quickly compared to normal Hydroxyapatite with an ideal stoichiometric ratio [35]. The inorganic structure can be easily substituted by chlorine, carbonate and carbonate as the Hydroxyapatite is receptive. It is easy to displace the hydroxyl ion present in the inorganic form [7].

2.1.4 Implant Interaction with Bone and Tissue

a) *HA-coated titanium implant inside the body*

When a HA-coated titanium implant is placed inside the body, several biological and physiological reactions occur: 1) Hemostasis, where blood clotting occurs immediately at a site; 2) Protein adsorption, where the protein is adsorbed onto an HA surface, mediates cell attachment; 3) Cell recruitment and attachment, osteoblasts and osteoprogenitor cells (bone-forming cells) are recruited to the implant; 4) Osteoconduction, where the HA coating acts as a scaffold guiding the growth of new bone; 5) Bone formation and mineralisation, osteoblast begin producing bone and calcium and phosphate ions (Ca^{2+} and PO_4^{3-} ions, respectively) from HA contributes to mineralisation; 6) Osseointegration, new bone directly forms onto the HA surface; 7) Bone remodelling and HA resorption: bone remodelling is a continuous process of bone building (osteoblasts) and bone resorption (osteoclasts), and HA resorption releases calcium and phosphorous ions, which can further stimulate bone remodelling; 8)

Mechanical stability; the strong bond between the bone and HA-coated implant ensures the mechanical stability of the implant and finally; 9) Functional integration; proper osseointegration ensures the efficient load transfer from implant to surrounding bone, reducing stress shielding.

b) Wollastonite-coated titanium implant inside the body

Similar to the HA implant inside the body, the Wollastonite-coated implant immediately interacts with the body, resulting in physiological and biological process. The process overview similar to HA but also different from HA as follows: 1) Hemostasis; 2) Protein adsorption; 3) Cell recruitment and attachment; 4) Ion release and osteoconduction; however, Wollastonite releases Ca^{2+} and Si^{4+} into the surrounding tissue; 5) Bone formation; 6) Bioactivity and osseointegration; Wollastonite promotes the formation of the apatite layer on its surface, similar to HA with osteoblasts and osteoclasts contributing to bone formation and remodelling mechanism; 7) Bone remodelling; 8) Mechanical stability, and finally 9) Mechanical stability. All the process is similar to HA-coated titanium implants, except Wollastonite releases silicon and calcium ions (Ca^{2+} and Si^{4+} ions, respectively) into the body (HA releases calcium and phosphate ions (Ca^{2+} and PO_4^{3-} ions, respectively)), and Wollastonite is more bioactive than Hydroxyapatite.

c) HA/Wollastonite coated titanium implant inside the body

The process leading to physiological and biological changes when an implant interacts with the body is like that of HA-coated titanium implants and Wollastonite-coated titanium implants. The only difference is that both Hydroxyapatite and Wollastonite release Ca^{2+} and Si^{4+} ions into the body, and both HA and Wollastonite promote the formation of an apatite layer on their surface.

d) Advantages of HA/Wollastonite coated hip implant over monolithic HA hip implant

The major benefits of using HA/Wollastonite-coated hip implants are: 1) Enhanced bioactivity; 2) Ion release; 3) Higher tensile strength and modulus of elasticity resulting in improvement in durability and mechanical stability; 4) The properties of HA/Wollastonite implant can be tailored based on needs of the patient; and 5) Cost-effectiveness, as Wollastonite is less expensive than HA.

2.2 Biomaterials

The main criterion for a bioactive material is the ability to induce bone formation mechanisms during its participation in bone remodelling. In the 1960s, metals and polymers such as stainless steel, polyethene and polymethylmethacrylate were used as biomaterials [36]. In the 1970s, a double-cup prosthesis system with a femoral component and acetabular cup was developed [36]. The materials used for the femoral component include metals such as high-grade stainless steel, cobalt-chromium alloys or titanium alloys [37]. In contrast, acetabular cups include polymers such as high-density polyethene or ultrahigh molecular weight polyethene, whereas the femoral head consists of alumina and zirconia [37].

Biomaterials are classified into four categories [38, 39]:

- Biometals.
- Biomedical polymers.
- Bioactive ceramics.
- Bioactive composites.

2.2.1 Biometals

Biometals have progressed, including metals ranging from bare stainless steel to the latest titanium alloys [36]. Cobalt-chromium alloys have better strength and corrosion resistance than stainless steel. Stainless steel is biocompatible, strong and cheap, but stainless steel can undergo oxidation and release ions in the body, leading to corrosion and ultimately causing implant failure [9]. Stainless steel has a modulus of elasticity ten times higher than bone, leading to a stress-shielding effect [9]. The cobalt-chromium elastic modulus is approximately 240-250 GPa compared to 200 GPa for stainless steel [36].

Due to its strength and low density, titanium alloy with a modulus of elasticity half of the stainless steel and cobalt chrome-nickel alloys leads to less stress shielding effects [36]. Ti-6Al-4V is still used in the biomedical industry [1]. Another material is Ti-13Zr-13Nb, which is stronger than Ti-6Al-4V and has a lower modulus of elasticity but is still beneficial for biomedical applications [36]. Ti-6Al-7Nb and Ti-5Al-2.5Fe can be helpful due to their minimum elastic modulus and excellent biocompatibility [1]. Shape memory alloys such as NiTi, where modulus varies at different states, can benefit load-bearing

applications [1]. Metallic ions play a crucial role in improving bone quality, including bio-inorganic ions such as calcium, magnesium, strontium, silicon, zinc, copper and cobalt [40].

A significant drawback of biometals is the stress shielding effect [1]. Due to high elastic modulus, the metal absorbs all the load, leading to quicker resorption of the bone [1]. Not every biometal is bioactive; therefore, surface modification becomes vital to increase metal bioactivity [1].

2.2.2 Biomedical Polymers

Biocompatible polymers participate in the formation of bone without toxic effects on the body, and biodegradable polymers are primarily suitable for drug delivery applications [41,42].

Joint replacement components mostly employ polymers such as polyethene (PE), acrylic bone cement, thermoplastic polyether, ketone, etc. Medical-grade silicone elastomers replace joints in rheumatoid arthritis [1].

Biopolymers have applications in other bone/joint fixation. Medical grade silicone replaces the smaller bone in hand joints with finger motion improvement [1]. Carbon fibres have been tested for spine surgery, hip replacement and internal fixation [1]. Polyester and polytetrafluoroethylene are tested for ligament prostheses. Variable chemical composition to match the rigidity of cortical bone is any significant polymers advantage [1]. There are other bioresorbable polymers such as polyglycolide (PGA), polylactide (PLA), polydioxanone (PDS), polyorthoester biodegradable systems, chitosan and poly (2-hydroxyethyl-methacrylate) (PHEMA) and hydrogels [1].

Biodegradable polymer mostly has drug-delivery applications. Biodegradable polymer causes less inflammation and tissue death than prostheses [43]. PLA, PGA, PCL and PHB scaffolds have a highly interconnected porous structure that enables tissue growth, vascularisation and nutrient growth [1]. Micro-based polymer particle such as polylactide (PLA), polyglycolide (PLG), polyactidecoglycolide (PLGA), and polycyanoacrylate (PCA) has a drug delivery application [1]. The attached drug is either absorbed or encapsulated for site-specific drug release to treat tumours, antigens, and inflammatory sites [44].

a) *Polymer cement*

Polymethylmethacrylate cement (PMMA) is one of the initial development in acrylic bone cement [45]. PMMA cement is still widely used to support bone and implants. The main advantage of PMMA is the ease of manufacturing and quick fixation at the initial stages [1,45].

i. Drawbacks of Polymer cement

Some disadvantages of polymer cement include bioinertness, wear, debonding, ill effects of polymerisation, and cell necrosis [3, 45, 46]. Wear, bone/cement interface debonding due to relative motion causes resorption leading to aseptic loosening [46]. The difference in stiffness between the prosthesis and cement causes fracture and failure of cemented hip arthroplasty [46]. Stress shielding may occur because of the higher load-bearing implant resulting in the weakening of the bone with minimal stress [46]. The cytotoxic effect of monomer, high inflammation due to exothermic temperature of polymerisation, and interference of the body cells with polymerisation and hardening of the cement are three main drawbacks of cement hip arthroplasty [3]. Cell necrosis due to exothermic reactions can hamper the process of bone regrowth [3]. Proper knowledge of the cement, curing characteristics, and surgical procedures are required to reduce cemented hip arthroplasty drawbacks [47].

2.2.3 Bioceramics

Bioceramics with biofunctionality properties can induce biological activity to repair damaged organs [48]. This biofunctionality refers to the properties a medical device must perform from the standpoint of physical, mechanical and biocompatibility throughout its life as an implant and must be closely related to the interaction between the biomaterials and living tissues with which they come in contact [39]. The earliest use of bioceramics was in the 1970s [1]. Unlike biometal, bioceramic does not emit harmful ions [49]. Unlike biometal and biopolymer, bioceramic implanted inside the body does not lead to wear debris [50]. The significant bioceramic advantages over the other material include biocompatibility, appropriate mechanical strength, low friction, wear resistance, and chemical stability [51].

Calcium phosphate is present in tooth enamel, with high bioactivity of calcium phosphate due to the increased presence of calcium and phosphate in the body [49]. The bone tissue is a dense organic matrix consisting mainly of collagen and inorganic deposits of

Hydroxyapatite [$Ca_{10}(PO_4)_6(OH)_2$] and calcium carbonate ($CaCO_3$) [52]. **Figure 4** describes three different bioceramic types; bioinert, bioactive and biodegradable. **Table 1** details the bioceramic types, their interaction with tissue, their type of attachment and some examples.

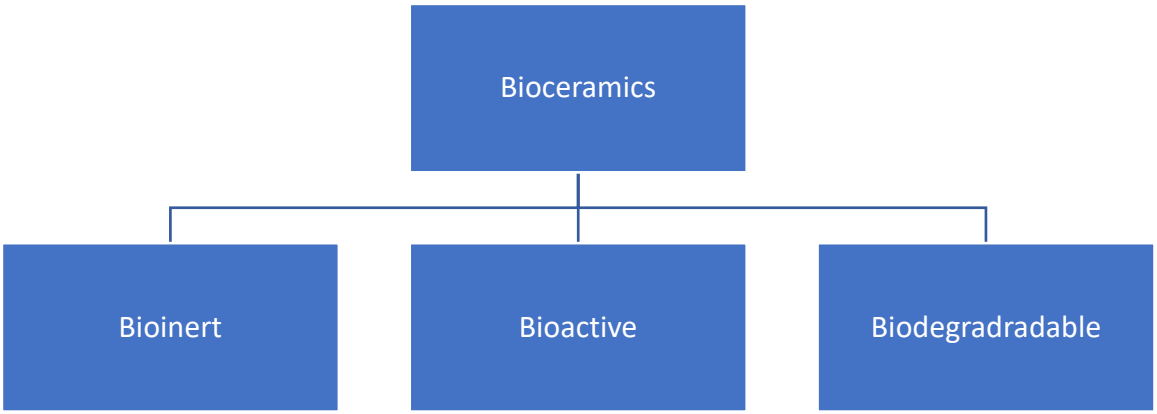

Figure 4, Types of bioceramics [53]

Table 1, Classification of bioceramics [48]

Type of ceramics	Interaction with tissue	Type of attachment	Example
Bioinert	Little or no response	Mechanical fixation	Alumina (Al_2O_3), zirconia (ZrO_2)
Bioactive; resorbability and promote bone integration	Promote a distinct and positive response from the tissue	Chemical bonding	Hydroxyapatite, bioglass, Wollastonite and glass ceramics
Biodegradable	Gradually dissolve within the body	Replaced by tissue	Calcium phosphate cement and tri-calcium phosphate.

a) *Bioinert ceramics*

Bioinert bioceramic implants have minimum interactivity between the implant and surrounding tissue [54]. There are mainly two materials classes: zirconia and alumina. The chemical inertness, abrasion strength, and resistance of alumina have made them more suitable for dental and bone, and the main application of zirconia is THR (total head replacement) [55].

Alumina ceramics have an elevated biocompatibility level, no biological degradation, hardness, and a fine surface, suitable for application in the modular femoral ball and the acetabular-femoral combinations [1]. Relative micromotion occurs in bioinert implants due to a lack of biological bonds between the implant and host tissue leading to the formation of fibrous tissue between the implant and the bone [51,56]. Some application of the alumina implant includes rabbit eye socket, knee joints, and sputtering bioactive glass film to the alumina layer for bioactivity enhancement [51].

Zirconia was mainly used as a pigment in ceramics [55]. The addition of oxide to stabilise zirconia became imperative [55]. Therefore, yttria stabilised zirconia and magnesium oxide partially stabilised zirconia [55]. High mechanical strength and fracture toughness applications mainly require zirconia [51]. The significant shortcomings of zirconia are strength reduction with time in the liquid, wear properties and potential radioactivity of the material [56]. The wear resistance of zirconia is 5000 times poorer than alumina [56]. Zirconia with radioactive material like thorium and uranium can destroy soft and hard tissue cells [56]. Zirconia has high fracture toughness strength but a lower modulus of elasticity than alumina [56]. The stress shielding effect occurs due to the superior elastic modulus of zirconia and alumina (of the order 15X to 7600X) compared to natural bone [56].

2.2.4 Bioactive Ceramics (HA; Bioglass; Wollastonite; and Glass-Ceramic)

Allografts, autografts and artificial materials are three techniques used to replace damaged bone or tissue when the bone cannot heal itself [6]. Autograft is a technique where a healthy human bone part is transferred to replace damaged tissue, whereas allograft transplants bone tissue from one human to another [6]. Though widely used, these techniques (allografts and autografts) have limitations, such as the risk of infection, limited availability and possibility of damage to the donor [6]. Therefore, artificial

material for bone replacement is a preferred technique [6]. The need for direct bone bonding with favourable tissue reaction led to the bioactive ceramic discovery in the 1980s [57]. The bioactive material creates a bioactive environment at the materials interface, which results in bonding between tissues and material [39]. Bioactive ceramics form a direct bond between the bone and soft tissue of living organisms [58]. The bioactivity leads to a process where implant material firmly bonds to the host bone through growth or ingrowth without bone cement [59]. Bioactive ceramics can be grouped into three categories in the present study: calcium phosphate (Hydroxyapatite), bioactive glasses, Wollastonite and glass-ceramic [48].

a) *Hydroxyapatite (HA)*

Hydroxyapatite (chemical formula $Ca_{10}([(PO)_4]_6(OH)_2)$) has a composition similar to the inorganic part of the bone [60]. Natural bone has a composition of 69 wt.% of the inorganic part of the bone, collagen 20 wt.%, and water 9 wt.% [60]. The stoichiometric ratio (Ca/P) should ideally be 1.67, with CaO formation at a stoichiometric ratio of more than 1.67 and the formation of α-TCP (tricalcium phosphate) or the β-TCP when the Ca/P ratio is less than 1.67 [60]. The bending, compressive, and tensile strength of HA range from 38-250MPa, 120-900 MPa, and 38-300 MPa, respectively [60]. Data show an incremental increase in strength up to a Ca/P of 1.67 and a reduction from 1.67 onwards [60].

i. Method of synthesis of Hydroxyapatite

Solid-state and liquid-state reactions are the two main processes used to synthesise HA [34]. In solid-state synthesis, the combination of precursors of calcium and phosphorous is fired at elevated temperatures without solvent use [61]. Liquid state synthesis is mostly a solution-precipitation process, immersing precursors of calcium and phosphorous in a solvent [62]. **Table 2** describes the two methods along with their advantages and disadvantages.

Table 2, Advantages and disadvantages of solid-state and liquid-state methods [33, 34]

Method	Advantages	Disadvantages
Solid-state synthesis (Solid State Reaction, Mechanochemical Synthesis)	Phase pure HA is formed.	1. Complicated procedure. 2. High reaction temperature. 3. Long heat treatment time. 4. Low sinterability. 5. High risk of contamination. 6. Milling is always required.
Liquid state synthesis (Precipitation, Hydrothermal, Hydrolysis and Sol-Gel Techniques)	1. High purity as the by-product is only water 2. Simple, low-cost procedure 3. Small particle size	1. Low crystallinity. 2. Poor property of powder as it is susceptible to agglomeration.

Several other routes exist to manufacture HA with different raw materials [34]. The hydrothermal technique employed coral to manufacture HA [63]. For example, eggshells were calcined at 900 °C at 4 °C/min, and phosphoric acid was mixed [64], at an acid weight ratio (wt.%) varied from 1:1.0 to 1:1.7, synthesising HA at a weight ratio of 1:1.20 and Ca/P ratio of 1.65 [64].

The sol-gel process uses alkoxide precursors to produce monophasic HA [65]. The sol-gel technique is a wet precipitation technique with a chemical reaction between calcium and phosphorous ions under particular pH and temperature conditions [66]. In the aqueous sol-gel process, a solution of acetate monohydrate (precursor of calcium) and ammonium–hydrogen phosphate (precursor of phosphorous) mixed in distilled water and tartaric acid leads to the formation of precipitate [67]. The precipitate underwent various thermal treatment processes in the sol and gel, leading to the formation of powder [67]. A novel approach for the manufacturing of HA was to use an ethylene glycol solution of ($Ca(OAc)_2.xH_2O$), and a butanol solution of P_2O_5 utilised as precursors for calcium and phosphorous, respectively [68]. Adding acetic acid and ammonium nitrate to this solution resulted in rapid precipitation synthesis of HA [68]. The sol-gel technique can also manufacture nanosized powder with thermal treatment to a powder size of 50-150 nm

[69]. Precipitation of calcium nitrate tetrahydrate and dibasic ammonium phosphate synthesised nanostructured HA [70].

The mechanochemical technique in solid-state synthesis was employed to manufacture HA [71]. In mechano-chemical processes, the $(NH_4)_2HPO_4$ solution was added slowly to the $Ca(OH)_2$ suspension, followed by vigorously stirring by a magnetic stirrer [71]. After mechanochemical hydrolysis, the materials were washed and milled to form HA powder [71]. Another mechanochemical method consisting of calcium pyrophosphate (precursor for phosphorous) and calcium carbonate (precursor of calcium) was mixed in a ratio of 3:4, leading to the synthesis of HA with a stoichiometric ratio of 1.67 [72]. In the neutralisation technique, phosphoric acid was added to the mixture of calcium hydroxide and lime suspension in the reactor at 600 °C. The introduction of phosphoric acid at the stirring rate of 700 rpm to the mixture can lead to the manufacture of HA [73]. Hydration of α-TCP in the microwave heating technique by changing reaction conditions (increasing reaction temperature and decreasing pH) can also lead to the manufacture of HA [74].

According to FDA regulations, the HA used in hip implants must have a 50-70% crystallinity, while the purity of HA used in hip implants must be more than 95%, according to ASTM F1185-03. HA synthesised by solid-state techniques is pure and generally follow the ASTM regulation. Both crystallinity and purity are crucial for the HA used for hip implants and need to be balanced to an optimal level. Crystallinity affects the mechanical properties and bioactivity. A balanced crystallinity maintains strength and resorbability and promotes bone integration without adversely affecting structural integrity. High purity is necessary to ensure biocompatibility. Moreover, a pure-HA implant reduces the possibility of inflammation, toxicity or any adverse biological reactions without compromising implant safety and performance. The crystallinity of HA for hip implant application can be measured by XRD and FTIR, where XRD provides information about crystalline structure and FTIR gives insight about chemical bonding and structured order. The purity of HA for hip implant can be measured using; XRF, ICP-OES/MS, TGA and chemical analysis. XRF and ICP-OES/MS are sensitive and accurate in detecting chemical composition and impurities. TGA gives information about thermal stability and presence of volatile impurities. Hence this research uses XRD and FTIR as part of its characterisation.

Porous HA can be synthesised due to pore-creating volatile particles, such as the admixture of water-soluble porogen; a marine coral skeleton; the natural ceramic foaming technique; and the polymeric sponge method [75].

Some crucial forms of HA include whisker and nano forms [60]. Precipitation of calcium nitrate tetrahydrate and dibasic ammonium phosphate synthesised nanostructured HA, where the precipitate obtained can be stabilised by polyacrylic acid during the hydrothermal treatment, which leads to HA synthesis with rod-like structures [70]. Nanosized HA in the form of residue was collected in the cyclone after the evaporation of the HA precipitate solution in the spray drying technique [76]. HA whiskers can be manufactured by a precipitation-hydrolysis technique using 0.167mol/l calcium ions, 0.1 mol/l of phosphate ions and 0.5-1 mol/l urea [77]. The HA whiskers could not form directly from the saturated solution; therefore, hydrolysis of fibrous OCP (octacalcium phosphate) provided framework for the growth of HA whiskers with an aspect ratio in the range of 40-100 [77].

The thermal stability of HA depends on the Ca/P ratio [78]. The thermal treatment of HA showed adsorbed water release in the temperature range of 30-570 °C [78]. Dehydroxylation removes water molecules that resumes when HA is heated at 600 °C-1200 °C [78]. Thermal decomposition studies from 1000 °C to 1500 °C conducted on HA showed no change in structure up to 1350 °C but a difference in chemical composition changing to TTCP (tetra- calcium phosphate) and α-TCP (tricalcium phosphate) after 1350 °C [79].

b) Bioglass

Due to the poor bioactivity of polymers and metals, bioglass was developed. Bioglass mainly consists of calcium, potassium, sodium, and silicon oxides [59]. Only four oxides: SiO_2, P_2O_5, Na_2O, and CaO, are FDA-approved [80]. Bioglass mainly has the chemical composition of 46.1 mol% SiO_2, 24.4 mol% Na_2O, 26.9 mol% CaO and 2.6 mol% P_2O_5 [80]. Biomedical application mainly employs silicate-based glasses [81]. Other oxides, including boron, aluminium, strontium, magnesium, and titanium, can be used as an additive to regulate bioglass properties based on the application [80, 82]. Due to its resorbability, bioglass (45S5) has inferior mechanical properties compared to Hydroxyapatite [39]. 45S5 bioglass has a higher Ca/P ratio of 5 compared to 1.67 that of

Hydroxyapatite which makes it reactive in the physiological environment, whereas Hydroxyapatite is stable towards bioresorption [83–85].

i. Techniques to manufacture bioglass

Melt quench, sol-gel, and microwave-assisted techniques are used to manufacture bioglass [80]. In the melt quench technique, the raw material mixture is melted in a platinum crucible at 1100-1650 ºC for 1-3 hours, followed by water pouring which leads to frit (mixture of silica and flux fused at high temperature to make glass) formation [86]. The frit formed undergoes a port processing technique such as drying, milling, and sieving, leading to powder formation [86]. Powders obtained by the melt quench technique have poor porosity and lesser apatite formation but better mechanical properties than the sol-gel technique [86].

Sol-gel technique involves the synthesis of the sol, which is metal-organic and metal salt precursors [87]. The precursor leads to gel formation, followed by drying, and calcination leads to bioglass formation [87]. The bioglass formed by this technique has superior bioactivity, with the possibility of intricate structures like mesoporous and lattice [88].

In the microwave-assisted technique, the precursor solution in deionised water is transferred to the ultrasonic bath [89]. Cost-effectiveness with lesser time for synthesis and the possibility of modification of powder size to micro and nano by ultrasonic irradiation are some of the pros of the microwave-assisted technique [90].

ii. Bioactivity mechanism in bioglass

The possibility of bioactivity is higher with oxides such as SiO_2, CaO and Na_2O combinations than with P_2O_5 [59]. The formation of rich HCA (hydroxyl carbon apatite) takes place with bioglass immersed in SBF fluid [59]. Dissolution is followed by three steps: leaching, dissolution, and precipitation [59]. The leaching process releases ions, whereas dissolution is created by breaking the Si-O-Si-O-Si bond [59]. The precipitation process involves forming a rich calcium phosphate layer on its surface [59]. The HCA crystallisation occurs within two hours for the glasses up to 53% mole of SiO_2 [59]. For 53 to 58 moles per cent SiO_2, it takes 4-5 days to form the HCA crystallisation, and the bonding is only to the bone [59]. For the >60%, the HCA crystallisation does not occur [59]. When a tight bond between the bone tissue and HCA formed on the surface of bioglass is established, it can have a silica rate ranging from 42-54 % after one week; for

54-60%, the bond sets after 2-4 weeks, whereas bioglass having more than 60% of silica lose their bioactivity [91].

Cacciotti et al. [91] observed a higher temperature heat treatment of 45S5 (45%wt SiO2) glass. 45S5 bioglass underwent weight losses at 100 ºC, due to reduction in water and hydroxyl ions at 400 °C and weight loss at 610 ºC due to crystallisation [91]. At around 550 ºC, the bioglass homogeneity reduced with high viscosity, and the silica-rich phase dominated flow behaviour [92].

c) Wollastonite

Wollastonite is a calcium metasilicate with a molecular formula of $CaSiO_3$ with a molecular mass of 114 g/mol [93, 94]. Theoretically, Wollastonite consists of approximately 48.3% CaO and 51.7% SiO_2 [94]. Wollastonite has a specific gravity of 2.91; a specific surface area of 845 m^2/kg, a pH of 9.9; a water solubility of 0.0095 g/100 cc and a density of 2.9 g/m^3 [93]. Wollastonite has an acicular structure, poor electrical conductivity of 1.5 E-11 mho/m and a high Mohr hardness of 4.5; a brilliantly white colour with brightness ranging from 80 to 95; a melting point of 1540 ºC; a low thermal conductivity of approximately 2.70 W/m °K and low coefficient of thermal expansion of 6.5 X 10^{-6} mm/mm/°C [95]. Wollastonite has good mechanical properties with Young's modulus of 303-530 GPa and tensile strength of 2700-4100 MPa with the compressive strength of 1.6 MPa at 1100 °C [93, 96].

Wollastonite can occur naturally or synthetically [97]. Calcinating silica (99% purity) and CaO (calcium oxide) at 900 ºC led to the synthesis of Wollastonite [97]. Thermal treatment ranging from 900 ºC to 1250 ºC produced amorphous β-Wollastonite, and sintering at 1400°C led to stable synthesised α-Wollastonite (pseudo-wollastonite) [98]. Rice husk ash and limestone with a precursor ratio of 55:45 (rice husk containing 90% silica and limestone consisting of 97% calcium oxide) also led to the synthesis of Wollastonite [99]. Heating a mixture of 75g silica and 125g calcium carbonate in the platinum-rhodium crucible at 1600ºC for five hours led to frit (the mixture of silica and calcium carbonate at elevated temperature) formation [100]. Immersion of the frit in chilled water followed by milling led to Wollastonite synthesis with the required microstructure [100]. Waste soda-lime silicate and calcium oxide prepared by the conventional melt quench method led to the manufacture of Wollastonite-based glass-ceramic with Ca/P (stoichiometric ratio) from 1.65 to 2.24 [22]. The mixture of silicon

dioxide and calcium carbonate in the sodium and potassium flux salt, followed by calcination at 950 °C, led to deionised salt synthesis [101]. This technique is known as the salt fusion method, where a deionised salt reaction leads to the production of Wollastonite [101].

Wollastonite is bioactive due to its ability to bond with the bone tissue. Wollastonite cannot be typically classified as resorbable. Wollastonite degrades over time but the degradation rate is slow compared to resorbable materials such as β-TCP and bioglass. Wollastonite cannot be considered bioglass as it is amorphous, contributing to its bioactivity. Wollastonite is bioactive by releasing calcium and silicon ions in contact with bodily fluids. It facilitates the formation of a hydroxyapatite layer on its surface, whereas bioglass releases ions into the surrounding bodily fluid, forming a hydroxycarbonate layer on the surface of a glass. [102]

Wollastonite can be used as a bone graft material, bone cement, or scaffold for tissue engineering. Its slow degradation rate and excellent bioactivity make it suitable for long-term applications in bone repair and regeneration. Bioglass, due to its bioactivity and excellent bonding with soft and hard tissue, can be used for bone regeneration, dental application and as a coating for implants. [102]

i) Bioactivity mechanism in Wollastonite

The bioactivity of the Wollastonite can be explained in 5 steps: 1) Immersion of Wollastonite in SBF fluid; 2) Ion exchange, where calcium ions (Ca^{2+}) exchange ions with hydrogen in SBF fluid; 3) Formation of silanol, there is a formation of Si-OH on the surface; 4) pH increase, pH of the SBF fluid increases due to calcium ions, OH^- ions in SBF fluid exchange ions with the surface layer, leading to the production of $Si\text{-}O^-$ ions on the surface layer; and 5) Apatite precipitation, the calcium in the SBF reacts with the surface layer, resulting in the apatite formation on the surface layer. [102]

d) Glass-ceramic

Another class of bioresorbable ceramics is A-W (Apatite-Wollastonite) glass-ceramic. Glass-ceramics are polycrystalline prepared by controlled crystallisation of glasses [103]. The composition of A-W glass ceramic is 34.2 wt.% SiO_2, 44.9 wt.% CaO, 16.3 wt.% P_2O_5, 4.6 wt.% MgO and 0.5 wt.% CaF_2 [104]. This material class has the mechanical

strength of Wollastonite and the ability to form natural bone similar to Hydroxyapatite [103]. A-W glass-ceramic has a density of 3.07 g/cm^3; a bending strength of 215 MPa; compressive strength of 1080 MPa; Young's modulus of 118 GPa; Vicker's microhardness of 680 HV and fracture toughness of 2.0 MPa$^{1/2}$ [105]. The chemical composition of A-W glass-ceramic was 4.6% magnesium oxide, 44.9% calcium oxide, 34.2% silicon dioxide and 0.5% calcium difluoride with the percentage of material as 35-40-25 (apatite-wollastonite-glass) respectively [106]. The compressive strength of A-W glass-ceramic was 127.3 MPa, and the flexural strength was 43.2 MPa when an equal quantity of apatite and Wollastonite was used [107]. Composite of A-W glass-ceramic obtained by 3D printing when sintered at 1300 ºC for 3 hours produced the optimal mechanical results in terms of flexural strength and compressive strength [108]. The A-W glass-ceramic composite formed had less porosity and led to the formation of bioactive calcium phosphate when immersed in SBF fluid after one day [108]. Therefore, the ceramic composite achieved a higher relative density of 80% due to sintering effects [109]. Glass ceramic scaffold manufactured by melt quenching technique showed better biocompatibility as tested by planting MSC (mesenchymal cells) and measuring via MTT assays [110]. A-W glass-ceramic is bioactive, biocompatible, and can grow bone activation cells on its porous scaffold [110]. RGD peptide used with A-W ceramic as a binder improved cell adhesion and proliferation [111].

A-W glass-ceramic used as an intramedullary plug instead of PMMA cement with a porosity of 70% and pore size of 200μm had identical compressive strength to the cancellous bone (rabbit) [112].

Crystalline apatite and β-Wollastonite introduced in the MgO-CaO-SiO_2-P_2O_5 glassy matrix showed bioactivity, biocompatibility, and good mechanical properties [113]. This glass-ceramic is mainly suited for dental applications [113]. Alternatively, the reagent grade of MgO, $CaCO_3$, SiO_2, $CaHPO_5.2H_2O$, and CaF_2 was put in the crucible, calcined, and then melted in a SiC furnace [113].

2.2.5 Biodegradable Ceramics

Calcium phosphate bioceramics occur mainly in amorphous material, primarily in restorative surgery in dental and orthopaedic applications [114]. But their application remains vital due to their bioresorbable properties, where the rate is nearly equal to the new bone tissue formation rate [51]. Calcium phosphates exhibit excellent

biocompatibility leading to bone integration—these phenomena show the closest chemical resemblance to mineral bone [115].

Calcium phosphate cement has strong crystal bonds, increasing cellular activity and stimulating bone proliferation [51]. Calcium phosphate dissolves in SBF and releases calcium and phosphorous ions, which reprecipitates and leads to bone formation [51]. They can bond with the bone without medication and a non-fibrous interface layer [1]. The resorption rate of calcium phosphate should be equal to bone formation to make it an ideal biomaterial [1]. Calcium phosphate cement can be more advantageous than PMMA cement as it does not lead to cell necrosis and promotes biological fixation [116]. Ooms et al. [117] compared calcium phosphate cement consisting of 61% α-TCP, 26% $CaHPO_4$, and 10 % calcium carbonate with 3% HA with PMMA cement. The PMMA cement had a fibrous layer, whereas a thin layer of bone was deposited on the site where calcium phosphate cement was implanted showing its bone-bonding ability [117]. **Table 3** describes various calcium phosphate components with their chemical formula and Ca/P.

Table 3, Various calcium phosphates with their respective Ca/P stoichiometric ratios [61, 115, 116]

Ca/P	Name	Formula
2.00	Tetracalcium phosphate	$Ca_4O(PO_4)_2$
1.67	Oxyapatite	$Ca_{10}(PO_4)_6O$
1.67	Fluorapatite	$Ca_{10}(PO_4)_6F_2$
1.67	Hydroxyapatite	$Ca_{10}(PO_4)_6(OH)_2$
1.50	Tricalcium phosphate (α,β)	$Ca_3(PO_4)_2$
1.33	Octacalcium phosphate	$Ca_8H_2(PO_4)_6.5H_2O$
1.20-2.20	Amorphous calcium phosphate	$Ca_xH_y(PO_4)_z.nH_2O$ n=3-4.5, 15-20%H_2O
1.00	Dicalcium phosphate dihydrate	$CaHPO_4.\ 2H_2O$
1.00	Dicalcium phosphate	$CaHPO_4$
1.00	Calcium pyrophosphate	Ca_2P2O_7
1.00	Calcium pyrophosphate dihydrate	$Ca_2P_2O_7.2H_2O$
0.70	Heptacalcium phosphate	$Ca_7(P_5O_{16})_2$
0.67	Tetracalcium dihydrogen phosphate	$Ca_4H_2P_6O_{20}$
0.50	Monocalcium phosphate monohydrate	$Ca(H_2PO_4)_2\ H_2O$
0.50	Calcium metaphosphate (α,β)	$Ca(PO_3)_2$

In **Table 3**, as mentioned above, the Ca/P ratio of various calcium phosphates is given. Ideally, the Ca/P ratio of a calcium phosphate should be 1.67. The Ca/P ratio of a substance is measured by X-ray fluorescence (XRF), inductively coupled plasma optical emission spectroscopy (ICP-OES), energy dispersive X-ray spectroscopy (EDS or EDX), X-ray diffraction (XRD) and chemical analysis. describes various calcium phosphate components with their chemical formula and Ca/P. XRF and ICP-OES are used to measure the Ca/P of a large sample accurately. EDS equipped with SEM is used for detailed, localised analysis within a sample. XRD provides detailed information about

the crystallinity and phase change, and chemical analysis provides a benchmark for accuracy. [118–122]

There are various calcium phosphate compounds. Some calcium phosphates include Hydroxyapatite (HA), fluorapatite, β-TCP (beta-tricalcium phosphate), octacalcium phosphate, amorphous calcium phosphate and tetra calcium phosphate [116]. Some calcium phosphate substitute material performs rapid resorption, while others are slow [123]. Slow resorption material restores the bone part towards better quality, but recovery is longer, whereas quick resorption material becomes more similar to their reference bone material [123]. Below is the relationship between different calcium phosphate materials in terms of solubility [52]:

Fluorapatite < Hydroxyapatite < β-TCP <α-TCP < Amorphous Calcium Phosphate < Tetra Calcium Phosphate

The formation of calcium phosphate cement is due to a combination of one or more calcium phosphate powders in an aqueous solution [116]. For example, the eggshell and phosphoric acid reaction led to the synthesis of the biphasic β-TCP and HA mixture [64]. The solid-state reaction between calcium carbonate ($CaCO_3$) and dicalcium phosphate dihydrate ($CaHPO_4 2H_2O$) in the molar ratio of 1:2 at 1300 ºC for five hours led to the formation of α- TCP [113]. β- TCP is stable up to the temperature of 1120 °C, whereas it transforms to α-TCP beyond 1120 °C [124]. α-TCP is stable in the temperature range of 1120 °C and 1430 °C [124].

Calcium phosphate cement and materials have some biological applications [115]. Fluorapatite and carbonated apatite are primarily helpful in dental applications due to their high stability [125, 126]. Calcium phosphate is used in medicine to improve function and reduce the pain of the calcified tissue of the whole body [127]. The calcium phosphate application includes healing bone defects, fracture treatment, total joint replacement, bone augmentation, orthopaedics, craniomaxillofacial reconstruction, spinal injury, ophthalmology and percutaneous devices, and dental fillings [127].

Due to non-exothermic reaction and intrinsic porosity, calcium phosphate cement has drug delivery applications [128]. The drug to be incorporated into the body can be mixed in the solid or liquid form of calcium phosphate cement [128]. Calcium phosphate cement application includes drug carriers for antibiotics, anticancer, anti-inflammatory, anti-resorptive and therapeutically active proteins [128].

2.2.6 Bioactive Composite

A composite material combines organic and inorganic materials to improve bone quality [129]. Biocomposites can be modified in terms of properties to adjust to a complicated environment in the body [130]. The composite combines the bioactivity of one material (mainly ceramics or polymers) with superior mechanical properties of mostly metals [4]. For tissue engineering, polymers are currently used in biodegradable applications (degradable materials where specific cells can be seeded) [38]. The use of bioceramics is due to its biocompatibility (chemical composition does not lead to a harmful reaction in the body) and bioactivity (biological response leading to the strong bond between tissue and implant) [38]. The use of metals stills remains prominent for their load-bearing ability despite the emission of toxic ions into the body [38].

Based on the matrix combination, there are three types of composite [1]:

- Polymer matrix composites, e.g., carbon/PEEK, HA/HDPE.
- Metal matrix composites, e.g., HA/Ti, HA/Ti–6Al– 4V.
- Ceramic matrix composites, e.g., stainless steel/HA, glass/HA.

Based on the bioactivity, there are three types of composite combinations [1]:

- Bioinert composites, e.g., carbon/carbon, carbon/ PEEK.
- Bioactive composites, e.g., stainless steel/Bioglass, HA/HDPE, HA/Ti–6Al–4V.
- Bioresorbable composites, e.g., TCP/PLA, TCP/PHB.

Reinforcements used in the biocomposite have superior mechanical properties. **Table 4** shows the list of biocomposites of bioceramics with their metal reinforcement.

Table 4, Bioactive composites with a fracture tough reinforcing phase [39]

Matrix	Reinforcing phase
Bioglass	Stainless steel fibre
Bioglass	Titanium fibre
HA	Fe-Cr-Al fibre
HA	ZrO_2 (Y_2O_3 fibre)
HA	TiO_2 fibre
A/W glass-ceramic	ZrO_2 (Y_2O_3 fibre)
A/W glass-ceramic	Ti particle

The reinforcing material in fibre or particulate form significantly increases fracture toughness and bending strength. For example, bioglass with stainless steel reinforcement had a bonding strength of 340 MPa and fracture toughness of 3.0 MPa.$m^{1/2}$ with superior mechanical properties compared to dense HA (strength 115-120 MPa and fracture toughness of 1.0 MPa. $m^{1/2}$) [39].

Table 5, Bioactive composites of polymer and bioceramic [39]

Matrix	Reinforcing phase
Polyethene	HA
Polymer	Phosphate Powder
PMMA	Phosphate-silicate-apatite glass fibre
Collagen	HA
Polyethene	Bioglass
Polysulfone	Bioglass

Table 5 describes the second group of materials, a group of biocomposites that includes the organic matrix with a reinforcement of bioactive material [39]. Though they provide the ideal combination, durability and fatigue strength are still under question [39].

a) Hydroxyapatite (HA) biocomposite

Bone analysis at the microscopic level was required to overcome the limitations of allographs and autographs [131]. This phenomenon led to the development of biomaterials [131]. HA is an important biomaterial with structural and functional similarities to the mineral part of bone and teeth [131]. The primary disadvantages of HA are low resistance to fracture, fatigue failure and brittleness [132].

HA was used in combination with metal and a polymer to improve the performance of the biomaterial in implant application [133]. HA coating on a titanium implant by the biomimetic method may have had a thinner layer thickness but had better adhesion strength than plasma spraying [134]. HA coating on a titanium implant showed quicker and stronger bone apposition [134]. HA implanted in the body led to quicker bone ingrowth than the metallic implant [4]. In the case of a titanium implant, there is cell growth from the bone side with no change from the titanium implant side [4]. In HA, cell growth in both the body and the HA side led to quicker osseointegration without releasing metallic ions [4]. One such biocomposite combination was a mixture of titanium, bioglass, and HA [135]. The bioglass added had higher bioactivity, yet the biocompatibility of all three blends were moderate [135]. Titanium powder was reinforced with Hydroxyapatite and bioglass separately (bioglass/titanium and Hydroxyapatite/titanium composite) and was coated onto a titanium substrate by the LENS (Laser Engineered Net Shaping) technique [136]. The morphological and biological evaluation showed higher hardness of composite powder coating (720-750 HV) as compared to titanium (approximately 148 HV), with more cell proliferation in composite coating than on the titanium surface [136]. A composite of HA, zirconia, and bioglass was manufactured, which resulted in an increase in apatite formation due to bioglass; and higher density and hardness due to HA and zirconia [137].

Bakar et al. [138] studied the biocomposite of HA and PEEK (polyetheretherketone). The raw material, in this case, was flame spheroidised HA, and the biocomposite of

HA/PEEK was formed using the injection moulding technique [138]. PEEK demonstrated better mechanical properties with bio-inertness; therefore, the loading of HA increased its bioactivity [138]. HA up to 40 wt.% was compatible with the PEEK matrix, and 30 wt.% HA in combination with PEEK had a similar mechanical property to cortical bone [138]. The biocomposite of HA with biopolymers such as PLGA, PMMA, and PCL was studied for drug delivery applications [139]. HA in the biocomposite improved the roughness and delivery efficiency by incorporating blood cells into its porous structure [139]. The existence of polymer reduced its brittleness and increased its strength with drug release properties depending on the HA/polymer ratio [139]. The composite was prepared by blending chitosan, polycaprolactone (PCL) and HA powders with the help of the hot pressing technique [140]. Due to the composite slow biodegradability and processibility, the presence of PCL reduced the brittleness of HA; moreover, the presence of chitosan improved PCL processability and degradability, which ultimately enhanced the overall quality of biocomposite [140]. The presence of HA improved the composite crystallinity, hydrophilicity and Young modulus [140]. Citric acid was added to the biocomposite of HA and chitosan; where 3 wt.% addition of citric acid improved the composite mechanical strength [141].

HA has a similar structure to the inorganic part of the bone [142]. In contrast, glass-ceramics have superior mechanical properties to HA [142]. Therefore, glass-ceramic was used as a reinforcement material in the HA matrix. Çalişkan [142] investigated the addition of HA to a composite material consisting of A-W glass-ceramic particulate material. The A-W glass-ceramic was added to the biocomposite with a range of 0-20 wt.% [142]. The addition of 15 wt.% A-W glass-ceramic particles to HA followed by sintering at 1250 ºC for 2 hr led to 36% more hardness than HA, suitable for dental applications [142]. Sabree and Mahdi [143] studied the biocomposite by adding the binary glass (70% SiO_2, 30% CaO) in quantities ranging from 20% to 40 wt.% to HA. The addition of binary glass increased the microhardness and compressive strength of the composite [143]. The biocomposite of bioglass 45S5/HA had higher bioactivity than HA due to the active surface of bioglass and its quicker dissolution [135]. However, adding HA ranging from 0 to 20 wt.% led to enhanced density, compressive strength, Young's, shear and bulk modulus [137]. The biocomposite of gel-derived powder with HA was prepared by manual mixing [144]. The designation of gel-derived powder was as follows:

S2: 80 mol% SiO_2–16 mol% CaO– 4 mol% P_2O_5; A2: 40 mol% SiO_2–54 mol% CaO–6 mol% P_2O_5 with the preparation of four samples mainly: 10 wt.% A2/HA, 10 wt.% S2/HA, 50 wt.% A2/HA, and 50 wt.% S2/HA [144]. Out of the four different samples, while 50 wt.% S2/HA and 10 wt.% A2/HA had better Young's modulus close to that of bone, while based on the bioactivity index, 10 wt.% A2/HA had a faster apatite layer formation [144].

b) *Bioglass biocomposite*

Many researchers have demonstrated the biological capability of the commercial bioglass *in vitro* and *in vivo* with suitable attachment with the bone tissue [145]. Himanshu et al. [146] experimented with the effect of titania and zirconia mixture (TiO_2:ZrO_2=3:2) in 1,2,3,4 wt.% substitution of SiO_2 in bioglass using the melting method. The new composite surface was bioactive with enhanced mechanical performance with the addition of zirconia [146]. The mechanical properties of bioglass/stainless steel composite can be varied, making it suitable for orthopaedic application [147]. Nano-based bioglass had superior mechanical and biological properties compared to micro-based bioglass [148].

Due to its superior bioactivity, bioglass was used with many biocompatible materials [145]. However, its use is limited due to its poor mechanical properties [145]. Bellucci et al. [149] studied bioglass coating (composition 4.6 mol% K_2O, 45.6 mol% CaO, 2.6 mol% P_2O_5 and 47.3 mol% SiO_2) on the zirconia substrate. There was an enhancement in sintering temperature, microhardness, and Young modulus due to the presence of zirconia; with the addition of bioglass, the apatite layer was formed after immersion in SBF after seven days [149]. Bioglass was coated on titanium substrate by anodic technique in temperatures ranging from 200-500 ºC by applying D.C. current [150]. The composite surface was rough and provided an excellent bioactive response with immersion in SBF fluid [150]. Bone growth was observed with the infiltration of nanometre-sized bioglass in a porous titanium layer on a titanium-based substrate and compared with the uncoated titanium implant [151]. Results showed 38% bone with bioglass infiltrated titanium implant compared to 22% with titanium implant [151].

The addition of bioglass to HA delayed HA decomposition due to the lesser quantity of β-TCP in HA/bioglass biocomposite [152]. Carvalho et al. [153] investigated the biocomposite of HA/bioglass with a bioglass quantity of 50 wt.% and 10 wt.%. The

deposition efficiency and bio-resorbability of bio-composite were improved due to the addition of bioglass [153]. Ragel et al. [154] investigated Hydroxyapatite/ glass biphasic material. The molar composition of biphasic glass in mol% was 26-CaO, SiO_2-70, and P_2O_5-4, respectively. The quantity of biphasic glass was 40 wt.% with 60 wt.% HA [154]. The composite immersed in SBF fluid showed higher bioactivity than HA and biphasic glass [154]. HA has a higher thermal expansion coefficient (9.9 - 10.6*10^{-6}/°C) than Ti-6Al-4V (8.7*10^{-6}/°C) at room temperature, thus leading to stress generation [155, 156]. 6P57 and 6P68 forms of bioglass (compositions in wt.% were 56.5 SiO_2, 11 Na_2O, 3.0 K_2O, 15.0 CaO, 8.5 MgO, 6 P_2O_5 and 67.7 SiO2, 8.3 Na_2O, 2.2 K_2O, 10.1 CaO, 5.7 MgO, 6 P_2O_5, respectively) used in the interface of HA/glass and glass/Ti-6Al-4V led to the reduction of residual stress [157].

c) Wollastonite biocomposite

Wollastonite has higher degradability making it suitable for tissue regeneration [158]. Hydroxyapatite does not resorbs easily but is brittle [159]. Therefore, Wollastonite, with better bioactivity, biodegradability and mechanical properties, was added to HA to form biocomposite [159]. A sol-gel technique was used to manufacture the biocomposite of Wollastonite and HA [159]. Wollastonite did not alter the structure and morphology of HA even after heat treatment of 1000-1400 ºC [159]. Wollastonite was added in quantities of 20, 50 and 80 wt.% in the form of suspension to HA, followed by sintering [160]. The mixture was porous with constant mechanical and superior biological properties, with no decomposition observed until 1200 ºC [160]. The HA/Wollastonite biocomposite powder sintered was a cylindrical tablet and showed crystalline boundaries with micropores. The Wollastonite fibres embedded well with the Hydroxyapatite agglomerate [160]. The isostatic pressing technique was used to prepare a mixture of Wollastonite (10, 30, 50, 70 and 90 wt.%) and remaining quantities of HA in the form of biocomposite powder to evaluate biological and mechanical properties [18]. Compressive strength was near the cortical bone; bending strength increased from 98 to 221 MPa in the samples covered by apatite in 30 wt.% Wollastonite biocomposite [18]. Morphological characterisation of Wollastonite material with different proportions of HA showed that the irregular structure of Wollastonite became more homogeneous and smooth when HA was added [161]. Padmanabhan et al. [162] studied the foam replica method to manufacture Wollastonite/HA scaffolds with 500µm porosity. Adding up to 50 wt.% Wollastonite to

scaffolds increased bioactivity and compressive strength from 0.51 MPa to 1.02 MPa [162].

Polymer bonding with the tissue is ineffective, whereas Wollastonite can be brittle [163]. Therefore, polymer/Wollastonite bioceramic can mitigate the drawbacks of both Wollastonite and biopolymers [163]. Li et al. [164] investigated the co-precipitation method to prepare PHBV and Wollastonite composite scaffolds with a 75-85% porosity. The addition of Wollastonite improved the bioactivity and mechanical property with controlled degradability [164]. Li and Chang [165] studied the manufacture of collagen/Wollastonite scaffold by the freeze-drying method. The addition of Wollastonite to collagen improved apatite formation and tensile strength from 29 to 71 KPa [165]. The melt blending technique with a twin-screw extruder was employed to synthesise the biocomposite of Wollastonite/PCL/PLA [166]. According to the MTT assay and bending test, the cell metabolic activity and bending strength increased due to the addition of Wollastonite [166]. Wei et al. [163] studied the solvent casting particulate leaching methods to manufacture the scaffolds of Wollastonite and polycaprolactone. The biocomposite improved the properties of both Wollastonite and polycaprolactone by reducing the brittleness of Wollastonite due to the addition of polycaprolactone [163].

In calcium silicate cement, Wollastonite mixed with the water leads to the formation of calcium silicate hydrate [167]. The calcium silicate hydrate formed solidifies into a hard substance [167]. The addition of β-Wollastonite (quantity ranging from 25-50%wt) to newberyite [$Mg_3(PO_4)_2.8H_2O$] led to an increase in cement compressive strength. 50% wt β-Wollastonite may be suitable for orthopaedic application [167]. Adding 5% wt Wollastonite fibres to calcium phosphate cement led to an increment in compressive strength of calcium phosphate cement by 250%, with an improvement in cell viability and ALP activity [168]. Domingues et al. [101] added Wollastonite fibres (0, 5%, 10%, 15% and 20% wt) to the calcium phosphate cement mixture consisting of tetra-calcium phosphate and dicalcium phosphate anhydrous, followed by mixing for 1 minute. No adverse reaction was observed with the Wollastonite addition, and the amount of new bone formation was 65% compared to 16% when not added [101].

2.3 Application of Biomaterials

A biomaterial is any substance that repairs and replaces the defective organ of the body [169]. Biomaterials include ceramics, polymers and metals. The advantages of biomaterials are easy handling, great availability of shapes and sizes and ample resources for their production [170]. Biomaterials with specific characteristics enhance the recovery process without causing any allergic or inflammatory response [171]. The properties of the biomaterials include bioinertness, bioactivity, chemical and mechanical stability, biodegradability, biofunctionality, biostability and biotolerance [171].

In orthopaedics, biometals are mostly used as support in the form of plates, screws and implants for the replacement of missing joints or bone [170]. In dental applications, biometals can be used to manufacture dental implants and metallic meshes to stabilise bone grafts in guided bone regeneration [170].

Some biomaterials, such as polymers, have the potential for tolerance of cyclic load without cracking [171]. Therefore, they can be used in orthopaedic and dental applications. This application includes alveolar ridge augmentations and artificial ligaments and tendons, as described in **Table 6**.

The biomaterial must possess a good amount of compression strength for vertebrae issues due to compression caused by the body weight or surrounding muscles [171]. For this reason, alumina (compressive strength of 3.5 GPa) can have applications in vertebrae spacers and extensors [172], as described in **Table 6**.

Calcium phosphate bioceramics have wide applications in the field of bone regeneration. This calcium phosphate chemical composition resembles bone tissue minerals [173]. The main characteristics of calcium phosphate are good cell attachment and easy and cost-effective production [173]. Calcium phosphate (HA) as a bone substitute is mainly used as a coating for orthopaedic, dental, or drug delivery applications [174]. However, due to its resorbability, calcium phosphate cement is used as a bone filler. It is replaced by a new bone as soon as it heals, such as chemical bonding coatings [174]. The primary objective of this study was to coat Hydroxyapatite onto a titanium implant for orthopaedic application. Biometals have good mechanical strength but lack biocompatibility and osseointegration; therefore, HA was used in the current study due to its bioconductive

properties, resulting in direct, intimate bone-implant bioactive bonding without any adverse effects [174, 175].

Bioglass can be used in a solid or porous form (in the form of scaffolds) or powder form to coat the biomedical implant or a filler in a composite [176]. Bioglass can bond with the mineralised bone tissue in the physiological body environment [176]. Therefore, bioglass can have a wide range of applications, including spinal fusion, dental, which includes the replacement of damaged or diseased teeth and orthopaedics, which includes bioglass coated on the metal implant for a hip replacement, as described in **Table 6**.

Table 6, Applications of biomaterials [51, 52]

Application	Function	Material
Orthopaedic	Load bearing application	Al_2O_3
Chemical bonding coating	Coatings include bioactive material, which provides for maxillofacial, dental and orthopaedic	HA, surface-active glass and glass ceramics
Dental	Implants which mainly substitute teeth	Al_2O_3, HA, surface-active glass
Alveolar ridge augmentations	Alveolar ridge augmentation improves shape and size to retain and receive a dental prosthesis	Al_2O_3, HA, HA-autogenous bone, HA-PLA composite, surface-active glasses
Otolaryngologic applications	This application includes the ear, nose, and throat and helps to retain the structure of the head and neck	Al_2O_3, HA, surface-active glasses and glass ceramics
Artificial ligaments and tendons	To keep the structure of bone, especially in the knee stable	PLA carbon fibre composite
Coatings for tissue ingrowth	A coating that favours bone growth, especially on cardiovascular, orthopaedic, dental and maxillofacial prosthetics	Al_2O_3
Temporary bone space fillers	Fillers generally include resorbable materials, which are substituted by new bone as soon as it heals	Trisodium phosphate, calcium and phosphate salts.

Periodontal pocket obliteration	Periodontal pocket obliteration generally relates to the teeth where there is pulp tissue which is related to supporting, preventing and repairing teeth	HA, HA-PLA composite, surface-active glasses, trisodium phosphate, calcium and phosphate salts.
Maxillofacial reconstruction	To properly function jaws and face	Al_2O_3, HA, HA-PLA composite, surface-active glasses
Percutaneous access device	This form of material accesses the coronary artery of the heart	Bioactive glass-ceramics.
Orthopaedic fixation device	This device relates to fractures, knee, joints, limbs	PLA-carbon fibres, PLA-calcium/ phosphorous glass fibres
Artificial knee, hip, shoulder, wrist, elbow	Repair fracture joints and reconstruct fracture	High density, alumina, metal bioglass coating
Bone plates, screws, and wire	Reconstruct fracture	Bioglass-metal fibre composite, polysulphone-carbon fibre composite
Intramedullary nails	Co-ordinate fracture to improve posture	Bioglass-metal fibre composite, polysulphone-carbon fibre composite
Harrington rods	Improve the dimension of spinal curvature	Bioglass-metal fibre composite, polysulphone-carbon fibre composite
Permanently implanted artificial limbs	Substitute extremities that disappear due to an accident	Bioglass-metal fibre composite, polysulphone-carbon fibre composite
Vertebrae spacers and extensors	Replace the bone which is affected by congenital deformities	Al_2O_3
Spinal fusion	Stabilise vertebrae to keep spinal cord protected	Bioglass
Endosseous teeth replacement implants	Replace damaged, diseased or lost teeth	Al_2O_3, bioglass, dense Hydroxyapatite, vitreous carbon
Orthodontic anchors	Assist in stress application to change deformities, especially in load-bearing application	Bioglass-coated Al_2O_3 and bioglass-coated valium

The primary objective of this study was to coat Hydroxyapatite and Wollastonite onto a titanium implant for orthopaedic application. Metals have good mechanical strength but lack biocompatibility and osseointegration; therefore, HA was used in the current study due to its bioconductive properties, resulting in direct, intimate bone-implant bioactive bonding without any adverse effects [174, 175].

2.4 Biocoatings

Biocoatings are biocatalyst coating on the surface of the substrate [177]. Biocoatings are evaluated based on bio-functionality and biocompatibility [52]. Biofunctionality (bioactive material) is the ability to mimic the function of the body part. Biocompatibility can occur only through ions in the physiological environment (like calcium, magnesium, potassium or sodium) [52]. Bioinert substrate (mostly metals) with biocompatibility properties may not be bioactive but do not lead to any adverse release of ions in the body [36]. Mostly alumina and yttria-stabilised zirconia are used as bioinert substrate [48]. These materials are used due to their superior mechanical and tribological properties, such as fracture toughness and reliability, leading to mechanical bond formation [36]. The bioactive material (mostly ceramics) leads to biological bonding to the bone [48]. Bioactive materials stimulate bone growth by mimicking biological function, which leads to a strong biological bond on the interface of bone and material [48]. Bioactive materials mostly consist of bioglass, A-W ceramic and Hydroxyapatite [48]. Bio coating mostly elicits four kinds of response; toxic, bioinert, bioactive and resorbable responses [38, 52].

2.4.1 Toxic Response

This type of tissue response (toxic) leads to tissue death. For example, PMMA (polymethylmethacrylate) cement used to connect a femur with a hip leads to cell necrosis due to the exothermic reaction occurring due to polymerisation [47].

2.4.2 Bioinert Response

In a bioinert response, the fibrous layer is formed without any biological activity [48]. Reaction kinetics is extremely slow and may lead to corrosion or release of ions in the body [39]. Examples of bioinert response included, alumina, zirconia, titanium, stainless steel, and Co-Cr-Mo alloy [39]. The fibrous layer thickness depends on the implant materials chemical stability [39]. Due to the chemical stability of alumina, it has a thin

fibrous layer, whereas other materials have a thick fibrous layer [39]. Micromotion can occur when the interface is not chemically or biologically bonded [39, 52].

2.4.3 Bioactive Response

This bioactive response is based on biological acceptance due to interfacial bond formation between bone and implant material [49]. Examples of bioactive response materials included, Hydroxyapatite, A-W glass-ceramic, bioglass and Wollastonite [52]. Wollastonite degradation rate is slow as compared to α-TCP and β-TCP; therefore, it can be classified as bioactive. Such bioactive ceramics reacts with the physiological fluids leading to a reaction followed by new bone formation [39]. This material can perform a distinct function, such as replacing and mimicking the replaced bone part [39]. Porous bioceramics promote the formation of bone [39]. The pore size in the 100μm-150μm provides a good platform for blood flow for the host tissue and interfacial fixation [39].

2.4.4 Resorbable Response

In resorbabale response, the material degrades followed by replacement of new bone [52]. Resorbable materials included; Ca-P cement, α-Tricalcium phosphate, β-Tricalcium phosphate, and polylactic acid [39]. Material replacement by bone occurs due to the exchange of ions, bone growth stimulation and new bone formation [39]. The only two conditions required, are that the constituents should be metabolically acceptable, and the rate of resorption of this material should ideally be equal to the rate of bone formation [39]. **Figure 5** shows the inert and bioactive response when a biomaterial is implanted in the rabbit femur.

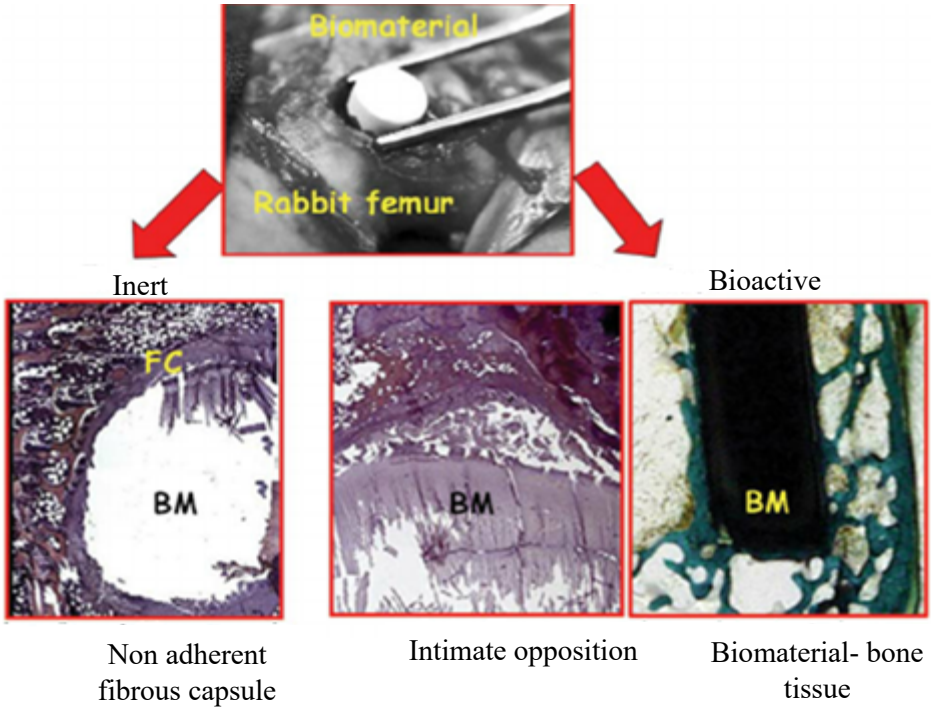

Figure 5, Two behaviours of a biomaterial (BM) after four weeks of implantation in a rabbit femur [178]

2.5 Protective Overlays and Coatings

Stress shielding and thermal stress can cause delamination [179]. Delamination may occur due to an abrupt change in the microstructure of ceramics and metals [180]. This phenomenon can cause a reduction in durability and increase surgery costs [179]. Therefore, protective overlays are used over the substrate to improve the biocoating properties [179]. For example, functionally graded coating have been developed to overcome delamination [179]. Different materials with different properties and volume ratios are mixed layer by layer in functionally graded coating [181]. The mixture formed is coated onto the substrate [181]. **Figure 6** shows different types of coatings on substrate.

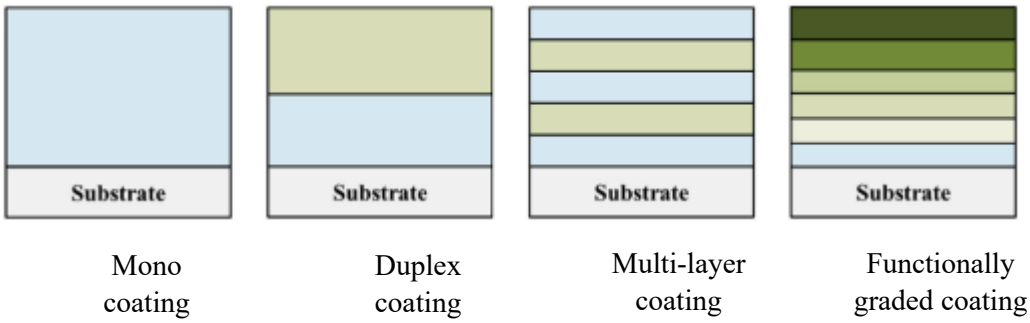

Figure 6, Schematic of different types of coatings on the substrate [181]

2.5.1 Functionally Graded Coatings for Hydroxyapatite (HA)

Hydroxyapatite (HA) is biocompatible with good bonding, whereas the reported metal toxicity has been mentioned previously [182]. Therefore, HA is generally coated onto a metal substrate [183]. This HA coating acts as a biological barrier between the body tissue and metal [183]. HA was coated onto aluminium substrates using a porcelain bond coat layer in one study [184]. This study used three powders; 100% HA, 50% HA and 50% porcelain and 100% porcelain [184]. The study showed that 50% HA and 50% porcelain structure was uniform with higher bond strength [184]. Chen et al. [185] experimented with a mixture of HA and titanium plasma sprayed onto a Ti-6Al-4V substrate. The bond coat layer consists of titanium with 30 µm thickness, an intermediate layer of alternative titanium and HA with 40 µm thickness, and the top HA layer with 30 µm thickness [185]. The bond strength of the functionally graded coating was higher (23.2 MPa) than monolithic HA coatings (14.2 MPa). The graded layer reduced the external stress caused due to a difference in the coefficient of thermal expansion [185]. **Figure 7** illustrates the functionally graded coating of titanium and HA on titanium substrate.

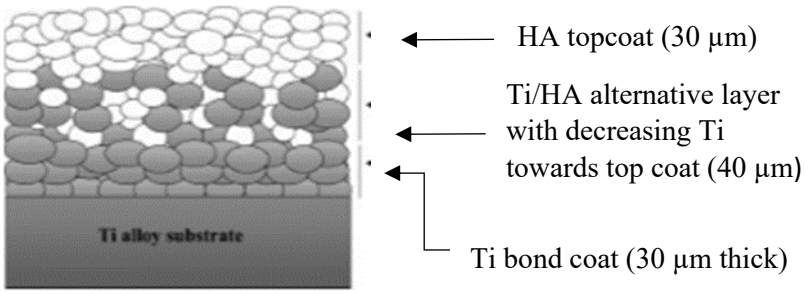

Figure 7, Schematic illustration of the fabrication of the functionally graded HA/Ti composite coatings [185]

2.5.2 Functionally Graded Coatings for Bioglass

Bioglass has inferior mechanical properties and better osseointegration than most biomaterials [186]. The functionally graded coating enhances the performance of the materials by gradual variation in the microstructure in terms of mechanical and biological

properties [187]. Goller [188] experimented with plasma spraying of bioglass on the titanium substrate. The coating was characterised with and without the Amdry 6250 (60% Al_2O_3 and 40% TiO_2) as a bond coating layer of 20 μm thickness [188]. The bond strength increased three-fold with the bond coat with a homogeneous layer formation [188]. Cattini et al. [189] experimented with functionally graded coatings of the mixture of BG_Ca wt.% (4.7% Na_2O, 42.3 CaO, 6 P_2O_5, 47 SiO_2) and HA by suspension plasma spraying. There were three types of coatings; composite, where bioglass and HA were pre-mixed in the same quantity, and the second type was a duplex with the third type a functionally graded coating [189]. The comparison showed that functionally graded coating yielded the best results in terms of biological (apatite formation) and mechanical aspects (scratch test) [189].

2.5.3 Functionally Graded Coatings for Wollastonite

Some studies were conducted about the functionally graded coating of Wollastonite. Noor et al. [190] added Wollastonite particles to epoxy at quantities 0, 2, 4, 6, and 8 wt.%, respectively, separately and together as a graded material. The addition of Wollastonite in graded composition increased the fracture toughness and hardness [190]. Hydroxyapatite-based Hydroxyapatite, boron nitride and Wollastonite film were coated onto a titanium alloy by plasma laser deposition [191]. The addition of boron nitride and Wollastonite doped with Hydroxyapatite increased the wear resistance, whereas titanium substrate consisting only of Hydroxyapatite improved the corrosion resistance [191]. Singh et al. [192] conducted studies on bi-layer coating of Wollastonite and Hydroxyapatite on titanium alloy substrate obtained by plasma spray technology, with top layer of Wollastonite and bottom layer of Hydroxyapatite. The Wollastonite was smaller in size (less than 0.5 μm). Therefore, Wollastonite was mixed with polyvinyl alcohol and water-based solution in the form of paste, dried and pulverised to make it easily flowable [192]. The addition of Wollastonite (in monolithic HA coating or composite coating) increased the hardness and bioactivity of the coating, whereas corrosion resistance was higher in monolithic HA coating [192].

2.6 Surface Engineering

Most interaction occurs at the interface when artificial biomaterial is implanted in the body via surgery [193]. A bioinert implant often reacts with the cells and tissue because a bioactive material is coated on its surface [193]. This phenomenon is known as surface

engineering. In surface engineering, a material with superior properties coats a substrate material [193]. The material surface assists in the understanding of the bone and cartilage response [194]. Osteogenesis (bone formation process) favours high oxygen tension areas, whereas chondrogenesis (cartilage formation procedure) favours low oxygen tension areas [194]. The increased surface roughness leads to more osteogenesis [194]. The surface reactivity of the bio-active ceramic includes simple steps such as; dissolution, precipitation of ions, ion exchange between tissue and ceramic, interdiffusion from the tissue surface to ceramic, cellular activity, deposition of mineral, integration with the ceramic, dissolution of bioceramic, cell attachment, proliferation, and cell differentiation [195]. **Figure 8** demonstrates a step-by-step procedure for apatite layer formation on ceramic by surface engineering.

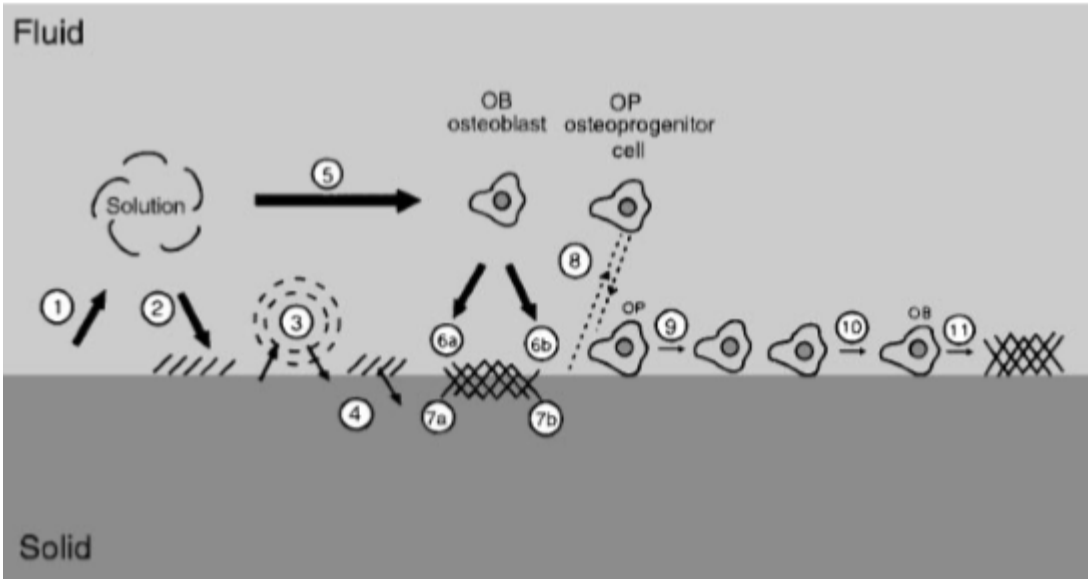

Figure 8, Events which take place between bioactive ceramics and the surrounding environment resulting in apatite layer formation [195]

2.6.1 Surface Engineering of Biomaterials

a) *Surface engineering of the Hydroxyapatite (HA)*

When an HA-coated titanium implant is placed inside the body, several biological and physiological reactions occur, as detailed in **Section 2.1.4 (a)**. Hydroxyapatite (HA) does not have high reactivity, which may lead to slow bone formation [195]. HA use with a superior bioactive materials leads to an increment in its bioactivity [195]. HA reinforced

Ti and bioglass reinforced Ti were laser processed on titanium implant and amongst all of the coatings verified by MTT assays, the cell proliferation was higher for bioglass at 200 W, with all surfaces allowing cells to grow and spread [136]. ALP enzymes can enhanced HA precipitation kinetics [196]. Cattini et al. [197] investigated the deposition of functional bioglass topcoats on plasma-sprayed HA coating on the stainless-steel substrate. The deposition of HA was performed by plasma spraying, whereas suspension plasma spray deposited bioglass, both techniques were compared [197]. The comparison concluded that a lower thickness, fine and porous structure, with superior bioactivity of bioglass was found compared to plasma-sprayed HA coating [197]. Separately immobilisation of RGD peptide on the surface of porous A-W ceramic showed a good covalent bond, where the cell adherence to the RGD modified surface was dramatically higher, with no fibrous encapsulation in the RGD modified surface and A-W ceramic surface [111].

b) *Surface engineering of the bioglass*

In the case of bioglass 45S5, ion exchange, dissolution, and precipitation are the three mechanisms in SBF fluid that lead to active CaP on the surface. Na^+ and Ca^{2+} ions release into SBF in the ion-exchange process, which leads to a broken Si-O-Si bond layer due to dissolution, form a silica-rich layer [92]. HCA (hydroxycarbonate apatite layer) rich in calcium and phosphates is formed due to hydration and precipitation on the silica-rich layer in the precipitation process [92]. The quicker and higher the HCA, the higher the bone formation. [92]

c) *Surface engineering of the treated titanium*

When a titanium surface is treated with sodium hydroxide it increases its bioactivity. The surface sample is heat-treated at various temperatures, followed by the analysis of apatite formation [198]. Increasing sodium ions leads to the formation of sodium titanate gel formation. Further NaOH treatment converts the sodium titanate into anatase, which induces apatite formation on the surface [198].

To explain apatite formation, firstly, amorphous sodium titanate is formed by titanium immersion in a sodium hydroxide solution [198]. Secondly, the ions attack the SBF fluid, afterwards, there is the formation of amorphous calcium titanate leading to the release of sodium ions [198]. The next step is the formation of amorphous calcium phosphate due

to the phosphate ion exchange with the SBF fluid [198]. In the last step, a thicker apatite layer forms [198].

d) *Surface engineering of Wollastonite*

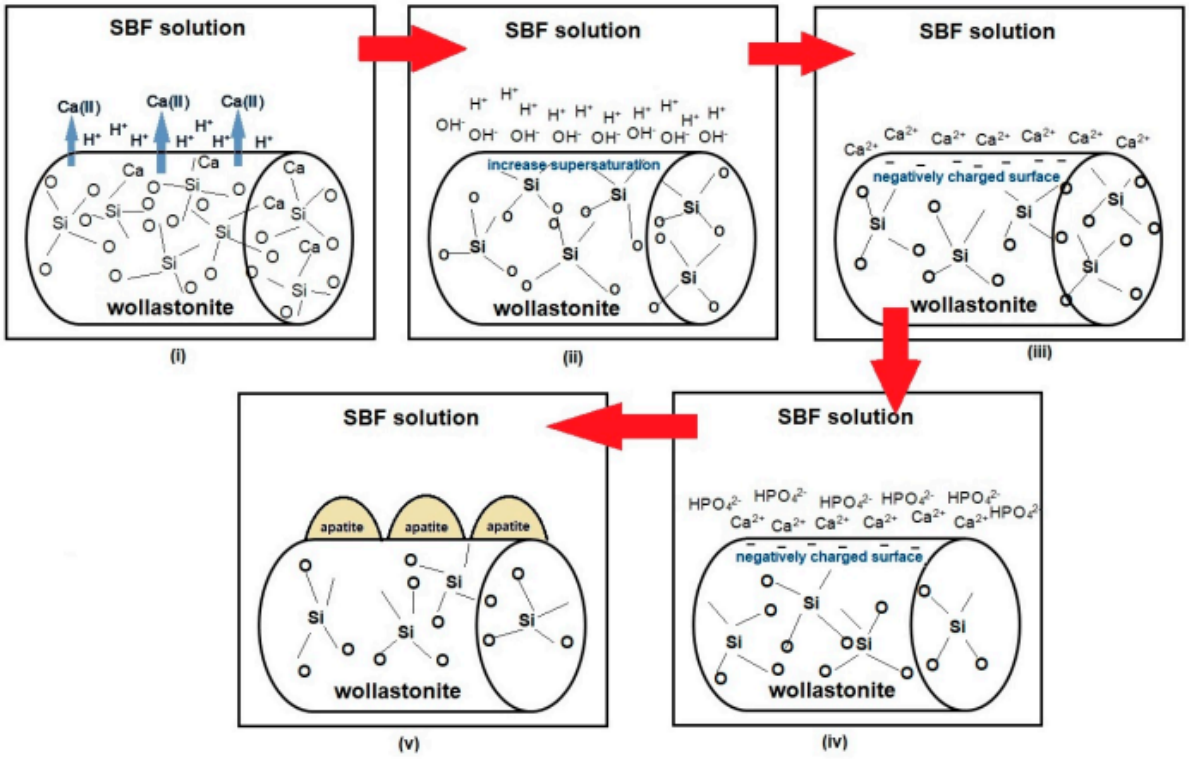

Figure 9, Apatite formation mechanism in Wollastonite when immersed in SBF fluid [199]

Figure 9 shows the apatite formation on the surface of the Wollastonite. It is the step-by-step process: 1) At first, there is ion exchange between the calcium of Wollastonite with hydrogen ions present in SBF fluid; 2) There is an increased supersaturation due to this process; 3) The Wollastonite layer surface is negatively charged due to the exchange of calcium ions; 4) The phosphate ions present in SBF fluid combine with calcium ions near the Wollastonite surface layer; 5) Finally, there is an apatite layer formation on the surface of Wollastonite. [199]

Similar to the HA implant inside the body, the Wollastonite-coated implant immediately interacts with the body, resulting in physiological and biological process. The process overview is as follows that described in **Section 2.1.4 (b)**.

e) *ISO standard for using HA and Wollastonite in medical implants*

i. ISO standard for the use of HA in medical implants

ISO 13779 series specifies the requirements for HA in surgical implant. ISO 13779-1:2018 deals with the chemical composition, physical properties and mechanical properties of HA intended for use as surgical implant material. ISO 13779-2:2018 deals with coating thickness, crystallinity, phase purity and adhesion strength of HA coatings applied to metallic implants. ISO 13779-3:2018 provide guidelines on using techniques such as XRD and infrared spectroscopy. ISO 13779-4:2018 specifies the method for determining the adhesion strength of Hydroxyapatite coatings on metallic substrates. ISO 13779-5:2018 focuses on chemical composition, particle size distribution and other relevant properties.

ii. ISO standard for the use of Wollastonite in medical implants

For Wollastonite coatings on hip implants, there is no specific ISO standard dedicated exclusively to Wollastonite. However, the ISO standard for material characterisation, biocompatibility, and surface coatings can be applied to Wollastonite.

ISO 13779 series, which mainly relates to Hydroxyapatite, can be applied to Wollastonite. ISO 13175 series covers the standard synthetic bone graft substitutes can be applied to Wollastonite. ISO 10993 series outlines the principles for evaluating the biocompatibility of medical devices, including coating, to ensure that the material is safe for use in the body. ISO 5832 series mentions the standard for the metallic material used in surgical implants. It is necessary to understand this standard as Wollastonite coating is applied to the metallic implants. ISO 22442 series applies standards for the coating obtained from natural sources, which can be applied to Wollastonite manufactured from rice husk and eggshells. This standard also addresses biocompatibility and safety.

2.7 Spray-Drying Technology

Spray drying has been used for a long time, since the 19th Century [200]. Spray drying technology was used during World War II to reduce the food volume and weight making it easier to transport [200]. Spray drying removes moisture from the powder, improving its durability and stability by enhancing its properties [201]. Since the 1920s, spray drying technology had used in the; dairy industry, detergent, polymers, ceramics, metal powders,

food industry, flavours, electronics, enzymes, and the pharmaceutical industries [202]. In recent times, spray dryers have been used in pharmaceutical formulation and drug delivery dosage applications [202].

In the spray drying technique, the liquid from the suspension is fed to a nozzle via a peristaltic pump, where the nozzle performs the liquid atomisation [203, 204]. The compressed air atomises the fluid stream into tiny droplets by force [204]. This droplet enters a higher temperature zone in which the hot air is blown [203, 204]. The liquid droplets are then dried and vaporised by evaporation of the solvent in the liquid, followed by a discharge through an exhaust tube which leads to the formation of dried powder [203, 204]. The cyclone separates the powder with the collection of micro-sized powders in the collection tube [203, 204]. The inlet drying air temperature, airflow rate, feed flow rate, and pressure determine directly affect the powder content, moisture content, particle size distribution and powder yield of the final powder [205, 206]. **Figure 10** describes the schematic diagram of spray drying technology.

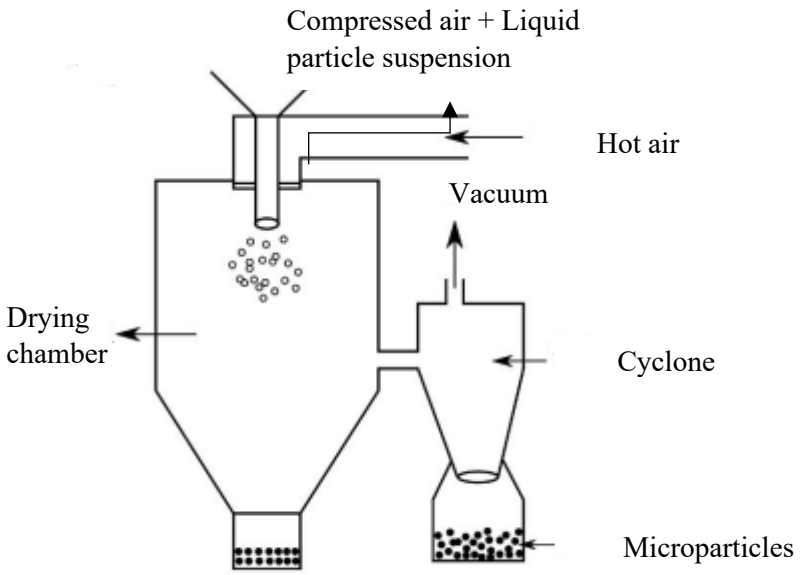

Figure 10, Schematic diagram of the spray drying process [204]

The spray drying technology has certain advantages. Spray drying technology is constantly evolving and developing, as it is rapid, constant, quick, scalable, and single-step with less need for modification, making it suitable for industrial and laboratory

applications [207]. Spray drying technology is energy efficient, and the powder produced generally does not require further modification, unlike freeze-drying techniques [207]. Quick evaporation of the slurry to dried powder does not alter the properties of the raw material, thus it is possible to spray dry heat-sensitive powder [207]. However, there are issues associated with the use of spray drying equipment [207]. Spray drying technology is suitable for industrial applications where a higher quantity of raw material is used, and much of the powder is spray-dried [207]. However, it is not appropriate for use in laboratory settings because spray-dried powder efficiency is only 20-70% [207]. Much of the powder gets adhered to the main chamber, which reduces the yield of the spray drying equipment [207]. Moreover, finer particles of less than 2 μm cannot be spray dried because cyclones cannot separate the fine particles, therefore most finer particles pass through the exhaust tube [207]. Submicronic particles cannot be efficiently compressed to obtain atomised droplets [207].

In the case of plasma spraying discussed later, if the spray-dried powder is spherical, free-flowing, then it easily feeds through the plasma gun. Its high flowability helps achieve better green density and precise dimension when sintered for plasma spraying [208]. Spray-dried microstructure and nanostructure Hydroxyapatite has been plasma sprayed [76]. Nano-sized Hydroxyapatite synthesised with carbonic acid, and acetic acid contained different properties than micro-sized Hydroxyapatite [76]. Bastan et al. [209] synthesised spray-dried Hydroxyapatite, where its atomisation pressure and slurry influenced the production of spray-dried Hydroxyapatite powders. Up to 1250 ºC, the spray-dried powder was stable; after 1450 ºC, it decomposed [209]. Murtaza [210] spray-dried Hydroxyapatite powder for thermal spray application. Hydroxyapatite particles were spray-dried at 398K, 421K, and 461K, with a viscosity of 25, 50, and 75 mPa.s, respectively [210]. Hydroxyapatite powder showed a narrow particle size distribution at 25-50 mPa.s viscosity range with high porosity and spherical shape [210].

20 wt.% Wollastonite was added to the Hydroxyapatite slurry, and the mixture was spray-dried by Bastan et al. [211], spray-dried Hydroxyapatite/Wollastonite mixture was compared with the spray-dried Hydroxyapatite. Both the samples were the plasma sprayed; the results concluded higher porosity, a higher decomposition rate and higher adhesive strength for spray-dried Hydroxyapatite/Wollastonite compared to spray-dried Hydroxyapatite [211]. Before plasma spraying, the spray dried HA/Wollastonite powder

was heat treated at 1000 °C to improve the crystallinity [211]. The process parameters for plasma spraying used were current of 50 amperes; argon supply of 50 NLPM; hydrogen supply of 3 NLPM; powder feed rate of 10 g/min, and spraying distance of 120 mm [211]. The HA/Wollastonite powder obtained by the study was spherical. The research similar to Bastan et al. [211] was conducted but the powder did not flow. Therefore, the other alternative method was used for coating of Hydroxyapatite and Wollastonite onto a titanium substrate.

2.8 Thermal Spray Technique

Though still prevalent, the thermal spraying technique dates back 100 years ago [212]. The thermal spraying technique has several applications, including coating, resurfacing, repair, and forming [212]. The coating material is semi-solid or liquid in the thermal spray process and is deposited onto a substrate [213]. They are droplets until they touch the substrate, but they become splats called lamellae upon interaction with the substrate [213]. Rapid solidification leads to particle homogeneity [213]. **Figure 11** describes the various thermal spray processes [214].

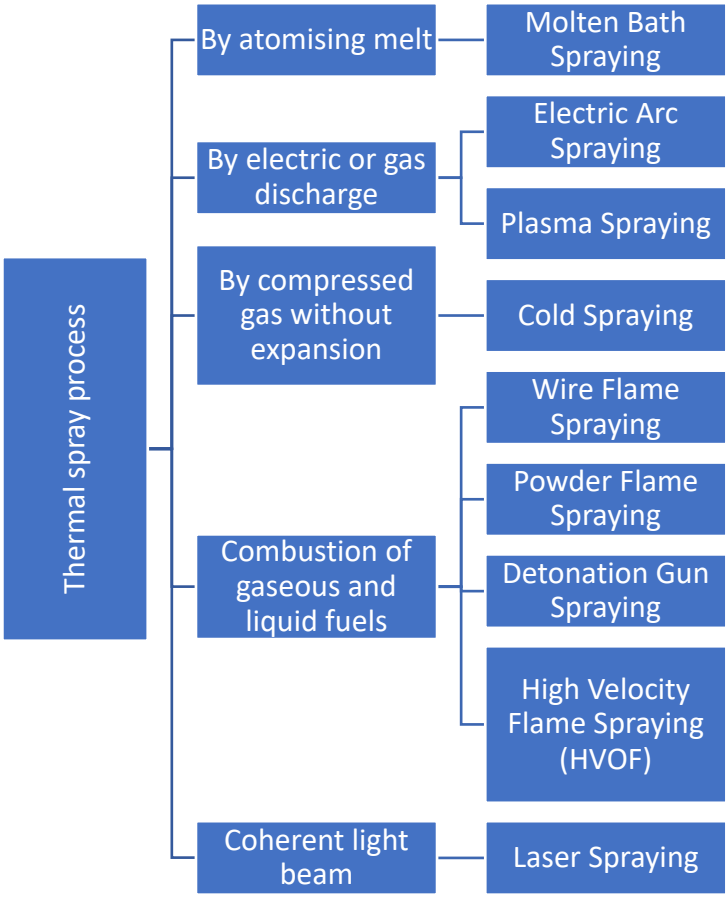

Figure 11, Classification of the thermal spray process [214]

Thermal spray coatings can be generated by two means: electric and combustion-based energy systems [215]. In combustion-based energy systems, there are three thermal spray techniques: flame spray, detonation gun and high-velocity flame spraying (HVOF) [215]. In electric-based energy systems, two processes are involved: plasma spray and electric arc spray [215].

The cold spray process is a solid-state coating technique [215]. The coating material velocity and kinetic energy are higher than the thermal processes [215]. **Table 7** describes the characteristics of various thermal spray techniques

Table 7, Characteristics of various thermal spray techniques [216]

Spray type	**Feed type**	**Flame temperature**	**Particle velocity (m/s)**	**Materials**	**Microstructure characteristics**	**Applications**
Combustion	Wire/powder	~ 3000 ºC	40 - 100	Metals, polymer and ceramics	High porosity and oxidation	Corrosion protection

HVOF	Powder	~3000 ºC	400 - 800	Metals, cermets and low-melt ceramics	High density and good adhesion	Wear protection
Two-wire arc	Wire	3000-6000 ºC	50 - 150	Metals, cermets	Thick, dense	Wear coatings
Plasma	Powder or wire	5000 – 25000 ºC	80 - 300	Ceramics, metals	SEM in ceramic coatings	Insulators, thermal barrier coatings
Cold spray	Powder	Room temperature	400 - 800	Metals	Dense	Conductors, cladding

2.8.1 Plasma Spray Technology

Plasma thermal spray works because when an electron recombines into the nucleus, kinetic energy transfers to heat the particle, resulting in a plasma [217]. **Figure 12** describes a schematic diagram of the plasma spray technique.

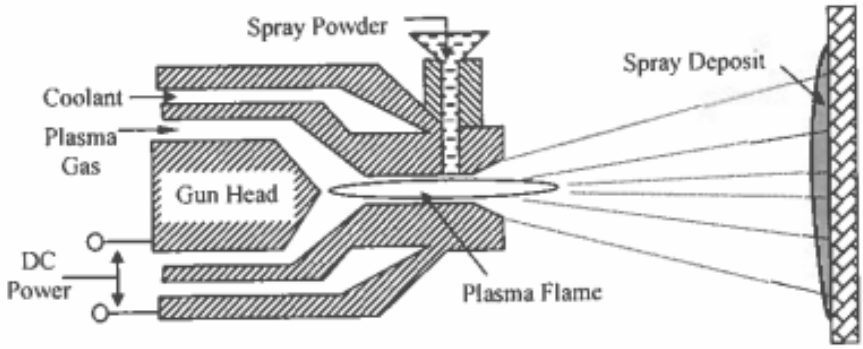

Figure 12, Schematic diagram of the plasma spraying technique [218]

a) *Plasma Spraying of Biomaterials*

Atmospheric plasma spray can coat high melting temperature material such as refractory metals and ceramics [219]. Al_2O_3-13% TiO_2 was deposited using atmospheric plasma spray using submicron alumina with nanometric titania, where the alumina particle size was 0.35 μm, whereas the titania size was 40 nm with a weight ratio of 87:13 [10]. The coatings adhered well to the substrate with the determination of microhardness, toughness, adhesion and tribological behaviour [10].

b) Plasma Spraying of Hydroxyapatite (HA)

HA plasma-sprayed has a different structure than monoliths HA [220]. Plasma-sprayed HA have more dissolution than feedstock HA [220]. Kweh et al. [221] analysed the plasma spraying of the flame spheroidised HA particles. The samples with heat-treatment at 800 ºC with particle sizes ranging from 20-45 µm and a spraying distance of 10 cm had better fracture toughness and mechanical resilience [221]. Plasma spraying of HA resulted in calcium phosphate formation [220]. Khor et al. [222] investigated the different particle sizes of HA-coated by the plasma spraying technique. Particles less than 10 µm contained more CaO [222]. Particle size less than 30 µm had a more amorphous structure [222]. Particle size ranging from 30-55 µm had a mixture of the amorphous and crystalline phases [222]. Particles above 75 µm were crystalline and tended to form porous microstructure [222]. Chang et al. [223] studied the crystallisation kinetics of plasma-sprayed HA coatings. The as-sprayed coating was 7.8% crystalline, and post-heat treatment increased crystallinity from 34% at 600 ºC to 90% at 800 ºC [223]. Kweh investigated [224] heat-treated HA samples and as-sprayed immersed in SBF fluid. The result showed similar bioactivity with enhanced mechanical strength in the heat-treated plasma-sprayed HA sample [224]. Yang and Chang [225] analysed the mechanical properties of plasma-sprayed HA on the different substrate positions. The substrate was stationary in plasma spraying of HA on a titanium substrate (represented by A-HACs) [225]. In another case, the substrate was rotating (represented by B-HACs) [225]. The value of Youngs modulus was 16.2 MPa for A-HACs and 24.1 MPa for B-HACs [225]. Increased power decreased the crystallinity and the size distribution shifted towards smaller size, as shown by the analysis of plasma spraying of HA [226].

Levingstone [4] optimised the effect of process parameters on HA coating on the titanium alloy (Ti-6Al-4V) substrate. The process parameters considered were current, gas flow rate, powder feed rate, spray distance and carrier gas flow rate [4]. Out of all the process parameters mentioned, current, gas flow rate and spraying distance had the most prominent effect on the coating properties [4]. The crystallinity of the coating increased due to increased coating thickness; purity was higher at a lower carrier gas rate, and coating porosity was higher at a lower powder feed rate and higher spraying distance [4]. Moreover, the Hydroxyapatite bi-layer coating was produced with a stable, crystalline base layer and an active, porous top layer [4].

Osseointegration directly connects the bone tissue and implant surface [227]. Therefore, ceramic is coated on the biomaterial to improve osseointegration [227]. HA was plasma sprayed on various substrates such as titanium oxide, yttria-stabilised zirconia (YSZ), titanium, and alumina [227]. Heat treatment of coating at 600 ºC converted the amorphous HA to a crystalline structure with improved mechanical properties [227]. Adding 10 wt.% zirconia to HA improved the composite strength and fracture toughness in plasma-sprayed HA coatings [228].

Polylactic acid is a biodegradable polymer, whereas plasma-sprayed HA induced bone formation [220]. The plasma-sprayed calcium phosphate was blended with polylactic acid polymer (PLLA) in the form of a scaffold, where, after seven immersion days, the obtained material was bioactive with apatite formation on its surface [220].

HA and 45S5 bioglass in mixture form were evaluated based on morphology and immersion behaviour, and the mixture was plasma sprayed, followed by the analysis of the formed coating [229]. The addition of bioglass increased the porosity and roughness and monolithic HA coating had highest bond strength [229].

c) *Plasma Spraying of Bioglass*

Bioglass is often coated on the top of the metal substrate to improve the osseointegration of the implant and protect the body tissue from harmful metal ions [230]. Monsalve et al. [231] studied plasma-sprayed bioglass (composition: $31SiO_2$-$11P_2O_5$-(58-x) CaO- x MgO, where x was 0 and 2, representing two different powders designated as P1 and P2) on titanium and steel substrate. The samples were bioactive with the formation of an apatite layer [231]. The atmospheric plasma spraying of bioglass contained no coating for particle sizes larger than 200 µm [232]. Low melting was observed for the particle size 63-200 µm coating, and the finer particle needed a fluidiser [232]. Glass ceramic of composition 35% SiO_2, 42% $CaCO_3$, 2.0% MgO, 7.0% Na_2CO_3, 1.0 K_2CO_3, 13.0 P_2O_5 was mixed with pre-treated protein-free bovine bone [233]. Particle size less than 63 µm was plasma-sprayed on titanium, aluminium, and stainless steel substrates [233]. The coatings obtained had high hardness, lower porosity, and higher compressive strength; dissolution was higher in titanium implants, with good bioactivity observed in all [233].

d) Plasma spraying of Wollastonite

As Wollastonite is a bioactive ceramic, apatite layer formation on the Wollastonite surface is quicker than most biomaterials [17]. Plasma-sprayed Wollastonite displayed superior mechanical and biological properties, therefore bioactivity but having poor bond strength [234]. Wollastonite is bioactive and has a thermal expansion coefficient near the titanium (the coefficient of thermal expansion of titanium is 8.8 * 10^{-6}/ ° C, whereas the coefficient of thermal expansion of Wollastonite is 8.1 - 9.2 * 10^{-6}/ °C from room temperature up to 600 °C) [234]. Therefore, Wollastonite coating on titanium may be suitable for hard tissue replacement [234]. The Wollastonite powder obtained from natural sources was plasma sprayed into water to convert the irregular shape of Wollastonite to near-spherical [235]. The process parameters used for spheroidisation were: plasma gas argon (Ar) supply of 40 slpm; plasma gas hydrogen (H_2) supply of 6 slpm; spray distance of 430 mm, powder carrier gas argon supply of 3.5 slpm; current of 400 A (amperes) and voltage of 63 V (volts) [235]. The atmospheric plasma spraying of spheroidised Wollastonite on Ti-6Al-4V substrate showed higher bond strength (42.8 MPa) compared to plasma-sprayed Hydroxyapatite (20 MPa) [234]. Immersion of Wollastonite sprayed titanium samples with porosity in SBF fluid showed no delamination, provided the nucleation site for the growth of cells and tissues [234]. Xue et al. [236] studied the dissolution and mineralisation of atmospheric plasma-sprayed Wollastonite on a Ti-6Al-4V substrate. This study showed heat treatment increased the crystallinity of as-sprayed Wollastonite samples from 45% to 92%, with increase in roughness after Wollastonite immersion in SBF fluid [236]. The mixture of Wollastonite and titanium oxide was atmospherically plasma sprayed on the titanium substrate at two ratios of W7T3 and W3T7 (W7T3- Wollastonite 70%, titania 30%; W3T7- Wollastonite 30%, titania 70%) [237]. The bonding strength of the composite was lower than Wollastonite due to poor wetting between Wollastonite and titania [237]. The addition of titania coatings enhanced the fracture toughness, while Wollastonite enhanced microhardness and bioactivity [237]. Li et al. [238] investigated atmospheric plasma spraying of the mixture of silver powder (size 20-100 μm) and Wollastonite powder. At Ca/P ratio of 1.65, a potent antibacterial activity in silver/Wollastonite was observed and no surface morphology difference between silver-loaded and as-sprayed coating was found [238].

2.8.2 Flame Spray Technique

The development of the flame spray technique dates to 1909 by Schoop [239]. However, the basic principle is still applicable to modern techniques [239]. In the flame spray technique, the combustion of fuel gases provides heat to the feedstock material (mostly wire or powder). Simultaneously, the expanding gas, in combination with feedstock material, results in the formation of the jet, which accelerates the coating material towards the substrate [239]. The flame temperature and enthalpy are dependent on the hydrocarbon (C_xH_y) (fuel gas) composition, fuel gas flow rate and oxidiser (either air or oxygen) flow rate [240]. The flame spraying rate ranges from 0.5 to 9 kg/h [217]. However, higher spraying rates are possible for low melting point materials [217]. The temperature and velocity ranges in the flame spray technique are 3000 K and 100 m/s, respectively [239].

The significant advantage of the flame spray technique (**Figure 13**) includes low operation and maintenance cost, user-friendly operation, flexible selection of gas-oxygen combination based on different temperature profiles, more adaptability to a method with small series and high deposition rate with good efficiency [24, 241, 242]. There are many disadvantages, which include: the least adhesive strength of the coating among all the thermal spray techniques, bigger grain size microstructure, lower bond strength, narrower working temperature range, highly porous coating and high heat transmission to the substrate than other thermal spray techniques [241–243]. **Figure 13** illustrates the schematic diagram of the powder flame spray technique.

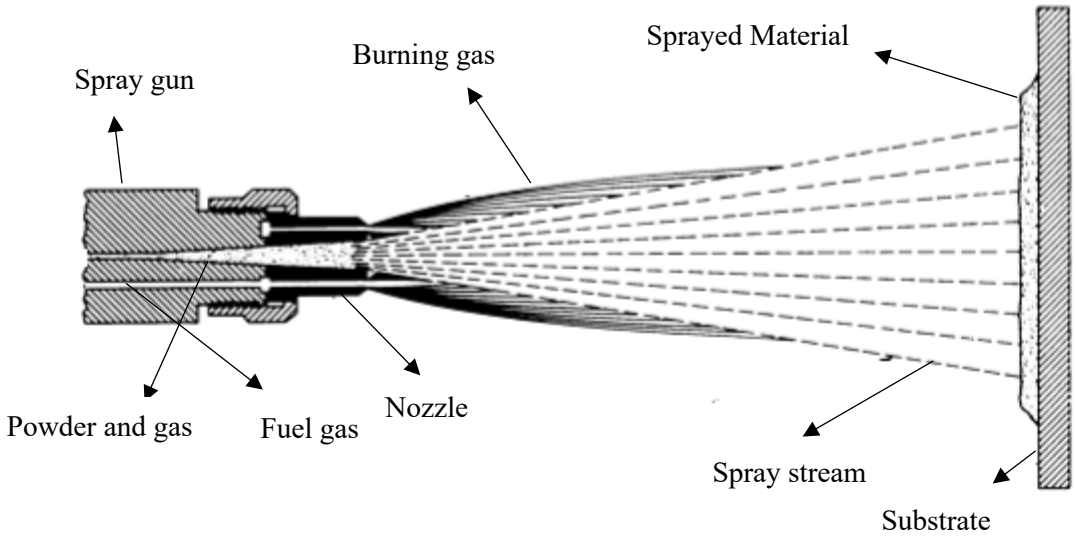

Figure 13, Flame spray deposition technique for powder [241]

Flame spray technology mostly has applications in remanufacturing worn-out parts or parts with incorrect dimensions [241]. Compared to plasma spray and HVOF, the flame spray-coated parts have limited use because of the inferior quality of the coating [216].

The coatings obtained from flame spray coatings are inferior to plasma spray and high-velocity oxy-fuel coating techniques, but their application remains useful [242, 244]. Garcia et al. [245] experimented with the flame spraying of Wollastonite and Wollastonite-diopside on titanium and stainless substrates. Wollastonite was added to 0.5 wt.% of a polyelectrolyte dispersant and 5 wt.% of a polysaccharide binder to prepare a solid phase [245]. Suspensions were stirred by blade mixing for 30 minutes and high shear mixing for 10 min [245]. These aqueous suspensions were subjected to freeze granulation to obtain powder with proper size and homogeneity for thermal spraying [245]. After immersion in SBF fluid, Wollastonite-coated samples developed an apatite layer on their surface [245]. Chebbi [246] experimented with the flame spraying of PHBV, PMMA and PCL on the bare titanium and titanium coated with HA. The results showed the capability of the flame spray technique for drug delivery and biomedical application [246]. The aim of this study is to compare other coating methods of Wollastonite and HA to that of plasma sprayed types; therefore, assessing if Wollastonite cold be deposited by flame spray without suspension or other techniques like sol-gel follow.

2.9 Sol-Gel Dip-Coating Technique

Sol-gel technology is one of the ancient technologies utilised in China to manufacture tofu [247]. One component compound was synthesised using sol and gel in the mid-19th century [247]. Currently, sol-gel technology can easily combine two distinct materials at the molecular level to attain a high homogeneity [247].

In solid-state reaction methods, two powder-form raw materials are mixed [248]. There is a possibility of inhomogeneity in solid-state reactions [248]. This inhomogeneity is overcome by liquid-state synthesis techniques such as the sol-gel [248]. The sol-gel technique transforms the sol into the gel network [248]. Sol generally forms due to hydrolysis and condensation of metal alkoxide precursors [248]. In the sol-gel dip-coating technique, the substrate is dipped into a fluid sol [249]. There are three significant steps after dipping: draining the substrate by gravity, evaporation of the liquid, and condensation reaction, which results in the deposition of the thin film [249]. The schematic diagram of the sol-gel technique with the flow chart is described in **Figure 14**.

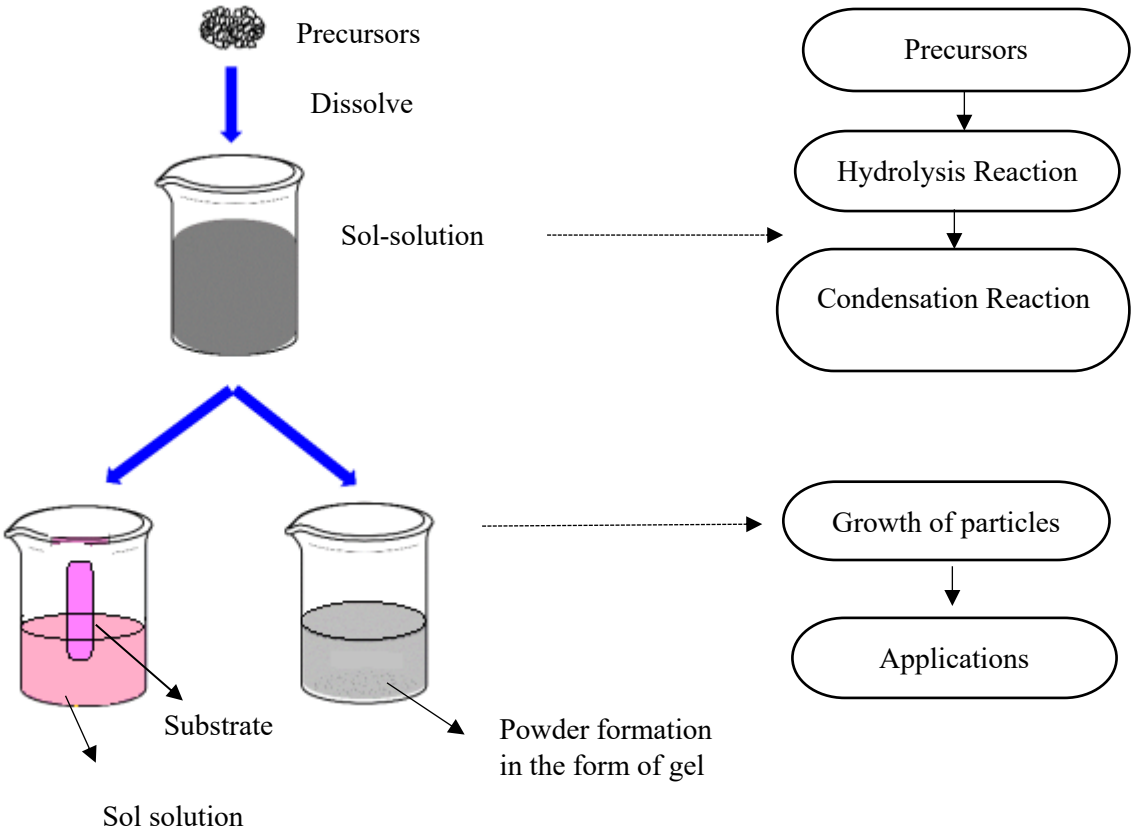

Figure 14, Schematic of sol-gel technique with flow chart [247]

The significant advantages of this technique are the ability to coat a thin layer of less than 10 μm, low-temperature process as compared to the thermal spray technique, coatings enhance the corrosion and oxidation resistance of the substrate metals, coating of the complex-shaped substrate and the possibility to modify the microstructure of coating material [249–253].

2.9.1 Sol-Gel Dip-Coating Technique of Hydroxyapatite (HA)

HA has been deposited on the titanium substrate by various techniques requiring high temperatures [254]. Moreover, these techniques might lead to a non-crystalline HA coating with phases other than Hydroxyapatite (calcium phosphates) [254]. Mavis and Taş [254] studied the sol-gel dip-coating of HA on the titanium substrate. The precursor used in this study was calcium nitrate tetrahydrate for calcium, with diammonium hydrogen phosphate for phosphorous, with ammonium hydroxide acting as a pH regulator [254]. Ün and Durucan [251] experimented on the pre-prepared HA same precursor of Ca and P (calcium nitrate tetrahydrate and diammonium hydrogen phosphate) with the same pH regulator. The obtained powder was introduced into a titanium alkoxide solution [251]. Ti6Al4V substrate was dip-coated in titania-HA solution [251]. Li et al. [253] experimented on the dip-coating of the pure titanium rods in the HA crystal solution. HA crystals were formed by the neutralisation reaction of the phosphoric acid solution and calcium hydroxide suspension [253]. The quantity of HA gel formed from the neutralisation ranged from 1.5 to 10 wt.%. [253].

2.9.2 Sol-Gel Dip-Coating Technique of Wollastonite

Ballare et al. [252] experimented with the sol-gel dip-coating technique of Wollastonite on the surgical grade stainless steel substrate. The precursors used were tetraethylorthosilane and methyltriethoxy silane with ethanol as a solvent and nitric acid as a catalyser [252]. 10 wt.% natural Wollastonite was added with the precursor reaction suspension with the application of double-layer coating [252]. Bao et al. [255] experimented with the dip-coating of Wollastonite on titanium substrate. Calcium nitrate tetrahydrate as a precursor for calcium and tetraethyl orthosilicate as a phosphate precursor was mixed with nitric acid acting as a pH regulator [255]. The formation of Wollastonite as a sol was coated on the titanium substrate by dipping five times [255].

2.9.3 Sol-Gel Dip-Coating Technique of HA/Wollastonite

Romero and Salinas [159] synthesised HA/Wollastonite bioceramic. Hydroxyapatite was manufactured by sol-gel technique, in which calcium acetate and triethyl phosphate were used as calcium and phosphorus precursors, followed by the addition of Wollastonite fibres at ratios of 20, 50 and 80 wt.% suspended in ethanol [159]. A low-temperature procedure (420 °C) was used, where the heat treatment was used to purify bioceramics [159]. In another study conducted by Romero et al. [160], an alternative sol-gel route was used to manufacture HA/Wollastonite. HA was manufactured using precursors such as calcium nitrate and ammonium phosphate, and high purity Wollastonite was dissolved in aqueous medium added to the solution in a ratio of 20, 50 and 80 wt.% to assess post-synthesis of the biocomposite sintered at 1200 °C for 5 hours, to assess the presence of Hydroxyapatite and Wollastonite and their unique phases [160]. Morsy et al. [256] synthesised HA/Wollastonite biocomposite by a co-precipitation method. In the first set, calcium hydroxide ($Ca(OH)_2$) and phosphoric acid (H_3PO_4) (precursors for Hydroxyapatite) and in the second set, calcium nitrate tetrahydrate ($Ca(NO_3)_2.4H_2O$) and sodium silicate nonahydrate ($Na_2SiO_3.9H_2O$) (precursors for Wollastonite) were added to form a biocomposite of HA/Wollastonite. The weight ratio of HA: Wollastonite components were 1:9, 3:7, 5:5, 7:3 and 9:1, respectively. After washing and heat treatment to improve the crystallinity, a biocomposite with a controlled composition consisting of an agglomerated size of less than 1 μm, was manufactured [256]. Lin et al. [18] also manufactured a biocomposite of HA/Wollastonite. Initially, a dropwise solution of 0.3 M $(NH_4)_2HPO_4$ was added to 0.5M $Ca(NO_3)_2$, and ammonia was added to balance the pH, resulting in HA synthesis [18]. Then, the remaining 0.5 M $Ca(NO_3)_2$ was mixed with 0.5 M Na_2SiO_3 to form a HA/Wollastonite biocomposite, with a Wollastonite weight ratio of 10, 30, 50, 70 and 90 wt.%. The biocomposite was cleaned, sintered and isostatically pressed [18]. The proliferation rate of Mesenchymal stem cells (MSCs) started to increase when the Wollastonite quantity was more than 30 wt.%, thus making it a promising candidate for hard tissue replacement [18]. Mesenchymal stem cells (MSCs) resident in the bone marrow or adipose tissue can differentiate into adipose tissue, cartilage, bone and skeletal muscle [257].

HA/Wollastonite scaffolds were also manufactured by the polymeric sponge replica method [162]. Ammonia was added to the aqueous phosphoric acid solution and stirred [162]. Calcium nitrate tetrahydrate was added to this solution, and HA was synthesised

[162]. Wollastonite was added, and the mixture of HA and Wollastonite in aqueous solution formed a slurry [162]. Polyvinyl alcohol was used as a binder, and polyurethane sponges were impregnated with slurries [162]. After that, infilterated slurries were heat treated to form a scaffold. The scaffold produced had a composition of 0, 25, 50, 75 and 100 wt.% Wollastonite [162]. The result showed the incorporation of 50 wt.% Wollastonite maintained a balance in terms of the bioactive and mechanical properties of scaffold [162].

2.10 Failure of a Biocoating

Cohesion between the splats and the adhesion between splats and surfaces directly affect coating properties [258]. The performance of the coating, which is less than 50 μm in thickness is better because, increased thickness leads to fatigue failure and brittleness, therefore splats may not be in complete contact with the substrate [246]. For the lower thickness of 50μm, the failure was in the coating (cohesion) and substrate-coating interface (adhesion), and for 200 μm, the failure was in the interlamellar splat and interface [259].

Due to their high strength, fracture toughness, biocompatibility, and wear resistance; metals are widely used in applications ranging from load-bearing to cardiovascular implants [260]. Non-cemented hip arthroplasty of the metal implants mainly leads to stress shielding, loosening and relative motion [261]. The transfer of load may cause stress by interface disruptions and ultimately lead to the failure of bone [261]. The thermal coefficient expansion of metal is often more than ceramic which produces more residual stresses [246]. Another reason for the failure in metallic implants is fatigue failure due to: cyclic loading, adverse host-tissue response and the release of ions from the metal substrate to the body, which can cause inflammatory response [262].

The long-term stability of the total hip arthroplasty depends on the mechanical bond between the implant, bone, and implant-bone interface [46]. In the case of cemented hip arthroplasty, there is a biological interaction between the metallic implant, polymer cement and bone. The failure, in this case, occurs from two phenomena [46]. The first phenomenon is due to the migration of the wear material (either metal or polymer) in the interface results in an inflammatory reaction, causing debonding [46]. In the second

scenario, the generation of microcracks in cement, cement/ bone interface and cement/implant interface lead to the implant relative motion [46].

A tribology study was conducted on different biocompatible implants, where according to a study on the metal and polymer cup and femur assembly, found polymer on metal assembly was more durable than metal on metal assembly [263]. However, an increased inflammatory response was observed in polymers due to the polymer inferior wear characteristic [263]. The material loss due to volumetric corrosion occurred in the ceramic-based implant, with pitting corrosion occurring at the local inhomogeneous areas of the passive film [263]. Fretting corrosion occurred due to micromotion, while galvanic corrosion occurred when a metal of a distinct type exposed itself to other corrosion sites [263].

The primary cause of the collapse of the cementless implant is generally delamination, aseptic loosening, dislocation, and infection [264]. Dislocations and grain boundaries lead to more dissolution in the case of calcium phosphate cement [4]. The mechanical testing of Hydroxyapatite (HA) and various calcium phosphate biomaterial cannot be done due to fatigue failure occurring in interfaces [147]. Therefore, due to the degradation of HA in a biological environment, there can be poor fixation between implant and tissue, the osseointegration of implant tissue might be severely affected if the HA coating does not adhere to the substrate [265].

Bioglass has poor strength and ductility, therefore, it is used chiefly with metals to improve its bioactivity [266]. Bioglass coatings applied onto titanium substrates using the bond coat layer of Amdry 6250 (60 wt.% alumina and 40 wt.% titania), however, showed delamination between the bond coat layer and substrate cracks between the glass and bond coat layer [188]. The synthesis of the scaffold from glass-ceramic (the composition of 57SiO_2, 34CaO, 6Na_2O, 3Al_2O_3) had compressive strength like cortical bone but lower flexural strength [82]. Bioglass (composition: 31SiO_2- 11P_2O_5- (58-x)CaO- x MgO, where x was 0 and 2, represented two different powders with a designation of P1 and P2) was plasma sprayed onto a stainless steel substrate, led to debonding for high thickness samples, with structural defects, which led to cracks and a reduction in the hardness [231].

Metal bioimplant leads to stress shielding, whereas polymer bioimplant leads to undesirable healing of bone [138]. When HA/polyether ether ketone (PEEK) biocomposite was synthesised, where PEEK was used as a matrix, the HA particles debonded from PEEK due to poor interfacial bonding with a reduction in tensile strength and strain after adding HA [138]. During a push-out test experiment, the fracture occurred in the HA-coated titanium interface [228].

Sin2Ψ measures the residual stress, whereas the three-point bending test measures the Young modulus of HA coatings on the titanium substrate [267]. Minimising the substrate temperature to less than the melting temperature during spraying reduced the residual stress level [268]. Residual stress might be due to the contraction of a single splat, different thermal contractions, CTE mismatches, and strain generated due to solid phase transformation [259]. Sergo et al. [269] identified the residual stress effect near the interface in plasma-sprayed HA. Compressive stress hindered dissolution, whereas tensile stress promoted dissolution, reducing mechanical strength by cracks and dislocation, especially in the interface [269]. In thermal barrier coatings, when the residual stress in the top coat/ bond coat was more than that bond coat/ substrate interface, this increased the probability of spalling delamination and surface cracks [270]. Yang and Chang [267] verified residual stress on plasma-sprayed HA on titanium alloy by destructive and non-destructive techniques. Most of the coating stress was compressive; the sample had more strain with poor cooling conditions, which ultimately transformed into residual stress [267]. The interface between HA and substrate had the highest residual stress [267].

In plasma spray technology, the coating degradation can be due to un-melted particles, secondary phase material, and interlayer pores, even with protective overlays and coatings [271]. The amorphous phase formation can be associated with the partial dehydroxylation of HA during the plasma spray [221]. Cohesive failure occurs in HA samples plasma sprayed at a lower particle size (less than 45μm) [221]. In contrast, cohesive and adhesive failure occur when the particle size is increased to more than 45μm [221]. Conditions arising from plasma-particle interactions generally cause incomplete and non-uniform treatment of particulates; therefore, the particle size range must be less [14]. Satisfying the requirement for pore sizes in the range of 200-400 μm for the

promotion of bone regeneration and growth has proven difficult with plasma spraying [14].

2.11 Design of Experiment (DOE) Analysis

The STATEASE design of experiment (version 13) software was used to analyse the data obtained from the experiments. Sir R. Fischer introduced the DOE technique in the 1920s to understand the cause-effect relationship of various fertilisers on land plots. The success of the DOE software resulted in its utilisation in various fields, including biology, engineering, and pharmaceuticals. Implementation of the DOE led to replacing the conventional one variable at the time (OVAT) approach used by engineers. The OVAT system was primarily utilised in the manufacturing sector. In the OVAT system, engineers vary one process parameter while keeping another process parameter constant. OVAT was unreliable and time-consuming; interaction factors could not be determined, making it impossible to determine the effect of one process parameter on another. [272] The DOE has substituted the OVAT approach due to its statistical method that plans, analyses and interprets data outputted from experiments. DOE achieves reasonable conclusions effectively and economically by varying one or more factors within a process parameter. Some factors may affect the overall process; while others may have moderate, or less impact. The objective of DOE is to specify the extent of effect each process parameter has on the overall process to achieve an optimum solution. [272]

Some of the important terms that are important for the analysis of the design of experiments (DOE) are factors, range, interaction, response, and ANOVA aspects, which determine if a factor affects a response. The factor is an independent variable or the variable over which one has control and can be modified to determine the point of optimal response [273]. The range is decided by the input and output, factors and response. The lower and upper value of response at the corresponding factor determines its range Interaction happens when the change in one factor has an effect on another factor [274]. DOE experiment is typically done at 2 or 3 levels of every factor, where the outcome of such an experiment is a response [273]. The effect of a factor on a response is determined by the difference between the mean of the (unrelated) groups or the significant difference between the groups [275].

2.11.1 Screening Design

The screening process helps investigate more information about the process. Screening design is performed before the response surface methodology experiment to determine the extent of the effect of the process parameter on the process. The screening design technique removes the process parameter with a negligible impact on the process, so it assist in developing a fine response surface methodology [272]. The two types of screening design aligned with this study are mentioned below.

a) *Fractional experiments*

Two-level and three-factor experiment screening tests have been presented in **Table 8** below. **Table 8** shows the design of the experiment for three factors and two levels. For example, the number of experiments is 2^3 (2^k, where the level is two and k is the number of factors). In this type of experiment, factors are denoted by +1 (high level) and -1 (low level). In factorial experiments, all factors and levels are investigated and considered by the two-level factor experiment. [276]

Table 8, 3 factor, 2 -level factorial experiment [4]

Run	***X_1***	***X_2***	***X_3***
1	-1	-1	-1
2	1	-1	-1
3	-1	1	-1
4	1	1	-1
5	-1	-1	1
6	1	-1	1
7	-1	1	1
8	1	1	1

b) *Fractional factorial experiments*

A fractional factorial design is $2^{k-p,}$ where k is the number of factors and p is the factor fraction. A significant variable response requires a few main effects and lower-order

interactions. In the fractional factorial method, there is a reduction in the number of runs without reducing the number of main effects to obtain an optimum response. Therefore, fractional factorial design is introduced. [276]. **Table 9** shows the construction of a 2^{5-2} matrix. In this case, there are five factors, but not all are significant. A full 2^3 are used for columns X_1, X_2, and X_3; the other columns are represented as $X_4 = X_1X_2$ and $X_5 = X_1X_3$. X_1X_2 is the interaction of the first and second factors, whereas X_1X_3 is the interaction of the first and third factors. X_2X_3 is not considered in the above table, as the interaction between the second and third factors is insignificant.

Table 9, 3-Factor, 2-Level fractional factorial experiment [277]

Run	X_1	X_2	X_3	X_4 (X_1X_2)	X_5 (X_1X_3)
1	-1	-1	-1	1	1
2	1	-1	-1	-1	-1
3	-1	1	-1	-1	1
4	1	1	-1	1	-1
5	-1	-1	1	1	-1
6	1	-1	1	-1	1
7	-1	1	1	-1	-1
8	1	1	1	1	1

The factorial design at the 2-level in the screening technique is only convenient for a smaller number of factors, i.e., 1, 2 or a maximum of 3. Suppose there are 8 factors; the possible number of experiments would be 2^8 (two levels: low (-1) and high (+1)) and 8 factors, which would be 256 experiments that is 2^8. Therefore, to reduce the number of experiments, fractional factorial design is used, which is represented by 2^{k-p}, where 2 is a level, k is a factor and p is the fraction of the full factor used. [276]

2.11.2 Response Surface Methodology

Response surface methodology combines techniques concerning mathematics and statistics to analyse and modulate the problem. Various factors influence the problem in a particular area of interest. Response surface methodology optimises the result by varying all the factors involved, using a scientific method, which requires observation and collection of information. For example, input x, a set of factors, influences the output

variable y, a response. Response surface methodology plans, designs, and analyses the output response from the collection of input factors. [278]

Response surface methodology can be specified as an independent variable in the equation below in **Equation 1** [279].

$$y = f(x_1, x_2, \ldots x_k) \quad \ldots\ldots\ldots\ldots$$

Equation 1

where k is the number of independent variables

In 1951, Box and Wilson introduced the first-order model. This model cannot be used for curved and large model surfaces. This model only concerns straight within a small model surface regions. First-order can approximate the response, but it is easily applicable and understandable, can be represented as the linear approximation of the independent variables to obtain a suitable response. [278]

The first-order equation is shown in **Equation 2**.

$$Y_i = \beta_0 + \beta_1 x_{i1} + \beta_2 x_{i2} + \ldots\ldots\ldots\ldots\ldots + \beta_q x_{iq} + \varepsilon_i \quad (i= 1,2,3,\ldots\ldots...n) \quad \ldots.. \textit{Equation 2}$$

A second-order approximation equation can evaluate the maximum, minimum and saddle points. The first-order equation cannot determine the response surface consisting of the curvature. Therefore, the second-order equation approximates the response for the curvature. The value of y determines the relationship between the independent variable and response surface methodology. A RSM second-order polynomial equation is given below in **Equation 3**, which can approximate the response of the curve over almost all regions. The two specific designs used in the second-order approximation are the Central Composite Design (CCD) and the Box-Behnken Design (BBD**).** Typically, a factorial design may have two levels per factor (-1 and +1), however the Central Composite Design can have up to 5-level factor (-α, -1, 0, +1, +α), whereas the Box-Behnken design is a 3-level factor (-1, 0, +1) [280].

In the current study, the design used was the Box-Behnken design.

$$\mathbf{y} = b_o + \sum b_i \chi_i + \sum b_{ij} \chi_i \chi_j + \sum b_{ii} \chi_{ii}^2 + \varepsilon$$

……...Equation 3

Let us discuss the box Behnken design in more detail: -

a) *Box-Behnken Design*

Box and Behnken developed this design in the 1960s. This design is obtained by combining incomplete two-level factor designs and adding a specific number of centre points [281]. Box Behnken design can have a number of design points based on the factors studied. The number of design points (experimental runs excluding centre points) is given by the formula 2k(k-1) + C, where C is the number of centre points and k is the number of factors. A BBD includes typically 3 to 5 centre points to improve the stability and reduce experimental error. In the current study, there are 3 factors: pump flow rate, airflow rate and Wollastonite wt. fraction and 5 centre-points. 3-level factor (**Figure 15**) comprising 12 design points and five centre points in this design offer enough information to accommodate ten polynomial equations [281]. **Figure 15** shows the diagram for BBD for three factors.

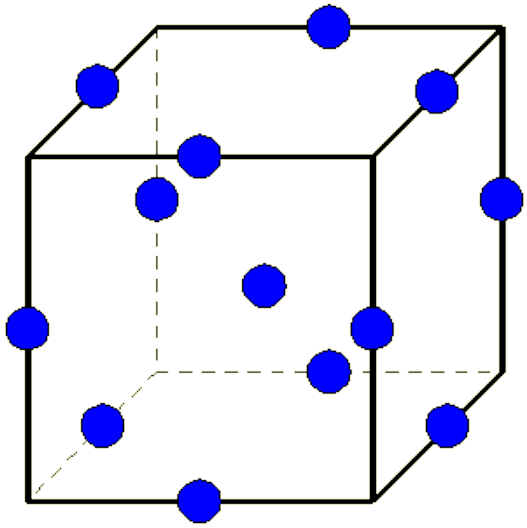

Figure 15, A schematic for BBD for three factors [282]

To understand why Box-Behnken design was chosen for the study, was based on characteristics as specified below [282]:

- This design type has specific positioning of design points
- It has three levels for each factor
- The quadratic model is generally estimated by this design.
- This type provides robust coefficient estimates near the centre of the design space compared to the cube corner.
- This design type is sensitive to irregularities in an experiment, which makes it accurate as compared to other designs

- The region of interest is almost like a region of operability.

The response surface methodology refines the models after determining important factors from a screening design. A response surface design is an advanced design of experiments (DOE) that helps understand and optimise the obtained response. RSM is used to optimise processes and employs designs like central composite design (CCD) and Box-Behnken Design (BBD). The primary goal of RSM is to find the optimal operating conditions or improve the performance of a process by understanding the relationship between input variables (factors) and the desired response. RSM commonly uses designs like CCD or BBD to fit a quadratic model (second-order polynomial). The Box-Behnken design does not contain an embedded factorial or fractional factorial design, and the design points fall at a combination of high-level factors, low-level factor, and their midpoints. [280]

2.11.3 ANOVA

To perform the ANOVA (Analysis of Variance) test on the results, one needs to have an understand of the basic terms which it uses. In the context of ANOVA (Analysis of Variance), a significant effect is represented by the p-value. The p-value gives evidence suggesting that at least one of the groups compared has a different mean value from the other, expressed as follows:

- Null Hypothesis: Null hypothesis typically states that there is no significant difference between the means of the groups compared.

- Alternative Hypothesis: The alternative hypothesis states that at least group mean is different from others.

- P-value Interpretation: The p-value in ANOVA indicates the probability of observing the data or extreme data. For example, if p-value is 0.05, it suggests that the observed difference between the groups is unlikely to have occurred by chance, thus proving null hypothesis wrong.

- Significance level: The significance level (often denoted by α) is the threshold below which a p-value is considered statistically significant.

- Interpretation: if the p-value is less than the chosen significance level (if $p<0.05$), the result is considered statistically significant. This means that the null hypothesis is

rejected in favour of the alternative hypothesis, indicating that at least one group's mean is different from others.

The means of two or more groups with one dependent variable are compared by ANOVA (analysis of variance). ANOVA compares the variation within one group to the equivalent variation within a groups mean variation. In ANOVA variance, the sample size should be more than 30 to reduce the errors caused by the null hypothesis or failure to declare the statistical difference. However, some errors can be reduced if a researcher reduces the significance level. [283]

a) *Estimation of co-efficient in model*

The Design Expert software uses regression analysis to calculate the coefficients in each response in the BBM design used in the experiment [279].

b) *Testing the adequacy of the model developed*

Adequacy of the model developed was done by the analysis of variance test (ANOVA) test [279]. Each term in the regression model and statistical significance of the model was tested by sequential F-test, lack-of-fit test and other adequacy measures (i.e. R^2, Adj- R^2, Pred. $R^{2,}$ and Adeq. Precision ratio) using the Design Expert software to obtain the best fit. The level of significance can be determined by the values of Prob (probability, sometimes called p-value) and F, and ANOVA calculates each term in the model [279]. If the p-value> F and each term do not exceed the level of significance, then the model may be termed significant within the interval (1-α) [279]. Lack of fit may be considered insignificant if prob >F [279]. **Table 10** shows ANOVA for the spray drying [279]. **Equations 4 to 8** shows the formula for different sources.

Table 10, Spray drying ANOVA

Source	SS	df	MS	$F_{cal.}$- Value	p-value or Prob > F
Model	SS_M	p	Each SS divided by its df	Each MS divided by MS_R	From table or software library
A-Pump Flow	SS_1	1			
B-Air flow rate	SS_2	1			
C-inlet temperature	SS_3	1			
AB	SS_{12}	1			
AC	SS_{13}	1			
BC	SS_{23}	1			
A^2	SS_{11}	1			
B^2	SS_{22}	1			
C^2	SS_{33}	1			
Residual	SS_R	N-p-1			-
Lack of Fit	SS_{lof}	$N - p - n_0$			From table
Pure Error	SS_E	n_{0-1}			-
Cor Total	SS_T	N - 1	-	-	-

$$R^2 = 1 - \left[\frac{SS_R}{SS_R + SS_M}\right] \quad \text{..... Equation 4}$$

$$Adj R^2 = 1 - \left[\left(\frac{SS_R}{df_R}\right) \times \left(\frac{SS_R + SS_M}{df_R + df_M}\right)^{-1}\right] \quad \text{..... Equation 5}$$

$$Pred R^2 = 1 - \left[\frac{PRESS}{SS_R + SS_M}\right] \quad \text{..... Equation 6}$$

$$PRESS = \sum_{i=1}^{n} (y_i - \hat{y}_{i,-i})^2 \quad \text{..... Equation 7}$$

$$Adeq.precision = \left[\frac{Max(\hat{Y}) - Min(\hat{Y})}{\sqrt{\frac{p \times MS_R}{n}}}\right] \quad \text{..... Equation 8}$$

Where: P = Number of model parameters (including intercept b_0), n = number of experiments

c) *Model reduction*

When the p-value is greater than the range of level of significance (e.g., 1-α), the full model consists of insignificant model terms that can be eliminated. All the possible terms in the regression model can be manually or automatically deducted. The 3-automatic procedure for eliminating insignificant model terms is given below [284]:

i. Forward selection procedure:

Initially, a constant term is added, followed by the addition of the first variable, which has a direct relation with y. If this variable regression coefficient is significant, it remains

in the equation. Then the second variable is tested, keeping the first variable regression coefficient as a standard. If the regression coefficient of the second variable is significant to the first variable, it remains in the equation. The process is continuous until the variable is insignificant.

ii. Backward elimination procedure:

The full equation is noted in this procedure and eliminates each variable in a sequence. The variable with the smallest T-ratio (ratio of regression coefficient to its standard error), which has a minor contribution to the reduction of error, is eliminated first, and so on. If there are many insignificant variables, the process starts by deducting the variable with the smallest insignificant T-ratio. The process stops when all the T-ratio of the regression coefficients in an equation are significant.

iii. Stepwise regression method:

This method is a fusion of backward as well as forward procedures. It considers the addition of variables at the initial stage in the forwarding procedure and the deletion of the variable in the backward procedure. Different levels of a significant variable can be eliminated or added in this method.

iv. Development of the final reduced model

Following the above steps, the final reduced model is noted. The terms only contain significant terms. The reduced ANOVA table is produced.

v. Post analysis

The model is verified and tested; midpoints test the adequacy of the model at any stage of the model. Important plots such as 3D plots, contours and perturbation plots help in the observation of the effects and their contribution to the response. The optimised process parameters for the spray drying operation can be noted with this developed model.

vi. Optimisation

1. Desirability approach

Overlaying the contour plot for each response, constrained optimisation problem, and desirability approach are the methods in statistical science available for the solution of response queries. The most common statistical software packages for multiple response optimisation techniques include GPSS, NEMROD and Design Expert. The major advantage of the desirability method is its simplicity, availability of software and flexibility in weighing an individual response. In this technique, multiple responses are combined into a dimensionless performance called the desirability function. In the desirability approach, each estimated response is bounded by the range $0<d_i<1$. As the value of di approached 1, Y_i became more desirable. The desirability of each response is calculated by the formula given below. The shape of each desirability goal can be changed by adding the weight field 'wti' (a value ranging from 0.1 to 10). weights are added to emphasise the target. Higher weight implies higher importance to the goal. The weight value of 1 makes the desirability curve linear. In the desirability function, each response is represented as (r). Value of importance varies from 1(+) least important to 5(+++++) most important. The overall objective function is shown below, where n is the number of responses and T_i is the target value of i^{th} response. [284].

The desirability for different goals is mentioned in **Equations 9 to 12**, respectively.

- **For the goal of maximum, the desirability would be defined by:**

$$d_i = \begin{cases} 0 & , \quad Y_i \leq Low_i \\ \left(\frac{Y_i - Low_i}{High_i - Low_i}\right)^{wt_i} & , \quad Low_i \langle Y_i \langle High_i \\ 1 & , \quad Y_i \geq High_i \end{cases}$$

.....Equation 9

- **For the goal of minimum, the desirability will define by:**

$$d_i = \begin{cases} 1 & , \quad Y_i \leq Low_i \\ \left(\frac{High_i - Y_i}{High_i - Low_i}\right)^{wt_i} & , \quad Low_i \langle Y_i \langle High_i \\ 0 & , \quad Y_i \geq High_i \end{cases}$$

…….Equation 10

- **For the goal as a target, the desirability will define by:**

$$d_i = \begin{cases} \left(\frac{Y_i - Low_i}{T_i - Low_i}\right)^{wt_{1i}} & , \quad Low_i \langle Y_i \langle T_i \\ \left(\frac{Y_i - High_i}{T_i - High_i}\right)^{wt_{2i}} & , \quad T_i \langle Y_i \langle High_i \\ 0 & , \quad Otherwise \end{cases}$$

…….Equation 11

- **For goals within range, the desirability will define by:**

$$d_i = \begin{cases} 1 & , \quad Low_i \langle Y_i \langle High_i \\ 0 & , \quad Otherwise \end{cases}$$

$$D = \left(\prod_{i=1}^{n} d_i^{r_i}\right)^{\frac{1}{\sum r_i}}$$

……...Equation 12

2. Optimisation approach in Design Expert software

Design Expert software identifies the combination of factors that satisfy the criteria of each factor (optimisation criteria) and process factors (multiple response optimisation). Numerical and graphical optimisation methods were used to determine each factor. Numerical optimisation finds one or more points in a domain that could maximise the objective function. In graphical optimisation, there are multiple responses. Therefore, the

software determines the region where maximum optimisation or response is possible. Superimposing of critical response contour is done on contour plot, and visual inspection of best possible combination is possible afterwards. The region that does fit the optimisation criteria is faded. In the case of multiple responses, numerical optimisation should be undertaken to uncover the feasible region. Graphical response displays the feasible response value in the region [284] .The flow chart of Design Expert software is shown below in **Figure 16.**

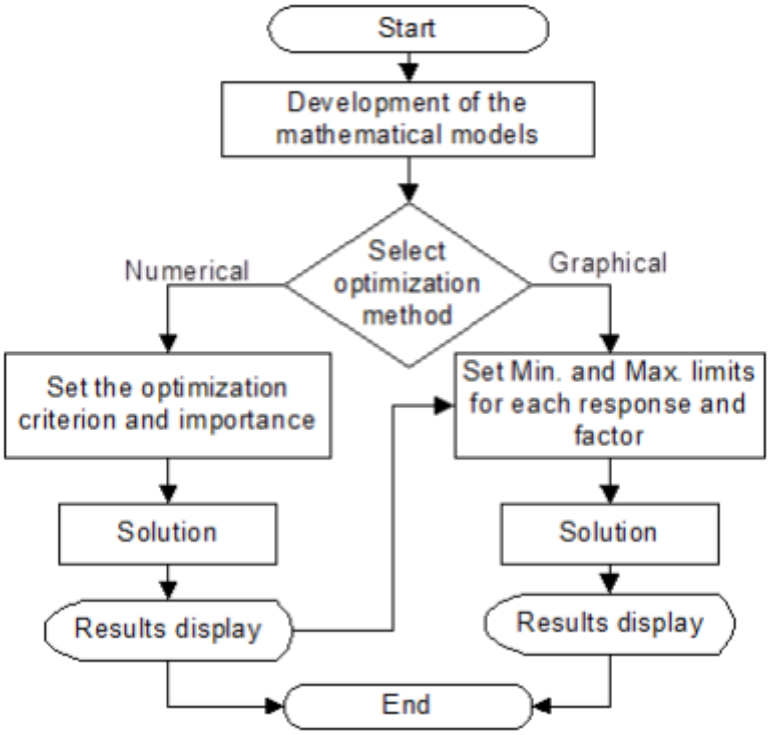

Figure 16, Design Expert software flowchart [285]

2.12 Summary

This research aims to develop orthopaedic implants for biomedical applications. Hydroxyapatite is commonly coated onto a titanium alloy substrate by plasma spraying. However, the mechanical properties of Hydroxyapatite are still questionable for load-bearing applications. For that reason, Wollastonite will be added to the biocoating containing Hydroxyapatite layer onto a titanium alloy substrate. Wollastonite use in biocoating remains limited despite its unique biological and mechanical properties. High-temperature deposition techniques of Hydroxyapatite (such as the thermal spray process) may lead to its decomposition, which may affect the stability of biocoating. Therefore, in

the current study, spray coating technique and sol-gel technique will be employed to coat Hydroxyapatite, Wollastonite and Hydroxyapatite/Wollastonite separately onto a titanium substrate. These techniques are low-temperature deposition (in the range of 30 ºC to 110 ºC). This low-temperature technique will ensure a homogeneous deposition of Hydroxyapatite, Wollastonite and Hydroxyapatite/Wollastonite without affecting the properties of titanium, Hydroxyapatite and Wollastonite. In the spraying technique, as-received Hydroxyapatite, Wollastonite and Hydroxyapatite/Wollastonite composite mixture will be dissolved in deionised water to form a slurry. The slurry of Hydroxyapatite and Wollastonite will be dried by hot air (temperature range of 100-110 °C) and sprayed onto a titanium alloy substrate. Both techniques will be compared with statistical tools such as Design of Experiments (DOE), and the results will be evaluated.

3 Experimental Equipment and Procedure

3.1 Introduction

The experimental procedure has been described in several stages:1) Coating material description, 2) Oven drying methodology equipment and experiment, 3) Hall flowmeter, 4) Characterisation study, 5) Substrate surface preparation, 6) Spray drying equipment and description of the Design of Experiment (DOE) method associated with the spray drying technique, 7) Steps to improve the flowability of Wollastonite and 8) Sol-gel coating method. The first subsection looks at the general information and types of equipment for the characterisation study of raw materials (Hydroxyapatite and Wollastonite in the current study), which includes oven dryer, Hall flowmeter, electric vibrator, scanning electron microscope, FTIR spectroscopy and X-ray diffractometer, their working principles and technical information. This subsection is followed by a brief description of titanium alloy and its preparation techniques, including grit blasting and polishing. The following subsection describes the basic spray drying operation, its advantages, technical data and Design of Experiment (DOE) technique used to optimise the spray drying operation. The following subsections describe the approach to improve the flowability of Wollastonite powder. This subsection illustrates heat treatment devices such as Nabertherm and Carbolite furnaces. Following that, spray-coating and sol-gel dip coating with three different procedure results is explained along with the figure.

3.2 Coating Material

3.2.1 Hydroxyapatite

A primary raw material used in this study was Hydroxyapatite. Hydroxyapatite has a spherical shape with an average particle size of 45 μm [286]. Plasma Biotal Limited supplied Hydroxyapatite used in this process with the registered name HA CAPTAL® 60-1 [286]. The as-received powder was sintered at 1150 °C and sieved to obtain a particular size. The particle was spray-grade material with the particle size distribution of D(10) = 15-25 μm, D(50) = 40 to 50 μm and D(90) = 70 to 90 μm [286]. **Figure 17** shows the Hydroxyapatite powder purchased from the supplier, whereas **Figure 18** shows the morphology of the as-received Hydroxyapatite powder at 100X.

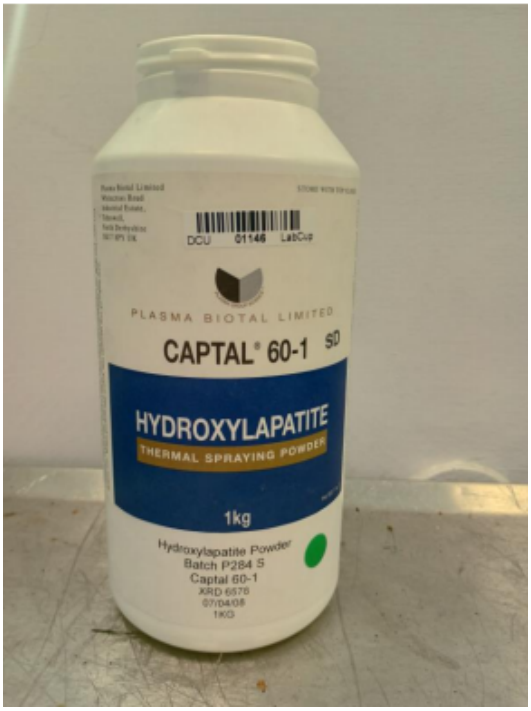

Figure 17, Hydroxyapatite powder

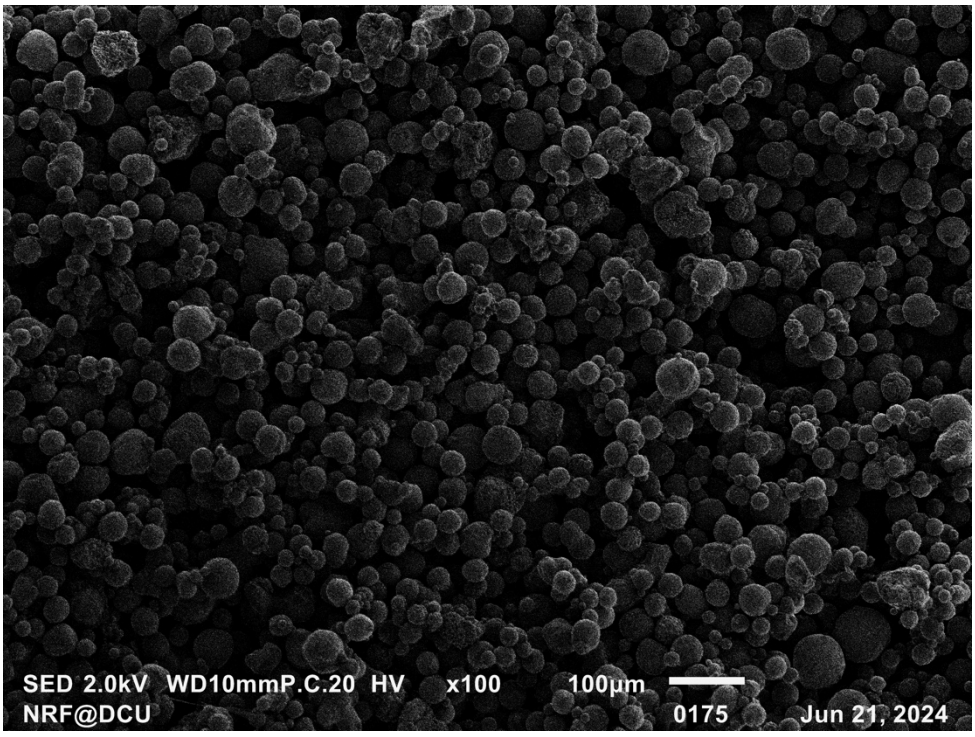

Figure 18, Morphology of as-received Hydroxyapatite powder at 100X

3.2.2 Wollastonite

The second significant raw material used in the present study was Wollastonite. Wollastonite has an acicular needle shape, white colour, and Mohr hardness of 4.5-5.0

[95]. It has been commonly used with ceramic and paint to improve its properties and durability [95]. A Wollastonite powder container image and morphology of as-received Wollastonite powder at 100X are shown in **Figures 19** and **20**.

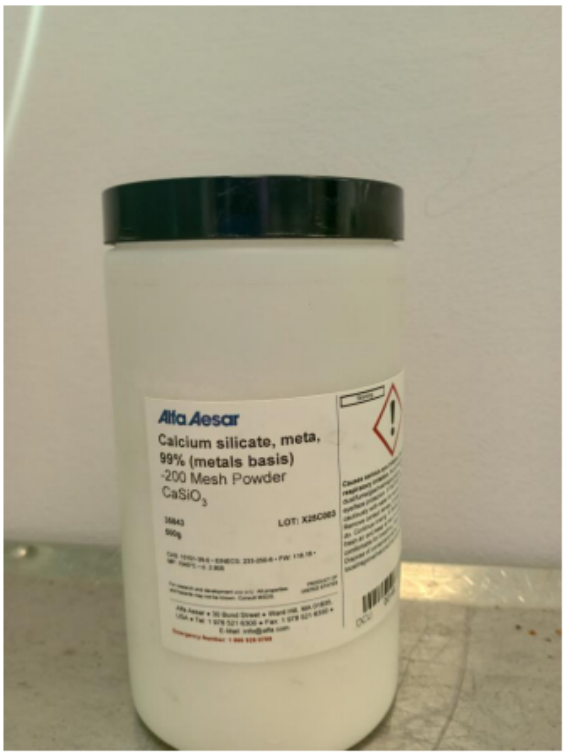

Figure 19, Wollastonite powder

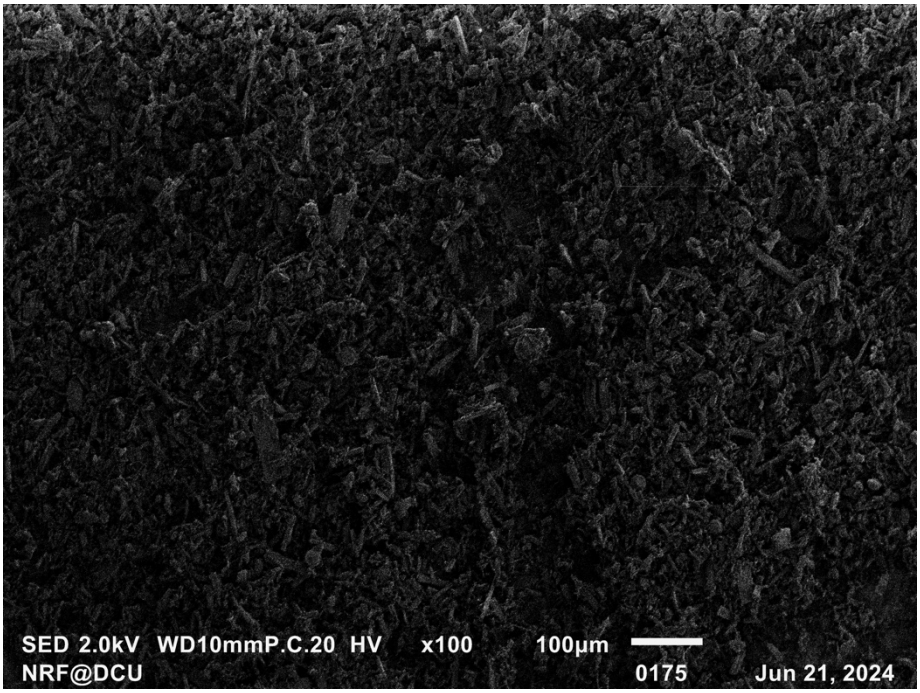

Figure 20, Morphology of as-received Wollastonite powder at 100 X

3.3 Powder Preparation and Characterisation

3.3.1 Oven Drying

The oven dryer used in the current study was a forced convection unit supplied by Venti-line prime [287]. The equipment has a real-time clock, digital timer, USB port, and test results ranging from 50-300 °C, with a microprocessor control with LCD and illuminated touch buttons [287].

The VENTI-line Oven dryer and inside view of the oven are shown in **Figures 21 and 22**, respectively. The oven-drying device is automatic and stores up to 3 programs, including adjustable ramps, temperature-time profiles, and a loop function to ensure continuity [287]. The VENTI-line prime oven fan speed and the manual air flap are adjustable and displayed on the LCD by buttons [287].

Figure 21, Venti-Line oven dryer [287]

Figure 22, Inside view of Venti-line oven dryer

a) *Oven drying methodology*

Hydroxyapatite and Wollastonite were used as raw materials in the present study. 80 grams of both Hydroxyapatite and Wollastonite were placed in a beaker. The temperatures used for this experiment set were 60 °C, 80 °C, and 100 °C. Each temperature was assigned a specific program; 60 °C was set for program one, 80 °C nominations for program two and 100 °C for program three, respectively. In the case of 60 °C, the oven was heated to 60 °C; after achieving the temperature of 60 ºC, a glass container containing Hydroxyapatite and Wollastonite powders was measured and placed in the heated oven. Both the containers were heated for one hour. The weight was measured and noted. The powders were then heated for one more hour, and the powder weight was measured and noted. The difference between the powder weight at all the conditions presented above was noted. The same procedure was repeated for 80 °C and 100 °C.

3.3.2 Hall Flowability Test of Initial Powder

Kehoe [33] designed and manufactured a Hall flowmeter, following the specification in ASTM B213 [288]. The flowability of Hydroxyapatite and Wollastonite and their difference were evaluated using the Hall Flowmeter. The Hall flowmeter consists of a calibrated orifice with a diameter of 2.54 mm (**Figure 23**). **Figure 24** shows a glass

beaker placed below the funnel. The distance between the orifice and the top edge of the glass beaker was 125.4 mm [33].

In the case of Hydroxyapatite, 30 grams of Hydroxyapatite was pre-weighed and used in this study. However, this study used only 20 grams of pre-weighed powder concerning Wollastonite. The difference in pre-weighed quantities was due to the difference in density of Hydroxyapatite and Wollastonite, which explains why only 20 grams of Wollastonite filled up the funnel [78, 289]. The procedure involved for powder flowability was evaluated based on the following steps: the funnel was filled with powder, then the finger was removed from the orifice opening, and the stopwatch was started immediately after removal to determine the powder flowability. The time taken until the whole powder exited the funnel was recorded accurately ($^{+}$ 1 second). The collected powder in the beaker was weighed to ensure all the powder was collected. The value of the powder weight was recorded in grams, and the flow rate was recorded in g/sec to an accuracy of 0.1 g/sec, respectively [290].

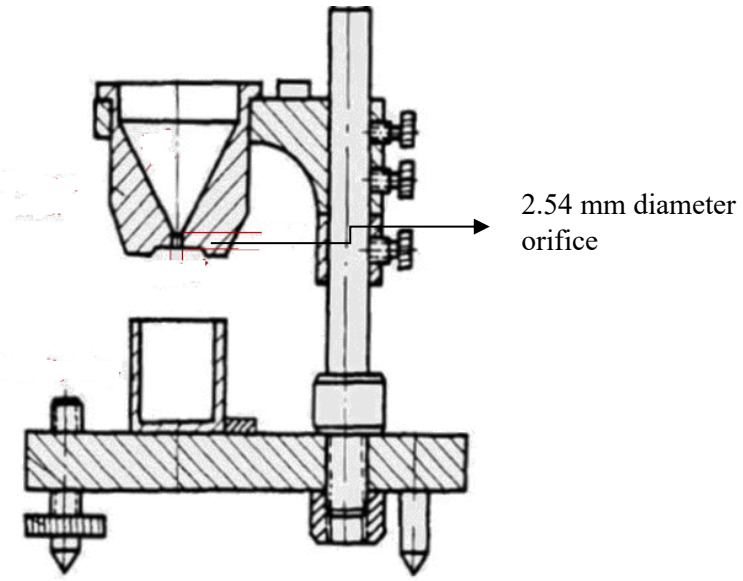

Figure 23, Hall flowmeter design [33]

Figure 24, Hall flowmeter

3.3.3 Sieving

In the sieving technique, particles were placed in different sizes of sieve and separated with the help of an electric vibrator. The sieved material was propelled and forced through the sieve mesh, leading to the material falling due to gravity [291]. The company Fritsch supplied the sieve with the vibrator equipment name 'Analysette'. This sieve system equipment caused oscillation vertically due to an electromagnetic drive [291].

Out of the various sieves sizes ranging from 25 µm to 5 mm, only three sieves, 45 µm, 75 µm, and 100 µm, were used in the present study, as shown in **Figure 25**. Hydroxyapatite and Wollastonite powder obtained from spray drying were transferred to a vibrator sieve, and all the powders were sieved for 20 minutes at 60% frequency.

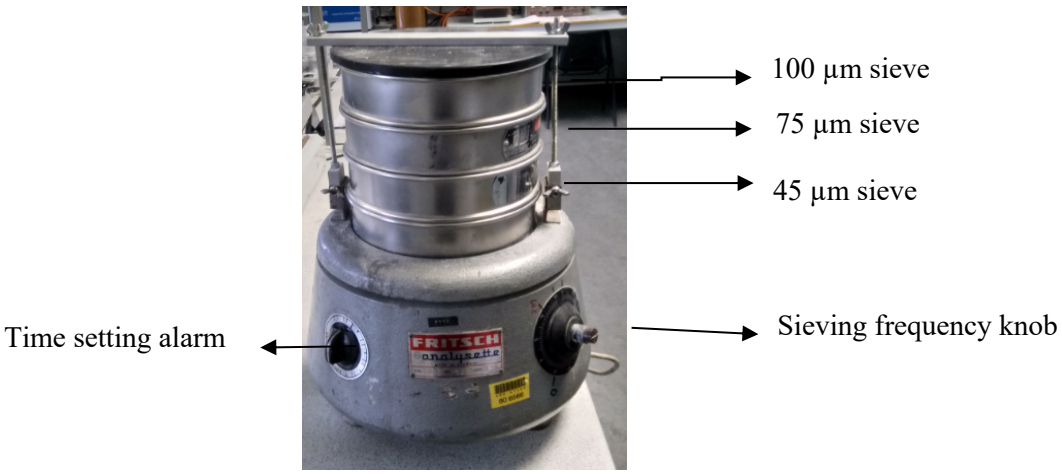

Figure 25, Vibrator sieve

3.3.4 Heat Treatment Test

a) *Nabertherm and Carbolite furnace*

Wollastonite is acicular in shape, as shown in **Figure 20**. Therefore, for the smooth-flowing powder, Wollastonite was heated at various temperatures from 700 to 1400 °C. 20 grams of the powder were selected for this study, and each was heated for 2 hours. Both the furnaces were user-friendly and programable, with a heating rate of 5 °C/min for the Nabertherm furnace and 5 °C/min for the Carbolite 1600 furnace.

Nabertherm furnace (**Figure 26**) was employed to heat 20 grams of Wollastonite powder from 700 °C to 1100 °C. This equipment has a quick heating time and reached higher temperatures in less time, with a maximum temperature of 1100 °C [292]. The inside view of the Nabertherm furnace is shown in **Figure 27**. A Carbolite furnace (**Figure 28**) was used to heat the Wollastonite at 1200, 1300 and 1400 °C, respectively. Silicon carbide elements heated the chamber furnace. It was an easily programmable, slower heating process as compared to Nabertherm. The Carbolite and Nabertherm furnaces were heated at 5 °C/min to reduce the crucible cracking.

Figure 26, Nabertherm furnace

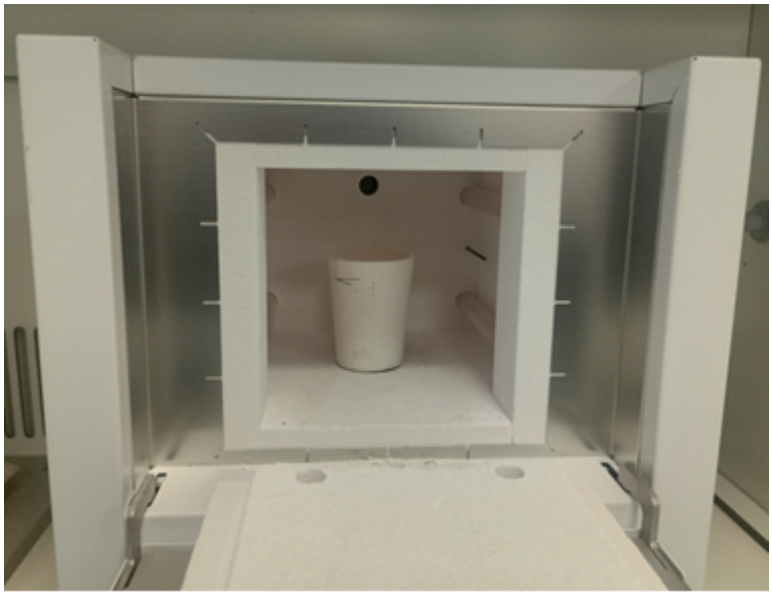

Figure 27, Inside view of Nabertherm furnace

Figure 28, Inside view of carbolite furnace

b) Carbolite Lenton tube furnace

The tube furnace used in the present study was the Carbolite 1400 ºC STF model, which created the inert environment for the heat treatment of the samples. The gas used to create an inert environment were nitrogen and argon gas. The furnace, which is made of stainless steel, is supplied with a work tube with a hollow structure placed inside the furnace to create a vacuum. The hollow structure at the end of the tube furnace ensures continuous entry/exit of the inert gas via a gas pipe. The whole operation is easily programmable, where the heating rate, dwell time and time of operation can be regulated [293]. **Figure 29** shows the Carbolite Lenton tube furnace.

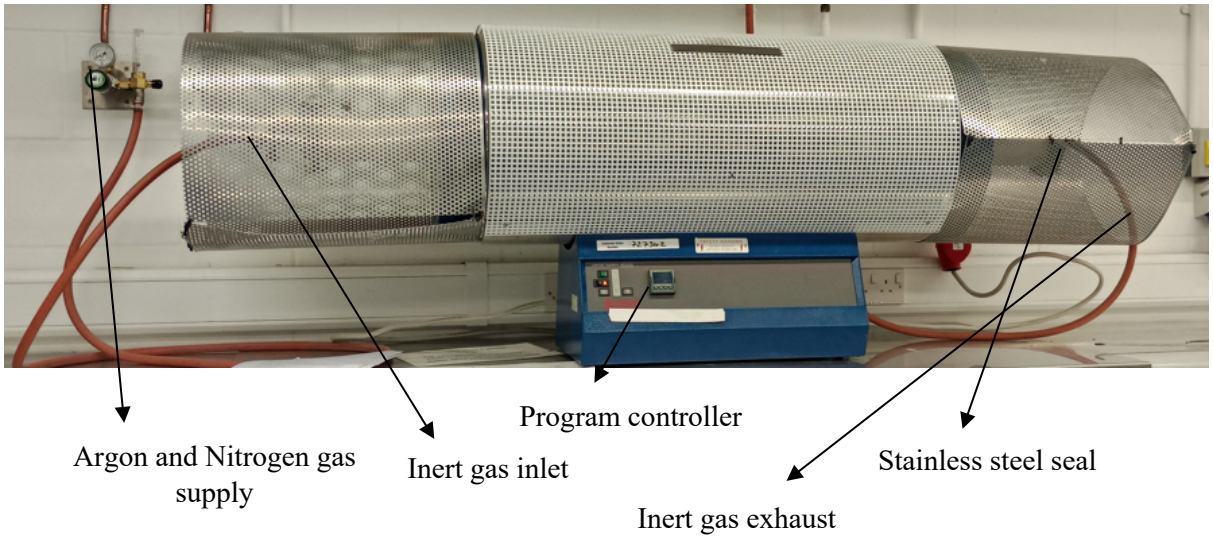

Figure 29, Carbolite Lenton tube furnace

A Carbolite Lenton tube furnace was used to pre-heat the titanium alloy substrate and post-heat the Hydroxyapatite and Wollastonite dip-coated titanium substrate in an inert atmosphere. Two sets of heat treatment conditions were programmed; in the first set, the substrate or the coating was heated from room temperature (20 °C), with a dwell time of 2 hours to temperature 840 °C at the heating rate of 2 °C/min and cooled to room temperature at the same cooling rate; in the second set, the substrate or coating was heated from room temperature (approximately 17 °C) to 650 °C at a dwell time of 5 hours with the heating rate of 1 °C./min and cooled to room temperature at the same heating rate.

3.3.5 Scanning Electron Microscope

The scanning electron microscope (EVO LS 15) used to characterise samples were supplied by ZEISS EVO. This instrument combines high-definition images with an automated throughput workflow [294]. This feature ensures fast, accurate, repeatable images across all the samples and provides SEM images with an analysis of broad range and size samples (stage movement of 125*125*50 mm (X, Y, Z) and a specimen height of 145 mm) [294].

a) Characterisation of Hydroxyapatite and Wollastonite powder

The powder and coated samples used in the present study were as-received Hydroxyapatite and as-received Wollastonite and their coated products. Samples obtained from the spray-drying experiment of both Hydroxyapatite and Wollastonite were also taken into consideration during the present study. The scanning electron microscope was used to characterise powder forms of Hydroxyapatite and Wollastonite

in terms of their morphology. Images of six samples were observed. Six samples were analysed; as received Hydroxyapatite, Hydroxyapatite spray-dried at trial 1 (process parameters:- pump flow:- 15 [scaled value], airflow:- 22 [scaled value] and inlet temperature:- 103 °C) and Hydroxyapatite spray-dried at trial 2 (process parameters:- pump flow:- 20 [scaled value], airflow:- 22 [scale value] and inlet temperature:- 103 °C), as received Wollastonite, Wollastonite at trial 1 (process parameters:- pump flow:- 15 [scaled value], airflow:- 22 [scaled value] and inlet temperature:- 103 °C), Wollastonite spray-dried at trial 3 (process parameters:- pump flow:- 15 [scaled value], airflow:- 33 [scaled value] and inlet temperature:- 103 °C). The scaled value of pump flow and airflow is given in **Tables 12** and **13**. Since all six samples were non-conductive ceramics, they were sputtered with low molecular weight carbon fibre. The sample preparation for SEM involved using a small amount of powder placed on a carbon tape, which was then inserted into a sputtering machine, followed by insertion into the SEM machine.

b) Characterisation of Hydroxyapatite and Wollastonite coated substrate

In the case of the coating, the substrate side with no coating was attached to a carbon tape, followed by insertion into the SEM machine. Twelve samples of Hydroxyapatite dip coated on titanium substrates were considered for SEM characterisation study; four samples of Hydroxyapatite coated on polished (average roughness: - 0.08 µm) titanium alloy substrate, four samples of Hydroxyapatite coated on mid-range roughness (average roughness: - 1.85 µm) titanium alloy substrate and four samples of Hydroxyapatite coated on grit-blasted (average roughness: - 4.01 µm) titanium alloy substrate; in the case of Wollastonite, six samples were considered for SEM characterisation study, two samples of Wollastonite coated on polished (average roughness: - 0.08 µm) titanium alloy substrate, two samples of Wollastonite coated on mid-range roughness (average roughness: - 1.85 µm) titanium alloy substrate and two samples of Wollastonite coated on grit-blasted (average roughness: - 4.01 µm) titanium alloy substrate. The parameters used for the powder characterisation were 200 µm resolution with 100X magnification, whereas the resolution was 50 µm and 300X magnification for the coating. The magnification and resolution were changed to observe the cracks and porosity in the coating case. The parameters are listed in **Table 11**.

Table 11, Parameters used for all SEM samples [295]

Parameter	Value
Probe current	5-25 pA
Accelerating Voltage	5-20 kV
Resolution	50-200 μm
Magnification	100-300 X

3.3.6 FTIR Spectroscopy

FTIR spectroscopy is mostly used to detect unknown chemicals, also helping one to identify some organic and inorganic compounds [296]. In FTIR, the vibrational excitation of molecular bonds leads to infrared absorption by the material and is transmitted as a signal, a unique molecular fingerprint of the material, making it possible to confirm or identify some known as well as unknown compounds [297]. When samples at various wavelengths absorb infrared radiation, the Fourier transform spectrometer converts the raw data from the broad-band light to obtain the absorbance level at each wavelength. FTIR spectroscopy can be performed on solid, liquid, and gaseous samples [296]. The material required is small, and most analyses can be done quickly with little preparation [296].

The FTIR spectrometer used in the present study was Perkin Elmer Spectrum Two FTIR, which has a depth of 30 cm, height of 21 cm and width of 45 cm, respectively. The wavelength of this spectrometer is 350-8300 cm^{-1}, with an operating temperature range of 5-45 °C [298]. In the current study, only Hydroxyapatite and Wollastonite dip-coated prepared titanium alloy substrates were considered for FTIR spectroscopy study.

3.3.7 X-Ray Diffractometer

As per ASTM FII85-03 and ISO 13779-series, X-ray diffraction is an important technique for characterising coatings on implants, and one of the best is the Bruker XRD. The equipment used in this research for X-ray diffraction was the BRUKER D2 phaser. The

D2 phaser is lightweight, compact and easy to use. The D2 phaser has an energy resolution of less than 380 eV and is fitted with a unique digital monochromator to reduce unwanted radiation and eliminate loss in detection speed. [299]

The D2 phaser has an angular accuracy of 0.02 ° with single or 6-position rotation with horizontal positioning. The power requirement for this device is 110-220 V and 50-60 Hz with dimensions of 61*60*70 cm. The device is also equipped with DIFFRA.SUITE software to plan, measure and analyse the samples [299]. The XRD scanning time for each sample was approximately 30 minutes.

In the current study, four titanium substrates at different conditions were considered. The first the second polished titanium substrate was heated to 840 °C in a nitrogen atmosphere at a heating rate of 2 °C/min and cooled to room temperature at the same cooling rate [254]; the second polished titanium substrate was heated to 650 °C in an air atmosphere increasing temperature at 1 °C/min heating rate and then cooled to room temperature at the same cooling rate [300]; the third titanium substrate was heated to 840 °C at a heating rate of 2 °C/min and cooled to room temperature at the same cooling rate in an argon atmosphere; the fourth polished titanium substrate was heated to 650 °C in an argon atmosphere at a 1 °C/min and cooled to room temperature at the same cooling rate. Titanium substrates were heated in an argon atmosphere to understand the effect of inert environment on the phase change, coating morphology and coating microstructure.

The current study also considered four heat-treated titanium substrates: Uncoated titanium substrate; HA spray-coated on titanium substrate; Wollastonite spray-coated on titanium substrate; and HA/Wollastonite spray-coated on titanium substrate, along with four Hydroxyapatite dip-coated titanium substrate and two Wollastonite dip-coated titanium substrate samples, and HA/Wollastonite dip-coated titanium substrates. For each sample, the XRD scanning time was approximately 30 minutes. The XRD equipment also measured the crystallinity of the coated samples with the help of software compatible with the equipment.

3.4 Substrate Material

The substrate used in this study was Ti-6Al-4V used in hip implants. The substrate material was supplied by Impact Ireland. Each 500 mm length titanium alloy was

sectioned into 10 mm diameter * 2 mm height by the DCU workshop. **Figure 30** shows the titanium alloy substrate.

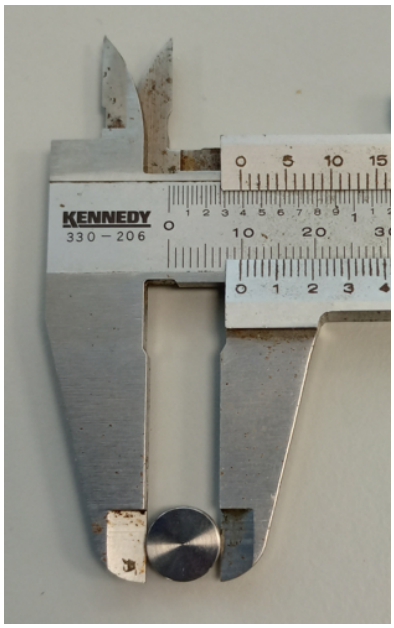

Figure 30, Titanium alloy substrate

3.5 Surface Roughness

The roughness tester used in the current study was an optical profilometer supplied by Bruker ContourX-500 GT 3D. This device has a dual LED which calibrates the surface roughness automatically with nanometre-scale resolution [301]. In the current study, the white lens focused on the surface, and the roughness was measured based on the fringes observed in the lens. The average roughness was denoted as S_a, the extension of R_a (centre line average roughness) and is defined as an average mean of the absolute height value within a sample area [302].

3.5.1 Grit Blasting Technique

The grit blaster used in the current study was the Ventublast Mammoth Guyson 690/40 model with external dimensions of 1200* 900* 1850 mm. The device has twin front doors, left-hand access doors, internal light, a foot pedal, and a separate dust extractor. [303]

The grit blasting equipment uses dry compressed air to propel the grit towards a surface. White alumina particle was used to grit blast on the titanium alloy substrate. The blasting medium used in the study was Saftigrit, which contains fused aluminium oxide. [304]

Two experiments with different pressure settings were used for the grit blasting technique. In the first setting, alumina particles of (size 500 μm and mesh 36) were grit blasted on a titanium substrate (size 10 mm diameter and 2 mm thickness). The pressure used in this technique was 5 bar, with a blasting angle of approximately 75° and an approximate 15 cm distance between the substrate and blasting nozzle. Marinosci et al. [305] found different average roughness of Ti-6Al-4V as a result of applying different pressure. Therefore, the titanium substrate in this study was grit blasted at a lower pressure to obtain mid-range roughness value. The titanium substrate was grit blasted at an angle of 75 ° and a pressure of 1.5 bar was applied at the same distance used as that in the case of 5 bar.

3.5.2 Polishing Procedure

The titanium substrates were polished with silicon carbide sandpaper. The sandpaper grades were; P240, P400, P600, P800 and P1200, respectively. Each substrate was polished for 2 minutes to obtain a near mirror-like finish.

3.6 Spray Drying Equipment and Experiments

Spray drying is user-friendly and efficient if the final product obtained is solid [306]. One of the significant applications of the spray drying technique is microencapsulation, where the protective film covers the liquid material [306]. In microencapsulation, the atomised spray dried product is hollow with approximately 10-20 μm diameter with liquid globules inside [306]. Other applications of the spray drying technique include englobulation, where the solid material is encapsulated inside the filmogen material or solvent [306].

LabPlant spray drying equipment (SD-05 by Keison company) was used to spray dry the powders [306]. The unit was positioned so that the exhaust pipe expelled air externally or via a window or a central laboratory fume cupboard [306]. The spray dryer has four main components; a) the main cabinet, b) the control panel, c) the spray assembly, and d) its auxiliary items [307].

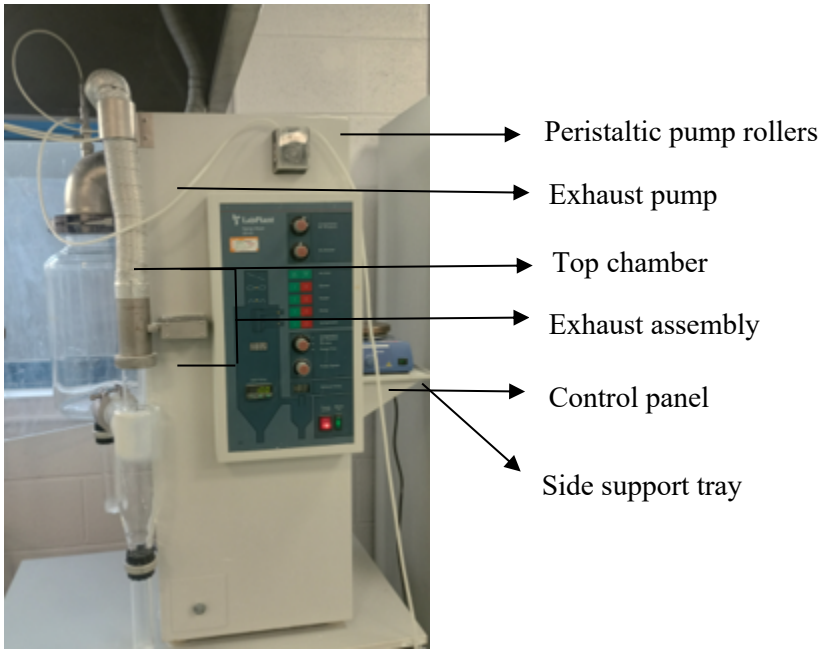

Figure 31, Main spray dryer cabinet

3.6.1 Main Cabinet

The main cabinet includes a control panel, inlet air filter, top chamber, side support tray, outlets from the compressor to a jet nozzle and jet de-blocker, as shown in **Figure 31**. The inlet air filter purifies the air; the peristaltic pump ensures a regular, continuous, and constant flow of the slurry when switched on and is connected to silicon tubes. Outlets from the jet nozzle and jet de-blocker allow the hot compressed air to exhaust through the top chamber. The exhaust tube is connected to the tapered exhaust assembly [307].

3.6.2 Control Panel

The control panel (**Figure 32**) regulates the pump flow, compressed air flow, and compressed air pressure. A multi-indicator control allows the slurry to flow, and the flow rate can be adjusted by pump speed control with the help of the digital indicator. The pump flow and airflow rate are represented by a nominal 0-50 and 10-50 scale, as shown in **Tables 12** and **13**. There are two controls at the top of the control panel; one is the de-blocker, and the other is the compressor air pressure. The multifunctional control in the middle of the control panel can switch to pump flow, airflow or compressed air pressure, and corresponding values can be noted accordingly. The compressor switch converts the liquid flowing to the main chamber into a jet spray. The higher the pressure, the finer the spray. Switching on the compressor also activates the de-blocker, controlled by a de-blocker control. The maximum air pressure for a 0.5mm jet is 2.0 bar. The pressure

reduces when the jet diameter increases. In the middle of the control panel, there are five switches: 1) airflow, where one can increase or decrease airflow when selected; 2) blower, which blows the air and its intensity depend on the airflow switch; 3) a heater which heats the air; 4) the pump transfers the slurry liquid inside the pipe into the jet spray assembly and 5) compressor whose switch converts the liquid into a jet spray. [307]

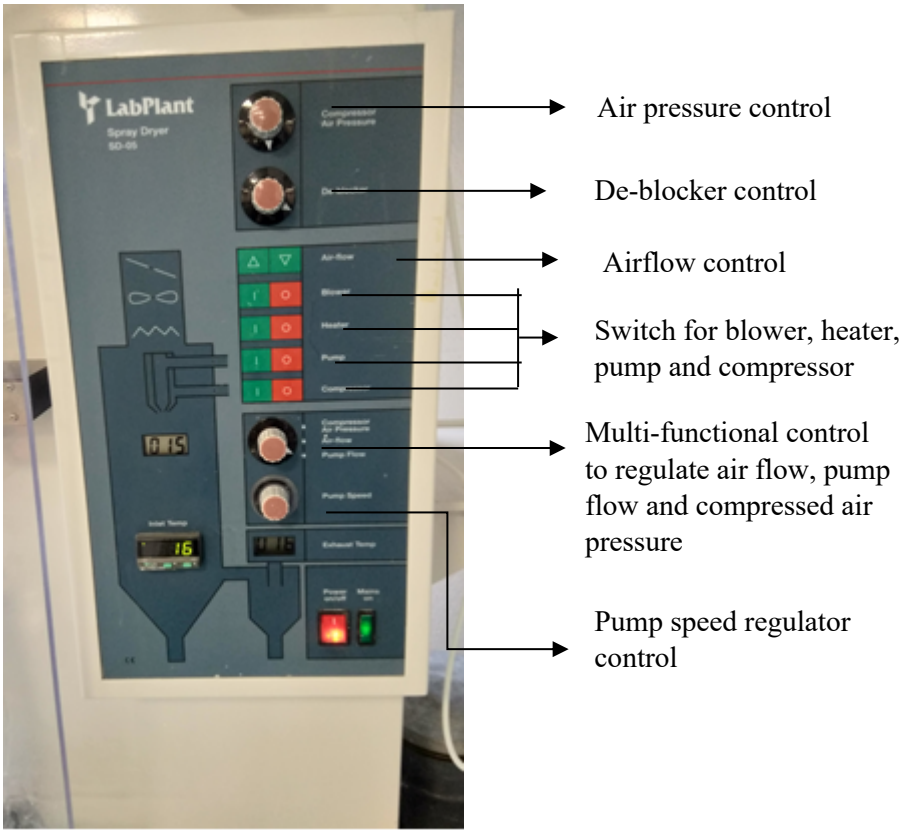

Figure 32, Spray dryer control panel

Tables 12 and **13** provide the digital scale information and their conversion to the S.I. unit based on the scaled values for pump and airflow rates and their conversion. [307]

Table 12, Scaled value of pump flow [307]

Scale	**ml/hr**
0	0
10	350
20	600
30	1000
35	1500
40	1900
45	3200
50	4600

Table 13, Scaled value of airflow [307]

Scale	**m^3/hr**
10	38
15	44
20	47
25	50
30	54
35	57
40	62
45	64
50	73

3.6.3 Spray Assembly

Figure 33 illustrates the spray dryer assembly. It consists of the main chamber, cyclone, collection bottle, and waste collection bottle. The main chamber length is 800 mm long in an overhang position, resulting in improved drying efficiency. In particle spray drying, the slurry mixture is pumped through a nozzle into a fine spray which enters the main chamber, which meets hot air that leads to the constant spiral flow of the powder in the cyclone to form a spray-dried powder. There can be the possibility of powder accumulating onto the cyclone walls. The accumulation of the powder on the walls may be reduced by adjusting the air flow rate and compressor pressure. There are two connecting tubes connected to the main chamber and the other connected to the cyclone. In this research experiment, the cyclone was used to collect the powder. The powder collected in the powder collection bottle was used for characterisation. If the liquid droplets were found to be deposited within the main chamber or the tube connected to the main chamber, then the experiment would be deemed ineffective. [307]

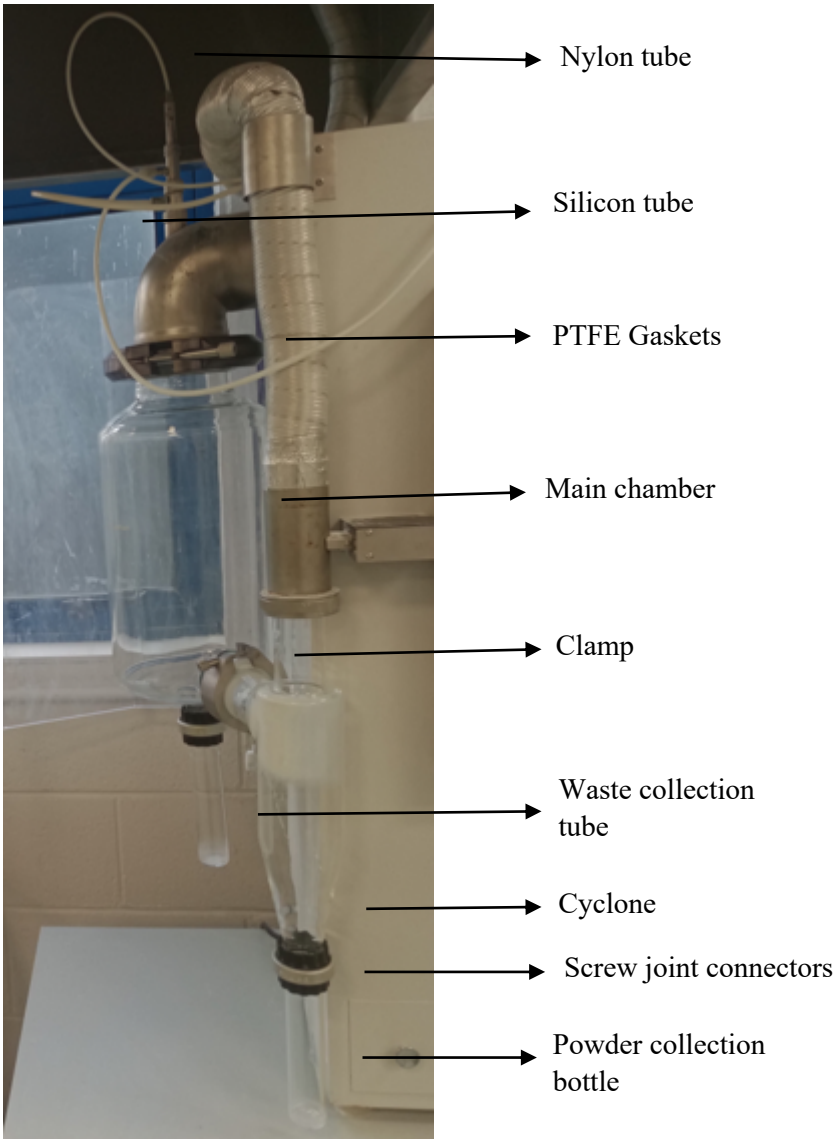

Figure 33, Spray dryer assembly

3.6.4 Jet Spray Assembly

A jet spray of 0.5 mm diameter develops the maximum air pressure required in spray drying equipment [307]. Two fluid nozzle forms the jet spray assembly. The inner nozzle facilitates the liquid jet, and the outer nozzle facilitates the outlet of the compressed air. A close gap between the inner nozzle and outer nozzle ensures a fine spray. The liquid drops emitted from the nozzle can be converted into a fine mist by the compressed air. The jet and outer nozzle (**Figure 34**) were removed by unscrewing the knurled rings from the central unit. The inner jet nozzle is a thin wall made of stainless steel, and there is

slight misalignment with the outer nozzle (**Figure 34**), which can affect the jet spray assembly efficiency. [307]

Figure 34, Side view of the jet spray assembly

3.6.5 Spray Dryer Auxiliary Items

The other items include nylon tubes, exhaust tubes, connectors, and PTFE gaskets. PTFE gasket connects and aligns the whole assembly with the main chamber. The jet assembly connects two nylon tubes to the control panel. There are two plastic screw joint connectors; one connects the main chamber and waste tube, and the other secures the cyclone and powder collection bottle. Most of the spray drying equipment connection is a screw joint, making it easy to disassemble and clean.

3.6.6 Spray Drying Operation

The peristaltic pump is self-contained in spray drying equipment, ensuring the air and liquid flow simultaneously. A silicon tube passes through the peristaltic pump and is immersed in a beaker containing liquid slurry. The slurry is sucked by the pump and transferred to the jet as a stream of liquid into the main chamber, concurrently with pumping, compressed air leads to the liquid emerging as a fine, atomised spray. The hot compressed air evaporates the liquid slurry into a mist spray to form the powder based on evaporation temperature. The powder formed flows through the main chamber separated by exhaust air in the cyclone. The cyclone collects the powder, and the exhaust airflow is directed through the 50 mm diameter hose. [306]

In the current study, Hydroxyapatite and Wollastonite powders were dissolved in de-ionised water, and the solution was continuously stirred for 2 hours by a magnetic stirrer at 40 °C. Initially, 80 grams of Hydroxyapatite was immersed in 500 ml of de-ionised

water. The process parameters for both powders were kept similar for comparison. The process parameters obtained from the previous literature were pump flow: - 15-20 (scaled value), airflow: - 22-33 (scaled value) and inlet air temperature: - 103-107 °C. The scaled value conversion of pump flow and airflow and its conversion to SI units are given in **Tables 12** and **13.** Five process parameters were varied with the control panel: pump flow rate, airflow rate, inlet temperature, deblocker and compressed air pressure. The compressed air pressure was kept at a maximum (1.7-1.8 bar instead of 2.0 bar theoretically), and the deblocker switch prevented the blocking of viscous flowing through the pipe by emission of sudden air. Therefore, three process parameters, pump flow rate, airflow rate and inlet air temperature having the maximum effect on spray dried Hydroxyapatite and Wollastonite powder, were selected and varied at low and high levels to obtain spray-dried Hydroxyapatite and Wollastonite powder.

a) Spray drying of Hydroxyapatite-Wollastonite Mixture

The spray drying operation was carried out in the same way as explained above**.** The process parameters for the spray drying of the Hydroxyapatite/Wollastonite mixture powder were selected based on the optimal process parameters of both Hydroxyapatite and Wollastonite. The highest response (45-75 μm) for Hydroxyapatite was observed in trial 2 at the pump flow rate: 20 (scaled value), air flow rate: 22 (scaled value) and inlet air temperature: 103 °C; for Wollastonite, the highest response was observed in trial 3 at the pump flow rate: 15 (scaled value), air flow rate: 33 (scaled value) and inlet air temperature: 103 °C, as mentioned in **Section 4.6**. The process parameters selected for the spray drying of the Hydroxyapatite/Wollastonite powder mixture were pump flow rate: 15-20 (scaled value), air flow rate: 22-33 and Wollastonite/HA wt. ratio (weight ratio): 0.2-0.5. The wt. ratio range was selected based on the previous literature [162, 211]. The inlet air temperature process parameter was kept constant at 103 °C as it had the same value observed in both best responses for Hydroxyapatite and Wollastonite spray drying.

The procedure was similar to the one detailed above. Initially, some quantity of Hydroxyapatite (HA in the range of 20 -32 grams) depending on mixture was added to the 500 grams of deionised water. The remaining quantity of Wollastonite mixture (8-20 grams) was added to the HA/deionised water suspension. The suspension was heated at the temperature of 40 °C for 2 hours and spray-dried. Overall, the HA/Wollastonite

weight was 80 grams like above. The powder collected in the cyclone was considered for study.

3.6.7 Technical Information

Table 14 describes the technical information of the spray drying operation and its equipment capacity.

Table 14, Technical information of spray dryer [306]

Evaporation rate of water at 250 °C	Approximately 1500 ml/hr
Air inlet temperature	40 °C- 250 °C
Drying air	From 38-73 m^3/hr
Heater capacity	3 K.W.
Compressor [flow and pressure]	1.4 m^3/hr at 1.0 bar to 0.25 m^3/hr at 4.0 bar
Sample feed	Peristaltic pump with flow rate up to 65 ml/min
Jet de-blocking	3 bar compressed air supply with variable de-blocker plunger frequency
Spray system	One liquid nozzle with a 0.5 mm diameter
Spray hot airflow	Downward co-current
Power supply	220/250V- 50/60 Hz -13 amps
Dimensions	1050X 625X 500 mm
Weight net/Packed	73/117 kg

3.6.8 Advantages of the Spray Drying Process [306]:

- The spray-drying technique can produce a uniform, free-flowing powder.
- Large range of slurries, including aqueous emulsions, solutions, suspensions, and colloids, can be spray dried with rapid results.
- Most drying processes like an oven, freeze-drying, and rotary evaporators produce a soft mass of cake and require post-processing. The requirement for the post-processing technique is almost nil in the spray drying technique.
- Spray drying technique can produce powders with a large particle size distribution.
- The whole assembly during which spray drying occurs is made of borosilicate glasses, ensuring visual monitoring.
- Spray drying equipment parts are easy to assemble, disassemble, and clean.
- Spray dried powder has flexibility in powder volume and chamber size.

3.6.9 Design of Experiment (DOE)

Design Expert software utilised the response surface methodology (RSM) for optimisation of process parameters in the current study. RSM has a sequence of steps that need to be performed to solve the problem. A mathematical model of spray drying was developed using the steps given below [279]:

a) *Identify the critical process variables*

The critical factors were identified by performing a screening study based on factorial design or partial factorial design. In this experiment, the input variables were determined by past literature. Process input factors, in this case, are inlet temperature, airflow rate, and pump flow rate [279].

b) *Finding the limit of each factor*

In this step, trials were performed on the experiment to determine the powder in the powder collection bottle. These experiments were done while changing one process variable and keeping the other constant. The Design Expert software can be used to find the limit of each factor by the formula $X_i = 2(2X - (X_{max} + X_{min}))/ X_{max} - X_{min}$ [279].

c) *Design matrix development*

The RSM design model in our experiment is the Box-Behnken design. The experimental run for BBD is 17 for three factors [279]. **Table 15** provides the matrix for current experimentation.

d) *Performing the experiment:*

Experiments were performed in a random order (based on run number) to avoid human error or bias [279].

e) *Recording the responses*

All the responses were recorded for future steps [279].

Table 15, RSM Design model of spray drying experiment

Run No.	Order No.	Pump Flow	Air Flow	Inlet temperature
1	10	-1	-1	0
2	17	1	-1	0
3	1	-1	1	0
4	11	1	1	0
5	13	-1	0	-1
6	14	1	0	-1
7	6	-1	0	1
8	7	1	0	1
9	12	0	-1	-1
10	15	0	1	-1
11	4	0	-1	1
12	2	0	1	1
13	5	0	0	0
14	3	0	0	0
15	16	0	0	0
16	8	0	0	0
17	9	0	0	0

f) *Development of mathematical model*

The relationship representing the response of interest can be represented as y= f(P, A, T).

The **Equation 13** formed from this response is as follows

$$Y = b_o + b_1P + b_2A + b_3T + b_{11}P^2 + b_{22}A^2 + b_{33}T^2 + b_{12}PA + b_{13}PT + b_{23}AT$$

Equation 13

The screening design (2-factor design) was used to identify the optimal results of Hydroxyapatite and Wollastonite spray drying. The Box-Behnken Design (BBD) experiment design was used to obtain the optimal results, which were then optimised by the software.

Box-Behnken Design (BBD) in Response Surface Methodology (RSM) was used to optimise the results obtained for spray drying the Hydroxyapatite/Wollastonite powder mixture. Moreover, Box-Behnken Design assisted in the determination of the response value at the centre point. The Box-Behnken Design was used due to its higher efficiency compared to the 3-level full factorial design and detection of lack of fit of the model [308]. Following that, DOE optimisation of the obtained results was carried out using the numerical approach. In the optimisation procedure, the pump flow rate (A) and airflow rate (B) were kept in the range, keeping the limit of Wollastonite wt.fraction to a maximum of 0.2. Wollastonite was kept at wt. fraction of 0.2 because any further increase in the quantity of the Wollastonite may result in the degradation of the composite powder when immersed, used in the body [162, 211].

3.7 Steps to Improve the Flowability of Wollastonite Powder

3.7.1 Flowability Test Using a Cartridge

Due to the non-spherical morphology of Wollastonite, it became impossible to use this in a plasma spray facility, previous literature showed that this powder was only achievable in a suspension-type plasma spray facility, unavailable in this research. Therefore, after careful deliberation and based on literature, the decision to use a flame spray facility was taken. A canister is mounted on the top of the spray gun, and the powder fed via a nozzle inside the spray gun coats the substrate in the flame spray technique [246]. Before using the flame spray technique, pretesting the powder flowability was carried out. A specific cap assembly with an air-tight lid with a central opening that allowed compressed air to push down the powder was designed for the flame spray equipment. A hollow shaft was joined along with the air-tight lid to ensure centralised air pressure for the powder flow. Both the air-tight lid and hollow shaft were threaded to seal any connections. **Figure 35** show the flame spray cartridge assembly. A 1- 7 bar pressure was applied through the top while 60 grams of Wollastonite was placed in the canister.

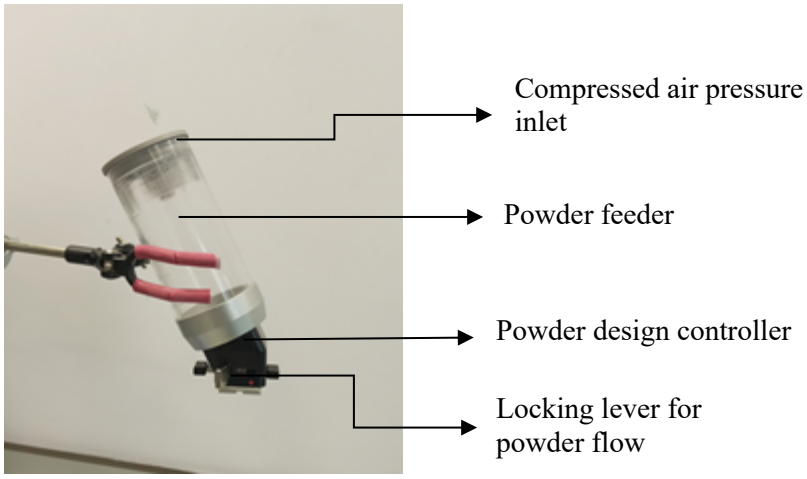

Figure 35, Flame spray cartridge [246]

After applying air pressure to improve the flowability of the Wollastonite powder, it was observed that the Wollastonite powder adhered to the walls of the powder feeder. Therefore, a vibrator was designed and connected to the top of the cartridge. The vibrator assembly was created in the SOLIDWORKS Software, and the whole assembly was manufactured in the DCU workshop. **Figure 36** shows the image of the whole assembly.

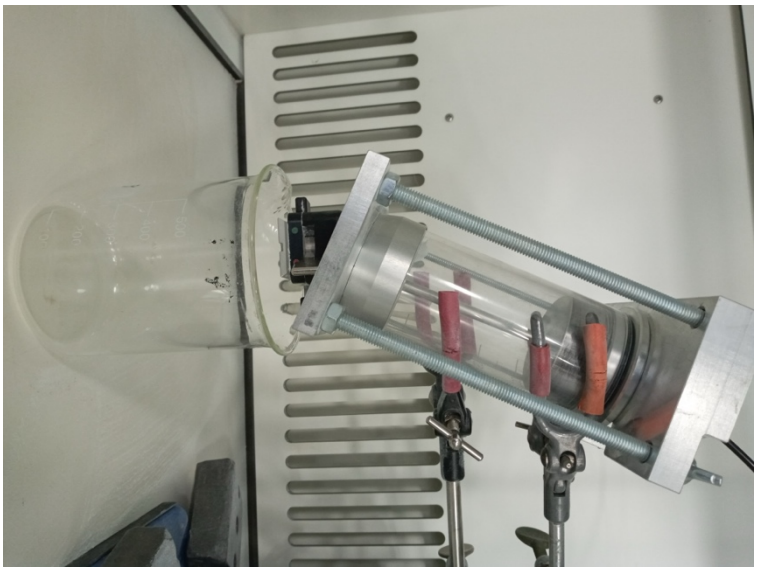

Figure 36, Whole assembly image

Figure 36 shows the image of the designed cartridge assembly with the vibrator. Three different settings were used. In the first setting, the pressure was increased up to 15 bar; in the second setting, the vibrator was dissembled, and separate pressures of 7 bar were applied to the cartridge and approximately 8 bar were applied to the vibrator. In the third setting, Wollastonite in 10 and 20 wt.% was added to Hydroxyapatite, and similar

pressure was applied as that of the first and second settings. As flowability of Wollastonite became a problem (**Section 4.6**), further detail was not presented here rather the focus was placed on other coating techniques, as the lack of flow of Wollastonite as a received powder means it is not suitable for plasma nor flame thermal spray.

3.8 Spray Coating Technique

3.8.1 Time Versus Temperature for Spray Dryer

The primary objective of the current study was to spray coat (using the spray dryer) either Hydroxyapatite, Wollastonite or HA/Wollastonite composite onto a prepared titanium substrate using the spray drying technique. During this part of the study, the spray drying of Hydroxyapatite/Wollastonite composite powder was dissolved in deionised water suspension and then coated onto a prepared titanium substrate. Part of this study involved understanding the temperature profile within the spray dryer chamber with respect to distance from the hot atomising nozzle, as it determines particle drying.

Therefore, a stand was manufactured to fit inside the spray dryer assembly to hold the substrate. **Figure 37** shows the assembly to study the temperature inside the spray dryer with respect to distance from the nozzle. The plastic substrate holder was attached to the top of the stand. Due to this set of beakers and blocks, one could vary the height of the sample, or the distance from the slurry nozzle to substrate was able to be varied from 1-10 cm from the nozzle. A thermocouple was attached near the substrate holder, to note the temperature at various substrate positions, accordingly.

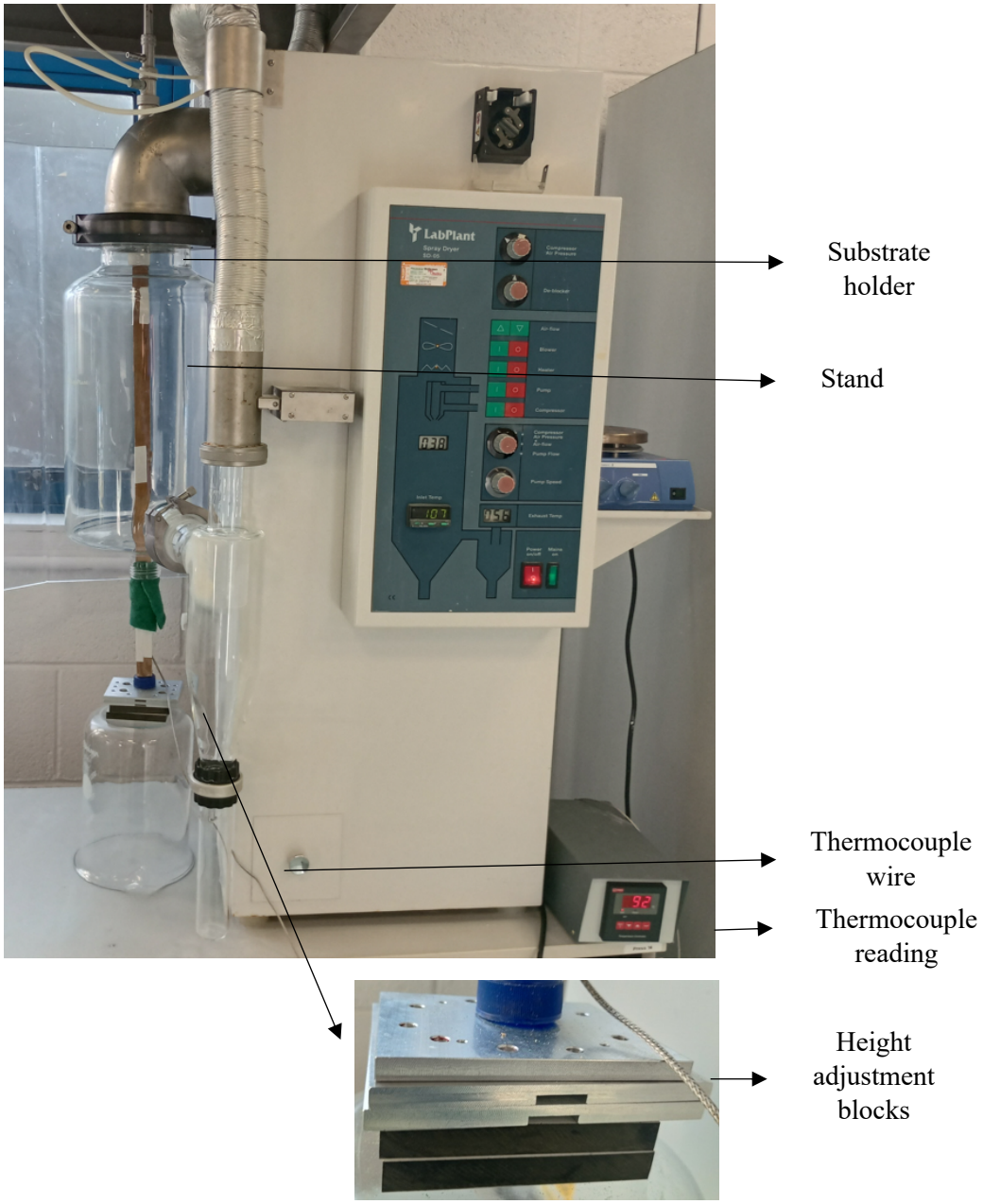

Figure 37, Assembly to determine temperature versus distance in spray dryer

As shown in **Figure 37**, the inlet temperature (reference temperature) could be varied by the spray dryer, whereas the distance between the nozzle and wooden stand was varied by height adjustment. Two sets of experiments were performed; in the first setup, the inlet temperature was 103 °C and airflow rate of 22 (scaled value), whereas in the second case, it was 103 °C and airflow rate of 33 (scaled value).

a) *First Setup at 103 °C and airflow rate of 22 (scaled value)*

The inlet temperature of the spray drying equipment was kept at 103 °C with the airflow rate of 22 (scaled value). The distance between the wooden stand and the nozzle was 1

cm, 1.5 cm, 2 cm, 3 cm, 4 cm, 5 cm, 6 cm, 7 cm, 8 cm, 9 cm and 10 cm, respectively. The time of the temperature calibration at each distance was kept constant at 5 seconds. The thermocouple calibrated the temperature inside the spray dryer at each particular distance and was noted.

b) *Second setup at 103 °C and airflow rate of 33 (scaled value)*

For comparison, the second setup was performed similarly to the first setup, where the inlet temperature was kept constant at 103 °C with only a variation in airflow rate of 33 (scaled value).

3.8.2 Spray Coating of Hydroxyapatite

The same quantities of Hydroxyapatite were immersed in deionised water (80 grams of as-received Hydroxyapatite dissolved in 500 ml) to form a slurry, as mentioned in **Section 3.6.6**. The titanium substrate was kept at 5 cm from the nozzle tip. The Hydroxyapatite/deionised water slurry was sprayed onto prepared titanium (polished (average roughness: 0.08 μm), mid-range roughness (average roughness: 1.85 μm) and grit blasted titanium substrate (average roughness: 4.01 μm) using the process parameters from trial 2 (pump flow: 20 (scaled value), air flowrate: 22 (scaled value) and inlet temperature: 103 °C) as mentioned above, as it had the highest response for spray dried Hydroxyapatite. The coating was performed for 10 minutes and the wooden stand on which the substrate was placed was then removed 5 minutes after applying the coating. **Figure 38** shows a picture of the spray coating setup. The obtained coating was post-heat treated at 1100 °C for 2 hours in an air atmosphere. **Figure 39** shows the schematic diagram for the spray coating of HA onto a titanium substrate.

Figure 38, Spray coating technique arrangement

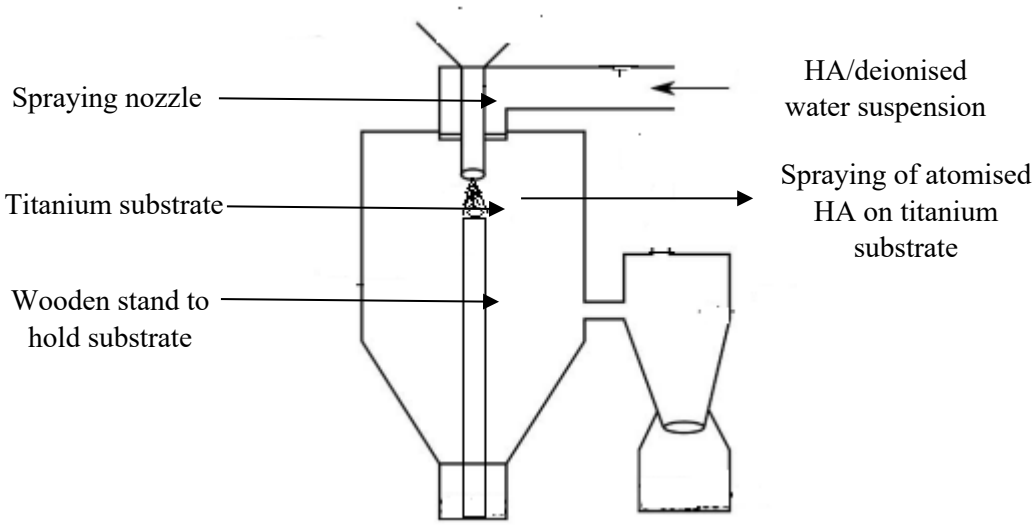

Figure 39, Schematic diagram of spray coating of HA onto a titanium substrate

3.8.3 Spray Coating of Wollastonite

The setup for the spray coating of the Wollastonite was similar to that of the Hydroxyapatite with the same quantities, distance from the nozzle, and spraying time. However, the process parameters obtained from trial 3 (pump flow: 15 (scaled value), air flow rate: 33 (scaled value) and inlet air temperature: 103 °C) were used in the spray coating of Wollastonite onto a prepared titanium substrate. Similar to the spray-coating of Hydroxyapatite, the obtained coating was post-heat treated at 1100 °C in an air atmosphere.

3.8.4 Spray Coating of Hydroxyapatite/Wollastonite Powder

The highest response for the spray drying of Hydroxyapatite/Wollastonite powder was obtained at trial 8 (pump flow: 20 (scale value), air flowrate: 28 (scaled value) and Wollastonite wt. fraction: 0.5). Therefore, 40 grams of Hydroxyapatite was pre-mixed with 40 grams of Wollastonite and immersed in 500 ml of deionised water with continuous stirring of the suspension solution. The experimental setup and spraying time were similar to the Hydroxyapatite and Wollastonite spray coating. The obtained coating was post-heat treated at the same temperature and environment as that of Hydroxyapatite and Wollastonite coatings.

3.9 Dip coating of Hydroxyapatite on Titanium substrate

In dip coating technique, the material (metal, polymer or ceramics) to be coated is dipped into the precursor solution and withdrawn from the solution at a particular speed. A layer is formed on the substrate surface due to substrate surface wetting and withdrawal, the evaporation of the layer leads to the coating. The thickness of the coated layer depends on the time of deposition of substrate into precursor solution, whereas the uniformity of the coating layer depends on the withdrawal speed. [309]

For dip coating of Hydroxyapatite on titanium alloy substrate, 0.1 gram of methyl cellulose was mixed with 1 litre of deionised water with a stirrer. 3 ml of 0.1 g/L methyl cellulose as an aliquot was added to the 1440 ml deionised water beaker and stirred. In the same solution, 0.152 mol of calcium nitrate tetrahydrate [$Ca(NO_3)_2.4H_2O$] (35.9 grams= 0.152 mol * 236.15 {molecular weight}) and the solution was stirred [310]. Then 0.09 mol (which equates to 11.88 grams) of diammonium hydrogen phosphate [$(NH_4)_2HPO_4$] was added to the same solution and mixed with the help of a stirrer. Following that, 115 ml of ammonium hydroxide was added to the solution. The whole

solution was stirred continuously and heated between 60-70 °C for 90 minutes [254]. The flow chart of the process for dipping titanium substrate is described in **Figure 40**. The coating obtained was post-heat treated in an argon environment at 840 °C. The stoichiometric equation for sol-gel synthesis of Hydroxyapatite is given in **Equation 14**:

$$10[Ca(NO_3)_2.4H_2O] + 6\,[(NH_4)_2HPO_4] = Ca_{10}(PO_4)_6(OH)_2 + 20NH_3 + 6N_2 + 49O_2$$

……...*Equation 14*

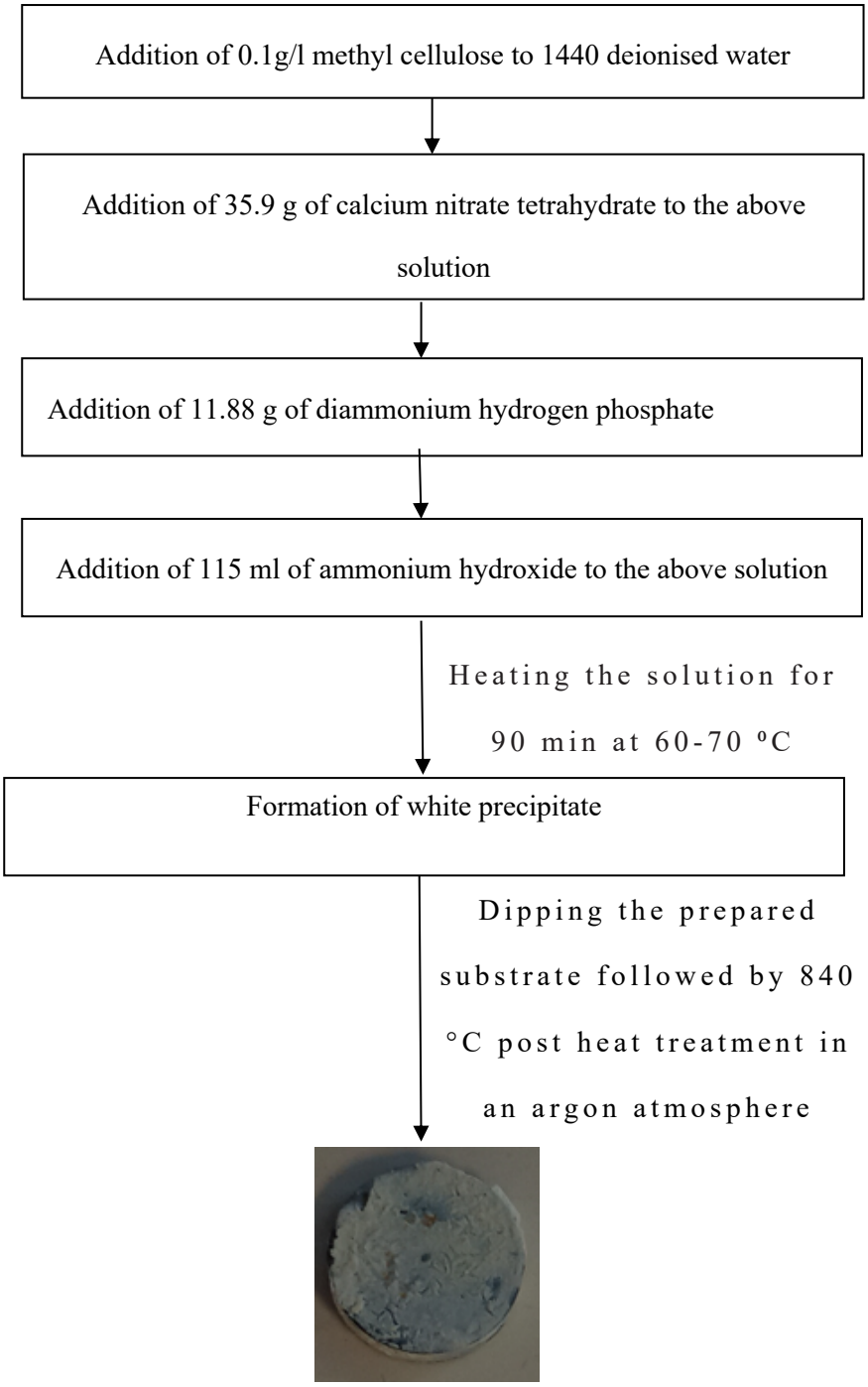

Figure 40, Flow chart for the dipping of Hydroxyapatite gel on titanium substrate

3.9.1 Comparison of the Techniques (Literature v/s DCU Research)

Table 16 compares the procedure for coating Hydroxyapatite gel onto a titanium substrate. In the DCU research facility, the as-prepared (polished, mid-range and grit blasted) substrates were preheated to 650 ºC at the heating rate of 1 ºC/min with a dwelling time of 5 hours in an air atmosphere [300]. The nitrogen atmosphere required a buddy system in the DCU laboratory. Moreover, there was less process control in the previous experiment compared to one conducted by Mavis and Taş [254]. The preheating prevented further development of the oxide layer because higher TiO_2 formation may lead to coating cracking [300]. The dip-coated samples underwent post-heat treatment at 650 ºC at 1 ºC/min with a dwell time of 5 hours in an air atmosphere.

Table 16, Comparison of literature v/s DCU research in for HA dip-coating heat treated at 650 °C in air atmosphere.

Materials or Methods	Technique used in the Literature review	Technique used in Current DCU research
Titanium substrate	Step 1: - The titanium alloy (Ti-6Al-4V) substrate stripes (dimension of 20 mm* 7 mm* 1 mm) were used. Step 2:- These were polished with silicon carbide paper (grit size ranging from P400-P1200) and washed in distilled water [254].	Step 1: - Three different titanium alloy (Ti-6Al-4V) substrates of dimensions (10 mm diameter* 2mm thick) were considered for the study. Step 2: - First substrate was polished with Silicon Carbide grit paper (ranging from P240 to P1200) to obtain a roughness of 0.08 µm followed by washing in distilled water. The second substrate was grit blasted to obtain an average roughness of 1.85 µm, and the third substrate was grit blasted to obtain an average roughness of 4.01 µm. Step 3: - The titanium substrates were pre-heated to 650 ºC for 5 hours at 1 ºC/min in air atmosphere [300].

Process to form Hydroxyapatite solution or Wollastonite gel	Step 1:- 3 ml aliquot of 0.1 g/l methyl cellulose was added to 1440 ml deionised water [254].	Step 1: - 3 ml aliquot of 0.1 g/l methyl cellulose was added to 1440 ml deionised water.
	Step 2: - Then 0.0152 mol (35.9 grams) calcium nitrate tetrahydrate was added to the above solution [254].	Step 2: - Then 0.0152 mol (35.9 grams) calcium nitrate tetrahydrate was added to the above solution.
	Step 3: - Following that, 0.09 mol (11.88 grams) diammonium hydrogen phosphate was added to the above solution [254].	Step 3: - Following that, 0.09 mol (11.88 grams) diammonium hydrogen phosphate was added to the above solution.
	Step 4: - 115 ml of 24 vol% ammonium hydroxide was added to the above solution [254].	Step 4: - 115 ml of 24 vol% ammonium hydroxide was added to the above solution.
	Step 5: - The above solution was stirred continuously at the hot plate for 90 min at 60-70 ºC [254].	Step 5: - The above solution was stirred continuously at the hot plate for 90 min at 60-70 ºC. The stirring rate was 720 rpm.
	Step 6: - There is a formation of a white precipitate [254].	Step 6: - There is a formation of a white precipitate.
	Step 7: - The gel was separated from the precipitate by vacuum filtration via a Bückner funnel [254].	Step 7: - Bückner funnel separated gel from the precipitate.
	Step 8: - The gel formed was preserved with the mixture of ethanol and glycerol [254].	Step 8: - It was not necessary to preserve the Hydroxyapatite gel. All the 9 prepared samples (3 polished, 3 grit blasted and 3 mid-range roughness titanium substrates utilised all the Hydroxyapatite gel.

Titanium substrate dipping procedure	Step 1: - The titanium stripes were attached to the belt and pulley system and dipped into prepared HA suspension and dipped at the constant speed of 15-300 mm/min [254]. Step 2: - The coated samples were heat treated on the mullite furnace with a nitrogen environment (flow rate of 4 L/min) at 840 ºC. The samples were heat treated at 840 ºC for 2 hours at the heating and cooling rate of 2 ºC/min [254].	Step 1: - The titanium substrates were dipped into the Hydroxyapatite gel. Step 2 : - The coated titanium substrates were again post-heat treated at 650 ºC for 5 hours at 1 ºC/min in an air atmosphere [300].

Table 16 compares the Hydroxyapatite coating onto a titanium alloy substrate conducted by Mavis and Taş [254] and the coatings conducted in the DCU research facility. The coating obtained in the literature review had a belt and pulley system where titanium stripes were immersed into the Hydroxyapatite gel (preserved in the mixture of gelatin and ethanol). The research conducted concerning literature had more process control. It was impractical to arrange for belt and pully arrangement in the DCU research facility. Moreover, the gel was preserved in a mixture of gelatin and ethanol in research conducted according to the literature. The titanium stripes were continuously in motion due to the belt and pulley mechanism and immersed in preserved Hydroxyapatite gel, whereas in one conducted in the DCU research facility, the as-prepared titanium substrates were immersed in Hydroxyapatite gel. The reasons were to synthesise the Hydroxyapatite gel in its pure form, the shape of the sample used in the DCU research facility was different (cylindrical than rectangular, which would make it difficult to mount in a belt and pulley), and the higher amount of as-prepared samples (polished, mid-range roughness and grit-blasted titanium substrate) as compared to one in literature (which were titanium stripes), utilising the complete Hydroxyapatite gel. The coating obtained in DCU research was post-heat treated at 840 °C in an argon environment, unlike the study conducted by Mavis and Taş (where the coatings were post-heat treated in a nitrogen environment at 840 °C) [254].

Tables 16, 17 and **18** detail hydroxyapatite-coated titanium samples being heat-treated in an air atmosphere at 650 °C, argon atmosphere at 840 °C and argon atmosphere at 650

°C, respectively. Heating titanium at an elevated temperature (700 °C- 1100 °C) in the presence of a nitrogen atmosphere leads to the formation of TiN and Ti_2N. These nitride layers result in the formation of the brittle surface layer and reduction in fatigue strength with deterioration of microstructure, therefore a nitrogen environment was not used [311]. Heating titanium or titanium alloys in an oxygen atmosphere at a temperature of more than 600 °C forms an oxide layer. This oxide layer formation on the surface of the titanium may affect its durability, which might result in premature failure of the coating [312]. Argon is insoluble in titanium at higher temperatures, which reduces its sensitivity to pores and improves stability. Heat treatment of titanium at an elevated temperature might help reduce this drawback and make it suitable for non-fatigue high-temperature applications [313]. To address this issue, Hydroxyapatite-coated titanium substrates were heat-treated at 840 °C in an argon environment with the same temperature conditions, as detailed in **Table 17**, in an argon environment. Moreover, Hydroxyapatite-coated titanium substrates were heat-treated at 650 °C, as detailed in **Table 18** in an argon environment

Table 17, Comparison of literature v/s DCU research in argon atmosphere at 840 °C for HA dip-coating

Materials or Methods	Technique used in the Literature review	Technique used in Current DCU research
Titanium substrate	Step 1: - The titanium alloy (Ti-6Al-4V) substrate stripes (dimension of 20 mm* 7 mm* 1 mm) were used.	Step 1: - Three different titanium alloy (Ti-6Al-4V) substrates of dimensions (10 mm diameter* 2mm thick) were considered for the study.
	Step 2:- These were polished with silicon carbide paper (grit size ranging from P400-P1200), followed by washing in distilled water [254].	Step 2: - First substrate was polished with Silicon Carbide grit paper (ranging from P240 to P1200) to obtain a roughness of 0.08 µm followed by washing in distilled water. The second substrate was grit blasted to obtain an average roughness of 1.85 µm, and the third substrate was grit blasted to obtain an average roughness

		of 4.01 µm, followed by washing in distilled water.
Process to form Hydroxyapatite solution or Wollastonite gel	Step 1:- 3 ml aliquot of 0.1 g/l methyl cellulose was added to 1440 ml deionised water [254]. Step 2: - Then 0.0152 mol (35.9 gms) calcium nitrate tetrahydrate was added to the above solution [254]. Step 3: - Following that, 0.09 mol (11.88 gms) diammonium hydrogen phosphate was added to the above solution [254]. Step 4: - 115 ml of 24 vol% ammonium hydroxide was added to the above solution [254]. Step 5: - The above solution was stirred continuously at the hot plate for 90 min at 60-70 ºC [254]. Step 6: - There is a formation of a white precipitate [254]. Step 7: - The gel was separated from the precipitate by vacuum filtration via a Bückner funnel [254].	Step 1: - 3 ml aliquot of 0.1 g/l methyl cellulose was added to 1440 ml deionised water. Step 2: - Then 0.0152 mol (35.9 gms) calcium nitrate tetrahydrate was added to the above solution. Step 3: - Following that, 0.09 mol (11.88 gms) diammonium hydrogen phosphate was added to the above solution. Step 4: - 115 ml of 24 vol% ammonium hydroxide was added to the above solution. Step 5: - The above solution was stirred continuously at the hot plate for 90 min at 60-70 ºC. The stirring rate was 720 rpm. Step 6: - There is a formation of a white precipitate. Step 7: - Bückner funnel separated gel from the precipitate.

	Step 8: - The gel formed was preserved with the mixture of ethanol and glycerol [254].	Step 8:- It was not necessary to preserve the Hydroxyapatite gel. All the 9 prepared samples (3 polished, 3 grit blasted and 3 mid-range roughness titanium substrates utilised all the Hydroxyapatite gel.
Titanium substrate dipping procedure	Step 1: - The titanium stripes were attached to the belt and pulley system and dipped into prepared HA suspension at the constant speed of 15-300 mm/min [254]. Step 2: - The coated samples were heat treated on the mullite furnace with a nitrogen environment (flow rate of 4 L/min) at the temperature of 840 ºC. The samples were heat treated at 840 ºC for 2 hours at the heating and cooling rate of 2 ºC/min [254].	Step 1: - The titanium substrates were dipped into the Hydroxyapatite gel. Step 2: - The as-prepared titanium substrate coated with Hydroxyapatite underwent a heat treatment process in the pipe furnace under an argon environment. The coated samples were post-heat treated at 840 ºC for 2 hours at the heating and cooling rate of 2 ºC/min and flow rate of 5L/min for first 2 minutes, followed by 0.8 L/min afterwards [254, 314, 315].

Table 18, Comparison of literature v/s DCU research in argon atmosphere at 650 °C for HA dip-coating.

Materials or Methods	Technique used in the Literature review	Technique used in Current DCU research

Titanium substrate	Step 1: - The titanium alloy (Ti-6Al-4V) substrate stripes (dimension of 20 mm* 7 mm* 1 mm) were used. Step 2:- These were polished with silicon carbide paper (grit size ranging from P400-P1200) and washed in distilled water [254].	Step 1: - Three different titanium alloy (Ti-6Al-4V) substrates of dimensions (10 mm diameter * 2mm thick) were considered for the study. Step 2: - First substrate was polished with Silicon Carbide grit paper (ranging from P240 to P1200) to obtain a roughness of 0.08 µm followed by washing in distilled water. The second substrate was grit blasted to obtain an average roughness of 1.85 µm, and the third substrate was grit blasted to obtain an average roughness of 4.01 µm. Step 3: - The titanium substrates were pre-heated to 650 ºC for 5 hours at 1 ºC/min in an argon atmosphere at the flow rate of 5L/min for first 2 minutes and 0.8 L/min afterwards [300, 314, 315].
Process to form Hydroxyapatite solution or Wollastonite gel	Step 1:- 3 ml aliquot of 0.1 g/l methyl cellulose was added to 1440 ml deionised water [254]. Step 2: - Then 0.0152 mol (35.9 grams) calcium nitrate tetrahydrate was added to the above solution [254]. Step 3: - Following that, 0.09 mol (11.88 grams) diammonium	Step 1: - 3 ml aliquot of 0.1 g/l methyl cellulose was added to 1440 ml deionised water. Step 2: - Then 0.0152 mol (35.9 grams) calcium nitrate tetrahydrate was added to the above solution. Step 3: - Following that, 0.09 mol (11.88 grams)

	hydrogen phosphate was added to the above solution [254]. Step 4: - 115 ml of 24 vol% ammonium hydroxide was added to the above solution [254]. Step 5: - The above solution was stirred continuously at the hot plate for 90 min at 60-70 ºC [254]. Step 6: - There is a formation of a white precipitate [254]. Step 7: - The gel was separated from the precipitate by vacuum filtration via a Bückner funnel [254]. Step 8: - The gel formed was preserved with the mixture of ethanol and glycerol [254].	diammonium hydrogen phosphate was added to the above solution. Step 4: - 115 ml of 24 vol% ammonium hydroxide was added to the above solution. Step 5: - The above solution was stirred continuously at the hot plate for 90 min at 60-70 ºC. The stirring rate was 720 rpm. Step 6: - There is a formation of a white precipitate. Step 7: - Bückner funnel separated gel from the precipitate. Step 8: - It was not necessary to preserve the Hydroxyapatite gel. All the 9 prepared samples (3 polished, 3 grit blasted and 3 mid-range roughness titanium substrates utilised all the Hydroxyapatite gel.

Titanium substrate dipping procedure	Step 1 : - The titanium stripes were attached to the belt and pulley system and dipped into prepared HA suspension at the constant speed of 15-300 mm/min [254]. Step 2: - The coated samples were heat treated on the mullite furnace with a nitrogen environment (flow rate of 4 L/min) at 840 ºC. The samples were heat treated at 840 ºC for 2 hours at the heating and cooling rate of 2 ºC/min [254].	Step 1: - The titanium substrates were dipped into the Hydroxyapatite gel. Step 2 : - The coated titanium substrates were again post-heat treated at 650 ºC for 5 hours at 1 ºC/min in an argon atmosphere at the flow rate of 5L/min for first 2 minutes and 0.8 L/min afterwards [300, 314, 315].

3.10 Sol-gel Technique for Wollastonite Coating

5.68 ml Tetraethyl orthosilicate (TEOS) was dissolved in 25 ml ethanol. Another solution consisting of 5.96 grams of calcium nitrate tetrahydrate was dissolved in a 25 ml ethanol solution. Sol-gel technique employed the addition of 5.68 ml TEOS/ 25 ml ethanol to 5.96 grams calcium nitrate tetrahydrate/25 ml ethanol solution for the synthesis of Wollastonite. [255]. The stoichiometric equation for the sol gel synthesis of Wollastonite is shown in **Equation 15**:

$$2Ca(NO_3)_2.4H_2O + 2Si(OC_2H_5)_4 = 2CaSiO_3 + 11CO_2 + C_3N_4 + C_2H_6 + 25H_2$$

…….Equation 15

3.10.1 Tetraethyl Orthosilicate (TEOS) in Ethanol

5.68 ml tetraethyl orthosilicate (TEOS) and 11.36 ml were immersed in either 25 ml or 50 ml ethanol solution respectively depending on the experiment. The solution was stirred, and the pH was measured along with the time and solution temperature. The pH and the solution temperature were measured at 30 seconds intervals, with the total duration of an experiment being 20 minutes. It was challenging to measure the weight at every 30 seconds interval as otherwise the beaker containing the solution had to be disconnected from the pH meter, thus would have provided inconsistent values of temperature and pH. Therefore, two sets (as repeats pH1 and pH2) of the experiment were

performed, and average weight of the two sets, temperature and pH were noted to improve the repeatability of the experiment.

3.10.2 Calcium Nitrate in Ethanol

5.96 grams of calcium nitrate tetrahydrate was dissolved in 25 ml ethanol. The initial experiment was performed similarly to the TEOS solution with continuous stirring for 20 minutes to determine a stabilisation and testing zone based on two repeat experiments, pH1 and pH2. The average weight of two sets was measured at 0 seconds and 20 minutes, and the average pH and average temperature were measured at 30 seconds intervals.

3.10.3 Wollastonite Synthesis by Three Methods

The primary objective of this experiment was to add TEOS solution to the calcium nitrate solution to synthesise Wollastonite. TEOS was added using three methods; (1) TEOS solution was added drop-be-drop via a peristaltic pump over 5 minutes; (2) A constant amount of TEOS solution was added each minute over 5 minutes; (3) Complete TEOS solution was added to calcium nitrate solution, and the pH change was measured over 5 minutes.

a) *Wollastonite solution by a peristaltic pump method*

The stabilisation time for 11.36 ml TEOS/ 50 ml ethanol solution used was 15 minutes, as mentioned in **Figure 105**. Therefore, 11.36 ml/ 50 ml ethanol solution was stirred for 10 minutes. After 10 minutes of stirring the TEOS/ethanol solution, 5.96 grams of calcium nitrate tetrahydrate was dissolved in 25 ml ethanol, and the calcium nitrate solution was stirred for 5 minutes separately. The pH meter was inserted into the calcium nitrate tetrahydrate/ethanol solution beaker immediately after initiating the calcium nitrate tetrahydrate/ethanol solution, as explained in **Figure 41**, which equates to 15 minutes of stabilisation time for the TEOS/ethanol solution and 5 minutes for the calcium nitrate tetrahydrate/ethanol solution, as mentioned in **Figures 105 and 106**, respectively. After 15 minutes, approximately only 30.68 ml of the TEOS/ethanol solution was added dropwise to the calcium nitrate tetrahydrate/ethanol solution via a peristaltic pump at the pump flow rate of 6 ml/min for 5 minutes. The reason why 11.36 ml TEOS/50 ml ethanol solution was used instead of 5.68 ml TEOS/ 25 ml ethanol solution is explained in **Section 4.8.2**. **Figure 41** shows the schematic diagram of the Wollastonite synthesis via the peristaltic pump method.

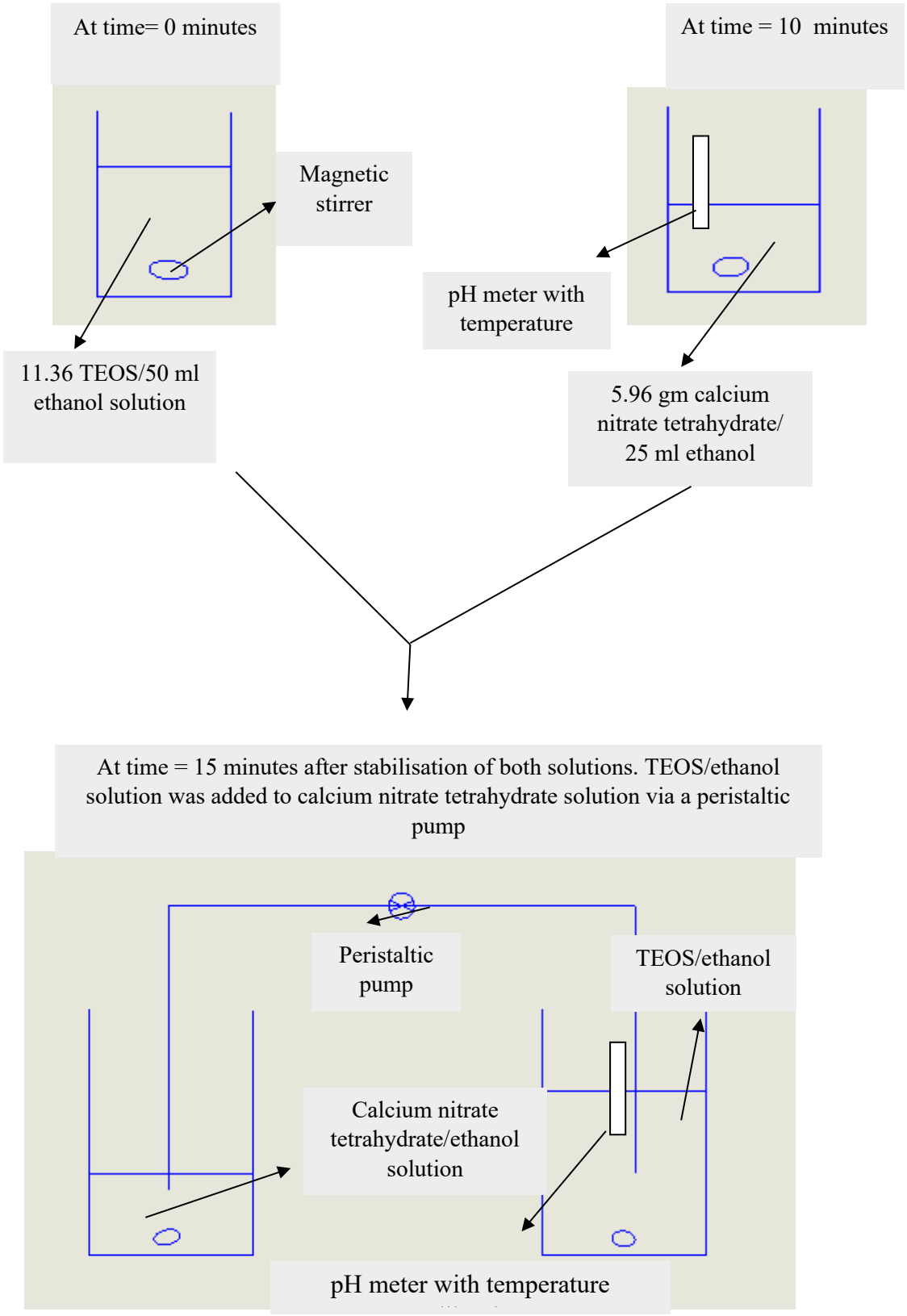

Figure 41, Schematic diagram for Wollastonite synthesis by peristaltic pump method

b) Wollastonite solution by constant addition method

In this method, 11.36 ml of TEOS was added to 50 ml of ethanol, and the solution was stirred. The stabilisation time of 11.36 ml TEOS/ 50 ml ethanol solution was 15 minutes, as mentioned in **Figure 105**. In contrast, the stabilisation time of the calcium nitrate solution was 5 minutes, as mentioned in **Figure 106**. Therefore, the TEOS/ethanol solution was stirred for 10 minutes. At 10 minutes, 5.96 grams of calcium nitrate was dissolved in 25 ml ethanol, and the solution was continuously stirred separately. The pH meter was inserted into the calcium nitrate tetrahydrate/ethanol solution immediately after initiation of stirring. After 15 minutes, the stabilisation of both the TEOS/ethanol solution and calcium nitrate tetrahydrate/ethanol solution was attained, as detailed in **Figure 41**. Some quantities of TEOS/ethanol solution were taken from the beaker every minute and added to the calcium nitrate tetrahydrate/ethanol solution via a 10 ml syringe. The total quantity of TEOS/ethanol solution was approximately half (30.68 ml). This equates to 7 ml of TEOS/ethanol solution each minute for 4 minutes (7 * 4 = 28 ml of TEOS solution) and 2.86 ml of TEOS/ethanol solution at the fifth minute. **Figure 42** shows a schematic diagram for Wollastonite synthesis by the constant addition method.

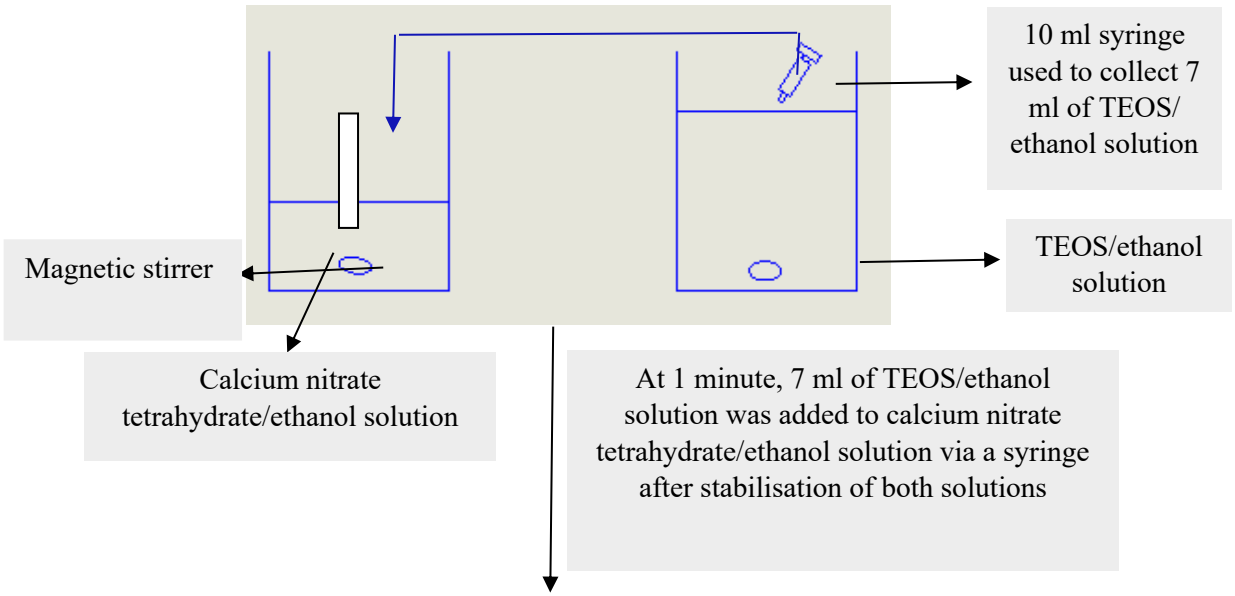

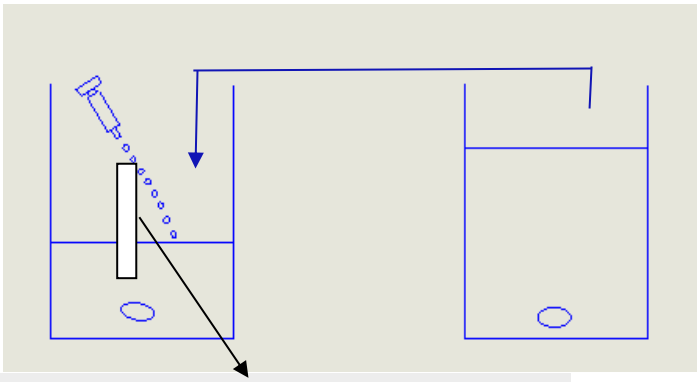

pH meter with temperature calibration

At 2 minutes, another 7 ml added giving total of 14 ml of TEOS/ethanol solution in total was added to calcium nitrate tetrahydrate/ethanol solution via a syringe

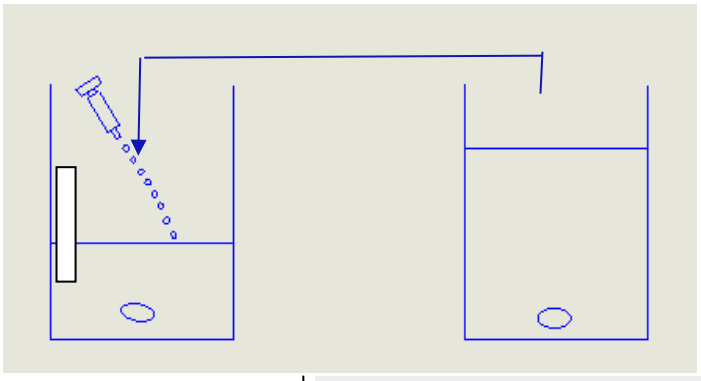

At 3 minutes, another 7 ml added giving total of 21 ml of TEOS/ethanol solution in total was added to calcium nitrate tetrahydrate/ethanol solution via a syringe

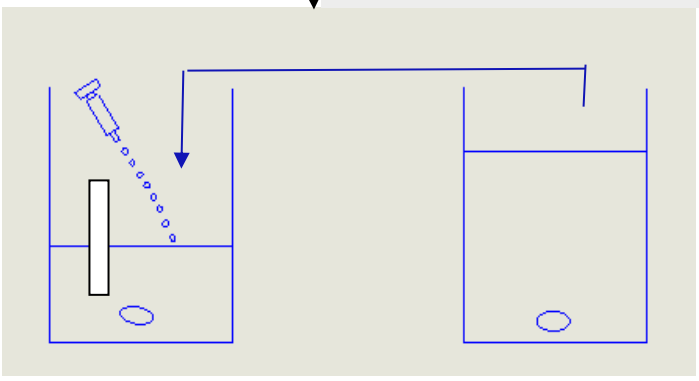

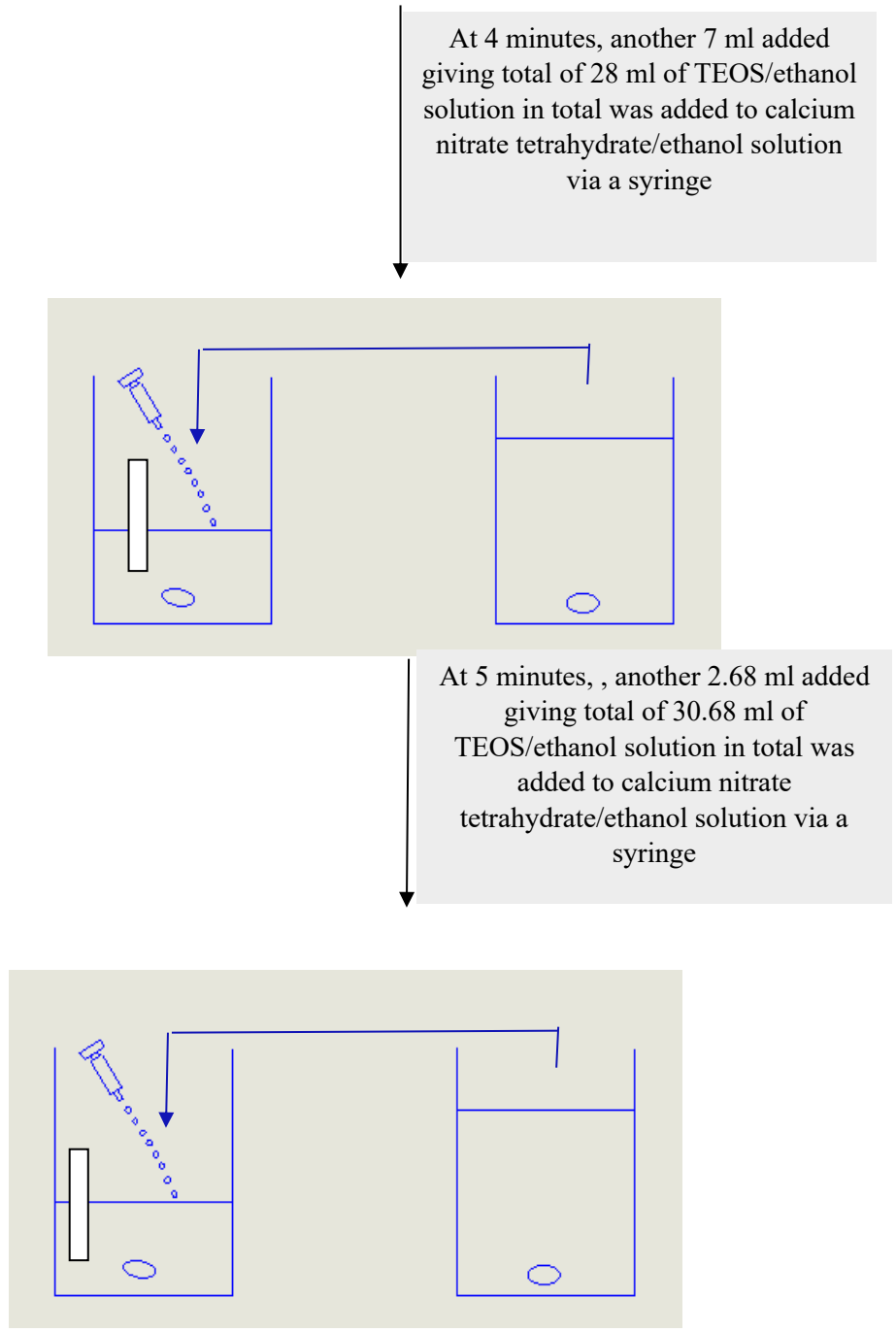

Figure 42, Schematic diagram of constant addition for Wollastonite synthesis

c) Wollastonite Solution by Direct Addition Method

This method completely added TEOS/ethanol solution to the calcium nitrate tetrahydrate/ethanol solution after the stabilisation of TEOS/ethanol solution and calcium nitrate tetrahydrate/ethanol solution. 11.36 ml of TEOS was dissolved in 50 ml ethanol in a solution. The solution was stirred continuously. After 10 minutes of stirring the TEOS/ ethanol solution, 5.96 grams of calcium nitrate tetrahydrate solution was added to 25 ml ethanol, and the solution was stirred separately. The pH meter was inserted into

the beaker containing calcium nitrate tetrahydrate/ethanol solution immediately after initiation of stirring. The stabilisation time of 11.36 ml TEOS/ 50 ml ethanol was 15 minutes, as mentioned in **Figure 105**. In contrast, 5.96 gm calcium nitrate tetrahydrate/ 25 ml ethanol was stabilised after 5 minutes, as mentioned in **Figure 106**. Therefore, after 15 minutes, the TEOS/ethanol solution and calcium nitrate tetrahydrate/ethanol solution attained the stabilisation time, as mentioned in **Figure 41**. After 15 minutes, approximately half (30.68 ml) of TEOS/ ethanol solution was added directly to the calcium nitrate tetrahydrate/ethanol solution. **Figure 43** shows the schematic diagram for Wollastonite synthesis by the direct addition method.

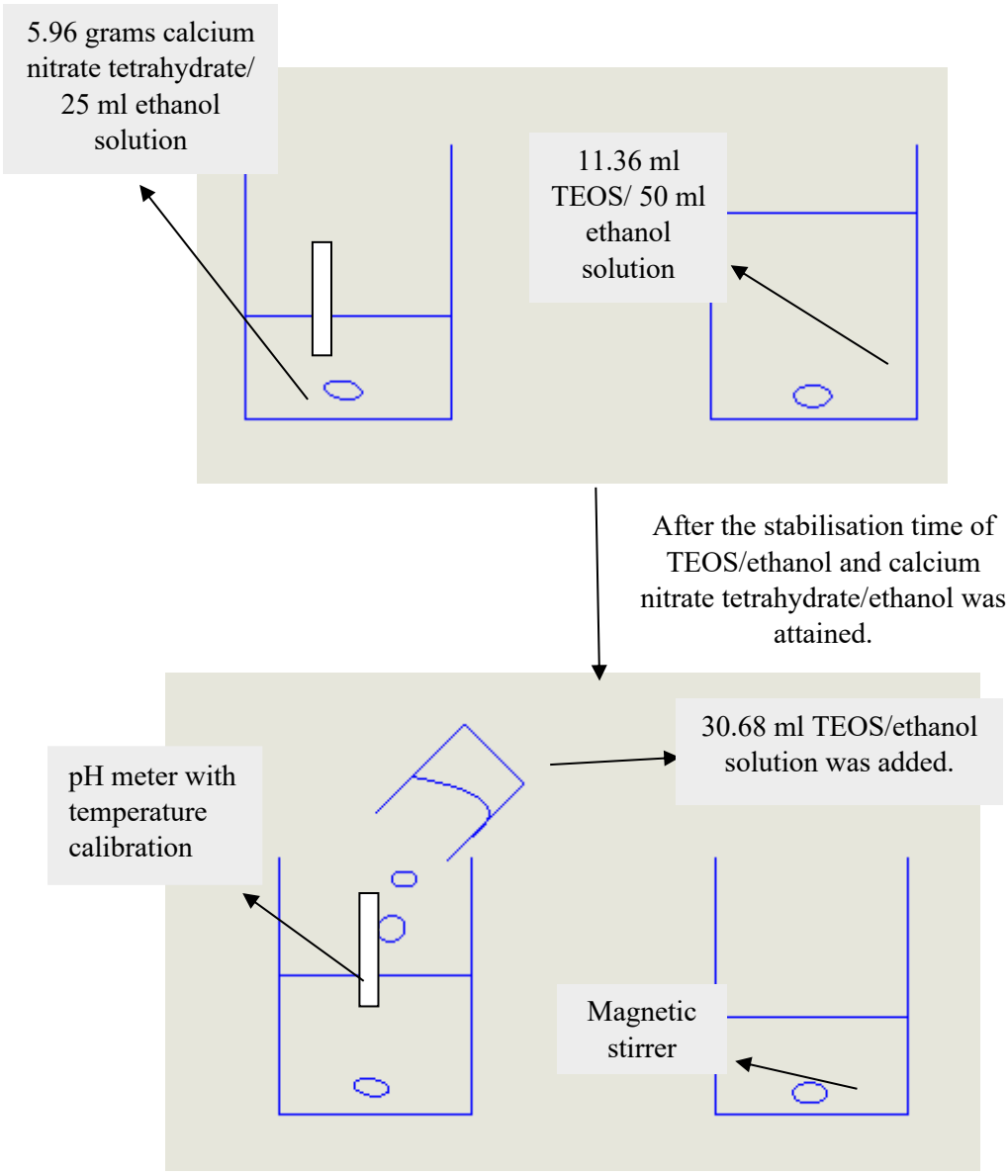

Figure 43, Schematic diagram for Wollastonite synthesis by direct addition method

3.10.4 Comparison between Literature and DCU Research

Table 19 compares the Wollastonite coating obtained by Bao et al. [255]. The titanium substrates of three different roughness were prepared in the DCU laboratory to understand the relationship or variation in the coating due to changes in surface roughness. There was an oxide layer formation on the titanium substrate when heat treated in the air atmosphere [300]. In high temperature application, there is a high possibility of the diffusion of oxygen inside the titanium alloy matrix [312]. The coatings obtained by the literature flaked and dissolved after each dipping. Therefore, the substrate was preheated to the temperature of 650 ºC at a slow heating rate of 1 ºC/min and a dwell time of 5 hours in an argon environment. Moreover, the post-coating temperature in the literature was 900 ºC, which might lead to the titanium oxide layer formation, resulting in titanium alloy embrittlement (heating temperature > 600 ºC) [312]. The oxide layer formation was almost nil when the titanium is heated at 650 ºC with a lower heating/cooling rate in an argon environment. Moreover, heat-treatment of the titanium alloy in an argon atmosphere improves its ductility [313]. In **Table 20**, the Wollastonite coated titanium substrate underwent heat-treatment at 650 °C in an argon atmosphere.

Table 19, Comparison between the literature and DCU research for Wollastonite coating heat-treated at 650 °C in an air atmosphere

Materials or Methods	Technique used in the Literature review	Technique used in DCU research
Titanium substrate	Step 1: - Polishing on bare titanium was done. The titanium substrates were ultrasonically cleaned with a mixture of ethanol and acetone.	Step 1: - In another titanium substrate set, as-prepared titanium substrates were preheated to 650 ºC with dwelling time of 5 hours at the rate of 1 ºC/min in air atmosphere [300]. The substrate was then cleaned with a mixture of distilled water, ethanol, and acetone.
Process to form Wollastonite solution or Wollastonite gel	Step 1: - 5.68 ml TEOS/25 ml ethanol was added to 5.96 gm calcium nitrate tetrahydrate/ 25 ml ethanol, and the solution was continuously stirred. To	Step 1: - 5.68 ml TEOS/25 ml ethanol was added to 5.96 gm calcium nitrate tetrahydrate/ 25 ml ethanol, and the solution was continuously stirred. To obtain a pH of 3.5, nitric acid

	obtain a pH of 3.5, nitric acid was added to form the Wollastonite solution [255].	was added to form the Wollastonite solution [255]. Step 2: - The Wollastonite solution formed was dried in an oven for 2 hours at 80 ºC. The Wollastonite solution was dried for 2 hours, similar to quenching time to avoid confusion. Since the boiling point of the ethanol is 78.4 °C [316]. Drying for 2 hours at 80 ºC resulted in the formation of the Wollastonite gel [255].
Titanium substrate dipping procedure	Step 1:- Titanium substrates were dipped into Wollastonite solution [255]. Step 2: - The titanium substrates were dried in the furnace at 350 ° C following dipping [255]. Step 3: - Steps 1 and 2 were repeated five times. Step 4: - Following the dipping procedure five times, the titanium substrates were calcined in the furnace at 900 °C for 30 minutes [255]. Step 5: - The other remaining sol was dried at 80 °C in an oven.	Step 1: - Titanium substrates were dipped into the Wollastonite gel for 5 minutes. Step 2: - After the dipping process, the titanium substrates were placed in the furnace for 15 minutes at 350 °C. Step 3: - The titanium substrates were removed from the furnace and dried in an air atmosphere for 10 minutes. (Note: - all the timing mentioned above, such as 5, 10 and 15 minutes, was evaluated by the experiment using an infrared thermometer). Step 4: - Steps 1,2 and 3 were repeated five times. Step 5 : - Following that, the substrates were post-heat treated to the temperature of 650 ºC for the dwelling time of 5 hours at 1 ºC/min heating rate in air atmosphere [300].

Table 20, Comparison between the literature and DCU research for Wollastonite coating heat-treated at 650 °C in argon atmosphere

Materials or Methods	Technique used in the Literature review	Technique used in DCU research
Titanium substrate	Step 1: - Polishing on bare titanium was done. The titanium substrates were ultrasonically cleaned with a mixture of ethanol and acetone.	Step 1: - In another titanium substrate set, as-prepared titanium substrates were preheated to 650 ºC with dwelling time of 5 hours at the rate of 1 ºC/min in an argon atmosphere at the flow rate of 5L/min for first 2 minutes and 0.8 L/min afterwards [300,314,315]. The substrate was then cleaned with a mixture of distilled water, ethanol and acetone.
Process to form Wollastonite solution or Wollastonite gel	Step 1: - 5.68 ml TEOS/25 ml ethanol was added to 5.96 gm calcium nitrate tetrahydrate/ 25 ml ethanol, and the solution was continuously stirred. To obtain a pH of 3.5, nitric acid was added to form the Wollastonite solution [255].	Step 1: - 5.68 ml TEOS/25 ml ethanol was added to 5.96 gm calcium nitrate tetrahydrate/ 25 ml ethanol, and the solution was continuously stirred. To obtain a pH of 3.5, nitric acid was added to form the Wollastonite solution [255]. Step 2: - The Wollastonite solution formed was dried in an oven for 2 hours at 80 ºC. The Wollastonite solution was dried for 2 hours, like quenching time to avoid confusion. Since the boiling point of the ethanol is 78.4 °C [316]. Drying for 2 hours at 80 ºC resulted in the formation of the Wollastonite gel [255].
Titanium substrate dipping procedure	Step 1:- Titanium substrates were dipped into Wollastonite solution [255]. Step 2: - The titanium substrates were dried in the	Step 1: - The preheated titanium substrates were dipped into the Wollastonite gel for 5 minutes. Step 2: - After the dipping process, the titanium substrates

	furnace at 350 ° C following dipping [255]. Step 3: - Steps 1 and 2 were repeated five times. Step 4: - Following the dipping procedure five times, the titanium substrates were calcined in the furnace at 900 °C for 30 minutes [255]. Step 5: - The other remaining sol was dried at 80 °C in an oven.	were placed in the furnace for 15 minutes at 350 °C. Step 3: - The titanium substrates were removed from the furnace and dried in an air atmosphere for 10 minutes. (Note: - all the timing mentioned above, such as 5, 10 and 15 minutes, was evaluated by the experiment using an infrared thermometer). Step 4: - Steps 1,2 and 3 were repeated five times. Step 5 : - Following that, the substrates were post-heat treated to the temperature of 650 ºC for the dwelling time of 5 hours at 1 ºC/min heating rate in an argon atmosphere at the flow rate of 5L/min for first 2 minutes and 0.8 L/min afterwards [300, 314, 315].

3.11 Sol-Gel Dip Coating for HA/Wollastonite

To enhance the bioactivity and mechanical properties of Hydroxyapatite, Wollastonite was added to the Hydroxyapatite to form a HA/Wollastonite composite [18]. There were three methods to synthesise the HA/Wollastonite biocomposite: 1) By co-precipitation, where the first sol of HA is synthesised and in that solution, a precursor for Wollastonite is added to form a Wollastonite sol, resulting in HA/Wollastonite biocomposite [256]; 2) By alternative sol-gel method, where the Wollastonite dissolved in the aqueous medium was added to the sol of the HA to form a HA/Wollastonite composite [160]; 3) Wollastonite in the particulate form was added to the sol of HA to form HA/Wollastonite scaffold [162]. It was difficult to synthesize the HA/Wollastonite composite by 2-step precipitation as the solvents for the precursors of HA and Wollastonite were different in the current study. Wollastonite dissolves in an aqueous medium added to the sol of HA, therefore would be challenging, as separating Wollastonite from its aqueous solution by

filtration would be time-consuming. Therefore, method 3) Wollastonite in the particulate form added to the Hydroxyapatite gel was applied in this research.

The sol of HA was synthesised using the same procedure explained in **Section 3.8** with the same stoichiometric equation for sol-gel synthesis of Hydroxyapatite as shown in **Equation 14**. The sol was dried with the help of vacuum filtration by placing filter paper on the Büchner funnel. After 24 hours of drying, the gel weight was checked. The total gel weight was 150 grams. The gel was divided into 3 equal portions, in the first portion, 5 grams of Wollastonite particulate (10 wt.%) material was added, in the second portion, 10 grams of Wollastonite particulate (20 wt.%) material was added, and in the third portion, 15 grams of Wollastonite particulate (30 wt.%) material was added; each to provide 10 wt.%, 20 wt.% and 30 wt.% of Wollastonite added to HA. The Wollastonite quantity was limited to 30 wt.%, because the use of Wollastonite increases the porosity of the HA/Wollastonite composite coating which is not desirable at higher levels as, it reduces the mechanical performance of a hip implant at high porosity once Wollastonite has been absorbed into the body [211]. Moreover, adding more than 30 wt.% Wollastonite can increase the bioactivity but also the degradability of the HA/Wollastonite biocomposite [18]. After addition of Wollastonite and mixing, the gel was allowed to dry for more than 12 hours to assist in mixing.

Polished substrates were considered for the study as it had the best results observed in **Sections 4.8.1** and **4.8.3**. The polished substrate was pre-heated at 650 °C in an argon atmosphere at 1 °C/min with dwell time of 5 hours and cooled at a same cooling rate, similar to studies conducted by Usinskas et al [300]. The prepared substrate samples (polished, in this case) were dipped in the dried gel and heat treated in an argon atmosphere at 650 °C at a heating rate of 1 °C/min, as mentioned in **Section 3.9.1**. **Figure 44** shows the flow chart of the dip-coated HA/wollastonite composite coatings.

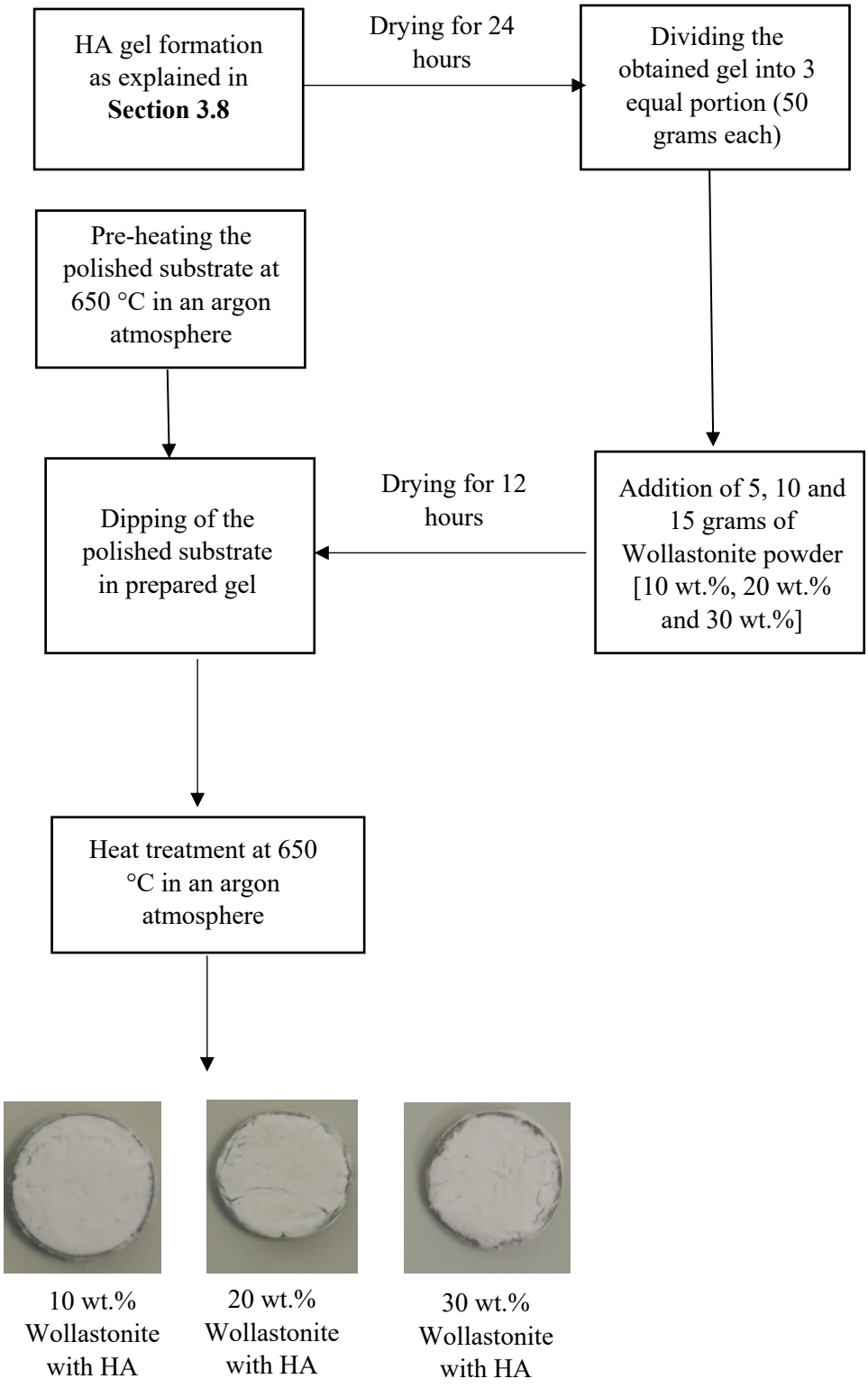

Figure 44, Flow chart of dip-coated HA/Wollastonite composite coating

4 Results and Discussion

4.1 Introduction

This chapter presents and discusses the results obtained from various experiments during this study. The chapter includes oven drying results obtained for Hydroxyapatite and Wollastonite; that is, the percentage loss at temperatures of 60 °C, 80 °C and 100 °C, respectively. Then flowability results of both the as-received powders are obtained, which is followed by the heat treatment test for the flowability of Wollastonite powder. The spray drying results of both Hydroxyapatite and Wollastonite powders at different process parameters were found, followed by the SEM images of the best obtained spray-dried Hydroxyapatite and Wollastonite, and the results are discussed. The design of experiment (DOE) results of spray drying of Hydroxyapatite, Wollastonite and Hydroxyapatite/Wollastonite composite mixture powder which includes a table and curve, are shown in the following subsection. This subsection is followed by the optimisation of Hydroxyapatite/Wollastonite spray-dried powders, then followed by a summary of the steps trialled to improve the flowability of Wollastonite powder. The results concerning the roughness calibration and XRD analysis of prepared titanium alloy substrate are then presented. Following that, the results related to spray coating and dip coating of Hydroxyapatite, Wollastonite and Hydroxyapatite/Wollastonite biocomposite, which include SEM, FTIR and XRD analysis of the obtained coatings, are discussed. This section is followed by the comparison of the spray-coated and dip-coated samples. Finally, the summary of discussion subheading concludes the chapter.

4.2 Oven Drying Results

Both powders, Hydroxyapatite (HA) and Wollastonite, were heated at the same temperature and same time (for example, two samples of Hydroxyapatite and Wollastonite were heated at 60 °C for the same time) to reduce the variation caused due to external factors. The powders were weighed before and weighed after each hour of drying. The weight of all the six samples after 2 hours of weight-stabilisation for Hydroxyapatite and Wollastonite at temperatures of 60 °C, 80 °C, and 100 °C are given in **Table 21.**

Table 21, Weight of Hydroxyapatite and Wollastonite powder at different temperatures

Oven drying	HA at 60ºC	Wollastonite at 60ºC	HA at 80ºC	Wollastonite at 80ºC	HA at 100ºC	Wollastonite at 100ºC
Density (g/cm^3)	3.16	2.9	3.16	2.9	3.16	2.9
Beaker wt. (g)	105.57	114.61	111.12	107.62	118.01	115.99
Beaker + powder wt. (g)	185.57	194.59	191.12	187.62	198.01	195.99
Powder wt. (g)	80	79.98	80	80	80	80
Beaker + powder wt. after one hour (g)	185.53	194.55	190.97	187.47	197.88	195.85
Beaker + powder wt. after two hours (g)	185.53	194.55	190.97	187.47	197.88	195.85
Plastic box wt. (g)	24.46	24.15	24.48	23.96	23.95	24.32
Plastic box+ Powder wt. (g)	104.29	104.13	104.3	103.85	103.72	104.18
Final powder wt. (g)	79.83	79.94	79.82	79.89	79.77	79.86

Percentage loss of powder (%)	0.2125%	0.05%	0.225%	0.1375%	0.2875%	0.175%

The measurement of different weights of each beaker were evaluated in the present study. The density of Hydroxyapatite was approximately 3.16 g/cm^3 [317]. The density of Wollastonite was 2.90 g/cm^3, obtained from the datasheet [289]. The measurement of powder weight was around 80 grams. The percentage loss of the powder was therefore low, around 0.2-0.3% for Hydroxyapatite, even when the temperature was increased from 60 to 100 °C. However, this loss slightly increased when the temperature increased from a percentage loss of 0.2125% at 60 °C and 0.2875% at 100 °C. The lower percentage loss may be due to the lack of adsorbed water or lattice water presence on the outer surface of the Hydroxyapatite. Any moisture on the Hydroxyapatite surface should diminish after 25 ºC [78]. Actual dehydroxylation, which is the loss of water from the molecule of Hydroxyapatite, begins at around 900 ºC [78]. This dehydroxylation is a slow process followed by decomposition at around 1300 ºC; therefore a 60 to 100 ºC temperature range should not substantially cause a change in the physical properties of the Hydroxyapatite [78].

The percentage loss of the Wollastonite powder increased but slightly less than Hydroxyapatite each temperature elevation, such as 0.05% to 0.2% when the powder was heated from 60 °C to 100 °C. The near nil loss of the Wollastonite may be due to the thermal stability of the Wollastonite powder up to a temperature of approximately 900 ºC [318]. The percentage loss in the theoretical density of the Wollastonite resumes at the calcination temperature of 950 ºC [318]. Any single phase of Wollastonite (α and β-Wollastonite) occurs at 950-1200 ºC [318]. The graph of both powders at various temperatures are shown in **Figure 45**.

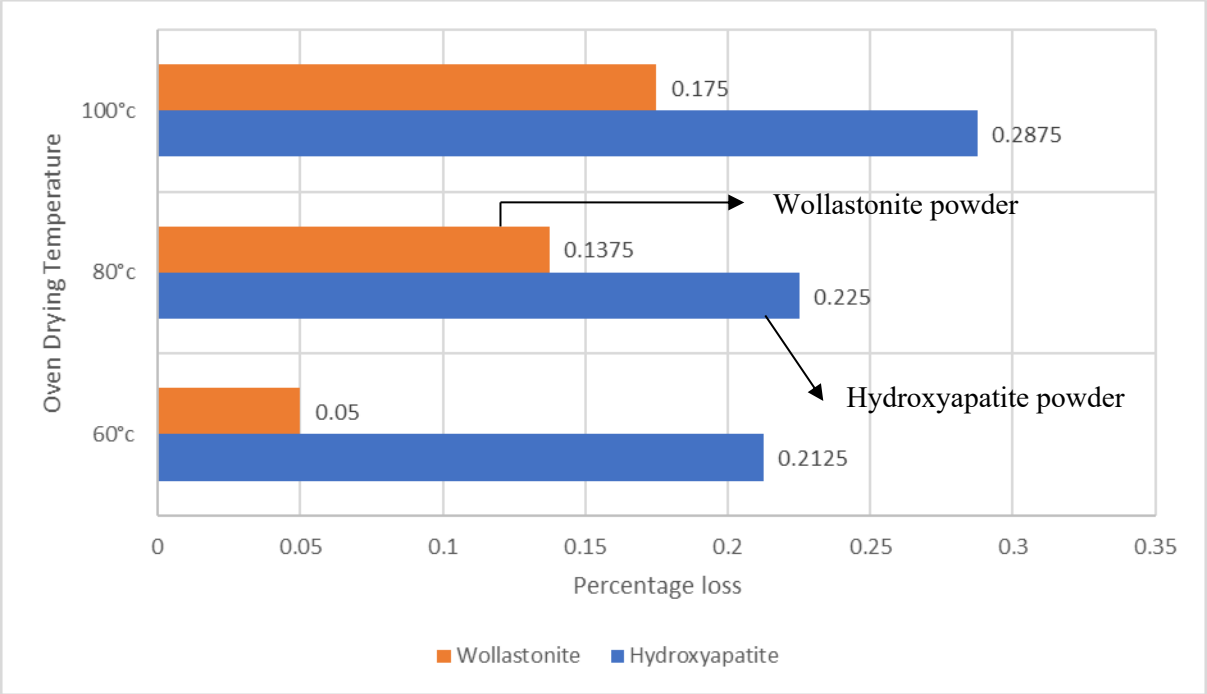

Figure 45, Percentage loss of both powders at different temperatures

4.3 Powder Flowability

Powder flowability particularly with respect to Wollastonite was conducted over a very long period. Unfortunately, as will be explained, due to the lack of flowability of a Wollastonite, detailing the various techniques used is not presented, rather a summary is presented. Hydroxyapatite was initially measured to determine its weight (30 grams). The experiment showed a flow rate of 0.214 g/s where 30 grams of powder took 2 minutes and 20 seconds to flow through the funnel completely. Pre-weighed 20 grams of Wollastonite was then inserted into the funnel. Initially, Wollastonite did not flow due to tendency to form lumps, irregular shape of Wollastonite and finer structure of Wollastonite. Even smaller quantities of Wollastonite (10 wt.% and 20 wt.%) hampered the flowability of the composite powder. Due to the exposure of the powder to high humidity and fine powder (less than 20 µm), the powder did not flow easily [288]. **Table 22** shows the flowability of the Hydroxyapatite powder, Wollastonite powder and composite powder.

Table 22, Flowability of Hydroxyapatite, Wollastonite and composite powder

Powder type	Flowability values
As-received Hydroxyapatite powder	0.21 g/s
As-received Wollastonite	Nil
As received Wollastonite powder heat treated from 700 °C to 1500 °C	Nil
Composite powder (90 wt.% HA and 10 wt.% Wollastonite)	Nil
Composite powder (80 wt.% HA and 20 wt.% Wollastonite)	Nil
Composite powder (90 wt.% HA/10 wt.% Wollastonite and 80 wt.% HA/20 wt.% Wollastonite, respectively) heat treated from 700 °C to 1500 °C	Nil

4.3.1 Wollastonite Powder Flowability Experiments

a) Wollastonite heat treated from 700-1500 °C

The flowability of the Wollastonite powder did not improve despite the use of the Hall flowmeter. As a result, a NABERTHERM and Carbolite furnace were employed to heat-treat the Wollastonite powder. The concept was that the heat treatment technique may reduce the irregularity in the Wollastonite powder morphology. As Wollastonite is relatively stable up to 700 ºC. The temperature for calcination of Wollastonite selected in the present study ranged from 700 ºC to 1500 ºC [318]. Wollastonite in 10 wt.% and 20 wt.% was added to Hydroxyapatite (90 wt. % and 80 wt.%, respectively) and heat treated at temperature conditions similar to as-received Wollastonite.

In the case of Wollastonite powder, It was possible to heat treat the powder only up to 1200 °C, as heat treatment beyond 1200 °C resulted in powder adhering to the crucible. In the case of HA/Wollastonite composite powder, the result was like the flowability of as-received Wollastonite, and the composite powder did not flow. Heat treatment techniques such as oven drying (heating the Wollastonite from 60 °C to 100 °C), furnace heat treatment (heat treatment of Wollastonite and HA/Wollastonite from 700 to 1400 °C) did not improve the flowability of the Wollastonite powder.

b) *Wollastonite powder via a cap assembly*

The cap assembly was designed and manufactured inside the workshop as mentioned in **Section 3.7.1**. Initially, the pressure varied from 1 to 7 bar; there was no change in flowability with 20 grams of powder. Then the powder quantity was increased to 60 grams, but there was no change in the flowability with the same pressure range. There was some flowability up to 5 seconds. However, the powder ceased to flow after 5 seconds.

c) *Wollastonite powder via a vibrator assembly*

The vibrator assembly was designed and manufactured in the workshop using the vibrator concept used in DCU thermal spray HVOF equipment. The retort stand supported the vibrator assembly on top of the cartridge assembly. The 1-7 bar pressure was not enough to create turbulence in the vibrator assembly, so the pressure was increased to 15 bar. Powder flowability was observed for up to 5 seconds, and it ceased after 5 seconds even after 15 bar pressure.

d) *Some modifications to the Wollastonite powder and assembly*

To improve the flowability of the powder, Hydroxyapatite was added to the Wollastonite powder in a ratio of 9:1 (90 wt.% of Hydroxyapatite, 10 wt.% Wollastonite) and a ratio of 8:2 (80 wt.% Hydroxyapatite, 10 wt.% Wollastonite), with the total amount of powder (HA/Wollastonite) was 20 grams. The vibrator assembly was dissembled and three setting were used: one using the vibrator only (without using compressed air) around the cartridge and the second with the help of only compressed air pressure. The flowability was observed for the first 5 seconds and ceased after 5 seconds, even after changing the pressure settings (like applying the same pressure to the cartridge and vibrator assembly or applying different pressure to the cartridge and vibrator assembly). **Table 23** shows the flowability test summary of the Wollastonite/composite powder with different settings.

Table 23, Flowability test summary of the powder at different settings

Powder	Settings	Powder collection in the beaker for up to 5 seconds	Powder collection in the beaker after 5 seconds
100 % Wollastonite	20 grams Wollastonite with pressure variation of 3-7 bar	The highest powder collection was 0.9 grams with 7 bar pressure	No collection
100 % Wollastonite	60 grams Wollastonite powder with the same pressure variation	The powder collection was in the range of 0.8 gram to 1.0 gram at 3-7 bar pressure	No collection
100 % Wollastonite	Removal of steel shaft in cap assembly	No collection	No collection
100 % Wollastonite	Attachment of plastic tube to the steel shaft in cartridge assembly	0.7-0.8 grams with 3-7 bar pressure	No collection
100 % Wollastonite	Use of vibrator assembly with 60 grams of Wollastonite powder and 15 bar pressure applied.	1.1 grams	No collection
HA/Wollastonite mixture (90 wt.% HA/10 wt.% Wollastonite and 80 wt.% HA/ 20 wt.% Wollastonite)	1. Only a vibrator was used 2. Only chamber pressure was applied. 3. Both vibrator pressure and chamber pressure were applied	1. No collection 2. 0.8- 0.9 grams 3. 1.1-1.2 grams	1. No collection 2. No collection 3. No collection
HA/Wollastonite mixture (90 wt.%	A chamber pressure (7 bar) and a vibrator	1.1 grams- 1.2 grams	No collection

HA/10 wt.% Wollastonite and 80 wt.% HA/ 20 wt.% Wollastonite)	pressure (8 bar) applied separately from 2 different pressure valves		

Table 23 shows the flowability summary of Wollastonite/composite powder at different settings. In all the settings mentioned above, the flowability ceased after 5 seconds. The powder placed near the cartridge outlet was only collected for up to 5 seconds. The remaining powder clogged the cartridge assembly and did not flow even after applying pressure, increasing the powder amount and using the vibrator assembly. Varying compressed air pressure (3-7 bar), the use of higher compressed pressure (15 bar), the use of vibrator assembly, higher quantities of Wollastonite powder and the addition of Hydroxyapatite along with the change of pressure settings did not lead to continuous flowability of Wollastonite powder suitable for thermal spray application. The collection of the powder in the beaker ranged from 0.7 grams to 1.2 grams upto 5 seconds, but the powder flowability ceased after 5 seconds. With no valid results regarding the flowability of Wollastonite, it became imperative to search for an alternative technique to coat Wollastonite onto the titanium substrate. Unfortunately, nor the heat treatment and spray-drying technique did not improve the flowability of the Wollastonite powder.

So, in conclusion, Wollastonite inability to flow ended any proposed methods to coat substrates using such methods like plasma thermal spray or flame thermal spray.

4.4 Spray Drying Results

A detailed description of the spray drying equipment is given in **Section 3.6**. The spray drying technique can produce a powder that is spherical, improving its flowability and reducing its surface area. For the powder to be viable for flowability, it must have a spherical or near spherical morphology and shape. Both Hydroxyapatite and Wollastonite have similar particle sizes but different particle morphology. A previous study evaluated plasma spraying of particles whose particle size ranges from 20 to 45 μm provided a dense coating [221]. If the particle size is less than 20 μm, it requires more carrier gas to supply powder and results in divergent trajectories at the injector exit [221]. Plasma spraying of particles at a larger size (around 100 μm) produces coatings with higher porosity and surface roughness, which is beneficial for bioactivity but only to a certain

extent [221]. The schematic diagram of the spray drying experiment is demonstrated in **Figure 46.**

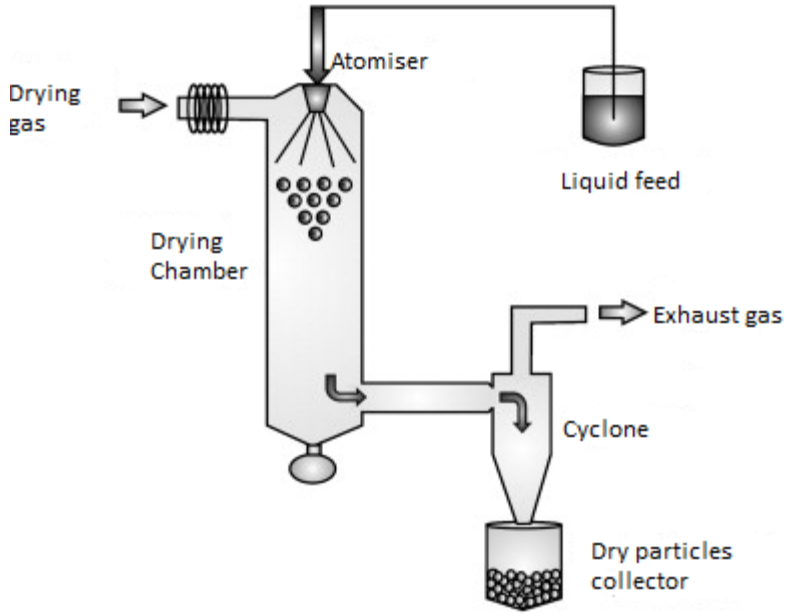

Figure 46, Schematic of spray drying process [207]

As per **Section 3.6.6**, the resulting slurry formed after stirring and heating was spray-dried with the process parameters. After spray drying, the powder collected from the cyclone was transferred to the electric sieving machine. The total percentage of the powder found over the 45-75 µm range was calculated using the percentage of the quantity of 45-75 µm to the total weight of the powder (80 grams)**.** According to the results mentioned by Kweh et al. [221], the particle with a size range of 20-45 µm produced the optimal coating. However, only 50 % of the Hydroxyapatite powder had a particle size range of 45 µm, whereas 90% of the Hydroxyapatite powder had a particle size range of 80 µm, according to the material safety data sheet [286]. Therefore, for maximum particle spherodisation, the 45-75 µm particle size range was considered for the current study. In the current study, 45-75 µm was taken into consideration as the maximum amount of the powder was collected in the sieve at this particle size range. Moreover, employing material reduction techniques such as spray drying and grinding might affect its acicular shape, ultimately affecting its mechanical properties [319]. Also, a 45-75 µm size range was used in the previous study for spray drying of HA powders [320]. Therefore, particle size range of 45-75 was considered in the current study. The

results obtained from spray drying of Hydroxyapatite and Wollastonite are shown in **Table 24**.

Table 24, Process parameters and experimentally recorded response values of Hydroxyapatite and Wollastonite

Trial	Pump Flow (Scaled value)	Compressed airflow (Scaled value)	Temperature (°C)	HA. (Percentage of 45-75 micron)	Wollastonite (Percentage of a 45-75 micron)
1	15.00	22.00	103.00	29.25%	36.63%
2	20.00	22.00	103.00	37.88%	25.50%
3	15.00	33.00	103.00	21.88%	42.15%
4	20.00	33.00	103.00	27.88%	28.00%
5	15.00	22.00	107.00	23.63%	19.70%
6	20.00	22.00	107.00	25.38%	16.43%
7	15.00	33.00	107.00	21.75%	30.66%
8	20.00	33.00	107.00	20.00%	21.13%

The reasons for selecting and varying pump flow rate, airflow rate and temperature for the current study are explained in **Section 3.6.6**. As shown above, the highest response for Hydroxyapatite was observed in trial 2. The process parameters were: a pump flow rate of 20 (scaled value of pump flow rate was taken into consideration), an airflow rate of 22 (scaled value), and a temperature of 103 °C. The response obtained was 37.88% of 45-75 μm HA. Wollastonite was immersed, heated, and stirred using the same method as Hydroxyapatite and spray-dried with the same range of process parameters, to understand its compatibility and difference between the production of Hydroxyapatite and Wollastonite. The study illustrated a lower response of 25.5% at process parameters of pump flow rate 20, airflow rate 22 (scaled value) and temperature of 103 °C.

For Hydroxyapatite, while the highest percentage response was observed during trial 2, therefore high pump flow, lower airflow, and lower inlet temperature favoured higher response; for Wollastonite, the highest response was observed for trial 3 process, using process parameters of pump flow 15 (scaled value), airflow rate 33 (scaled value) and an

inlet temperature 103 °C, therefore favouring a lower pump flow rate and lower inlet temperature.

4.4.1 Spray Drying of Hydroxyapatite-Wollastonite Mixture

The resulting slurry formed after heating and continuous stirring was spray-dried with the process parameters mentioned in the previous section. The spray-dried collected in the cyclone was transferred to an electric sieving machine, and the spray-dried powder in the particle size range of 45-75 μm was collected for the study. The powder percentage was calibrated by the same method described in **Section 4.6**. The process parameters were selected based on the optimum response obtained from the spray drying of Hydroxyapatite and Wollastonite, respectively, as shown in **Table 24**. A 2-factorial screening design was used to select the process parameters and optimise the response for the spray drying for Hydroxyapatite and Wollastonite. Therefore, the three factors used for the spray drying of HA/Wollastonite were: pump flow (15-20) (scaled values), airflow rate (22-33) (scaled values) and Wollastonite wt.fraction (0.2-0.5) at the temperature of 103 °C. The design used to analyse the response obtained was the Box-Behnken design (BBD) and the Wollastonite wt.fraction was based on the previous studies [162, 211]. Because the response (45-75 μm) was calculated in percentage (%), the Wollastonite quantity added to the mixture was taken in fraction (for example, 0.2 instead of 20 wt.%). **Table 25** shows the spray drying of the Hydroxyapatite/Wollastonite powder mixture.

Table 25, Spray drying of Hydroxyapatite/Wollastonite powder mixture at an inlet temperature of 103 °C

	Factor 1	Factor 2	Factor 3	Response 1 (45-75 μm) (%)
Trial	A: Pump flow (scaled value)	B: Airflow rate (scaled value)	C: Wollastonite wt. fraction	Woll/HA deposition
1	15.00	22.00	0.35	17.00
2	20.00	22.00	0.35	23.50
3	15.00	33.00	0.35	25.50
4	20.00	33.00	0.35	29.35
5	15.00	28.00	0.20	21.75
6	20.00	28.00	0.20	24.50
7	15.00	28.00	0.50	27.04
8	20.00	28.00	0.50	36.37
9	18.00	22.00	0.20	22.37
10	18.00	33.00	0.20	23.75
11	18.00	22.00	0.50	27.25
12	18.00	33.00	0.50	34.50
13	18.00	28.00	0.35	26.65
14	18.00	28.00	0.35	25.75
15	18.00	28.00	0.35	27.60
16	18.00	28.00	0.35	25.25
17	18.00	28.00	0.35	28.00

Table 25 shows the response (45-75 μm) of the Hydroxyapatite/Wollastonite mixture powder. The response value ranged from 17% to 36.37%, similar to the value observed in the case of spray drying results of Hydroxyapatite (the response value ranged from 20.11% to 37.98%) and Wollastonite (the response value ranged from 14.26% to 40.79%), as shown in **Table 24**. To understand the effect of each process parameter on the overall response in detail, average values of pump flow rate (18) (scaled value), average value of air flow rate (28) (scaled value) and average value of Wollastonite wt. fraction (0.35) was considered.

It can be observed from **Table 25** that the highest response was observed at trial 8 with the process parameters: pump flow rate: 20 (scaled value), airflow rate: 28 (scaled value) and Wollastonite wt. fraction: 0.5 at an inlet temperature of 103 °C, whereas the lowest response was observed at trial 1 with the process parameters: pump flow rate: 15 (scaled value), airflow rate: 22 (scaled value) and Wollastonite wt. fraction: 0.35. It can be

observed that the high pump flow rate, high airflow rate and higher Wollastonite wt. fraction favoured higher response. As seen previously, a higher pump flow rate and lower air flow rate favoured higher response in Hydroxyapatite, whereas a lower pump flow rate and higher airflow rate favoured higher response in Wollastonite. However, in the case of 50 wt.% HA and 50 wt.% Wollastonite, an increase in the pump flow rate and medium airflow resulted in more deposition of 45-75 μm powder in the cyclone. The extent of effect of all three process parameters on the overall response would be understood by the Design of Experiment (DOE), in the following section.

4.4.2 Morphology of Spray-Dried Hydroxyapatite Powder

SEM observed the morphology of the spray-dried Hydroxyapatite. The top two best results of Hydroxyapatite obtained from the spray drying experiment were from trial 1 (pump flow: 15 (scaled value), airflow rate: 22 (scaled value) and temperature: 103 °C) and trial 2 (pump flow: 20 (scaled value), air flow rate: 22 (scaled value) and temperature: 103 °C). The SEM images (at 100 X magnification) showed the morphology of both particles was spherical, whereas particles obtained from trial 2 were more spherical, which supports the higher powder flowability findings. **Figures 47** and **48** show the morphology of both spray-dried powders at 100 X magnification.

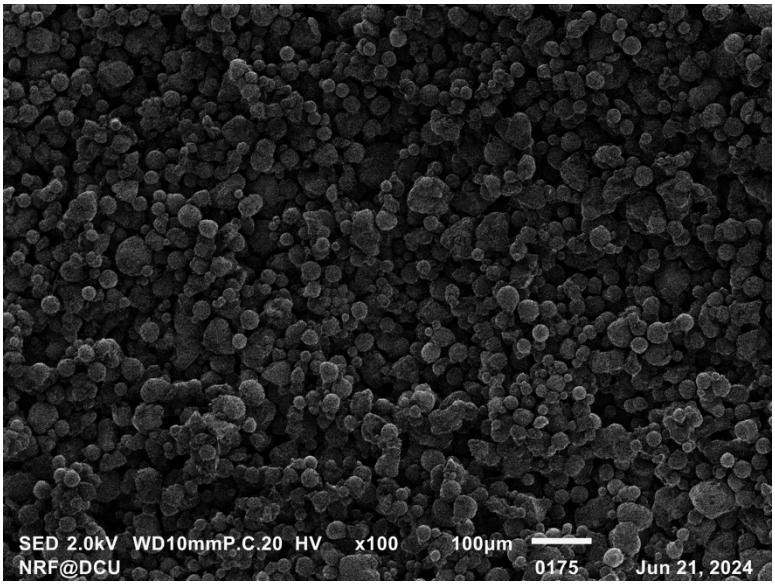

Figure 47, Morphology of spray-dried HA powder from trial 1 at 100 X

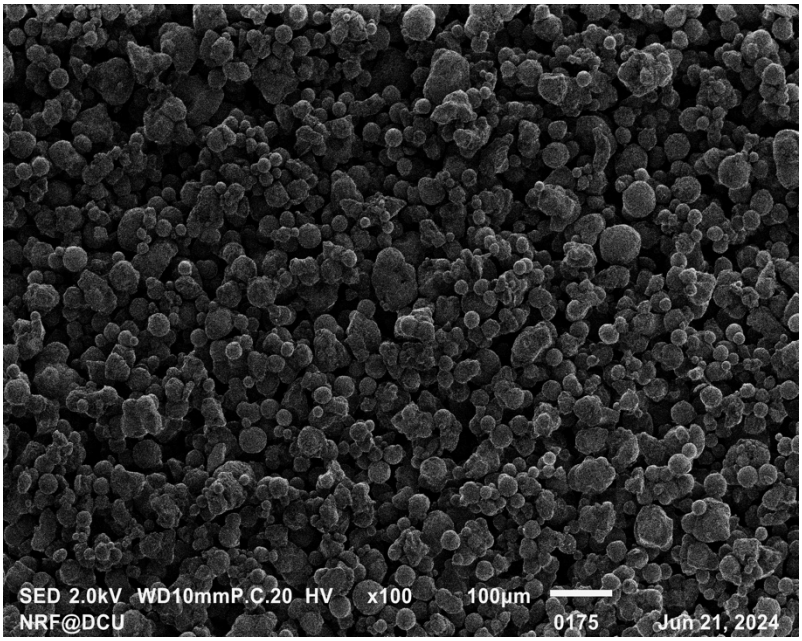

Figure 48, Morphology of spray-dried HA Powder from trial 2 at 100 X

While observing the powder by SEM, less HA powder was attached to the carbon tape from trial 1. Therefore, the HA powder was less dense than the powder observed in trial 2. The as-received powder shown in **Figure 18** was more spherical as it underwent proper post-processing treatment such as sintering and drying. Powders obtained from trials 1 and 2 were less spherical due to englobulation caused by the spray drying technique.

4.4.3 Morphology of Spray-Dried Wollastonite Powder

Like Hydroxyapatite, the morphology of the spray-dried Wollastonite powder was observed with the help of SEM. The two best results of Wollastonite obtained from the spray drying experiment were trial 1 (pump flow: 15 (scaled value), airflow rate: 22 (scaled value) and temperature: 103 °C) and trial 3 (pump flow: 15 (scaled value), airflow rate: 33 (scaled value) and temperature: 103 °C). The study showed that the spray drying method did not affect the morphology of the powder with an acicular shape like as-received powder, with no improvement in the flowability of Wollastonite powder. The morphology of spray-dried powder from trials 1 and 3 are shown in **Figures 49** and **50** at 100 X magnification.

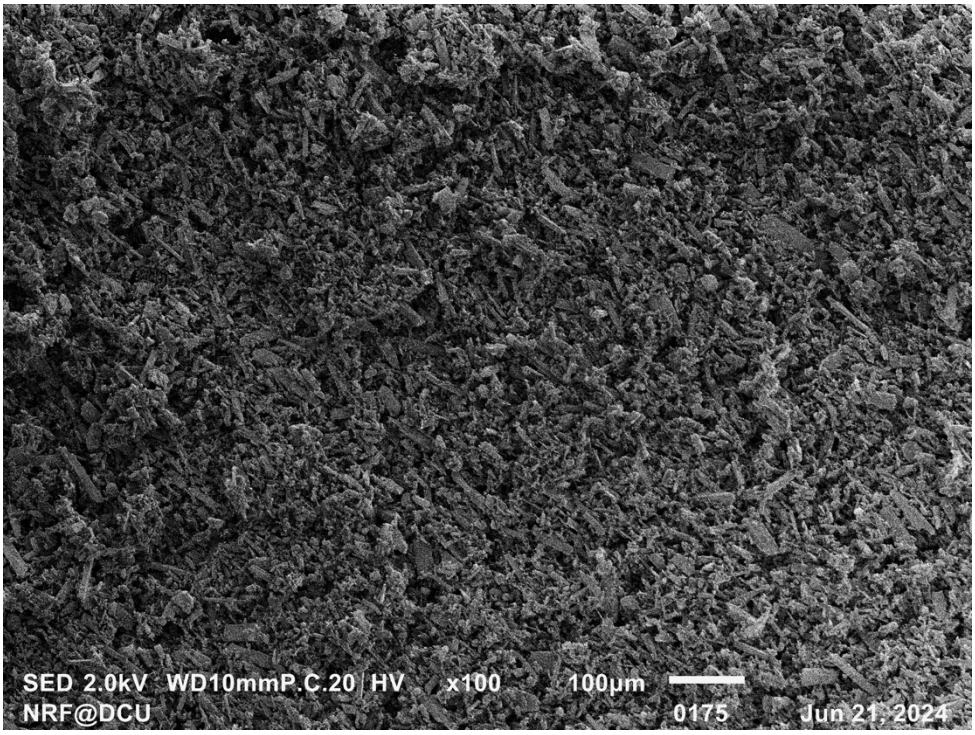

Figure 49, Morphology of spray-dried Wollastonite powder from trial 1 at 100 X

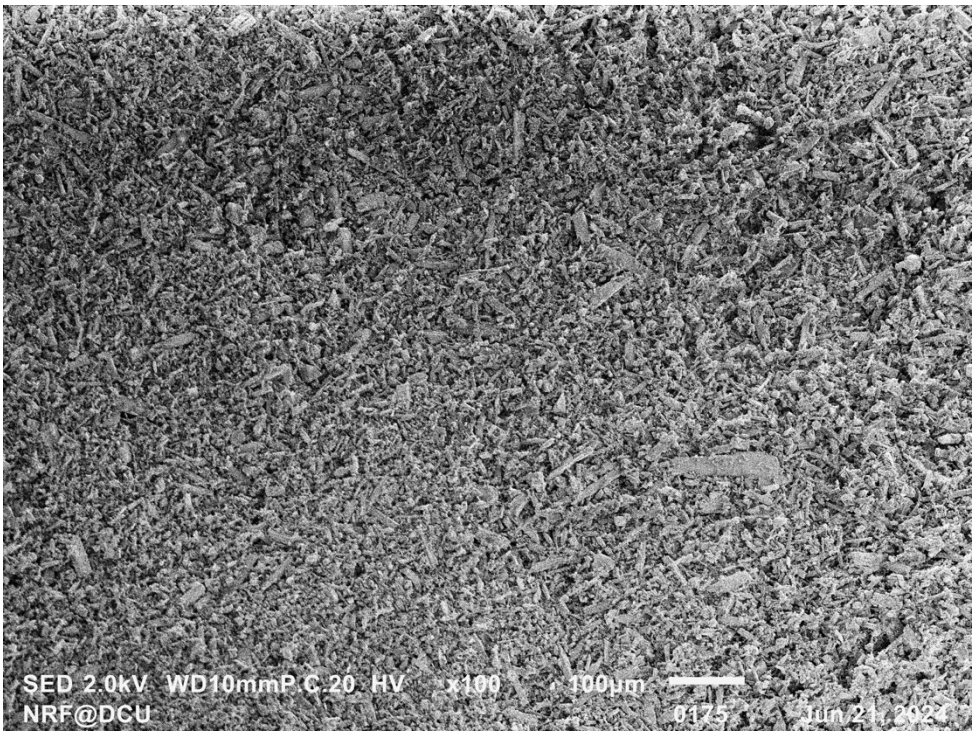

Figure 50, Morphology of spray-dried Wollastonite powder from trial 3 at 100 X

The as-received Wollastonite shown in **Figure 20** had irregular morphology. Like as-received Wollastonite, spray-dried Wollastonite powder from trials 1 and 3 had irregular

morphology. The spray drying technique did not improve the irregular shape observed in the as-received Wollastonite powder.

4.4.4 Morphology of Spray-Dried HA/Wollastonite Composite Powder

Figure 51 shows the SEM image of the spray-coated HA/Wollastonite powder obtained at the optimised process parameters: pump flow rate of 19 (scaled value), airflow rate of 30 (scaled value), and Wollastonite wt. fraction of 0.2 at 103 °C.

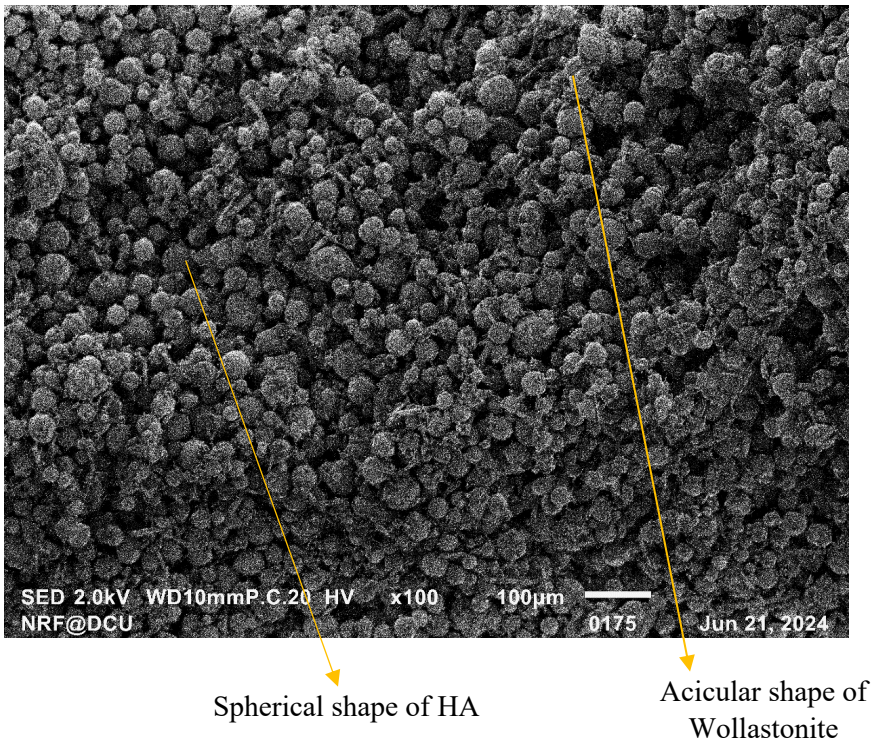

Figure 51, Morphology of spray-dried HA/Wollastonite (20 wt.% Wollastonite) with optimised parameters at 100X

Figure 51 shows the microstructure of the HA/Wollastonite powder at optimised process parameters. The structure mainly consisted of spherical HA powder due to its high quantity (80 wt.%) and some acicular Wollastonite powder (20 wt.%). HA and Wollastonite retained their respective morphology even after spray drying at optimised process parameters. The structure of HA/Wollastonite was not similar to the morphology of spray-dried HA/Wollastonite mentioned by Bastan et al. [211], where the Wollastonite particle was either inside the spherical HA particle or on the surface of the HA particle. The morphology obtained in the current study appeared distinct, and one could easily identify the spherical shape of HA or the acicular shape of Wollastonite.

4.4.5 Flowability of Spray-Dried Powders

The spray-dried Hydroxyapatite powder was also used for flowability assessment. The powders used for the assessment that were produced in trial 1 (pump flow: 15 (scaled value), airflow: 22 (scaled value) and temperature: 103 °C) and trial 2 (pump flow: 20 (scaled value), airflow: 22 (scaled value) and temperature: 103 °C), as these were the best powder results obtained from the spray drying experiment, which had the highest amount of 45-75 µm spherical powder for HA, as shown in **Table 24**. The powder flowability from trial 1 was 0.12 g/s, and the powder flowability at trial 2 was 0.19 g/s. The spray-dried powder was dried in an oven at 100 °C for 2 hours. As received, Hydroxyapatite powder has a spherical shape and was completely dry, making it flow easily. Trial 2 yielded the best value from the spray drying experiment, which signifies a spherical shape with a particle size range of 45-75 µm. Therefore, it had a higher powder flowability of 0.19 g/s. Moreover, as observed in **Figures 18**, **47** and **48**, as-received HA powder was more spherical in shape as compared to powder obtained from spray drying techniques. Therefore, the powder flowability relation of all the HA powders is given below:

As received Hydroxyapatite powder > Trial 2 Spray-dried Hydroxyapatite powder > Trial 1 spray-dried Hydroxyapatite powder.

The two best results yielded for Wollastonite powder in particle size range from 45-75 µm in spray drying experiments were obtained from trial 1 (pump flow: 15 (scaled value), airflow rate: 22 (scaled value) and temperature: 103°C) and trial 3 (pump flow: 15 (scaled value), airflow rate: 33 (scaled value) and temperature: 103 °C), as shown in **Table 24**. The results again had nil flowability similar to as-received powder, which clearly showed spray drying did not improve the flowability of the powder (in **Sections 4.3** and **4.4)**, which is confirmed by the morphology as observed in **Figures 20, 49** and **50**, respectively. **Table 26** summarises the flowability values of HA powder from trial 1, HA powder from trial 2, Wollastonite powder from trial 1 and Wollastonite powder from trial 3, respectively.

Table 26, Summary of flowability values of spray-dried Hydroxyapatite and Wollastonite powder

Powder type	Flowability values
Spray dried Hydroxyapatite powder at trial 1	0.12 g/s
Spray dried Hydroxyapatite powder at trial 2	0.19 g/s
Spray dried Wollastonite powder at trial 1	nil
Spray dried Wollastonite powder at trial 3	nil

4.4.6 Design of Experiment (DOE) for Hydroxyapatite (HA)

As shown in **Table 24**, spray-dried HA had the best results observed from trial 1 and trial 2. To optimise the results, the screening technique was used for the design of a spray-drying experiment. The design involved 3-factors and 2- levels (lower and higher). The three factors were the pump flow rate (A), compressed airflow rate (B) and inlet air temperature (C); out of the 5 factors that control the spray drying technique, which included compressor pressure, deblocker, airflow rate, pump flow rate and inlet temperature. The screening design narrowed down the three factors (pump flow rate, compressed airflow rate and inlet air temperature) that significantly affected the overall response (spray-dried Hydroxyapatite powder in a size range of 45-75 μm). Most of the spray-dried powder was obtained in the particle size range of 45-75 μm, as observed by the particle size normal distribution data in the safety data sheet of Hydroxyapatite [286]. The two levels in this experiment were pump flow rate (A): 15 (scaled value) and 20 (scaled value); air flow rate (scaled value): 22 (scaled value) and 33 (scale value) and inlet air temperature (C): 103 °C and 107 °C. **Table 27** shows ANOVA for Hydroxyapatite, and **Table 28** shows the fit statistics for Hydroxyapatite (HA).

a) Response 1: HA (percentage 45 to 75 µm)

Table 27, ANOVA table for Hydroxyapatite

Source	Sum of Squares	df	Mean Square	F-value	p-value	
Model	232.09	6	38.68	404.18	0.0381	significant
A-Pump Flow	26.74	1	26.74	279.37	0.0380	
B-Compressed Air Flow	75.80	1	75.80	792.02	0.0226	
C-Temp	85.31	1	85.31	891.45	0.0213	
AC	26.74	1	26.74	279.37	0.0380	
Residual	0.0957	1	0.0957			
Cor Total	232.19	7				

Factor coding is **Coded**.

The Sum of squares is **Type III – Partial**

It was a fractional factorial model because not all the factors and interactions between the factors affected the overall response of the model (spray-dried HA in the range of 45-75 µm). Therefore, some insignificant terms were deducted. In **Table 27,** the p-value of 0.05 (confidence level of 95%) was chosen. The p-value was 0.0381 (less than 0.05), means the model was significant to a 95% confidence level. The Model F-value of 404.18 implies the model is significant. There was only a 3.81 per cent chance that an F-value this large could occur due to noise. As shown in **Table 27**, pump flow (A), compressed air flow rate (B), inlet air temperature (C), and the interaction of pump flow and temperature (AC) were significant model terms. Model terms having a p-value greater than 0.05, such as the interaction of pump flow and compressed air flow (AB) and interaction of compressed air flow and inlet air temperature (BC), did not significantly improve the yield of the spray-dried powder (particle size range 45-75 µm) so were insignificant.

i. Fit Statistics

Table 28, Fit statistics data for Hydroxyapatite

Std. Dev.	0.3094	**R²**	0.9996
Mean	25.95	**Adjusted R²**	0.9971
C.V. %	1.19	**Predicted R²**	0.9736
		Adeq Precision	61.7702

Some of the terms mentioned in **Table 28** are mean, standard deviation and C.V.%. Mean is the sum of the observation divided by number of observations [321]. The standard deviation is the summary measure of the difference from the mean [321]. C.V.% is the percentage of standard deviation to mean (Std.Dev/Mean*100). R^2 determines the measure of goodness fit that means how well the regression line approximates the actual data [322]. When additional independent variables are added, then multiple regression of the dependent variables is calculated by Adjusted R^2 [322]. However, there might be error in R^2 and adjusted R^2 due to regressors, non-liner terms and outliers, which are removed by predicted R^2 [322]. By dividing the difference between the maximum predicted response and minimum predicted response by the average standard deviation of all the predicted responses, adequate precision, which measures the signal-to-noise ratio, was computed [323].

As shown in **Table 28**, the R^2 value determines the adequacy of the model using statistical measurement. Generally, R^2 values should be close to 1; however, using an R^2 value greater than 0.6 is generally acceptable. The R^2 value, in this case, was 0.996. The difference between the adjusted R^2 and predicted R^2 should be within 0.2, therefore the difference here between these two values for this model was 0.023. Adequate precision measures the signal-to-noise ratio, and a ratio greater than 4 is desirable. The adequate precision ratio of 61.770 indicates an adequate signal. This model can be used to navigate the design space. Therefore, observing the values of R^2, adjusted R^2, predicted $R^{2,}$ and adequate precision value, conclude that this was a satisfactory model and supported by **Figure 52**.

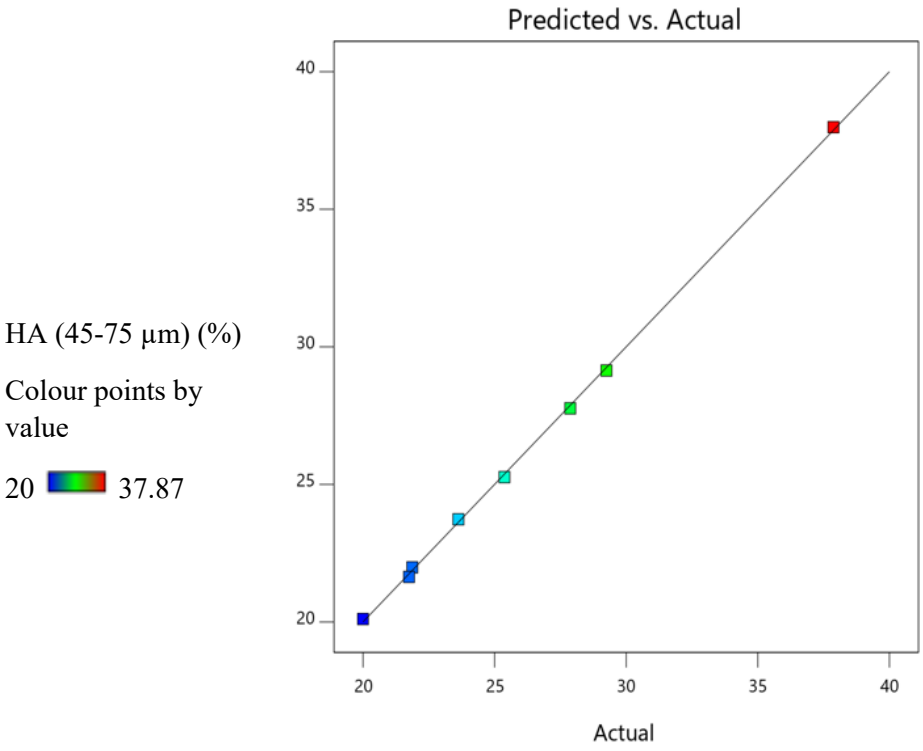

***Figure 52,* Predicted versus actual values for the response in Hydroxyapatite**

Figure 52 plots the actual values against the values predicted by the design model. The accuracy of the experiment can be predicted from this graph. It clearly indicates the good fit between the actual and predicted values, as all the experimental data points lie in a straight line.

ii. Final equation in terms of actual factors

HA(% 45 to 75 µm) =
-166.41406
+40.65313 Pump Flow
-11.66619 Compressed Air Flow
+1.60156 Temp
-0.365625 Pump Flow * Temp

……***Equation 16***

iii. Final equation in terms of coded factors

$$\begin{aligned} HA(\%\ 45 \text{ to } 75\ \mu m) = \\ &+25.95 \\ &+1.83\ A \\ &-3.08\ B \\ &-3.27\ C \\ &-1.83\ AC \end{aligned}$$

……*Equation 17*

The Design Expert software predicts equations in terms of actual and coded factors [323]. The coded factors are determined first, and the actual equation is determined from the coded equation [323]**.** The coefficient of the terms (in this case, A, B,C and AC), whether it is positive or negative can be used to compare against each other in terms of order of effect**. Equations 16 and 17** show the modelled (actual and coded) equations that can be used to achieve a yield of spray-dried Hydroxyapatite powder (in the range of 45-75 μm) when each factor was varied. The equation in terms of actual factors can be used to predict the response for given levels of each factor. Here, the levels should be specified in the original units for each factor. This equation should not be used to determine the relative impact of each factor because the coefficients are scaled to accommodate the units of each factor, and its intercept is not at the centre of the design space. It was during a fractional factorial design where non-significant terms were deducted from the final equation. As shown in **Equations 16 and 17,** inlet air temperature (C) was found to have the highest effect, followed by air flow rate (B), followed by pump flow rate (A), and then the interaction of the pump flow rate and inlet air temperature (AC) (equal). The order of the effect is shown below

Inlet air temperature (-C) (3.27) > Air flow rate (-B) (3.08) > Pump flowrate (+A) (1.83) = Interaction of the pump flow rate and inlet air temperature (-AC) (1.83)

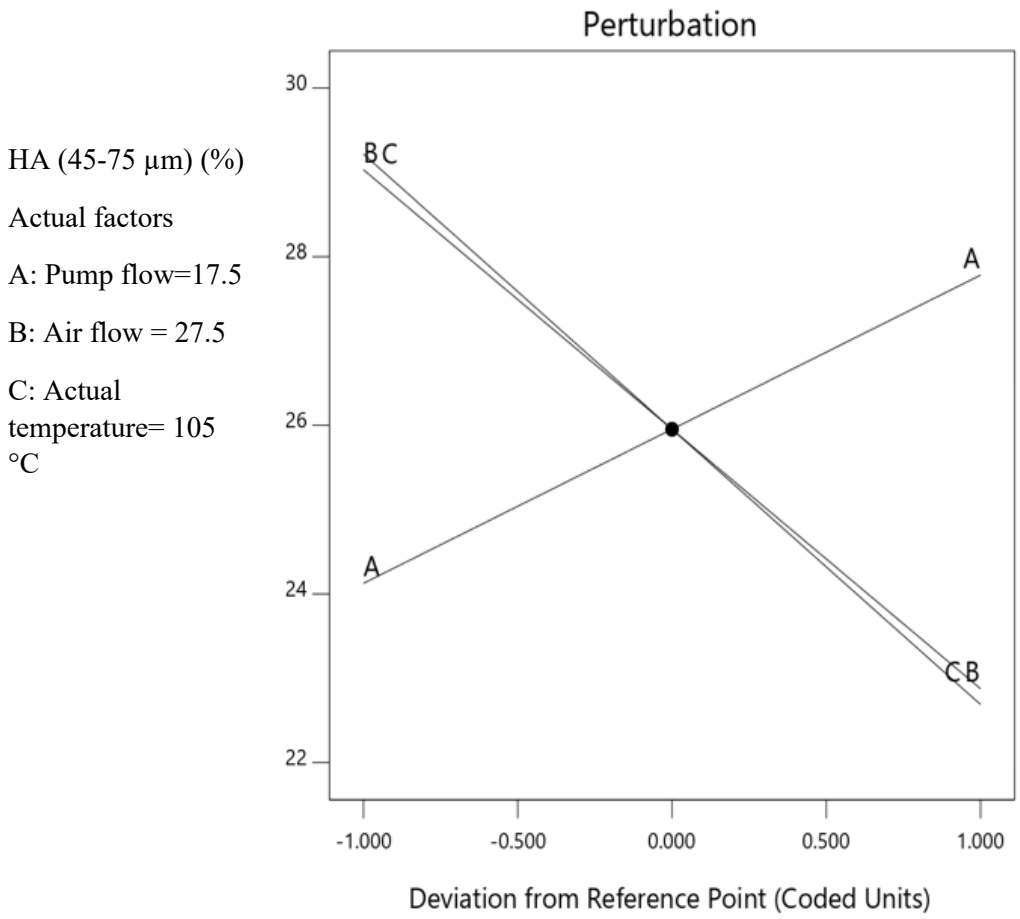

Figure 53, Perturbation graph of pump flow rate (A), airflow rate (B) and inlet air temperature (C) in Hydroxyapatite

The perturbation plot of Hydroxyapatite is shown above in **Figure 53**. This plot shows the effect of all three process parameters on response. This effect is shown by a reference point, which is the same in both cases. In this case, the reference point is taken as 0 at pump flow (A): 17.5 (scaled value), compressed air flow (B): 27.5 (scaled value) and inlet air temperature (C): 105 °C, whereas -1 is taken at pump flow (A): 15 (scaled value), compressed air flow (B): 22 (scaled value) and inlet air temperature (C): 103 °C and 1 represents pump flow (A): 20 (scaled value), compressed air flow (B): 33 (scaled value) and inlet air temperature (C): 107 °C. The slope in the perturbation curve determines the amount of effect of each process parameter on the overall product response. Pump flow rate (A) positively affected the overall response; the response value was 24% at coded factor -1 (minimum) and increased steadily to 28% at coded factor 1 (maximum). In contrast, the airflow rate (B) and inlet air temperature (C) had a negative effect on the overall product response. In airflow rate (B), the value of the response was approximately

29% at coded factor -1, which was reduced to approximately 23.5% at coded response 1. In inlet air temperature (C), the value of the response was approximately 29.5 % at the coded factor of -1 and reduced to approximately 23 % at the coded factor of 1. Overall, inlet air temperature (C) had a slightly more negative effect on the overall product response.

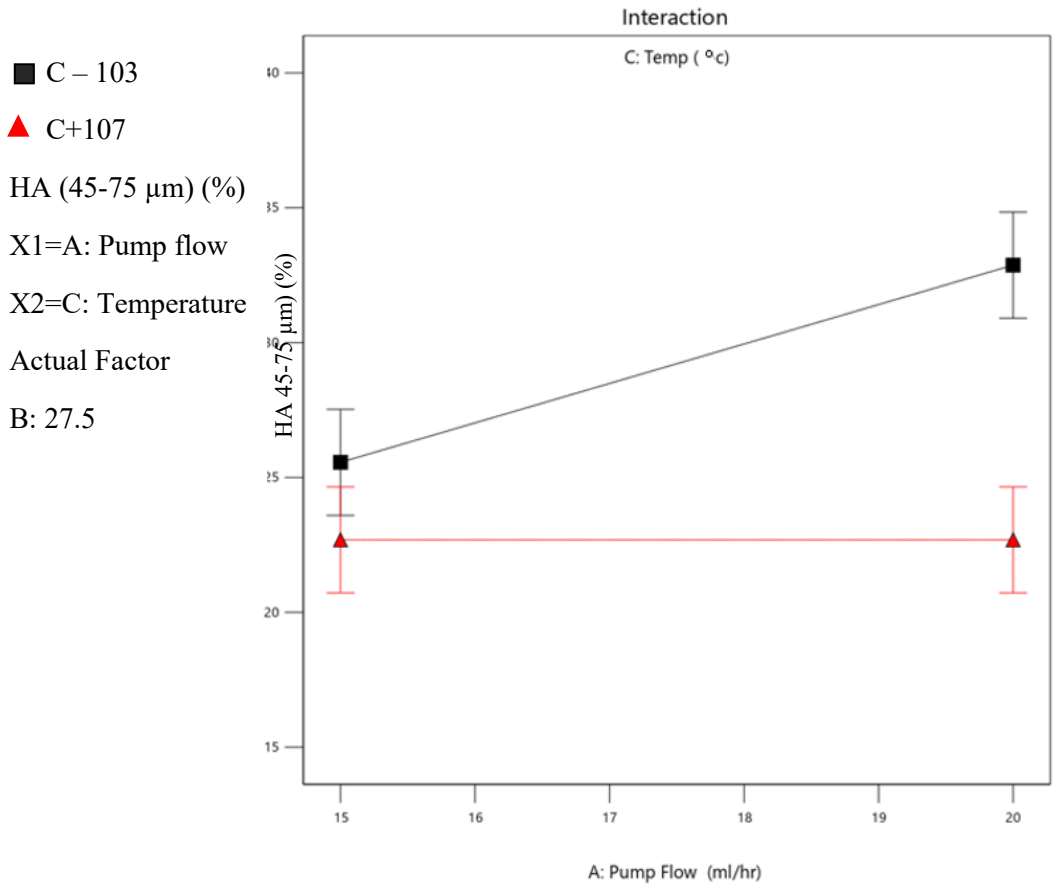

Figure 54, Interaction of pump flowrate and inlet temperature (AC) in Hydroxyapatite

There was a significant change in the difference in the response value at a particular factor, resulting in the interaction and intersection. For example, the response value was almost similar at a pump flow rate of 15 (scaled value) and different inlet temperatures (103 and 107 °C), which was 25% at an inlet temperature of 103 °C and 23.5% at 107 °C at constant pump flow of 15 (scaled value) with the difference in the total response of 1.5%. However, the response value reduced from 33% to 22% when the inlet temperature

changed from 103 °C to 107 °C at a constant pump flow of 20 (scaled value), resulting in a difference in response value of 11%.

Figure 54 shows the interaction of the pump flow rate (A) and temperature (C) at the constant airflow rate (B) of 27.5 (scaled value). This interaction (AC) was considered due to its significance on the overall yield of spray-dried HA powder. The airflow rate (B) increase negatively affects the overall response in all the sets of experiments; therefore, an average temperature of 27.5 (scaled value) was considered for the study. The temperature (C) varied around 103 °C, as shown by the black line, and around 107 °C, as shown by the red line. **Figure 54** clearly shows that the yield (45-75 µm Hydroxyapatite powder) can be maximised at a higher pump flow rate (A) and lower temperature (C) with a constant airflow rate of 27.5 (scaled value). In contrast, the lowest yield would be observed at the lower pump flow rate (A) and temperature (C). **Figure 54** above shows interaction with response value, which showed an increase from almost 25% at the interaction of pump flow: 15 (scaled value) and temperature: 103 °C (AC) to almost 33% at the interaction of pump flow: 20 (scaled value) and temperature: 103 °C (AC) (difference of 8% in the yield of spray-dried Hydroxyapatite powder). A slight decrease in the response value was observed from almost 23% at the interaction of pump flow: 15 (scaled value) and temperature: 107 °C (AC) to approximately 22% at the interaction of pump flow: 15 (scaled value) and temperature: 107 °C (AC) (1% difference in spray-dried Hydroxyapatite powder yield value). It was clear from the interaction graph above that the difference between the yield of the Hydroxyapatite (response value) was different at two levels of pump flow rate (A).

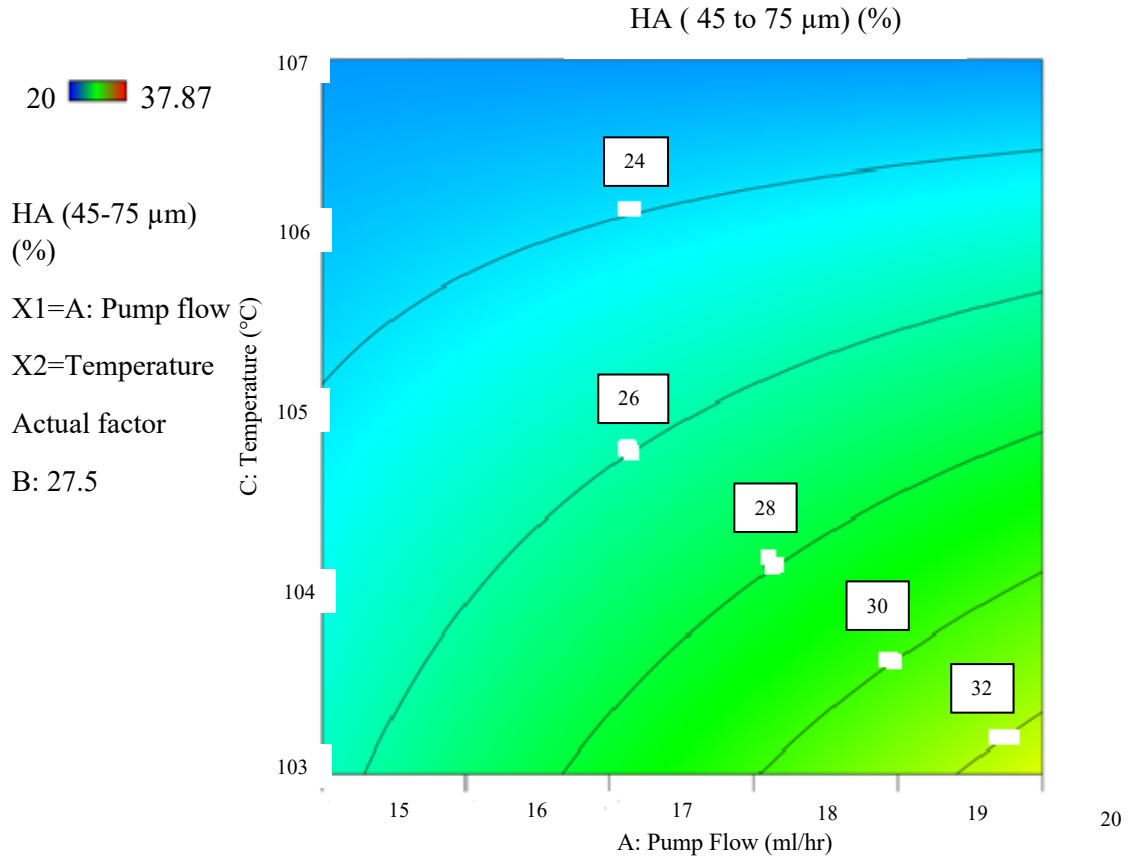

Figure 55, Effect of interaction of pump flowrate and temperature (AC) on the overall response in Hydroxyapatite

Figure 55 shows the effect of the interaction of pump flow rate and inlet temperature (AC) on the overall response. The interaction of pump flow rate and temperature (AC) had a negative effect, which can be observed from the coefficient of AC, as mentioned in **Equation 17** (-1.83); therefore, the graph has curvature. The figure above shows that the response value is depicted in the colour region. The blue region had the lowest response value, which was observed at a lower pump flow rate (A) and higher temperature (C). As the pump flow rate (A) increased and the temperature (B) decreased, the region became slightly yellow, showing the response value increase from 24% to 32%, shown at the top of the curve.

As one cannot verify the maximum response from **Figures 53-55**, as the maximum response value was only achieved at low inlet air temperature (C) and airflow rate (B), therefore **Figure 56** was required.

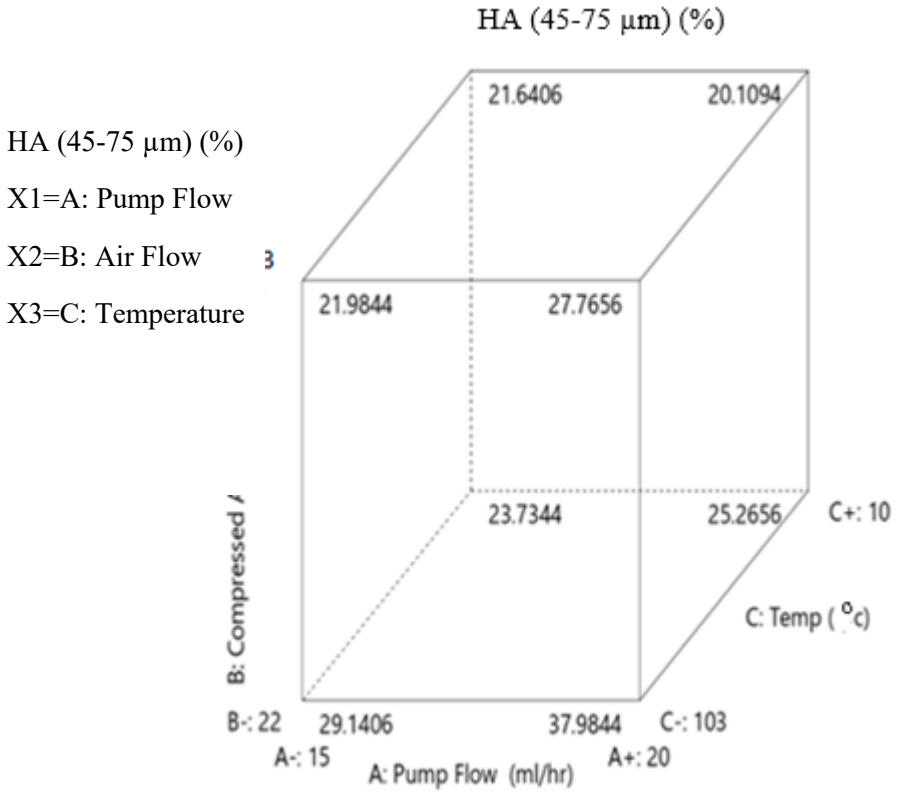

Figure 56, 3D cube of all the process parameters effect on overall response in Hydroxyapatite

Figure 56 shows the 3-D cube of the process parameters effect on the response. The process parameters, such as pump flow (A), airflow (B) and inlet temperature (C), were represented in the form of 3 axes: X1, X2 and X3, respectively. The corresponding response value was observed at a particular coordinate. For example, the product response value was 29.1 % at the X1=15 (scaled value), X2=22 (scaled value) and X3=103 °C, respectively. The highest response of value 37.98% (trial 2) was observed at X1=20 (scaled value), X2= 22 (scaled value) and X3= 103 °C, whereas the lowest response (trial 8) of value 20.1 % was observed at X1=20 (scaled value), X2= 33 (scaled value) and X3= 107 °C, respectively. The cube consisting of response values at different coordinates clearly indicated that higher pump flow rate (A), lower airflow rate (B) and lower inlet temperature (C) favoured higher response (yield of HA in the range of 45- 75 µm). As mentioned initially **(Table 24)**, the best results were observed at trial 2, with co-

ordinates X1= 20 (scaled value), X2= 22 (scaled value) and X3= 103 °C and the yield of 37.98% and second best results were observed at trial 1, with co-ordinates X1= 15 (scaled value), X2= 22 (scaled value) and X3= 103 °C and the yield of 29.14%.

4.4.7 Design of Experiment (DOE) for Wollastonite

a) Response 2: Wollastonite (percentage 45 to 75 µm)

Table 29, ANOVA Table for Wollastonite

Source	Sum of Squares	df	Mean Square	F-value	p-value	
Model	497.47	3	165.82	17.10	0.0096	significant
A-Pump Flow	181.33	1	181.33	18.69	0.0124	
B-Compressed Air Flow	70.14	1	70.14	7.23	0.0547	
C-Temp	246.00	1	246.00	25.36	0.0073	
Residual	38.80	4	9.70			
Cor Total	536.27	7				

Factor coding is **Coded**.
The Sum of squares is **Type III – Partial**

The sum of squares was partial, as mentioned above. The sum of squares calculated the total deviation of the whole model. The present study did not consider the complete as insignificant terms were eliminated, making it partial. **Table 29** shows the ANOVA for Wollastonite, where the p-value of 0.05 (confidence level of 95%) was chosen. The p-value of the model was 0.0096 (less than 0.05), which means the model was significant at a 95% confidence level, plus the model F-value of 17.10, implying the model was significant. There was only a 0.96 per cent chance that an F-value this large could occur due to noise. The p-values greater than 0.05 indicate the model terms were not significant. If there were many nominal model terms (not counting those required to support hierarchy), model reduction was required to improve the model. As shown in **Table 29**, pump flow (A) (p-value of 0.0124) and inlet air temperature (C) (p-value of 0.0073) were significant model terms. However, compressed air flow (B) (p-value of 0.0547) was not a significant model term but was required to support the hierarchy. No interaction was observed between the process parameters. As explained in **Figure 54**, interaction only occurred when there was a significant difference in response (in this case, spray-dried Wollastonite in the range of 45-75 µm) between the two levels of a particular factor

(either pump flow (A), air flowrate (B) and inlet temperature (C)). Either there was no difference, or it was not significant enough to be called an interaction. The response trend would be parallel to each other at two levels.

Table 30, Fit statistics for Wollastonite

Std. Dev.	3.11	**R²**	0.9277
Mean	27.52	**Adjusted R²**	0.8734
C.V. %	11.32	**Predicted R²**	0.7106
		Adeq Precision	12.0489

As shown in **Table 30**, the adequacy of the model is determined by the R^2 value. The R^2 value, in this case, was 0.928, therefore close to 1, so deemed adequate. The difference between the adjusted R^2 and predicted $R^{2,}$ in this case, was 0.163, which was within 0.2. An adequate precision ratio was greater than 4, at 12.04 for this model, thus desirable. Therefore, this model can be used to navigate the design space. Observing values of R^2, adjusted R^2, predicted R^2 and adequate precision value, it can be concluded that a satisfactory model was developed, proved by **Figure 57**.

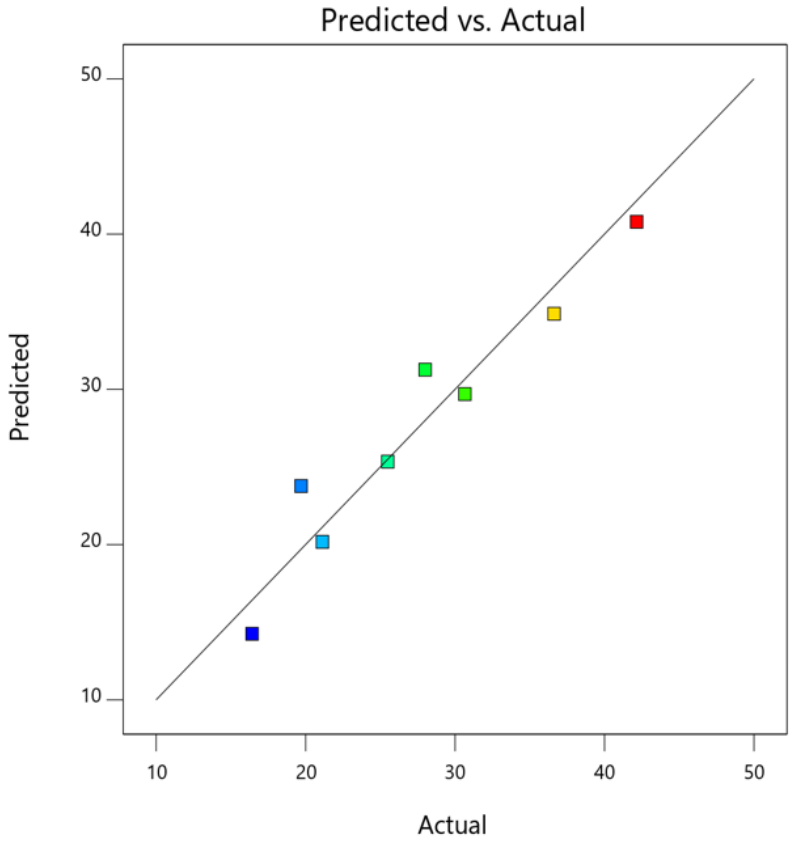

Figure 57, Predicted versus actual response for Wollastonite.

Figure 57 shows the predicted versus actual response in the case of the Wollastonite. In this graph, there was a comparison between the values obtained from the experiment and the values predicted by the model. The above graph confirmed a good fit because the data points obtained from the experiment follow the line predicted by the model.

b) <u>Final Equation in terms of actual factors</u>

Wollastonite (percentage 45 to 75 µm) =

+337.17422

-1.90438 Pump Flow

+0.538352 Compressed Air Flow

-2.77266 Temp

……..

Equation 18

c) *Final equation in terms of coded factors*

Wollastonite (% 45 to 75 μm) =
+27.52
-4.76 A
+2.96 B
-5.55 C

……..

Equation 19

Equation 18 shows the particle size of Wollastonite (in the range of 45-75 μm) in terms of actual factors, and **Equation 19** shows the response in terms of coded factors. The equation in terms of actual factors can be used to predict the response for given levels of each element, using original units for each factor. This equation should not be used to determine the relative impact of each factor because the coefficients are scaled to accommodate the units of each factor, and the intercept is not at the centre of the design space. As shown in **Equation 19**, inlet air temperature (C) had the highest negative effect, shown by the coefficient (5.55), followed by pump flow (A) with a negative effect, shown by the coefficient (4.76) and followed by the compressed airflow rate, with a positive effect, shown by the coefficient (2.96) (B). No interactions between the factors were observed to obtain the response (45-75 μm) in the case of Wollastonite. The effect of each response is shown below

Inlet air temperature (-C) (5.55) > pump flow (-A) (4.76) > compressed airflow rate (B) (2.96)

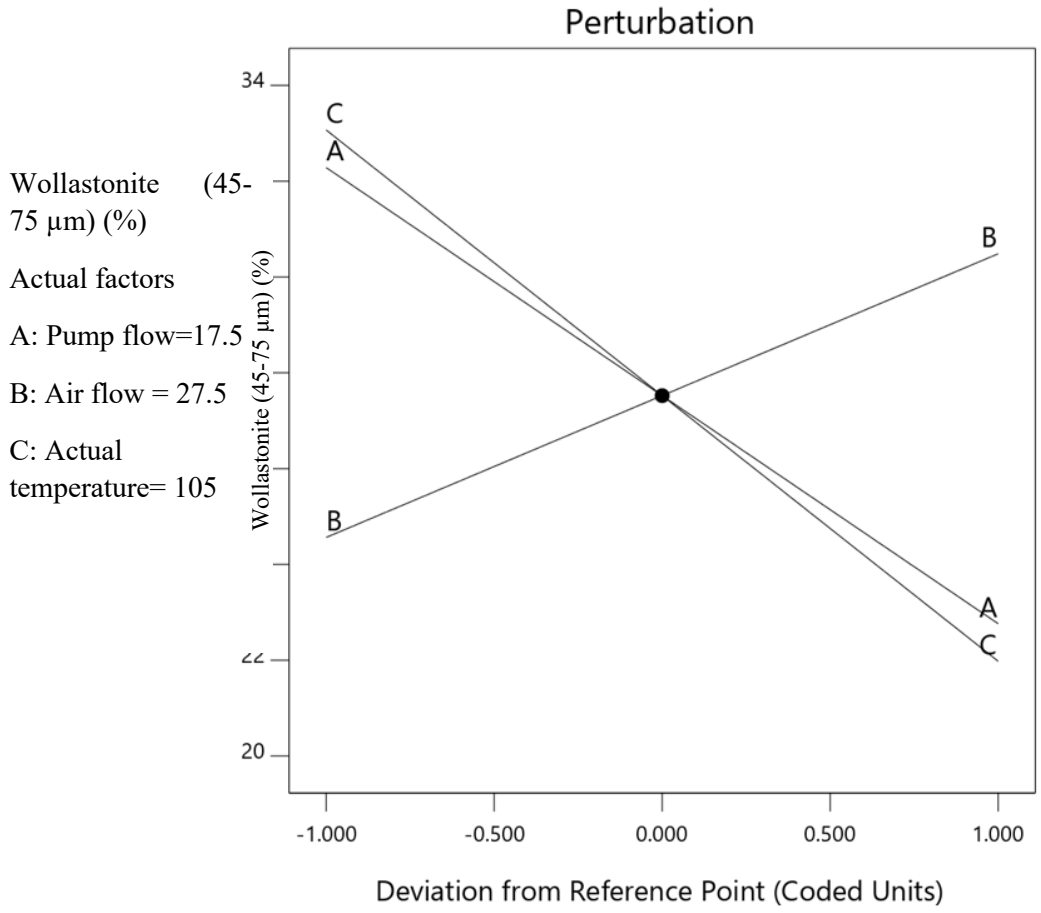

Figure 58, Perturbation graph of pump flowrate (A), air flowrate (B) and inlet temperature (C) in Wollastonite.

The perturbation graph of the actual response in Wollastonite was shown in **Figure 58**. The process parameters and their corresponding coded factors were explained in **Section 3.6.9**. The figure shows that airflow rate (B) positively affected the overall response. The response value was 24% at the airflow rate (B): 22 (scaled value) (coded factor = -1) (minimum) and increased to approximately 30% at the airflow rate (B): 33 (scaled value) (coded factor = 1) (maximum). Both pump flow rate (A) and inlet air temperature (C) negatively affected the overall response. The response value was 32% at the pump flow rate (A): 15 (scaled value) (coded factor = -1) and decreased to approximately 23% at the pump flow rate (A): 20 (scaled value) (coded factor = 1). Similarly, the response value was 33% at the inlet air temperature (C): 103 °C (coded factor = -1) and reduced to approximately 22% at the inlet air temperature (C): 107 °C (coded factor = 1). Overall, inlet air temperature (C) negatively affected the overall response more than the pump flow rate (A). However, airflow rate (B) positively affected the overall response with an

increase from 24.5% at an airflow rate of 22 (scaled value) (coded factor = -1) to 30.5% at an airflow rate of 33 (scaled value) (coded factor =1). To identify the actual minimum and maximum response value, a 3-dimensional cube was needed, which was shown in **Figure 59.**

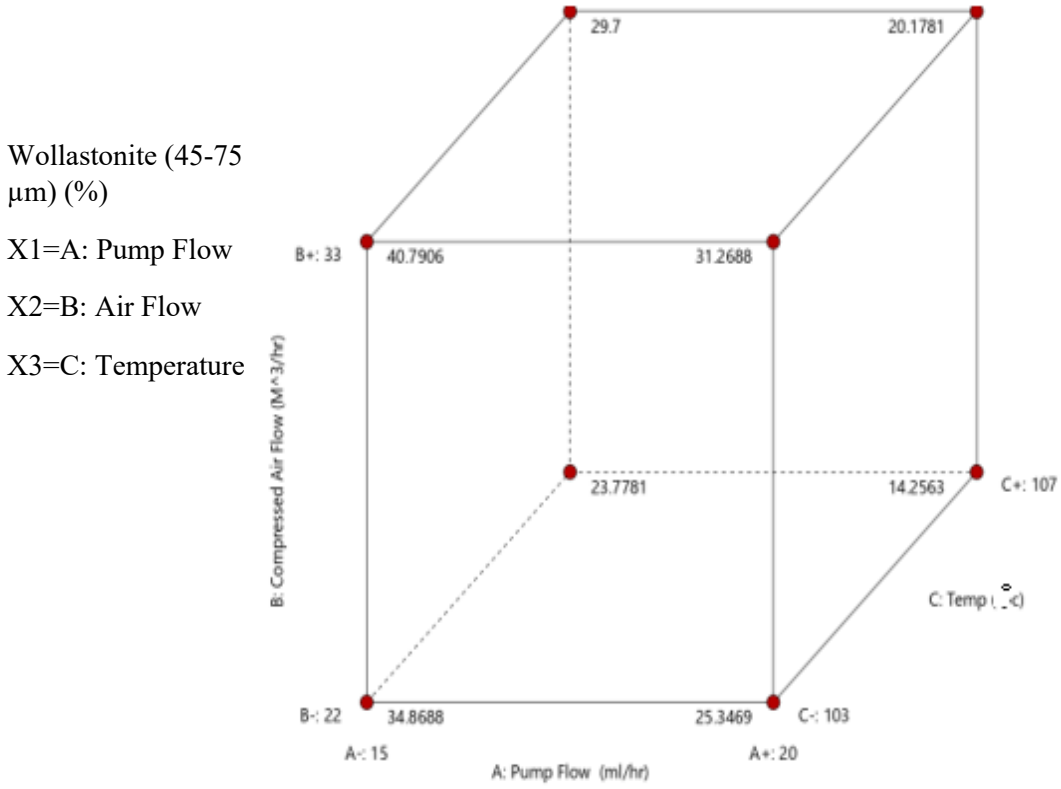

Figure 59, 3D cube of the process parameters effect on the overall response in Wollastonite

Figure 59 shows the response value corresponding to each coordinate in Wollastonite. The highest response (40.79 %) was observed at X1=15 (scaled value), X2= 33 (scaled value) and X3= 103 °C, whereas the lowest response value (14.26%) was observed at X1= 20 (scaled value), X2= 22 (scaled value) and X3= 107 °C. The graph clearly showed that lower pump flow rate (A), higher airflow rate (B) and lower inlet temperature (C) favoured higher response in spray-dried Wollastonite powder. The best results **(Table 24)** were observed at trial 3 (X1= 15 (scaled value), X2=33 (scaled value) and X3= 103 °C) and trial 1 (X1= 15 (scaled value), X2= 22 (scaled value) and X3= 103 °C), which yield values of 40.79% and 34.87%, respectively, as stated in **Section 4.4.3**.

4.4.8 Design of Experiment for HA/Wollastonite Powder

a) *ANOVA table for HA/Wollastonite powder mixture (percentage 45 to 75 µm)*

Table 31, ANOVA table for HA/Wollastonite powder

Source	Sum of Squares	df	Mean Square	F-value	p-value	
Model	314.30	8	39.29	26.18	< 0.0001	significant
A-Pump flow	62.89	1	62.89	41.90	0.0002	
B-Air flow	66.01	1	66.01	43.98	0.0002	
C-Wollastonite wt. fraction	134.40	1	134.40	89.55	< 0.0001	
AC	10.82	1	10.82	7.21	0.0277	
BC	8.61	1	8.61	5.74	0.0435	
A^2	5.89	1	5.89	3.92	0.0830	
B^2	11.19	1	11.19	7.45	0.0258	
C^2	15.97	1	15.97	10.64	0.0115	
Residual	12.01	8	1.50			
Lack of Fit	6.51	4	1.63	1.19	0.4366	not significant
Pure Error	5.50	4	1.37			
Cor Total	326.31	16				

Factor coding is **Coded**.
Sum of squares is **Type III - Partial**

Table 31 shows the ANOVA for HA/Wollastonite powder. The model obtained in the spray coating of HA/Wollastonite was quadratic, unlike the model obtained from the spray drying of HA and Wollastonite, which was linear. The sum of squares for the above model was partial, which means that not all the factors and their corresponding interaction did not significantly affect the overall response and were deducted. The model F-value was 26.18, implying that the model was significant. The p-value chosen for the model was 0.1 (which is generally 0.05), which implies any p-value above 0.1 was insignificant. This p-value of 0.1 was chosen to accommodate maximum factors and their interaction. The p-value of the model was less than 0.0001, which means that the model is significant. The p-values of pump flow (A) was 0.0002, airflow rate (B) was 0.0002, Wollastonite wt.fraction (C) was less than 0.0001, the interaction between pump flow and Wollastonite

wt.fraction (AC) was 0.028, the interaction between airflow rate and Wollastonite wt.fraction (BC) was 0.043, the square of pump flow (A^2) was 0.083, the square of airflow rate (B^2) was 0.026 and the square of Wollastonite wt.fraction (C^2) was 0.011. The F-value of the lack of fit was 1.19, meaning there was a 43.66 % chance that an F-value this large would occur due to noise. In this model, pump flow rate (A), airflow rate (B), Wollastonite wt. fraction (C), the interaction between pump flow and Wollastonite wt.fraction (AC), the interaction between airflow rate and Wollastonite wt.fraction (BC), the square of pump flow (A^2), the square of airflow rate (B^2) and the square of Wollastonite wt.fraction (C^2) were significant model terms.

i. Fit statistics for HA/Wollastonite powder mixture

Table 32 Fit statistics for HA/Wollastonite powder

R^2	0.9632
Adjusted R^2	0.9264
Predicted R^2	0.8010
Adeq Precision	19.9700

The adequacy of the model was determined by R^2, adjusted R^2, predicted R^2 and adequate precision. The R^2 value for this model was 0.9632. The R^2 value was very close to 1, although a value greater than 0.6 is generally acceptable. The difference between the adjusted R^2 and predicted R^2 should be within 0.2, which it was at 0.125, implying that the model was desirable. The adequate precision value was 19.97, (want greater than 4), implying that the model was suitable to navigate the design space. The fit statistics for HA/Wollastonite powder are shown in **Table 32**. Observing the values of R^2, adjusted R^2, predicted R^2, and adequate precision, it can be observed that a satisfactory model has been developed, as observed in **Figure 60**.

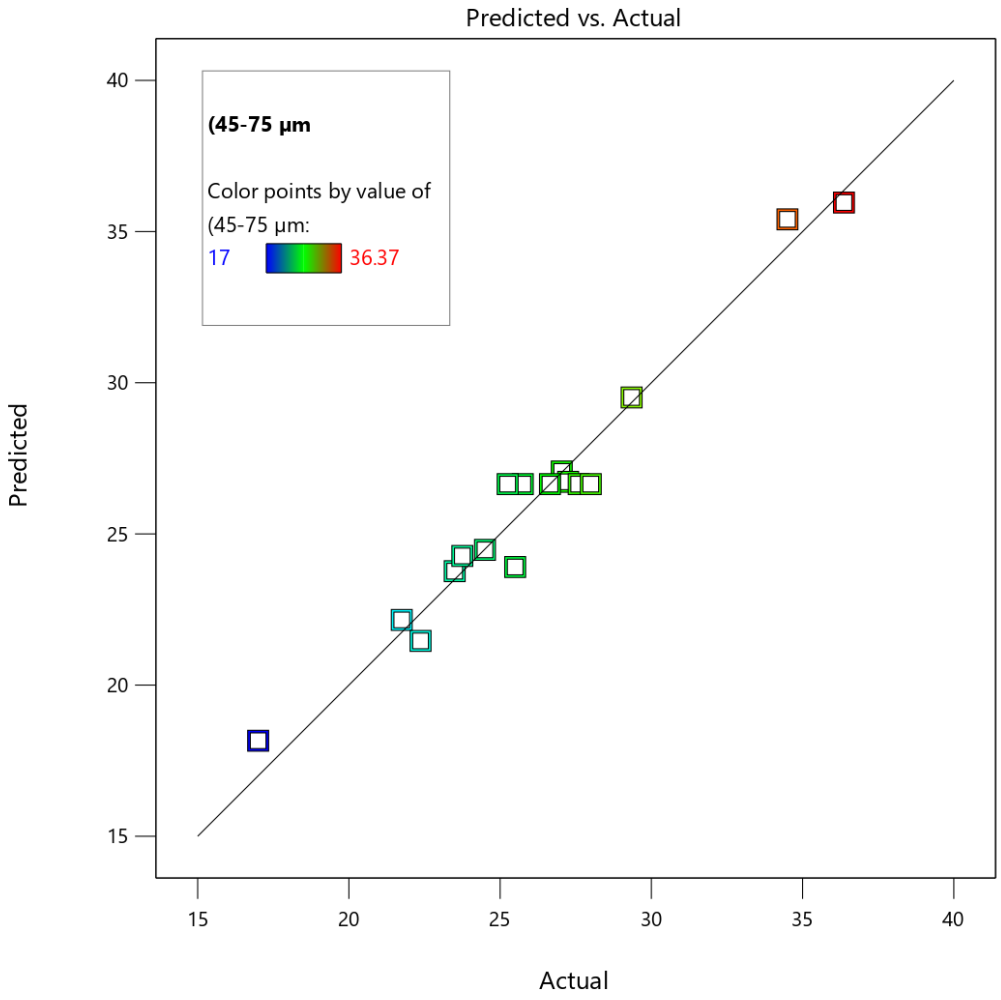

Figure 60, Predicted v/s actual for the response in HA/Wollastonite

Figure 60 shows the predicted versus actual values for HA/Wollastonite composite powder. Most of the actual data points corresponding to the response, lie on or near the predicted line of the response trend, indicating a good fit.

ii. Final equation in terms of actual factors

Response (45-75 μm) =

-61.00278	
+6.20817	Pump flow
+2.86333	Air flow
-158.94722	Wollastonite
+4.38667	Pump flow * Wollastonite
+1.77879	Air flow * Wollastonite
-0.189200	Pump flow ^{2}
-0.053884	Air flow^2
+86.55556	Wollastonite ^{2}

……***Equation 20***

Equation 20 shows the modelled equation of actual factors that can be used to achieve a yield of spray-dried Hydroxyapatite/Wollastonite powder in the range of 45-75 μm, when each factor is varied. Here, the levels should be specified in the original units for each factor. This equation should not be used to determine the relative impact of each factor because the coefficients are scaled to accommodate the units of each factor, and as its intercept is not at the centre of the design space.

iii. Final equation in terms of coded factors

Response (45-75 μm) =

+26.65
+2.80 A
+2.87 B
+4.10 C
+1.64 AC
+1.47 BC
-1.18 A^2
-1.63 B^2
+1.95 C^2

……***Equation 21***

Equation 21 shows the equation in terms of coded factors. This equation can be used to make prediction about the response at a given level at each factor. This equation identifies the relative impact of the factors by comparing the factor coefficients. As shown in

Equation 21, Wollastonite wt. % (C) had the highest positive effect on the overall response, followed by airflow rate (B), pump flow rate (A), square of Wollastonite wt.fraction (C^2), interaction of pump flow rate and Wollastonite wt.fraction (AC) and then by interaction of airflow rate and Wollastonite wt.fraction (BC). The equation also showed a negative effect of the square of airflow rate (B^2) followed by a negative of the square of pump flow rate (A^2). The effect is shown in the relationship below:

$$+C\ (4.10) > +B\ (2.87) > +A\ (2.80) > +C^2\ (1.95) > AC\ (1.64) > -B^2\ (1.63) > BC\ (1.47) > -A^2\ (1.18)$$

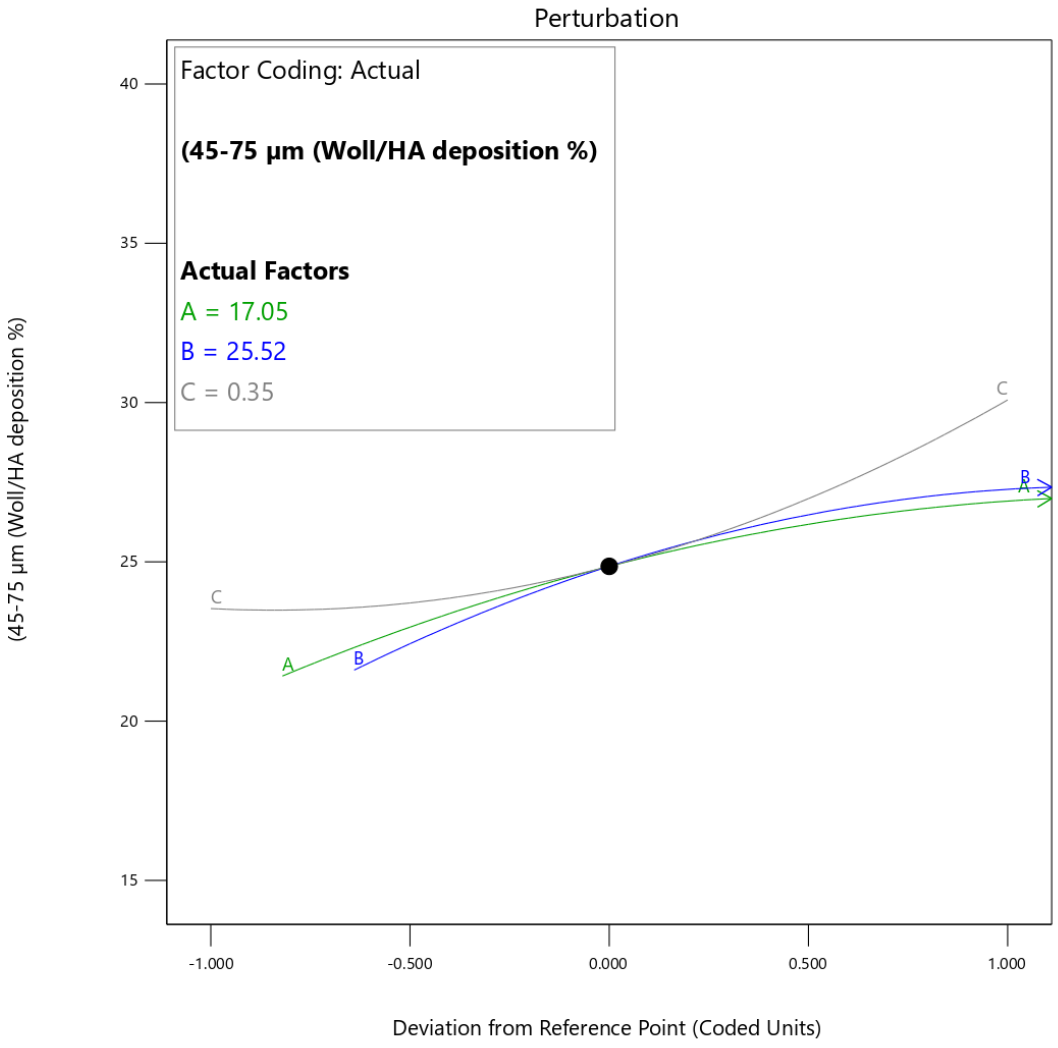

Figure 61, Perturbation graph of pump flow rate (A), airflow rate (B) and Wollastonite wt. fraction (C) in HA/Wollastonite powder

Figure 61 shows the perturbation graph of HA/Wollastonite powder, where the slope can predict the effect of each factor on the overall response. The graph had a curvature as the equation was quadratic. As shown in **Figure 61**, the pump flow rate was (A), the airflow rate was (B), and the Wollastonite wt.fraction was (C), which positively affected the overall response; the response value of pump flow rate (A) was 22.5% at coded factor -1 (minimum) and increased steadily to 27% at coded factor 1 (maximum). In airflow rate (B), the value of the response was approximately 22% at coded factor -1, and increased to approximately 24.5% at coded response +1. In Wollastonite wt.% (C), the value of the response was approximately 24 % at the coded factor of -1 and increased to approximately 30 % at the coded factor of +1. To identify the highest and lowest response values, a 3-D cube with all the factors and their corresponding response value was given in **Figure 66**.

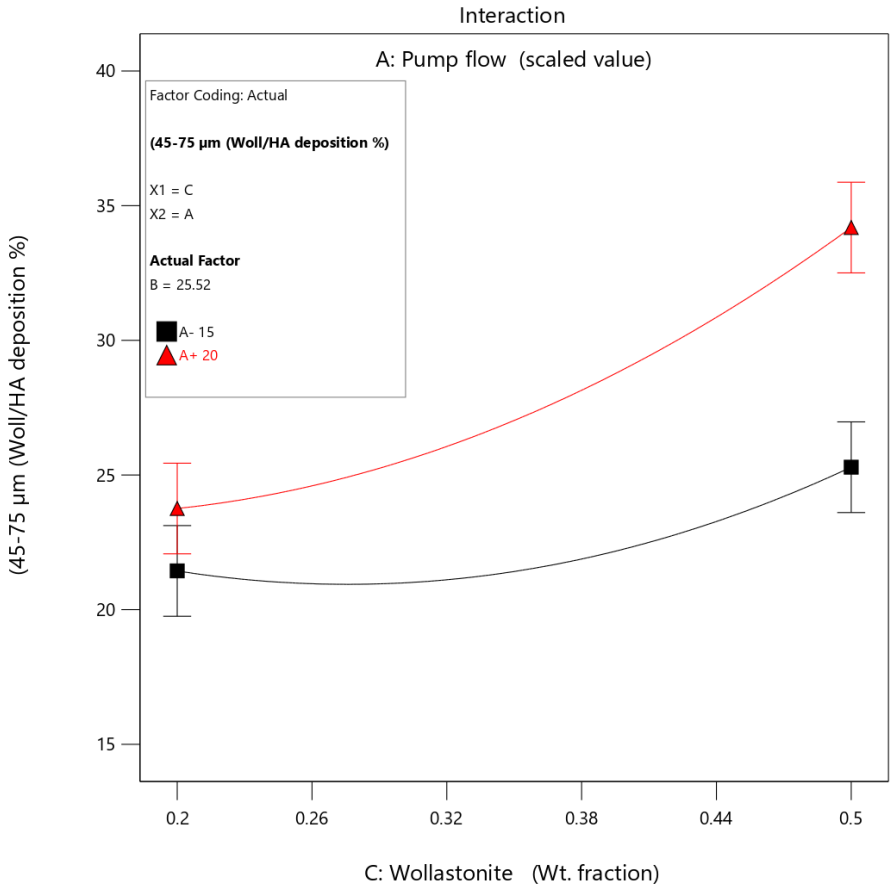

Figure 62, Interaction of Wollastonite wt.fraction and Pump flow rate (AC) in HA/Wollastonite powder

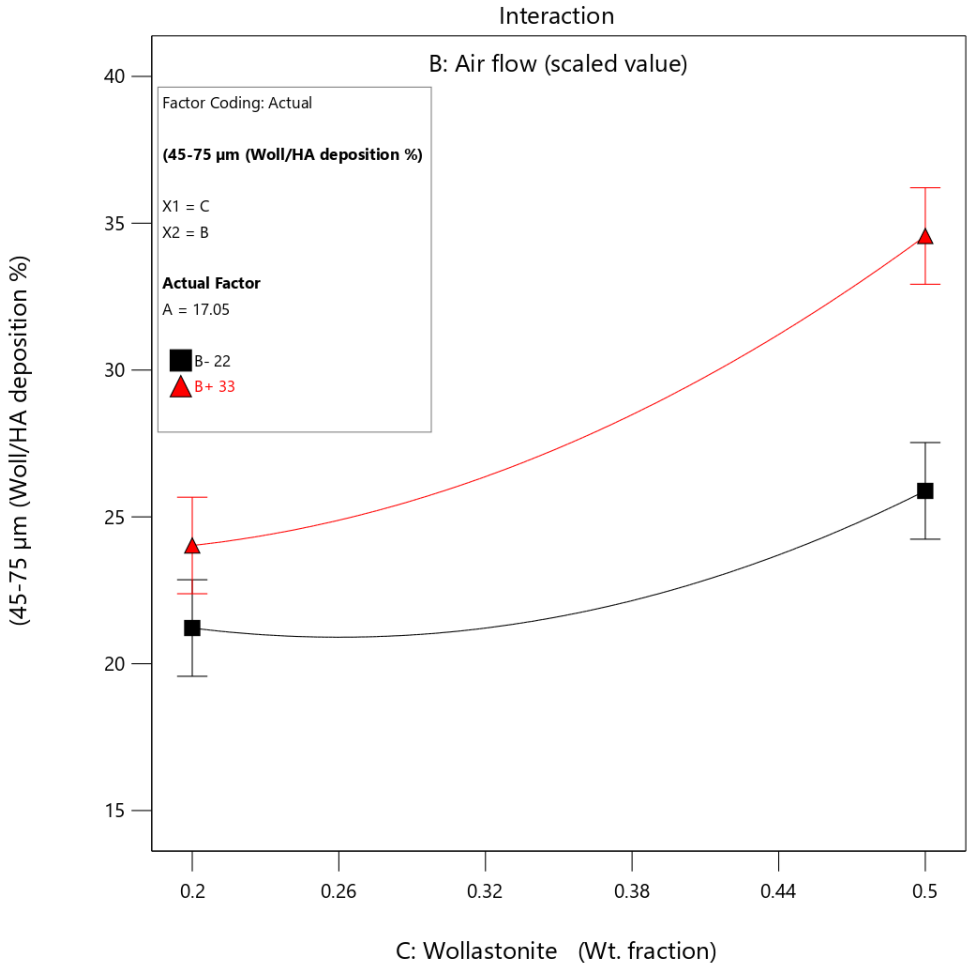

Figure 63, Interaction of Wollastonite wt.fraction and airflow rate (BC) in Hydroxyapatite/Wollastonite powder

Figure 62 shows the interaction of Wollastonite wt.fraction and pump flow rate (AC) in the Hydroxyapatite/Wollastonite powder at a constant airflow rate (B) of 25.52 (scaled value). It was observed that the response value increased from 24% at Wollastonite wt.fraction (C) of 0.2 to approximately 34% at Wollastonite wt.fraction (C) of 0.5 at a constant pump flow rate (A) of 20 (scaled value), and the response value increased from 21% at Wollastonite wt. fraction (C) of 0.2 to approximately 23% at Wollastonite wt.fraction (C) of 0.5 at a constant pump flow rate (A) of 15 (scaled value). The difference between the response at constant airflow rate (B) and pump flow rate (A) of 20 (scaled value) with varying Wollastonite wt. was 10%, whereas the difference between the response at constant airflow rate (B) and pump flow rate (A) of 15 (scaled value) with varying Wollastonite wt. was 2%, and could be observed from the **Figure 62**, there was an intersection of response at one factor and significant difference at other. **Figure 63**

shows the interaction of airflow rate and Wollastonite wt.fraction (BC) at a constant pump flowrate of 17.05 (scaled value). The response value increased from 22% at Wollastonite wt.fraction (C) of 0.2 to 24% at Wollastonite wt.fraction (C) of 0.5 at the airflow rate (B) of 22 (scaled value), whereas the response value increased from 23% at Wollastonite wt.fraction (C) of 0.2 to 34% at Wollastonite wt.fraction (C) of 0.5 at the airflow rate (B) of 33 (scaled value). The difference between the response at constant pump flowrate (A) and airflow rate (B) of 22 (scaled value) with varying Wollastonite wt. was 2%, whereas the difference between the response at constant pump flowrate (A) and airflow rate (B) of 33 (scaled value) with varying Wollastonite wt. was 11%, and could be observed from the **Figure 63**, there was an intersection of response at one factor and significant difference at other.

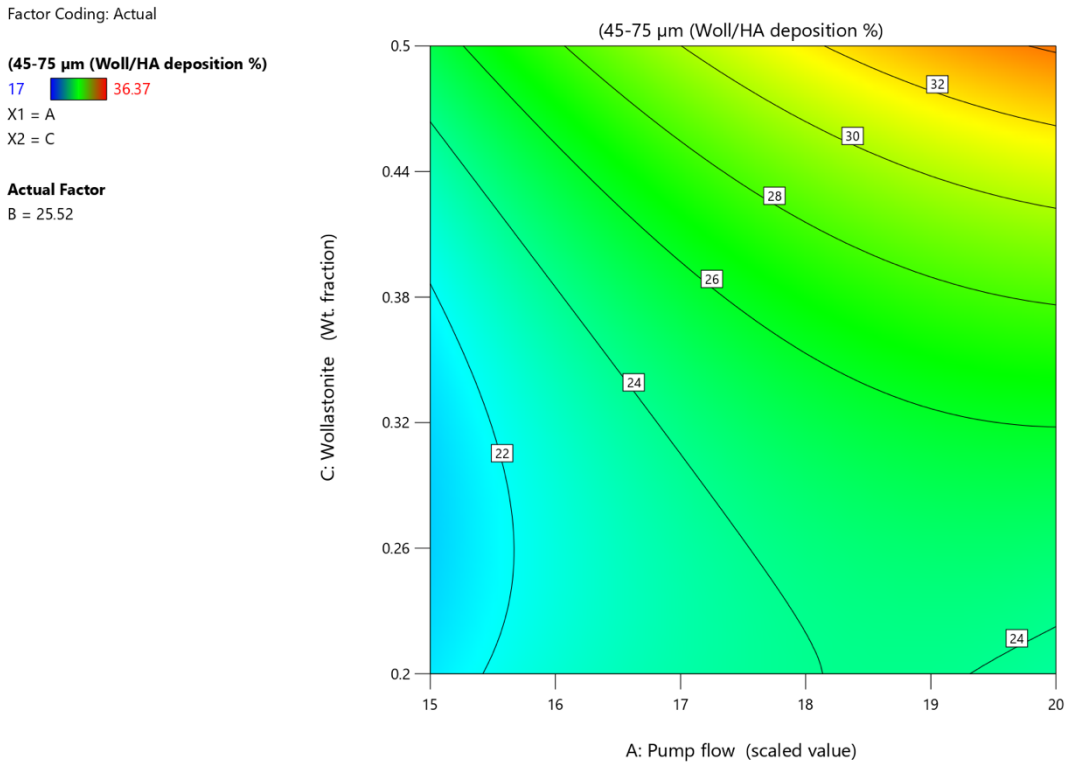

Figure 64, Effect of interaction of pump flow rate and Wollastonite wt.fraction (AC) on the overall response in HA/Wollastonite

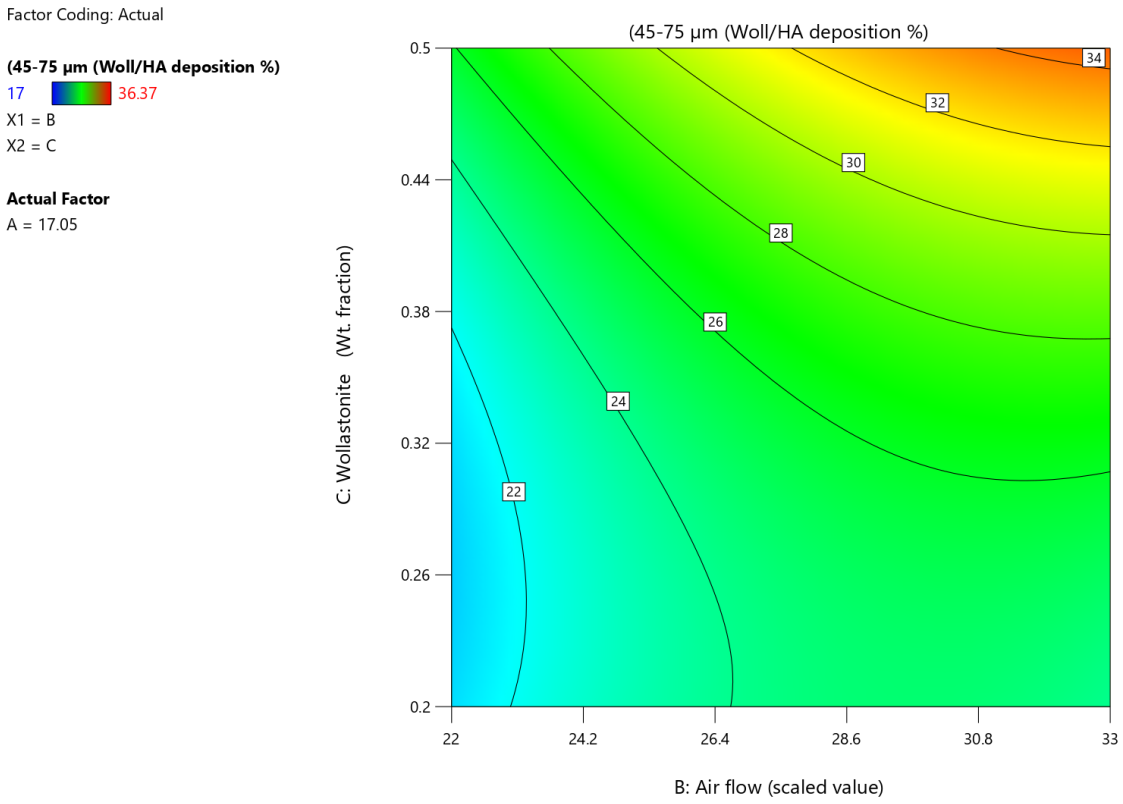

Figure 65, ***Effect of interaction of airflow rate and Wollastonite wt.fraction (BC) on the overall response in HA/Wollastonite***

Figure 64 shows the effect of the interaction of pump flow rate and Wollastonite wt. fraction (AC) on the overall response. The airflow rate (B) was kept constant at 25.52 (scaled value) to observe all the regions (lower response and higher response regions). Both pump flow rate and Wollastonite wt.fraction had a positive effect on the overall response. The response value increased from 22% to 32% with a corresponding increase in pump flowrate (15-20 (scaled value)) and Wollastonite wt.fraction (0.2-0.5). There was a small region of 24% response in the pump flow (19 (scaled value)) and Wollastonite wt.fraction (0.2). **Figure 65** shows the effect of interaction of airflow rate and Wollastonite wt.fraction (BC) on the overall response. Since both the airflow rate (B) and Wollastonite wt.fraction (C) had a positive effect on the overall response; the response value increased from 22% to 34% with the increase in airflow rate (B) from 22 (scaled value) to 33 (scaled value) and an increase in the Wollastonite wt.fraction (C) from 0.2 to 0.5.

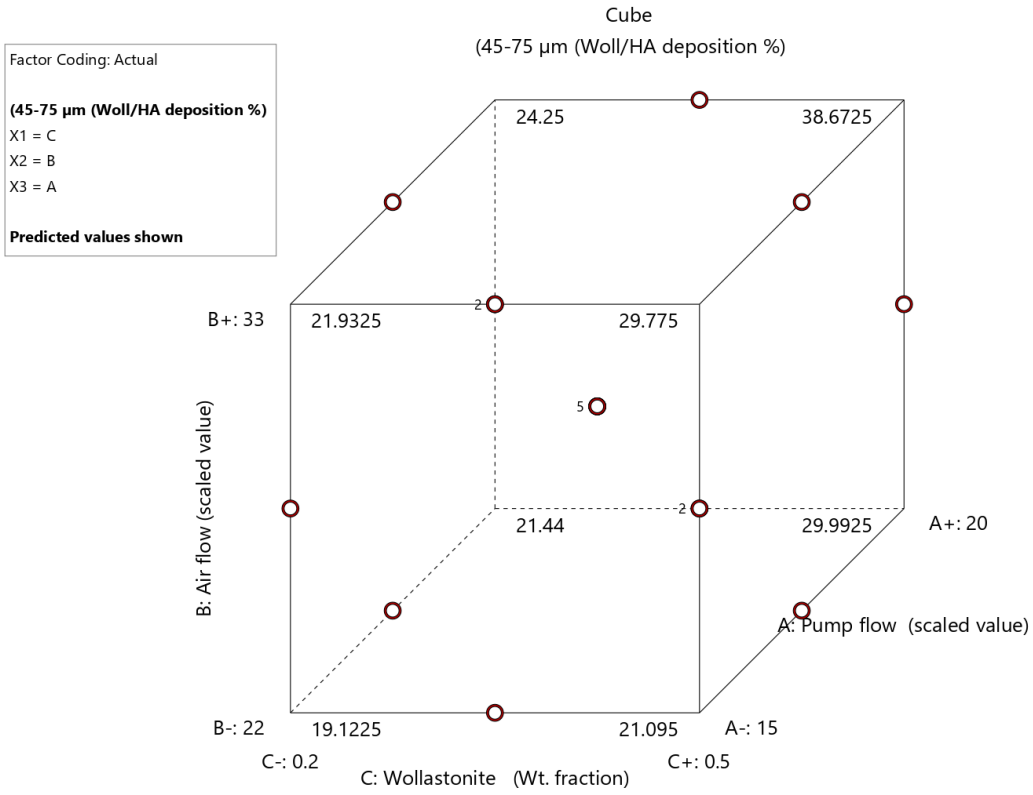

Figure 66, 3D cube of all the process parameters effect on overall response in HA/Wollastonite

Figure 66 shows the response value corresponding to each co-ordinate in HA/Wollastonite. In this figure, X1 was designated as Wollastonite wt.fraction (C), X2 was designated as airflow rate (B) and X3 was designated as pump flowrate (A). The highest response (38.67 %) was observed at X1= 0.5 (50 wt.% Wollastonite), X2= 33 (scaled value) and X3= 22 (scaled value), whereas the lowest response value (19.12%) was observed at X1= 0.2 (20 wt.% Wollastonite), X2= 22 (scaled value) and X3= 15 (scaled value). The 3D cube clearly showed that higher pump flowrate (A), higher airflow rate (B) and higher Wollastonite wt.fraction (C) favoured higher response in spray-dried Wollastonite powder.

b) *DOE optimisation of the spray-dried HA/Wollastonite powder*

For this optimisation, the pump flow rate and air flow rate were kept within the range. Wollastonite wt.fraction was kept at a maximum value of 0.2 (20 wt.% Wollastonite) and response was optimised to yield a maximum value of % of powder attained between a

powder size range of 45-75 µm. The modelled values obtained from software at 103 °C are given in **Table 33,** which shows the optimisation results from the software.

Table 33, DOE optimisation results obtained from software

Number	Pump flow	Airflow	Wollastonite	Response (45-75 µm) (%)	Desirability
1	18.70	29.90	0.20	25.10	0.60

The HA/Wollastonite composite was spray-dried using the process parameters mentioned in **Table 25**. The response value predicted by the software was 25.1% with desirability (score assigned to obtain maximum response with the set of process parameters), but experimentally the response of 22.25% was achieved. There was a percentage error of 11.35%. The reason for the error was due to incomplete HA/Wollastonite slurry transported via a peristaltic pump reaching the nozzle; some stuck inside the peristaltic pump. Moreover, even after atomising and drying the spray-dried powder, some of the powder got deposited in the connection of the cyclone and powder collection tube. Also, the spray drying equipment could not display fractions (18.7 and 29.9 (scaled value)) in this case. The equipment either displayed a pump flow value of 18 or 19 (scaled value) or an airflow value of 29 or 30 (scaled value), contributing to the error of 11.35%. The values selected for the current study for pump flow rate was 19 (scaled value) and air flow rate was 30 (scaled value). The overlay plot which shows the optimisation region is shown in **Figure 67**, where desirability was assigned as 0.6 (which is in between 0 and 1) because there were multiple responses corresponding to the factors (for example, Wollastonite wt. fraction of 0.2 had a separate response and Wollastonite wt. fraction of 0.5 had a separate response). Therefore, a particular score (0.6) was assigned. Any response value at a desirability value more than 0.6 was automatically discarded, and the response was maximised [324]. Every desirability has its errors and can contribute to the total error in the response [324].

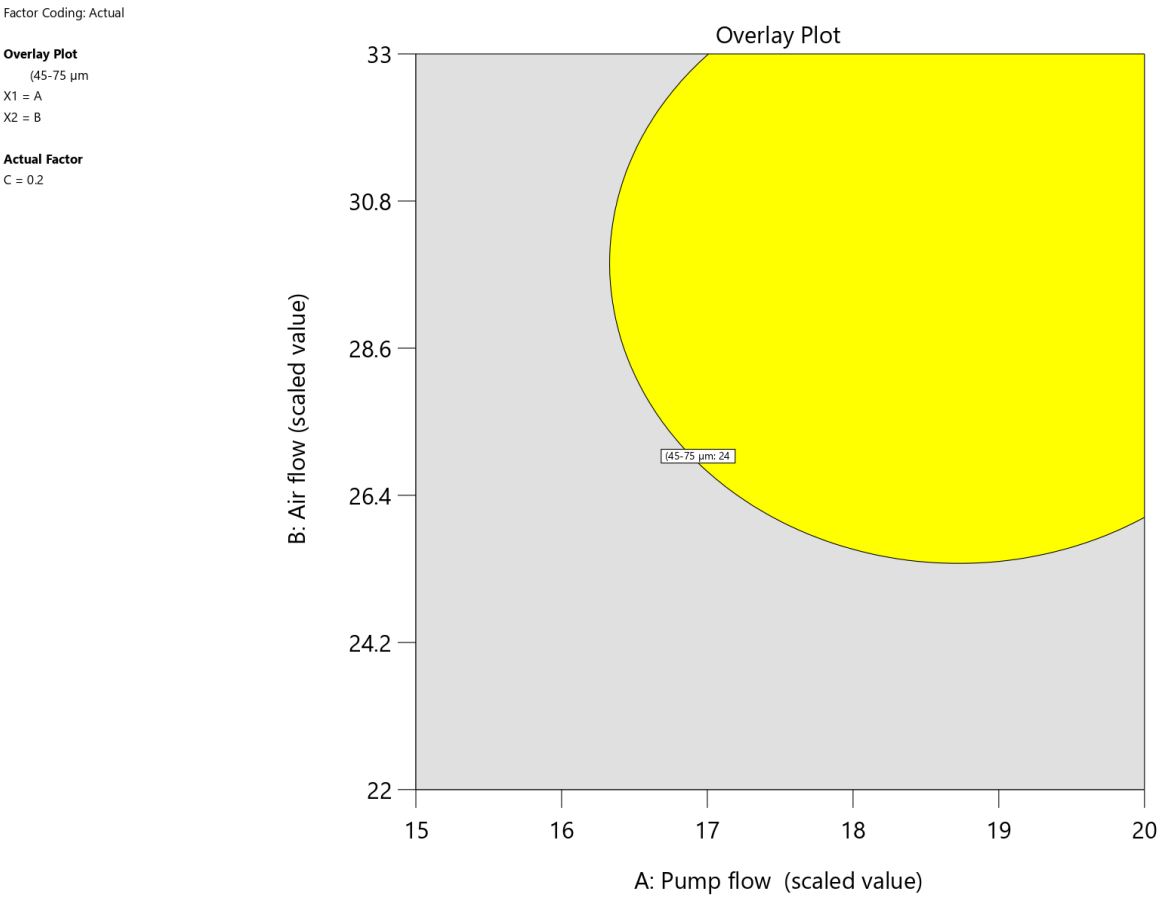

Figure 67, Overall plot to show optimisation region for the desired response

Figure 67 shows the plot to show the optimisation region for the desired response in the case of HA/Wollastonite composite powder. The optimised response or its range lies within the pump flow rate (A) region of approximately 16 to 20 (scaled value) and airflow rate region (B) of approximately 26 to 33 (scaled value) at constant Wollastonite wt. fraction of 0.2.

4.5 Titanium Substrate

The titanium (Ti-6Al-4V) substrate material was described in **Section 3.4**, and the associated substrate preparation equipment covered in **Section 3.5**. XRD analysis was conducted on the titanium substrate to identify phase changes caused by heat treatment at different temperatures, heating rate and environment, prior to any coating been applied.

4.5.1 Roughness Measurement of the Polished Sample

Eight titanium substrate samples were polished manually with the silicon carbide grit size paper P240, P400, P600, P800 and P1200, respectively. The roughness was measured

with BRUKER CounterGT Profilometer. This device measured the average roughness value in 3-dimensions, represented by S_a [325]. **Table 34** shows the average roughness value of the polished samples.

Table 34, Roughness value of the polished sample

Sample no	Average roughness value (S_a)
1	0.08 µm
2	0.05 µm
3	0.07 µm
4	0.07 µm
5	0.08 µm
6	0.07 µm
7	0.06 µm
8	0.14 µm
Average	**0.08 µm**
Standard Deviation	**0.02 µm**

The average roughness of the polished sample was 0.08 µm. This S_a value was comparable to the value suggested by Sneddon et al. [326]. The standard deviation in the average value of pH was 0.02 µm. The S_a was 0.14 µm. Though this value was almost double the next highest value (0.08 µm) , the difference was insignificant (0.06 µm), which indicates that the procedure is repeatable and results are suitable for this application [327].

4.5.2 Roughness Measurement of the Grit-Blasted Sample at 5 Bar Pressure

Like the polishing experiment, the average roughness of eight titanium substrates were measured. The average roughness value S_a are presented in **Table 35**. Eight titanium samples were grit blasted with alumina at 75 ° blast angle, 5 bar pressure and 2 minutes blasting time.

Table 35, Roughness values of grit-blasted samples at 5 bar pressure

Sample no	Average roughness value (S_a)
1	4.48 µm
2	3.74 µm
3	3.85 µm
4	3.96 µm
5	4.03 µm
6	4.32 µm
7	3.91 µm
8	3.80 µm
Average	**4.01 µm**
Standard deviation	**0.26 µm**

As expected, the average roughness value increased with the grit blasting pressure. The average roughness value in the present procedure was 4.01 µm which is the approximate value as suggested by Marinesci et al. [305] with a standard deviation of 0.26 µm (which indicted the repeatability of the experiment [327]. The standard deviation was calculated to prove the repeatability of the experiment. As mentioned in **Section 3.5**, the equipment calibrated the average roughness value at the nanometre level. Moreover, the position of the LED light that calculated the overall average roughness was not same for all of the titanium substrate samples. The average roughness value was calculated based on the fringes observed at a particular region of the substrate sample. Therefore, according to the study conducted by Bahbou et al. [327], standard deviation less than 1.00 µm concluded the repeatability of the grit blasting for a suitable application. Though the values were not same, the values of all of the titanium samples were close to the average roughness of all the substrate samples. The average roughness of sample was highest at 4.48 µm, whereas sample 2 had the least value (3.74 µm) of average roughness.

4.5.3 Roughness Measurement of the Grit-Blasted Sample at Lower Pressure

As shown in **Tables 34 and 35**, the average roughness of the polished sample was 0.08 µm, whereas the average roughness of the grit blasted sample at 5 bar pressure was 4.01 µm. It was necessary to find a mid-range roughness value around 1.8-2.2 µm for further assessment. Titanium samples were grit blasted with alumina at 75 ° blast angle, 1.5 bar pressure and 2 minutes blasting time. **Table 36** shows the average roughness value for the eight titanium substrate samples produced at 1.5 bar pressure.

Table 36, Roughness values of grit-blasted samples at 1.5 bar pressure

Sample no	Average Roughness (S_a)
1	1.78 µm
2	2.32 µm
3	1.54 µm
4	1.86 µm
5	2.05 µm
6	1.73 µm
7	1.68 µm
8	1.84 µm
Mean	**1.85 µm**
Standard Deviation	**0.24 µm**

The average roughness value in the above study was 1.85 µm which is the approximate value as suggested in the graph by Marinosci et al. [305] with a standard deviation of 0.24 µm (less than 1.00 µm), which indicated the repeatability of the experiment [327]. Since the average roughness value was in the range of 1.8-2.2 µm, no further experimentation was required to vary the pressure and calibrate the roughness of the titanium substrate. The maximum value of the average roughness was observed at sample 2, whereas the minimum value of the average roughness was observed at sample 3. The average roughness value (1.85 µm) was in the range of 1.54 µm – 2.32 µm when titanium alloy substrates were grit blasted at 1.5 bar pressure.

4.5.4 XRD Analysis of the Titanium Substrate

In the current study, four titanium substrates were considered under different conditions. A polished titanium substrate with an average roughness value of 0.08 µm was used in the current study. The polished substrate was considered because alumina particles roughened mid-range roughness and grit-blasted substrate, so impurity was possible even in small amounts. Moreover, polishing removed the surface of the substrate; hence titanium substrate in pure form was possible in the polished sample. The titanium substrate used in the current study was dip-coated in HA and Wollastonite gel. Therefore, heat treatment can relieve the residual and improve the adhesive performance of the coating [328]. Therefore, titanium substrates were heat treated at 650 °C. Substrates were characterised by a diffraction angle in the range of 10-80 °. The first polished titanium substrate was heated to 650 °C in the air atmosphere at a 1 °C/min heating rate and cooled to room temperature at the same cooling rate; the second titanium substrate was heated to 840 °C at a heating rate of 2 °C/min in an argon atmosphere and cooled to room temperature at the same cooling rate; the third polished titanium substrate was heated to 650 °C in an argon atmosphere at a 1 °C/min and cooled to room temperature at the same cooling rate.

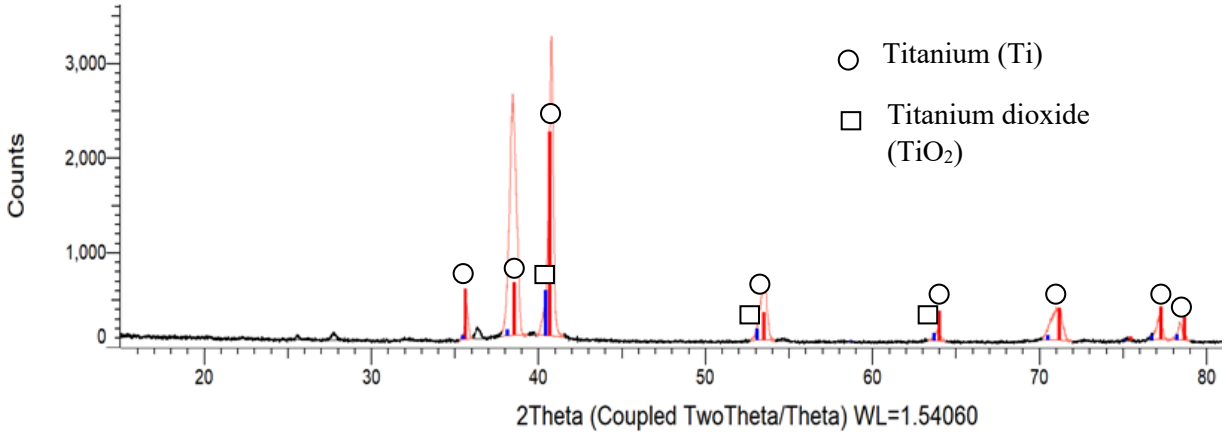

Figure 68, XRD analysis of polished titanium substrate (pre-heated at 650 °C in air atmosphere)

Figure 68 shows the XRD analysis of the titanium alloy substrate heated at 650 °C in an air atmosphere. There were two phases present; the first phase of titanium (Ti) was observed at an angle (2 θ) of 35 °, 38 °, 41 °, 54 °, 64 °, 71 °, 77 ° and 79 °, respectively , and the second phase of titanium dioxide was observed at an angle of 41 °, 53 ° and 64 °, respectively. The formation of titanium dioxide (TiO_2) was due to the heating of titanium at an elevated temperature (> 600 °C) [312]. The peaks observed were broader than those heated at 840 °C because heat treatment at an elevated temperature narrowed the XRD peaks in the case of titanium [329].

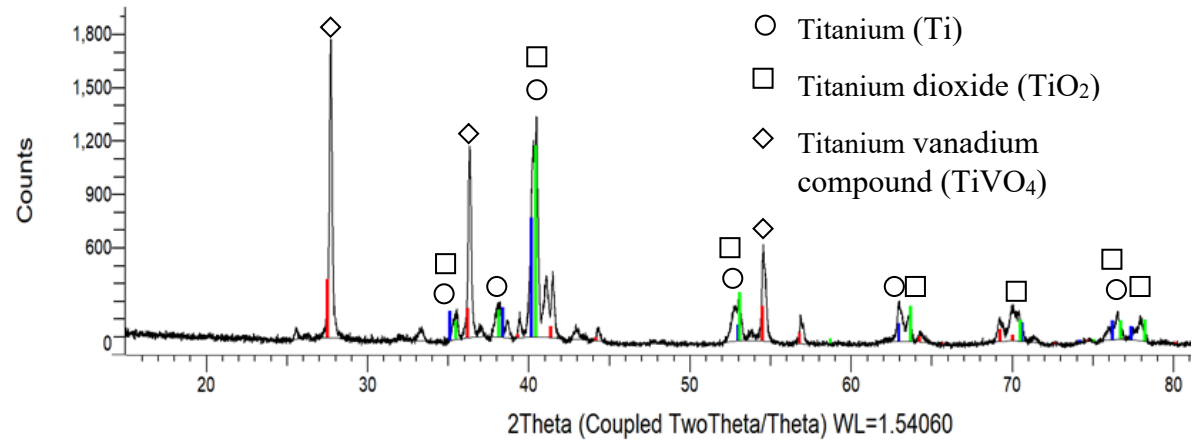

Figure 69, XRD analysis of polished titanium substrate (pre-heated at 840 °C in argon atmosphere)

Figure 69 shows the XRD analysis of the titanium alloy substrate heat treated at 840 °C in an argon atmosphere. There were phases of titanium vanadium compound ($TiVO_4$) at an angle (2θ) of 28 °, 36 ° and 55 °. The presence of this phase was due to higher temperature (temperature > 800 °C) [250]. Moreover, there were phases of titanium (Ti) present mostly at an angle (2θ) of 35 °, 38 °, and 40 °, and titanium dioxide (TiO_2) at an angle (2θ) of 35 °, 40 °, 54 °, and 64 °, respectively. The presence of titanium dioxide (TiO_2) was due to heat treatment of titanium at elevated temperature (> 600 °C) [312]. Therefore, the samples were not heat treated at 840 °C in an air atmosphere as there were not many studies conducted, and it might have resulted in more formation of titanium dioxide (TiO_2), and Titanium nitride (TiN).

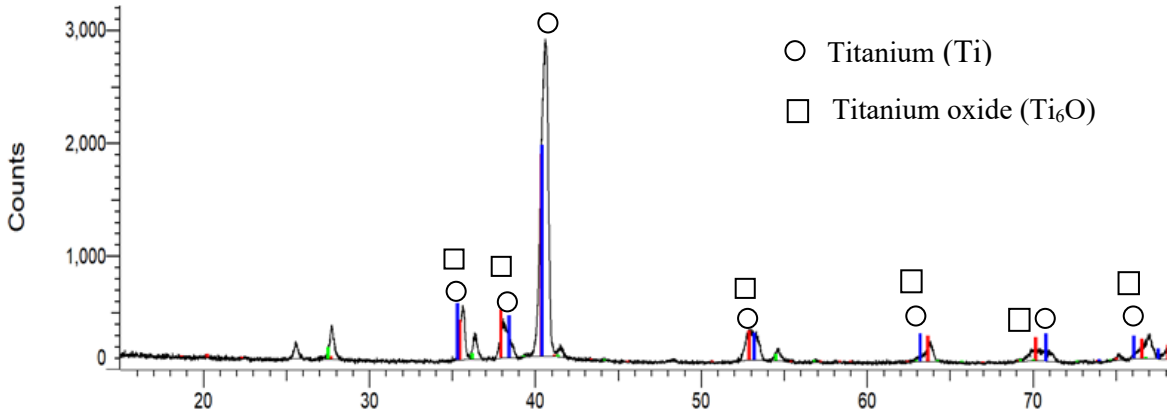

Figure 70, XRD analysis of polished titanium substrate (pre-heated at 650 °C in argon atmosphere)

Figure 70 shows the XRD analysis of the titanium alloy substrate heat treated at 650 °C in an argon atmosphere. The peaks of titanium were mainly observed at an angle (2θ) of 35-42 °, whereas the peaks of titanium oxide were observed mainly at angle (2θ) of 35 ° and 38 °. As shown in **Figure 70**, titanium was the predominant phase. There was a small presence of titanium oxide (Ti_6O), a metastable oxide phase formed due to heat treatment of titanium beyond 300 °C [330]. There was less formation of TiO_2 due to the presence of a vacuum environment and slower heating and cooling rates (1 °C/min). Therefore, a polished titanium substrate heat treated at 650 °C in an argon atmosphere was a viable titanium substrate for sol-gel dip coating.

Overall, the titanium alloy substrate heat treated at 650 °C in an argon atmosphere (**Figure 70**) was suitable for coating either Hydroxyapatite or Wollastonite because of the presence of peaks of pure titanium, less oxide formation as compared to titanium alloy heat treated in an air atmosphere and negligible phase change of titanium alloys. There has not been much research concerning the ill effects of titanium oxide (Ti_6O) observed in this case. Titanium dioxide was present in polished titanium substrates that underwent heat in an air atmosphere at 650 °C and titanium substrates that underwent heat treatment in an argon atmosphere at 840 °C, as shown in **Figures 68** and **69**. However, the International Centre for Cancer Research classified titanium dioxide (TiO_2) nanoparticles as carcinogenic [331].

4.6 Characterisation of Optimised HA/Wollastonite Powder

4.6.1 FTIR Spectroscopy

In the current study, the optimised powder was characterised using FTIR spectroscopy to identify the molecules in the composite powder. For the current study, the spray-dried HA, which had the highest response rate at a pump flow rate of 20 (scaled value), airflow rate of 22 (scaled value) and inlet temperature of 103 °C and spray-dried Wollastonite powder, which had the highest response at a pump flow rate of 15 (scaled value), airflow rate of 33 (scaled value) and inlet temperature of 103 °C was compared with HA/Wollastonite optimised powder obtained at process parameters with an airflow rate

of 19 (scaled value), a pump flow rate of 30 (scaled value) and a Wollastonite wt. fraction of 0.2.

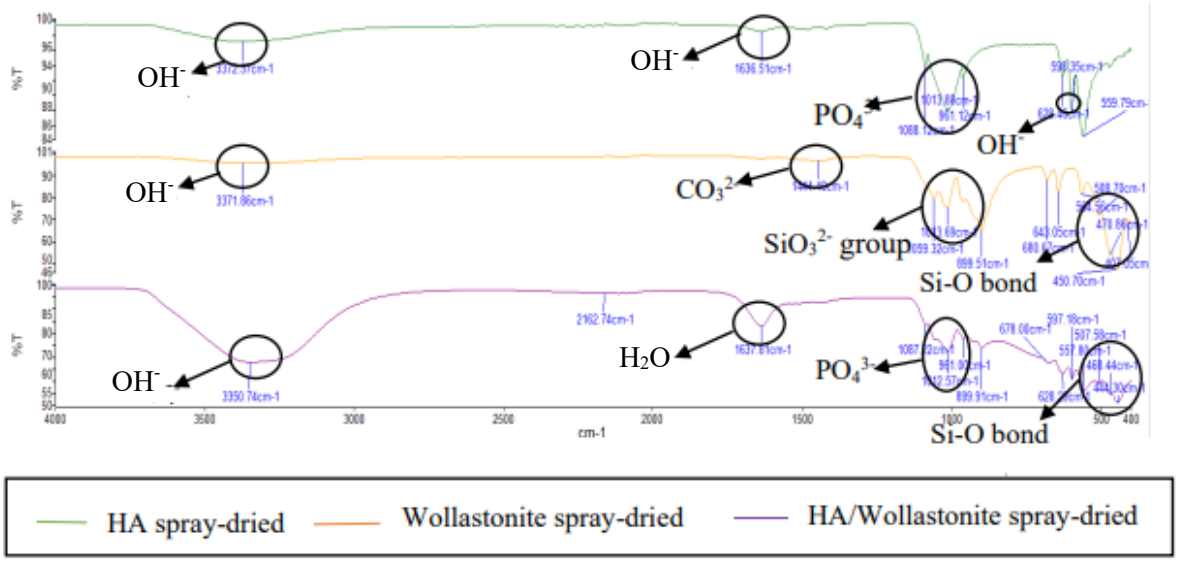

Figure 71, FTIR spectroscopy of spray-dried powders

Figure 71 shows the FTIR spectroscopy of the spray-dried powder. For spray-dried HA, there were bands observed at 3237 cm^{-1} and 1636 cm^{-1}, showing the presence of OH^- group in adsorbed water, which was due to the spray drying process as as-received powders were immersed in deionised water [332]. There was a presence of OH^- group in apatite at the wavelength of approximately 632 cm^{-1}, showing the presence of Hydroxyapatite [332]. Bands were present at wavelengths of 1088 cm^{-1}, 1013 cm^{-1}, and 962 cm^{-1}, showing the presence of the phosphate (PO_4^{3-} group) in the apatite [332].

In the case of spray-dried Wollastonite, bands were present at the wavelength of 3371 cm^{-1}, showing the presence of the adsorbed water (OH^- group) due to the spray-drying process. Another band at wavelength 1444 cm^{-1} showed the presence of carbonate ions (CO_3^{2-} ions). There was a presence of SiO_3^{2-} group in between the wavelength of 967 cm^{-1} and 1063 cm^{-1}, indicating Wollastonite [255]. Other bands present at wavelengths of 507 cm^{-1}, 467 cm^{-1}, and 453 cm^{-1} showed the Si-O bonds in Wollastonite [333].

In the case of spray-dried HA/Wollastonite, almost all the bands observed at different wavelengths were similar to Hydroxyapatite FTIR spectra with the presence of OH^- group due to adsorbed water at wavelengths of 3350 cm^{-1} and 1637 cm^{-1} and the presence of

phosphate group (PO_4^{3-}) at wavelengths of 1088 cm^{-1}, 963 cm^{-1} and 1014 cm^{-1}, respectively [332, 334]. However, more bands were present at 470 cm^{-1}, 450 cm^{-1} and 507 cm^{-1} wavelengths, showing the presence of Si-O bond in Wollastonite [333]. The minor presence of Wollastonite was due to less quantity of Wollastonite (20 wt.%) added to the Hydroxyapatite.

4.6.2 XRD Analysis of the Optimised Powder

XRD analysis was performed on the optimised powders with process parameters: pump flow of 19 (scaled value), airflow rate of 30 (scaled value) and Wollastonite wt.% of 0.2, keeping the inlet temperature constant at 103 °C. The optimised powder obtained was characterised using the XRD to observe the peaks of both Hydroxyapatite and Wollastonite. **Figure 72** shows the XRD analysis of the powder characterised.

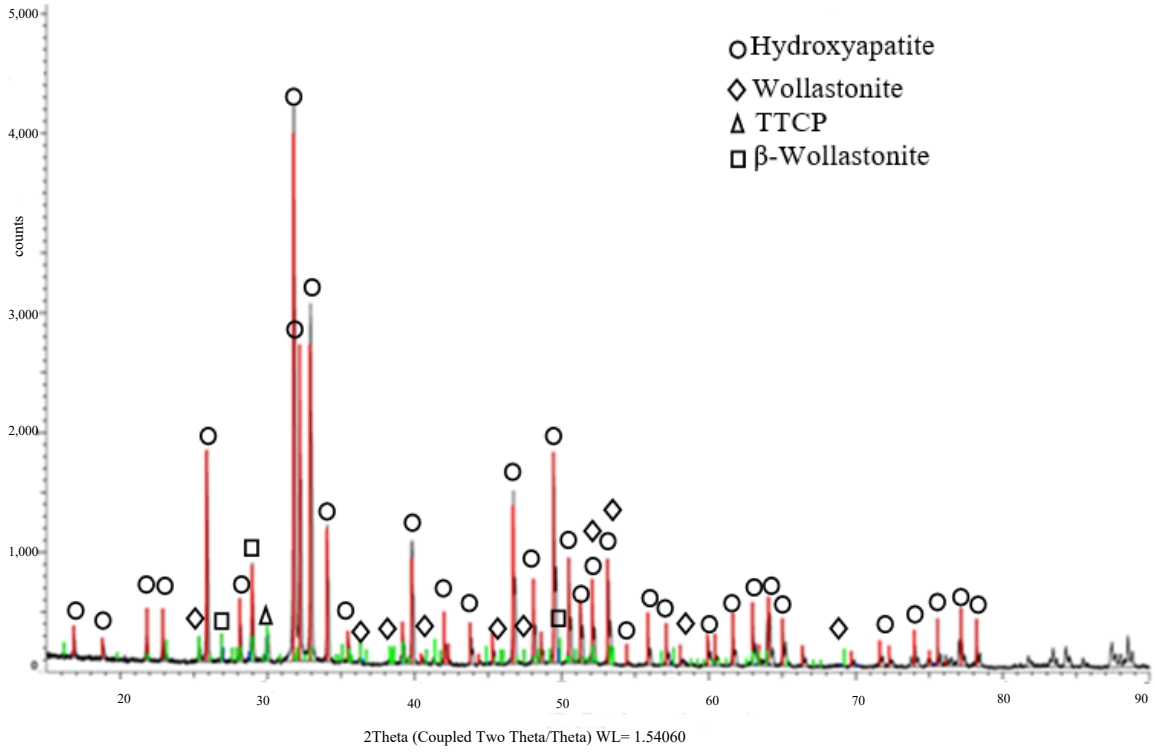

Figure 72, XRD pattern of optimised HA/Wollastonite powder

Figure 72 shows the XRD pattern of spray-dried HA/Wollastonite powder at optimised process parameters. Since it was processed at a relatively low temperature (at around 103 °C). There was no presence of β-TCP, α-TCP or α-Wollastonite [23, 53]. The 4 phases present in the optimised powder was Hydroxyapatite, Wollastonite, TTCP and β-Wollastonite. Hydroxyapatite was a major phase present at a diffraction angle (2θ) of approximately 4°, 18°, 22°, 23°, 26°, 28°, 31°, 32°, 33°, 34°, 35°, 40°, 42°, 44°, 47°, 48°,

51°, 52°, 53°, 55°, 56° 57°, 60°, 61°, 62°, 63°, 65°, 72°, 74°, 76°, 78° and 80°, respectively, as identified by Levingstone [4]. The other major phase was Wollastonite which was not so pronounced due to less quantity (20 wt.%). Wollastonite phase was present at a diffraction angle (2θ) of 24°, 36°, 38°, 41°, 46°, 52°, 53°, 58° and 69°, respectively, similar to studies conducted by Ma et al. [335]. There were a minor peaks of TTCP at an approximate diffraction angle (2θ) of 30° and a minor presence of β-Wollastonite at a diffraction angle (2θ) of approximately 27°, 29° and 49°, respectively [336]. The powder optimised was crystalline with a high peak height and narrow diffraction width [337].

4.7 Spray-Coating Using Spray Dryer

4.7.1 Spray Coating of Hydroxyapatite

HA was spray-coated with the process parameters obtained from 2 factorial screening. The process parameters were pump flow rate: - 20 (scaled value), airflow rate: - 22 (scaled value), and inlet temperature: - 103 °C. Before spray coating, one substrate was polished using grit paper (average roughness: - 0.08 μm), the second substrate was grit blasted to obtain mid-range average roughness of 1.85 μm and the third substrate was grit blasted to obtain an average roughness of 4.01 μm. The coatings obtained were spray-coated with the process parameters mentioned above. The obtained as- sprayed coatings were heat-treated at 1100 °C for 2 hours in an air atmosphere. The heat treatment was done after spray coating as pre-heat treatment would result in the formation of TiO_2 at 1100 °C [312].

a) *<u>SEM image of HA on prepared titanium substrate</u>*

i. SEM image of HA spray coated on polished sample heat treated at 1100 °C

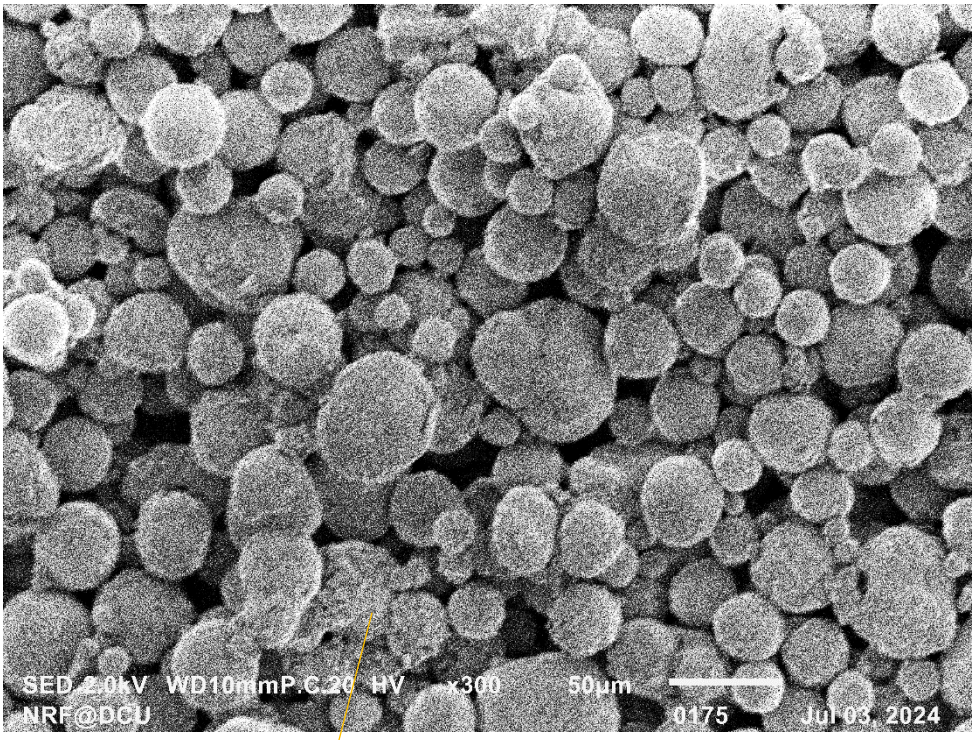

Figure 73, SEM image of HA spray coated on polished sample heat treated at 1100 °C in an air atmosphere at a magnification of 300 X

ii. SEM image of HA spray coated on mid-range roughness sample heat treated at 1100 ° C

Figure 74, SEM image of HA spray coated on midrange roughness sample heat treated at 1100 °C in an air atmosphere at a magnification of 300X

iii. SEM image of HA spray coated on grit-blasted sample heat treated at 1100 °C

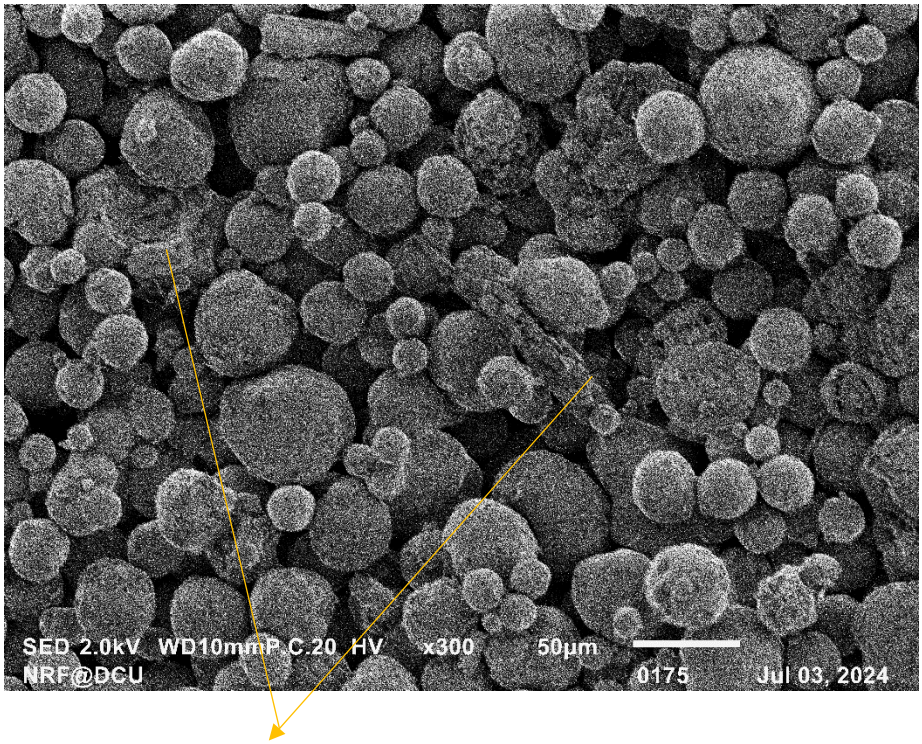

Figure 75, SEM image of HA spray coated on grit blasted sample heat treated at 1100 °C in an air atmosphere at a magnification of 300X.

Figures 73, 74 and 75 show the SEM image of spray-coated HA on the polished sample; SEM image of the spray-coated sample on the mid-range roughness sample; and the SEM image of spray-coated HA on the grit-blasted sample, respectively. Overall, the structure was porous due to the evaporation of the deionised water used in the suspension and dihydroxylation (between 800-900 °C) [53]. Most of the HA and Wollastonite particles retained their crystalline structure even after heat treatment at 1100 °C [338]. The structure was similar to the spray-dried powder heat treated at 750 °C, as mentioned by Bastan et al. [209]. Pores with a complex and different geometry tended to change over more spherical pores after heat treatment at 1100 °C [339].

Overall, the spray coated on HA on a grit-blasted surface had a better structure as more agglomerates were observed due to heat treatment and entanglement of HA and Wollastonite particles. Due to the higher roughness of the grit-blasted sample, both the HA, Wollastonite and HA/Wollastonite particles tended to adhere more to the substrate at a particular surface area [340]. The HA particles appeared isolated and dispersed in the

coatings obtained in polished and mid-range substrates due to less surface area caused by lower roughness. In the case of HA coated onto a grit blasted sample, agglomerates grew up and were more in number due to heat treatment at higher temperatures and higher roughness (1100 or more than 1100 °C) [339].

b) *FTIR spectra of spray-coated HA heat treated at 1100 °C*

It was impossible to characterise the coatings by FTIR as the coating was too thin. Moreover, the coating disintegrated due to pressure applied by the indenter, resulting in non-repeatability in the experiment. FTIR spectroscopy helps to determine the direct information of the molecule of the sample. Based on the characteristic infrared signals absorbed by the sample, one can easily determine the structure of the chemical and its content, and its location [341]. When the coating was placed on the indentor, the titanium substrate absorbed the infrared signals. Moreover, the coating thickness was not high enough to absorb the infrared signals from the equipment. Moreover, the FTIR results of the spray-dried Wollastonite powder post-heat-treated at 1100 °C for 2 hours would be like Wollastonite spray-coated onto a prepared titanium substrate post-heat-treated at 1100 °C for 2 hours because Wollastonite was spray-coated onto a titanium substrate using the optimised process parameters obtained from spray drying of Wollastonite. Therefore, spray-dried HA powder heat treated at 1100 °C for 2 hours was considered and characterised by FTIR spectroscopy. The FTIR spectra of spray-dried HA were used as a reference to observe the change caused by the heat treatment of the powder. **Figure 76** shows the FTIR spectra of spray-dried HA and spray-coated HA powder heat treated at 1100 °C

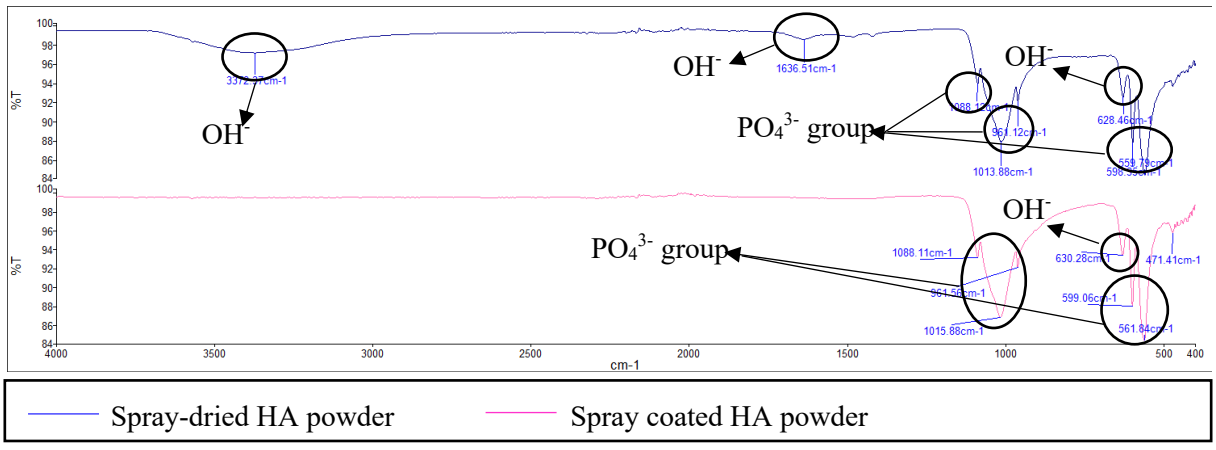

Figure 76, FTIR spectra of spray-dried HA and spray-coated HA heat treated at 1100 °C for 2 hours in an air atmosphere

There were 5 major broadbands observed at wavelengths 1086 cm^{-1}, 1016 cm^{-1}, 963 cm^{-1}, 600 cm^{-1}, 632 cm^{-1} and 563 cm^{-1}, respectively. The broadbands corresponding to wavelengths 1086 cm^{-1}, 1016 cm^{-1}, 963 cm^{-1}, 600 $cm^{-1,}$ and 563 cm^{-1} correspond to PO_4^{3-} group, whereas the broadband of wavelength 632 cm^{-1} corresponds to OH^- group. These FTIR spectra are similar to the HA heat treated at 1100 °C, as explained by Ahmed et al [332]. The difference between the FTIR spectra observed in **Figure 76** in relation to the spray-dried HA and spray-coated HA heat treated at 1100 °C as there were two additional bands observed at approximately 3372 cm^{-1} (adsorbed water) and a second band observed at a wavelength around 1640 cm^{-1} (presence of H_2O group), which was absent in the spray coated HA powder heat treated at 1100 °C due to heat treatment, resulting in dehydroxylation of spray dried HA powder [332, 338].

c) *XRD image of spray-coated HA on titanium substrate*

Since the grit-blasted spray-coated HA samples had better results than other prepared samples, it was considered for the study. The spray-coated HA samples were heat treated at 1100 °C for 2 hours.

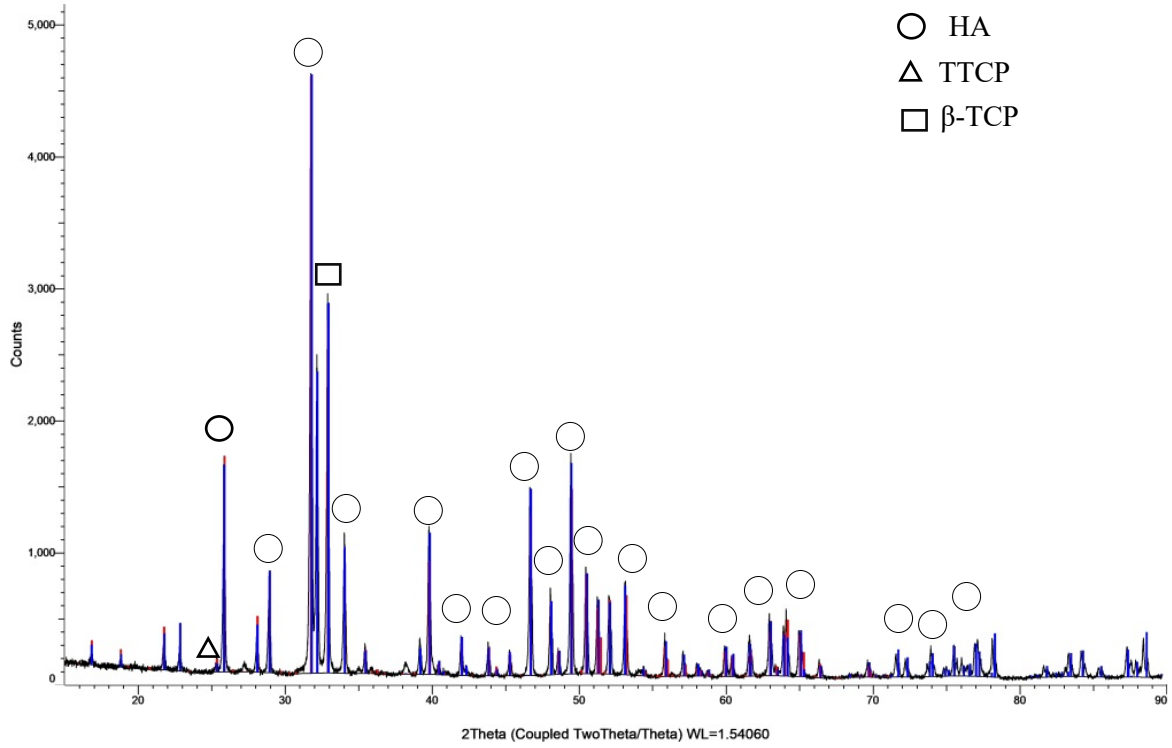

Figure 77, XRD pattern of spray-coated HA on grit-blasted titanium substrate heat treated at 1100 °C for 2 hours in an air atmosphere

Figure 77 shows the XRD pattern of the spray-coated HA onto a prepared titanium substrate. There was a peak of β-TCP observed at an angle (2θ) of approximately 32°, which may be due to heat treatment of Hydroxyapatite at elevated temperature [4]. There was a peak observed of TTCP at an angle of approximately (2θ) of 24° [4]. There were XRD peaks of HA observed at an angle (2θ) of approximately 25°, 31°, 34°, 40°, 42°, 46°, 50°, 53°, 56°, 60°, 62°, 64°, 65°, 72°, 74°, 76° and 80°, respectively, as investigated in the previous research [4, 342]. The coating presented was crystalline with a narrow and long peak due to heat treatment of HA at 1100 °C [332]. TTCP and β-TCP present can decrease the solubility of the HA coatings implanted inside the body as they are more soluble than HA [343]. HA has a near-perfect Ca/P ratio of 1.67, which makes it stable when implanted inside the body. In contrast, the Ca/P ratio of TTCP is 2 (more than HA which reduces its solubility and stability), and the Ca/P ratio of β-TCP is 1.5 (less than HA which reduces its solubility) [343]. According to ISO standard specification (ISO 13779:2-2000), the HA coating should have a Ca/P ratio of between 1.67 to 1.76 [53].

4.7.2 Spray Coating of Wollastonite

Wollastonite was spray-coated with the process parameters obtained from the two factorial screening. The process parameters used were pump flow rate: - 15 (scaled value), airflow rate:- 33 (scaled value) and inlet temperature:- 103 °C. Before spray coating, the substrates were prepared to obtain a polished sample (average roughness of 0.08 μm), mid-range roughness sample (average roughness of 1.85 μm) and grit blasted sample (average roughness of 4.01 μm). After sample preparation, the substrates were spray-coated with Wollastonite. The coatings obtained were heat treated at 1100 °C for 2 hours in an air atmosphere.

a) *SEM image of Wollastonite on prepared titanium substrate*

i. SEM image of Wollastonite spray coated on polished sample heat treated at 1100 °C

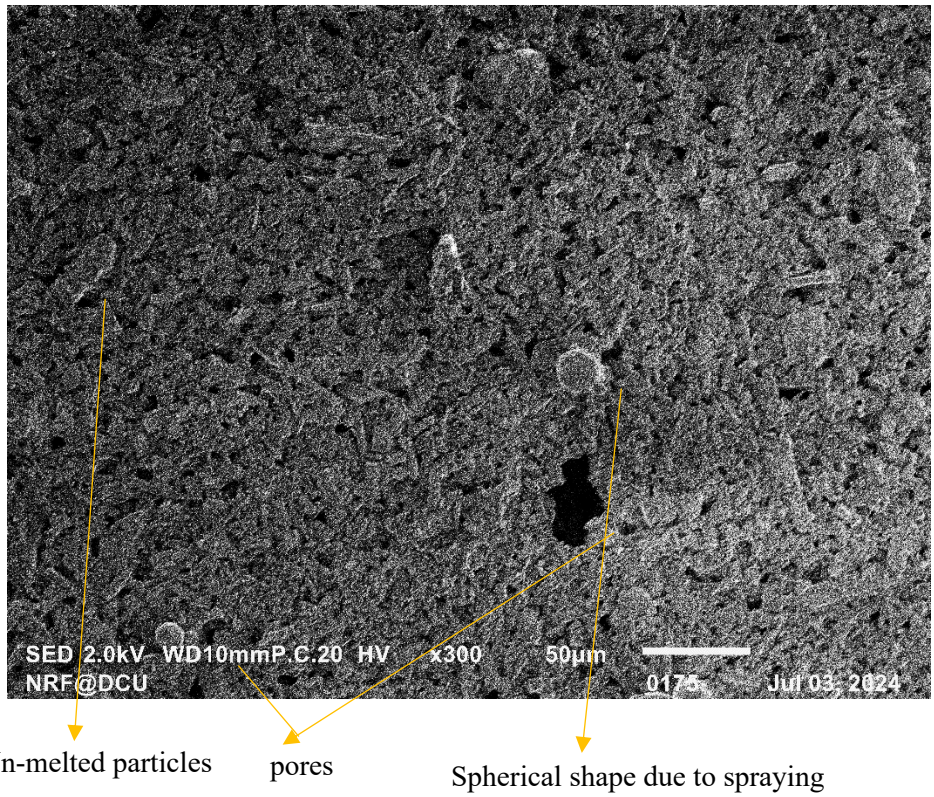

Figure 78, SEM image of Wollastonite spray coated on polished sample heat treated at 1100 °C in an air atmosphere at 300X magnification

ii. SEM image of Wollastonite spray coated on mid-range roughness sample heat treated at 1100 °C

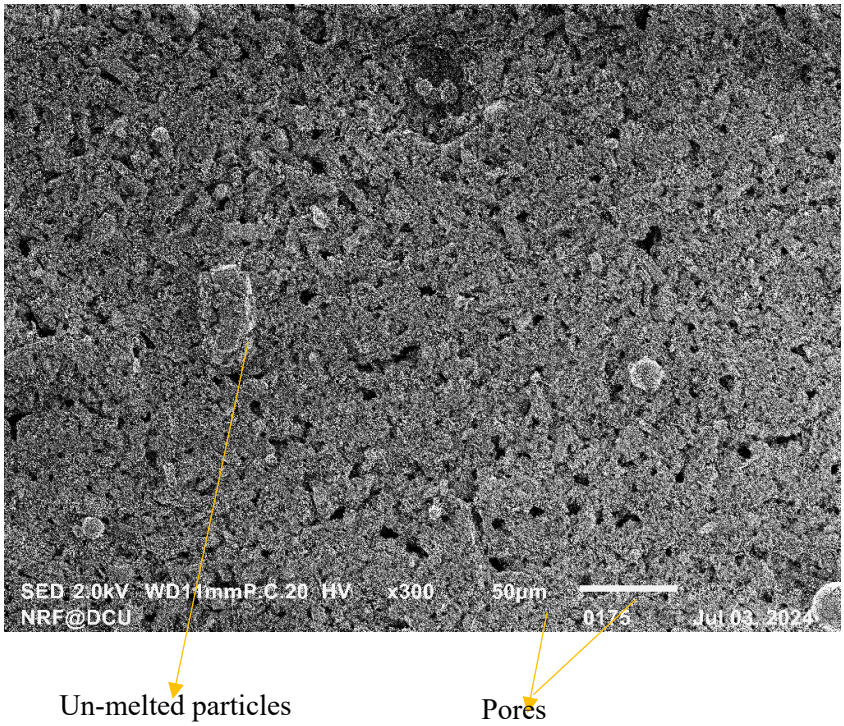

Figure 79, SEM image of Wollastonite spray coated on mid-range roughness sample heat treated at 1100 °C in an air atmosphere at 300 X magnification

iii. SEM image of Wollastonite spray coated on grit blasted sample heat treated at 1100 °C

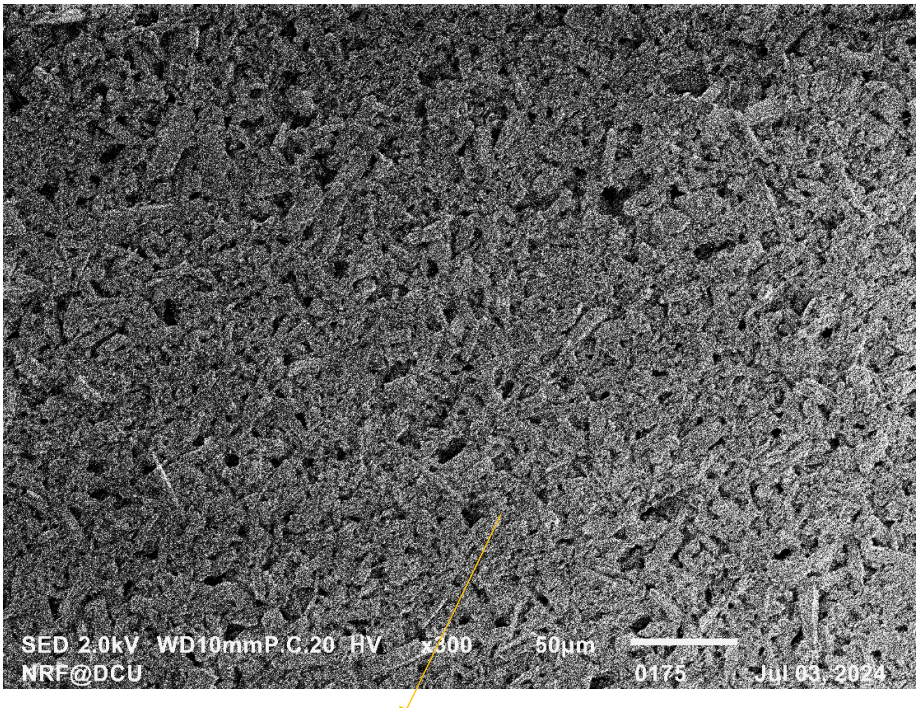

Figure 80, SEM image of Wollastonite spray-coated on grit-blasted sample heat treated at 1100 °C in an air atmosphere at 300X magnification.

Figures 78, 79 and 80 show the SEM image of spray-coated Wollastonite on the polished sample, spray-coated Wollastonite on the mid-range roughness sample, and spray-coated Wollastonite on the grit-blasted sample, respectively heat treated at 1100 °C for 2 hours in an air atmosphere. Wollastonite coated on all the prepared samples had a porous structure [237]. The Wollastonite coated onto a polished substrate contained more pores. Wollastonite coated onto a mid-range roughness consists of pores and some near-spherical shapes, which may be due to the un-melted structure of Wollastonite and some spherical shapes attained due to the spraying technique (though not enough to achieve desired flowability). Wollastonite spray coated onto a grit-blasted surface was porous with less spherical and minimal un-meltedstructure. Wollastonite spray coated onto a grit-blasted substrate has a high average roughness of 4.01 µm, due to which there was more surface area and less diffusion of the Wollastonite material [340]. The interlocking mechanism due to the high surface area ensured the uniform deposition of Wollastonite

particles with heating, resulting in fewer un-meltedparticles [340]. Therefore, Wollastonite coated onto a grit-blasted surface had a more desirable coating structure.

b) *FTIR spectra of spray-coated Wollastonite powder*

Similar to HA, it was impossible to characterise the Wollastonite coating by FTIR spectroscopy. The same issues were encountered when the Wollastonite coating disintegrated due to the high force applied by the indentor, resulting in the infrared light absorbed by the titanium substrate. In fact, the Wollastonite spray-coated onto a grit-blasted titanium substrate had less coating layer thickness than the spray-coated Hydroxyapatite layer due to the lower density of Wollastonite (density of Wollastonite is 2.9 g/cm^3 compared to 3.16 g/cm^3 of Hydroxyapatite). Moreover, the FTIR results of the spray-dried Wollastonite powder post-heat-treated at 1100 °C for 2 hours would be like Wollastonite spray-coated onto a prepared titanium substrate post-heat-treated at 1100 °C for 2 hours.

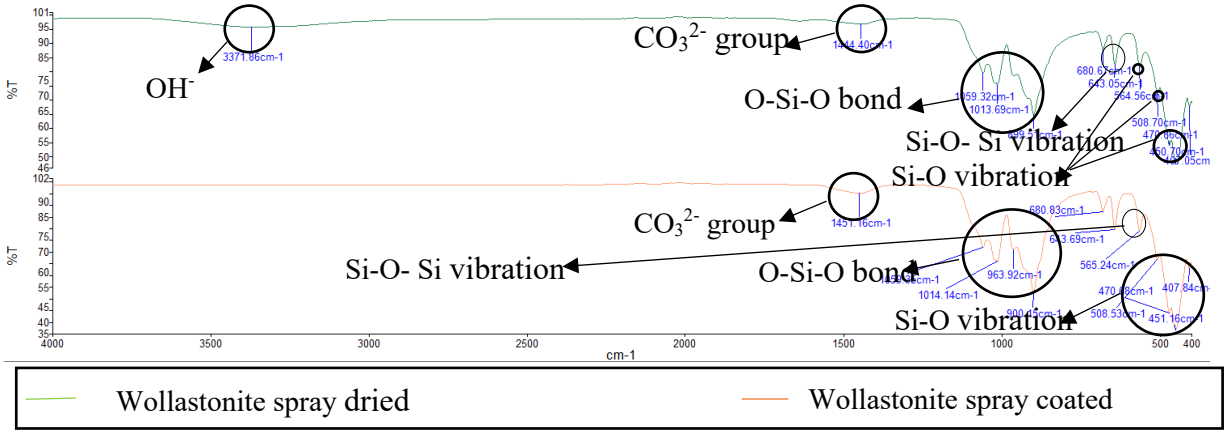

Figure 81, FTIR spectra of spray-dried Wollastonite powder and spray-coated Wollastonite coating heat treated at 1100 °C in an air atmosphere.

Figure 81 shows the FTIR spectra of the spray-dried Wollastonite powder and spray-coated Wollastonite powder heat-treated at 1100 °C. Since there was no phase change in Wollastonite up to the temperature of 1125 °C [162]. For reference purposes, the FTIR spectra of spray-dried samples were taken into consideration to observe the change caused by heat treatment at 1100 °C.

Broadbands in the range of 850-1100 cm^{-1} are O-Si-O bonds, which corresponds SiO_3^{2-}, showing the presence of Wollastonite [255, 333]. The other band at the wavelength of 645 cm^{-1} corresponds to a vibrational stretching O-Si-O bond, showing the presence of Wollastonite [333]. In addition, 4 bands corresponding to approximate wavelengths of

567, 509, 472 and 453 cm^{-1} were caused by Si-O vibration [333]. There was a presence of H_2O at a wavelength of around 3371 cm^{-1} in spray-dried powder due to the spray-drying technique where Wollastonite was immersed in deionised water before spray-drying [332]. The peaks in the case of spray-dried powder heat treated at 1100 °C disappeared due to heat-treatment at 1100 °C. Comparison of FTIR spectra of spray-coated Wollastonite with the FTIR spectra of spray-dried Wollastonite showed no band present at the wavelength of 3371 cm^{-1} (presence of OH^- group) and sharper bands present, possibly due to the heat treatment process [332].

c) *XRD image of spray-coated Wollastonite on prepared titanium substrate*

Wollastonite was spray-coated with the same conditions as Hydroxyapatite, where the coated sample was heat treated at 1100 °C for 2 hours. Wollastonite spray-coated onto a grit-blasted titanium substrate was considered for characterisation by XRD technique.

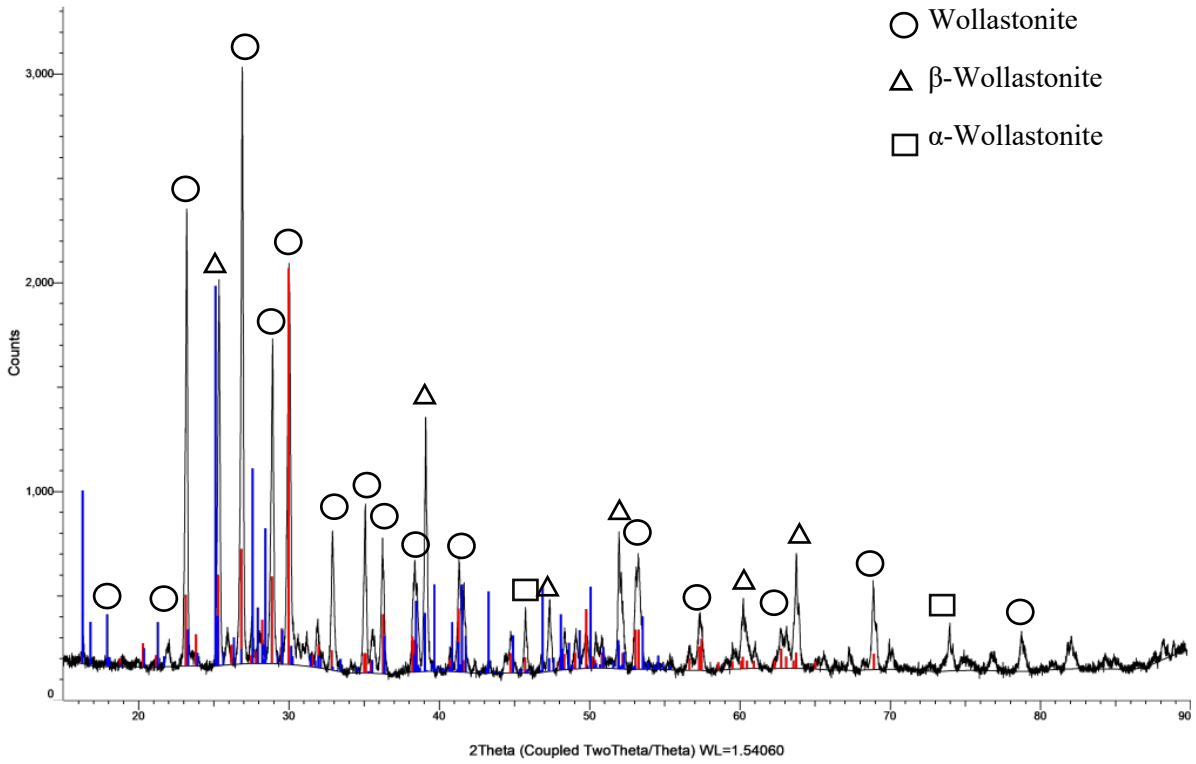

Figure 82, XRD pattern of spray-coated Wollastonite on a grit-blasted titanium substrate sample heat treated at 1100 °C in an air atmosphere

Figure 82 shows the XRD pattern of the Wollastonite spray coated on a grit-blasted substrate heat treated at 1100 °C in an air atmosphere. The XRD pattern mostly consists of pure Wollastonite material. However, there were some phases of β-Wollastonite and a

minor phase of α-Wollastonite due to heat treatment at higher temperatures (in this case, 1100 °C) [162]. α-Wollastonite was present at an approximate angle (2θ) of 46° and 74° [23]. β-Wollastonite diffraction peaks were present at an angle (2θ) of 25°, 38°, 47°, 52°, 60°, 63°, respectively. Similarly, the Wollastonite phase was present at a diffraction angle (2θ) of approximately 12°, 22°, 28°, 30°, 33°, 35°, 36°, 39°, 42°, 53°, 58°, 63°, 68° and 78° approximately [344]. There was a minor presence of α-Wollastonite and some β-Wollastonite due to heat treatment at 1100 °C. β-Wollastonite is stable at room temperature and more soluble than α-Wollastonite in SBF fluid and can increase the biodegradability of coating [23]. Therefore, an increase in the quantity of β-Wollastonite might reduce the crystallinity of the coating.

4.7.3 Spray Coating of HA/Wollastonite Composite Powder

The pre-mixed HA/Wollastonite powder was added to the deionised water. The composite mixture (64 grams HA and 16 grams Wollastonite) with 500 ml deionised water was spray coated onto a prepared substrate, similar to the spray coating of Hydroxyapatite and Wollastonite. The quantity of Wollastonite (20 wt.%) added to Hydroxyapatite was based on the optimisation studies obtained by DOE software mentioned in the previous section with reference studies conducted by Bastan et al. [211]. The process parameters used were a pump flow rate of 19 (scaled value), airflow rate of 31 (scaled value) and inlet temperature of 103 °C. the samples with 3 different roughness (polished sample with average roughness of 0.08 µm, mid-range roughness with average roughness of 1.85 µm and grit-blasted sample with average roughness of 4.01 µm. The samples were spray coated with HA/Wollastonite with the above `mentioned process parameters. The obtained coating was heat treated at 1100 °C for 2 hours. The flow diagram of the coating process is shown below in **Figure 83**.

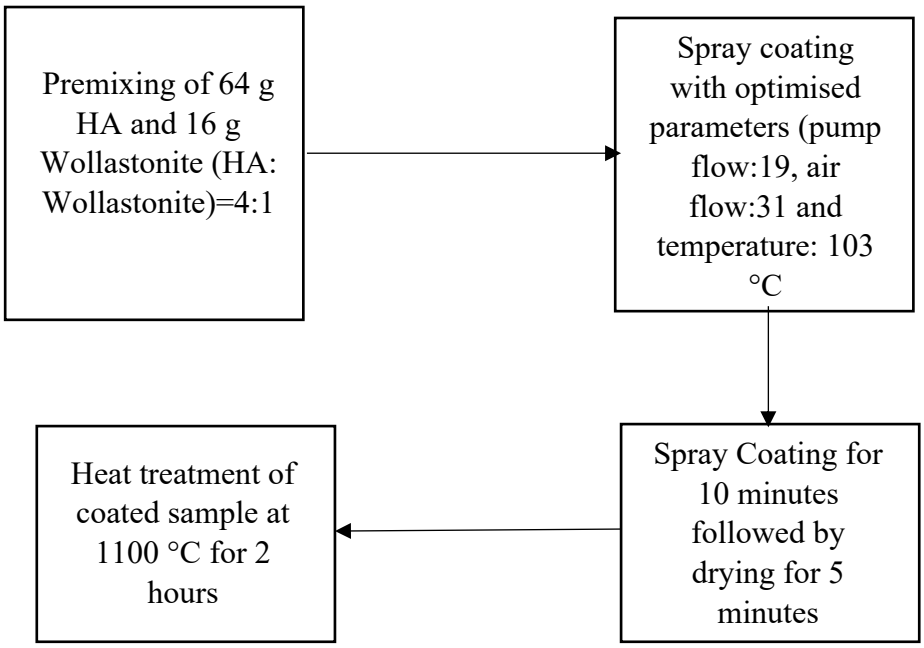

Figure 83, Flow chart of HA/Wollastonite composite spray coating

Figures 84, 85 and 86 shows the SEM image of spray-coated HA/Wollastonite on the polished sample, SEM image of spray-coated HA/Wollastonite on the mid-range roughness sample and SEM image of spray-coated HA/Wollastonite on the grit-blasted sample, respectively. The structure was porous due to the evaporation of the deionised water used in the suspension and dihydroxylation (between 800-900 °C) [53]. Unlike the morphological structure mentioned by Bastan et al., which was more spherical and the Wollastonite and Hydroxyapatite blended well [211], the structure observed had an acicular shape due to the presence of Wollastonite, which depicts the lack of flowability caused by the presence of an even smaller quantity of Wollastonite (20 wt.%, in this case).

The spray-coated HA/Wollastonite structure onto a polished sample appeared more fragmented and porous. The particles were not interlocked due to less surface area, and HA/Wollastonite particles appeared more dispersed on the polished substrate [340]. As the roughness of the substrate samples increased, the structure appeared less porous, with more interconnection between particles of different morphology (spherical and acicular, in this case). The higher the roughness, the higher the surface area, and therefore, there was more interlocking of the particles to the substrate, which resulted in the uniform

distribution [340]. In the case of HA/Wollastonite spray-coated onto a grit-blasted sample, more spherical HA grains were placed near the Wollastonite fibres due to higher surface roughness [160]. As the roughness of the substrate increased, the Hydroxyapatite particle agglomerated homogenously with the Wollastonite fibres [160]. Henceforth, the spray-coated HA/Wollastonite onto a grit-blasted surface had a better structure.

a) *SEM image of HA/Wollastonite on prepared titanium substrate*

i. SEM image of HA/Wollastonite spray coated on polished sample heat treated at 1100 °C

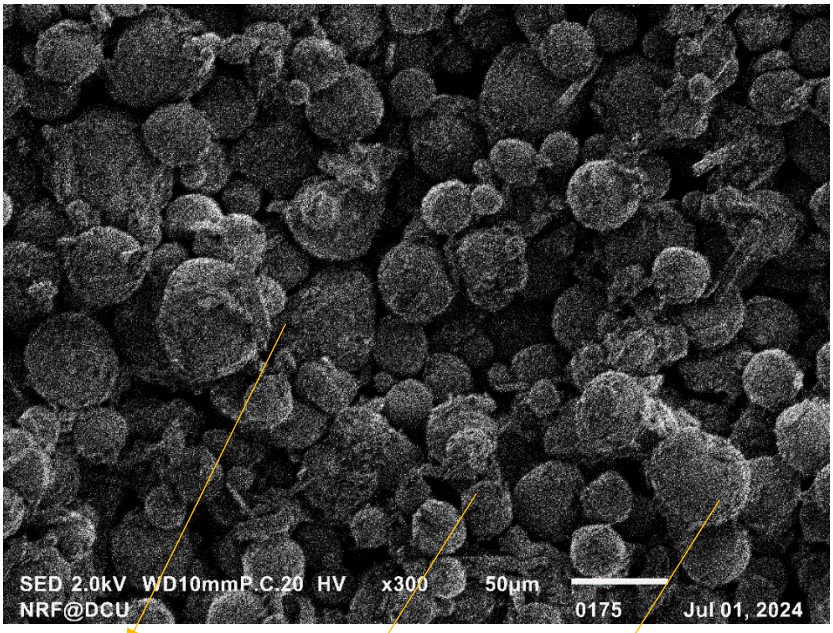

Figure 84, SEM image of HA/Wollastonite spray coated on polished sample heat treated at 1100 °C in an air atmosphere at 300X magnification

ii. SEM image of HA/Wollastonite spray coated on mid-range roughness sample heat treated at 1100 °C

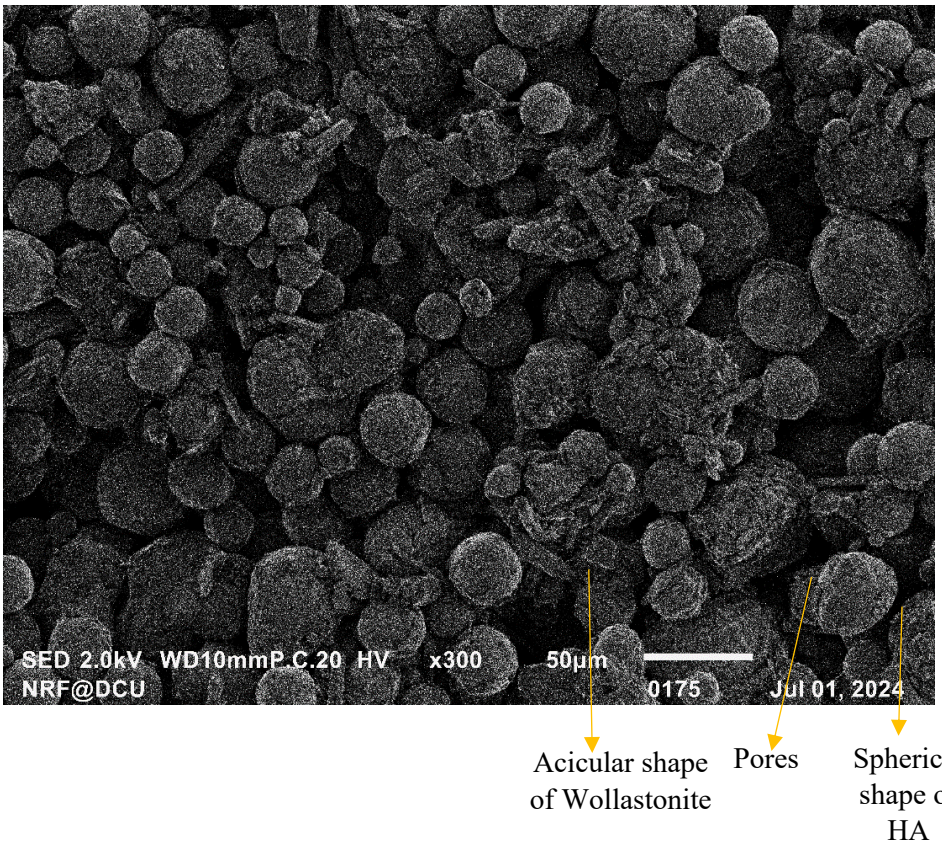

Figure 85, SEM image of HA/Wollastonite spray coated on midrange roughness sample heat treated at 1100 °C in an air atmosphere at 300X magnification

iii. SEM image of HA spray coated on grit-blasted sample heat treated at 1100 °C

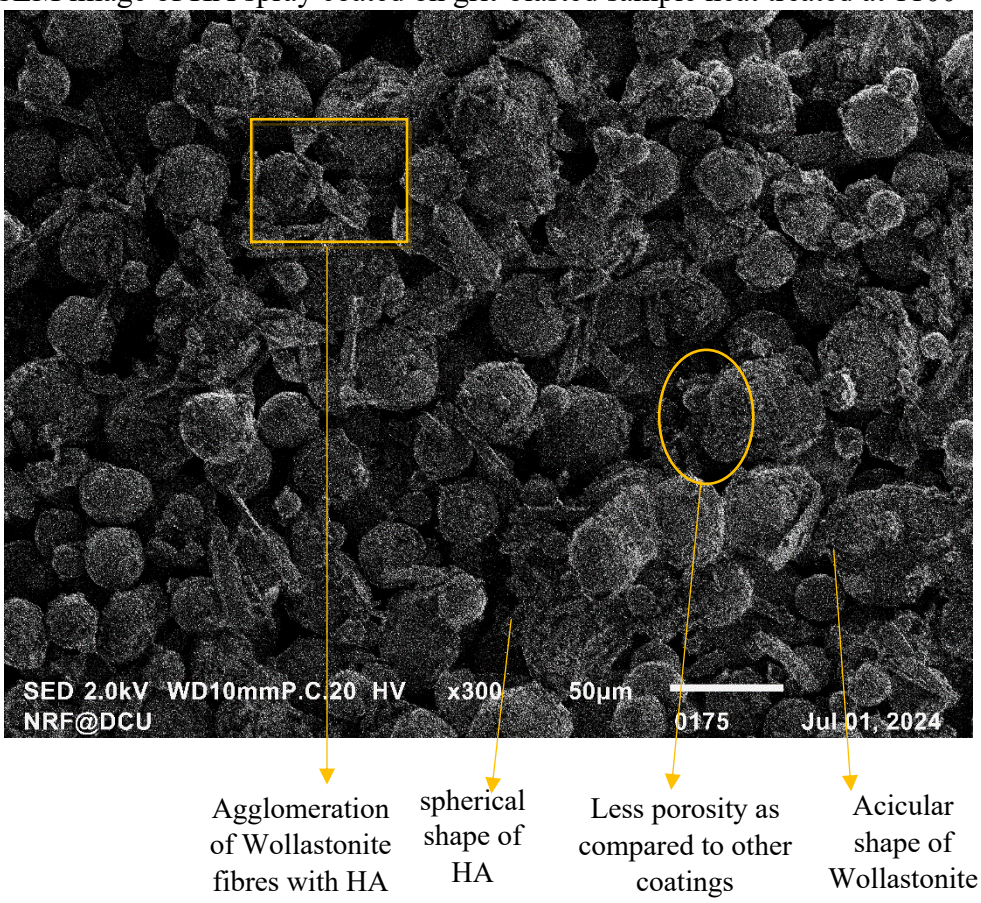

Figure 86, SEM image of HA/Wollastonite spray coated on grit blasted sample heat treated at 1100 °C in an air atmosphere.

b) *FTIR spectra of HA/Wollastonite at 1100 °C*

HA/Wollastonite was spray-coated onto a prepared (polished, mid-range, and grit-blasted) titanium substrate using a spray dryer. The obtained coating underwent post-heat treatment at 1100 °C for 2 hours in an air atmosphere. The FTIR results of the spray-dried HA/Wollastonite powder heated at the same temperature would be like HA/Wollastonite spray-coated onto a grit-blasted titanium substrate post-heat-treated at 1100 °C for 2 hours. Therefore, heat-treated HA/Wollastonite powder was considered for an FTIR spectroscopy study similar to those conducted on Hydroxyapatite and Wollastonite. Moreover, due to the thin layer thickness, one could not get the complete fingerprint of the molecular group present in the coating, and the HA/Wollastonite sample

did not absorb complete infrared lights due to the disintegration of the HA/Wollastonite coating caused by the indentor force.

To understand the change in FTIR spectra caused by HA/Wollastonite, the three FTIR spectra of heat-treated spray-dried HA powder, heat-treated spray-dried Wollastonite powder, and heat-treated spray-dried HA/Wollastonite powder were taken into consideration to identify the presence of Wollastonite and bands of Hydroxyapatite.

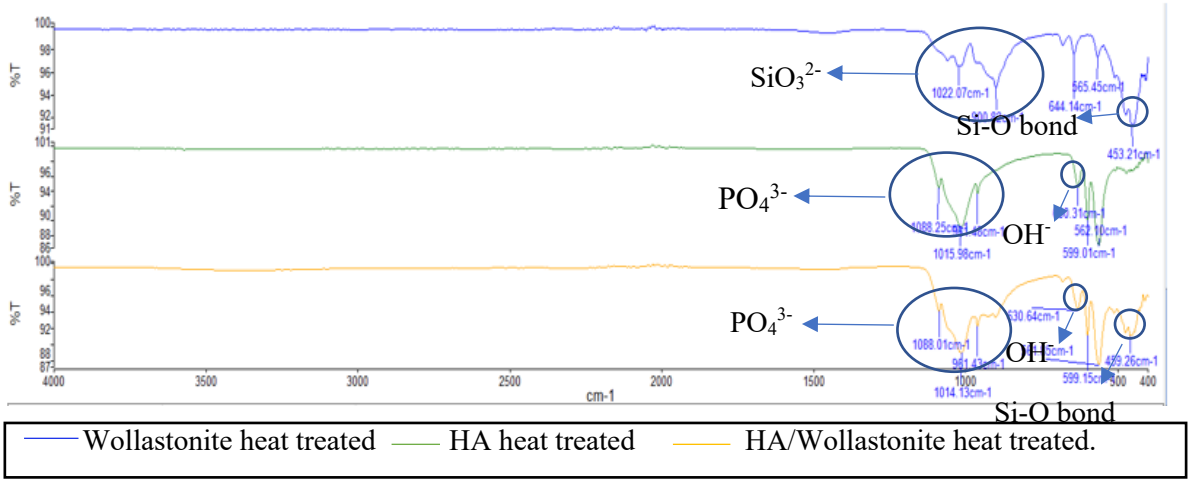

Figure 87, FTIR spectra of spray-coated powders heat treated at 1100 °C for 2 hours in an air atmosphere.

The peaks observed in spray-dried HA powder in **Figure 81** at a wavelength of approximately 3400 cm^{-1} corresponding to the OH^- group (present in adsorbed water) diminished due to heat treatment in the case of spray-coated powders heat-treated at 1100 °C for 2 hours. The FTIR spectra of the heat-treated powder are shown in **Figure 87**. In the case of HA, the broad bands observed at the wavelength of approximately 1088 cm^{-1}, 1024 cm^{-1} and 963 cm^{-1} show the presence of PO_4^{3-} group and bands observed at an approximate wavelength of 632 cm^{-1} show the presence of OH^- group [332, 334].

In the case of Wollastonite, the bands observed at a wavelength in the range of 850-1100 cm^{-1} show the presence of the Si-O-Si bond, indicating the SiO_3^{2-} group and bands observed at a wavelength of approximately 453 cm^{-1} show the presence of the Si-O bond [255, 333].

In the case of HA/Wollastonite coatings, the FTIR spectra pattern was almost similar to that of Hydroxyapatite, with the presence of PO_4^{3-} group at the wavelengths of approximately 1088 cm^{-1}, 1024 cm^{-1} and 963 cm^{-1} and the presence of OH- group at the

wavelength of 632 cm^{-1} [332]. However, a small broadband was observed at an approximate wavelength of 453 cm-1, indicating the presence of a Si-O bond [333]. The FTIR spectra of HA/Wollastonite clearly indicate the presence of HA and a minor presence of Wollastonite. This was due to the higher quantity (80 wt.%) of HA present in the composite powder.

c) *XRD analysis of HA/Wollastonite optimised coating*

The XRD pattern of the HA/Wollastonite was carried out in the same manner as previously mentioned. **Figure 88** shows the XRD pattern of the obtained optimised coating. The HA/Wollastonite (mixed in the ratio of 4:1) was spray-coated onto an untreated grit-blasted (average roughness of 4.01 µm) titanium substrate heat treated at 1100 °C for 2 hours in an air atmosphere. The obtained coating underwent post-heat treatment at 1100 °C for 2 hours in an air atmosphere, which was considered for the study.

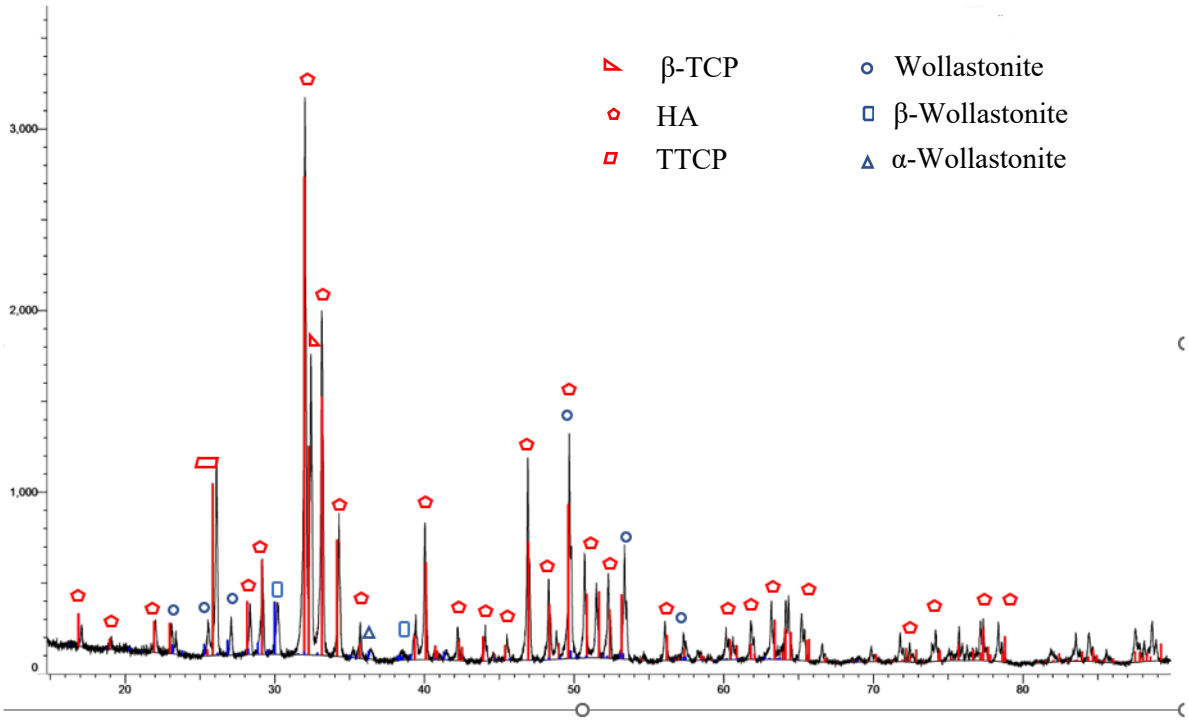

Figure 88, XRD pattern of HA/Wollastonite optimised coating on a grit-blasted sample heat treated at 1100 °C in an air atmosphere

Figure 88 shows the XRD pattern of the HA/Wollastonite spray coated onto a grit blasted post-heat-treated in an air atmosphere at 1100 °C. The peaks of the Wollastonite was not as pronounced as compared to Hydroxyapatite due to its lower quantity (20 wt.% Wollastonite).

In the case of HA, there were peaks observed at an angle (2θ) of approximately 26 °, showing the presence of TTCP and at an angle (2θ) of approximately 32°, showing the presence of β-TCP. The peaks observed at an angle (2θ) of approximately 10°, 18°, 24°, 28°, 30°, 31°, 33°, 34°, 35°, 40°, 42°, 46°, 48°, 50°, 51°, 52°, 56°, 60°, 62°, 64°, 65°, 72°, 74°, 76° and 80°, respectively, shows the presence of Hydroxyapatite, similar to the studies conducted by Levingstone [4].

In the case of Wollastonite, there were peaks of Wollastonite observed at an angle (2θ) of approximately 25°, 23°, 27°, 50°, 53°. Minor peaks of β-Wollastonite observed at an angle (2θ) of approximately of 30° and 39°. There was a smaller presence of α-Wollastonite at an angle (2θ) of approximately 36°. The XRD pattern observed for Wollastonite was similar to the pattern observed by Obeid [345]. The pattern observed was more crystalline than the XRD pattern observed for sol-gel dip-coated samples. There were no peaks of titanium oxide and titanium nitride, which shows the coating covered the substrate layer uniformly. The presence of TTCP, α-TCP, β-TCP, α-Wollastonite and β-Wollastonite was due to the heat treatment of the composite at the higher temperature (1100 °C) [53,162]. β-Wollastonite was more soluble than α-Wollastonite, and α-Wollastonite was more soluble than α-TCP and HA [23, 346]. Therefore, β-Wollastonite and α-Wollastonite are quite soluble in the physiological environment, and the presence of these phases of Wollastonite, along with β-TCP and α-TCP, could increase the amorphous nature of the HA/Wollastonite composite coating, resulting in the early resorption of the coating [23, 343]. In accordance with FDA regulations, the crystallinity of the HA/Wollastonite composite coating should be between 50% and 70%. The crystallinity of all the coating will be presented in **Table 48.**

4.8 Sol-Gel Dip Coating

4.8.1 Dip Coating of Hydroxyapatite

In order to produce a coating of HA, a white precipitate was formed after heating the solution, as mentioned in **Section 3.9 (Figure 40)**. This white precipitate was separated from the deionised with the help of a Büchner funnel with straight sides and perforated plates. It took almost 24 hours for the water to separate from the white precipitate to form a gel. During that time, three titanium alloy substrates; a polished substrate with an average roughness of 0.08 μm, a mid-range roughness substrate with an average roughness of 1.85 μm and grit blasted titanium alloy substrates with an average roughness

of 4.00 µm. In the first set, the as-prepared samples (polished, mid-range and grit-blasted samples) were pre-heated in an air atmosphere at 650 °C. Following that, the as-prepared pre-heated samples were dipped into Hydroxyapatite gel and post-heat treated to 650 ºC in an air atmosphere, similar to studies conducted by Usinskas et al. [300]. In the second set, the as-prepared substrates were dipped into a Hydroxyapatite gel and post-heat treated to 840 ºC in an argon environment, similar to an experiment carried out by Mavis and Taş [254], but heating in a nitrogen environment resulted in the formation of titanium nitride (TiN). Therefore, substrates were heated at 840 °C in an argon environment to create an inert atmosphere [254]. In the third set, the as-prepared sample was preheated to 650 ºC, dipped into Hydroxyapatite gel and post-heat treated to 650 ºC in an argon atmosphere. Usinskas et al. [300] studied sol-gel dip-coating of Hydroxyapatite onto a substrate which was preheated at 650 °C, dipped into Hydroxyapatite and post-heat treated in an air atmosphere at 650 °C at the heating rate of 1 °C/min and the dwell time of 5 hours. The substrates were pre-heated in an argon environment at a similar heating rate and dwell time to arrest the formation of TiO_2 [300]. Moreover, the substrates were heat-treated in an argon atmosphere to reduce TiO_2 formation or other compounds by creating a vacuum.

Figures 89, 90 and **91** show the SEM image of Hydroxyapatite coated on the polished (average roughness: 0.08 µm), mid-range roughness (average roughness: 1.85 µm) and grit blasted (average roughness: 4.01 µm) titanium alloy substrate heat treated in 650 °C in an air atmosphere. **Figures 92, 93** and **94** show the SEM image of Hydroxyapatite coated on the polished (average roughness: 0.08 µm), mid-range roughness (average roughness: 1.85 µm) and grit blasted (average roughness: 4.01 µm) titanium alloy substrate heat treated at 840 °C in an argon atmosphere. **Figures 95, 96** and **97** show the SEM image of Hydroxyapatite coated on the polished (average roughness: 0.08 µm), mid-range roughness (average roughness: 1.85 µm) and grit blasted (average roughness: 4.01 µm) titanium alloy substrate heat treated at 650 °C in an argon atmosphere.

a) *SEM image of dip-coated Hydroxyapatite on titanium alloy*

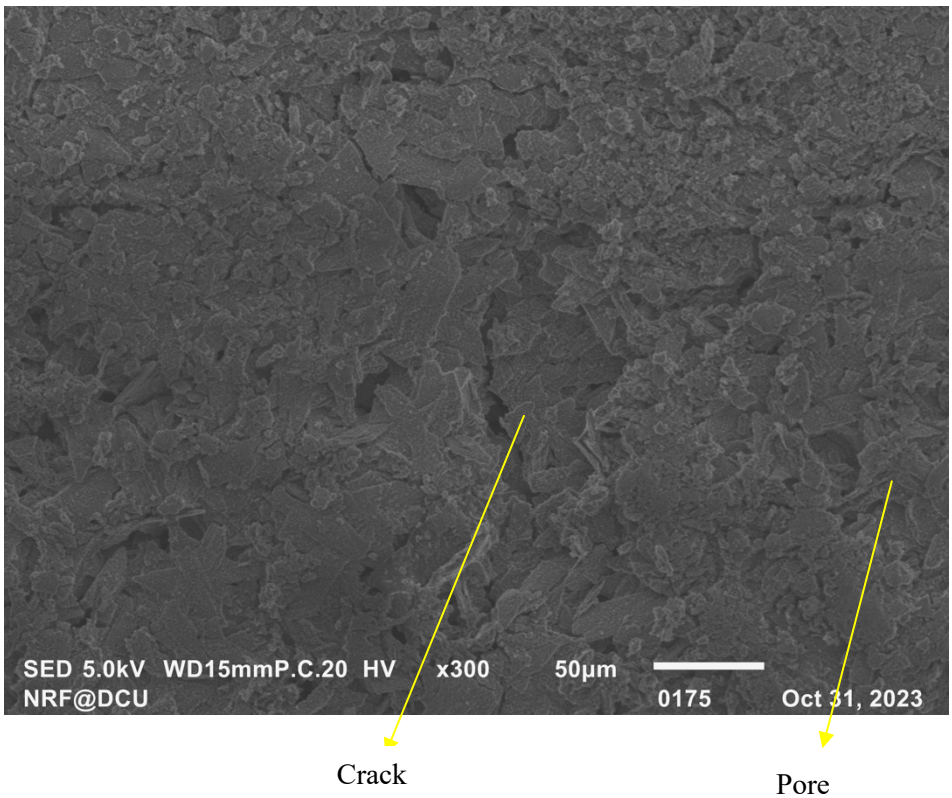

Figure 89, SEM image of Hydroxyapatite gel coating on polished titanium substrate at 650 ^{0}C heat treated in an air environment

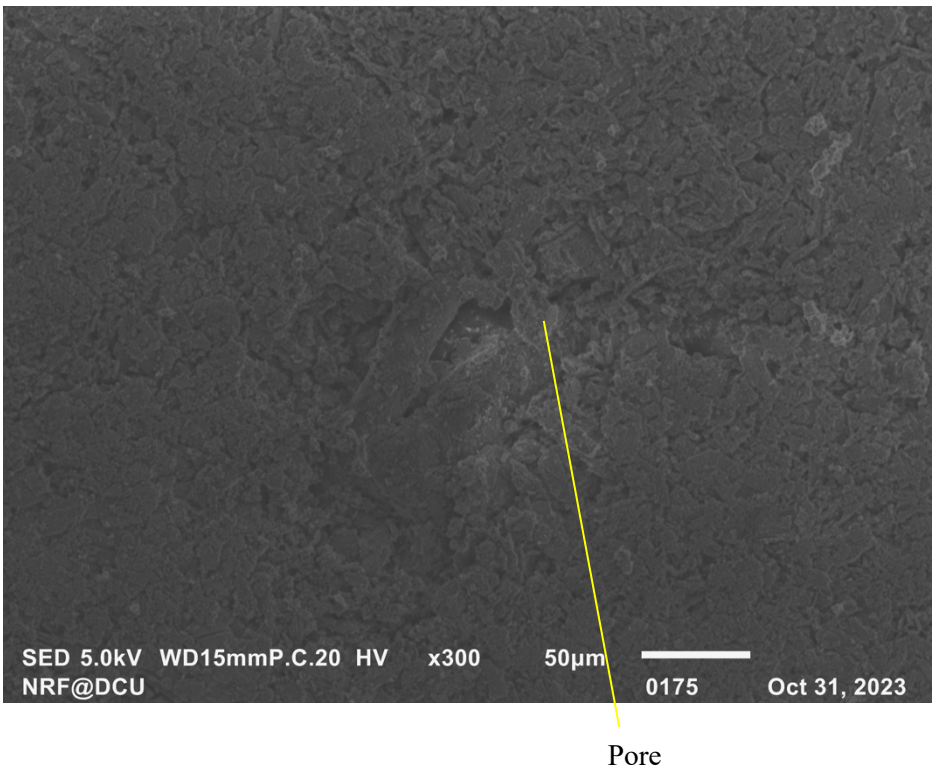

Figure 90, SEM image of Hydroxyapatite gel coating on mid-range titanium substrate at 650 ^{0}C heat treated in an air environment

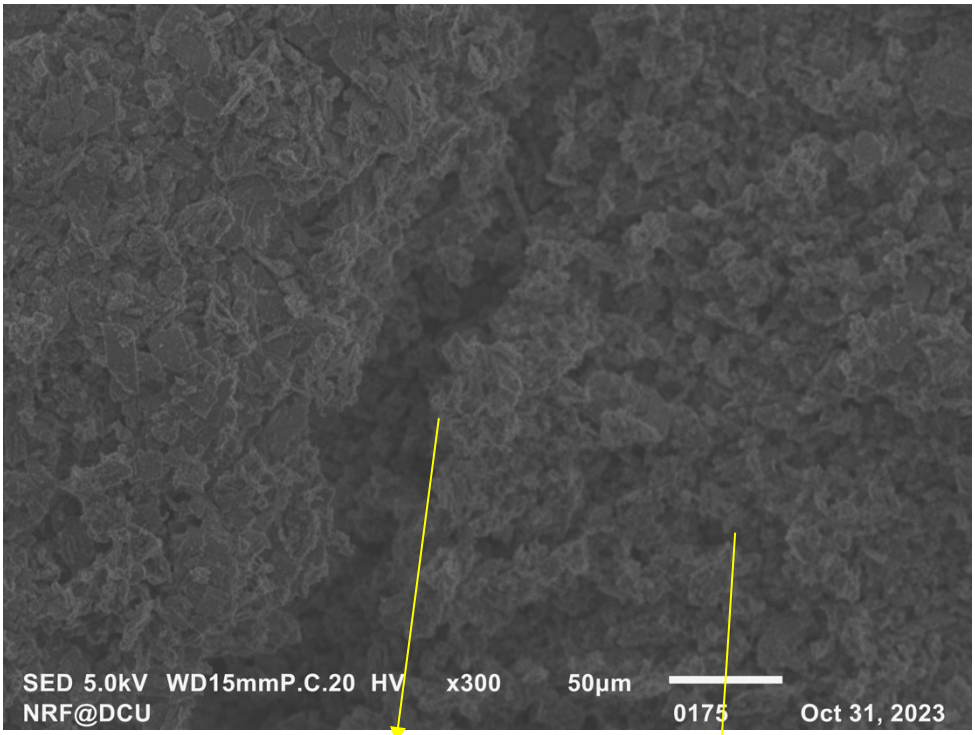

Figure 91, SEM image of Hydroxyapatite gel coating on grit-blasted titanium substrate at 650 ºC heat treated in an air environment

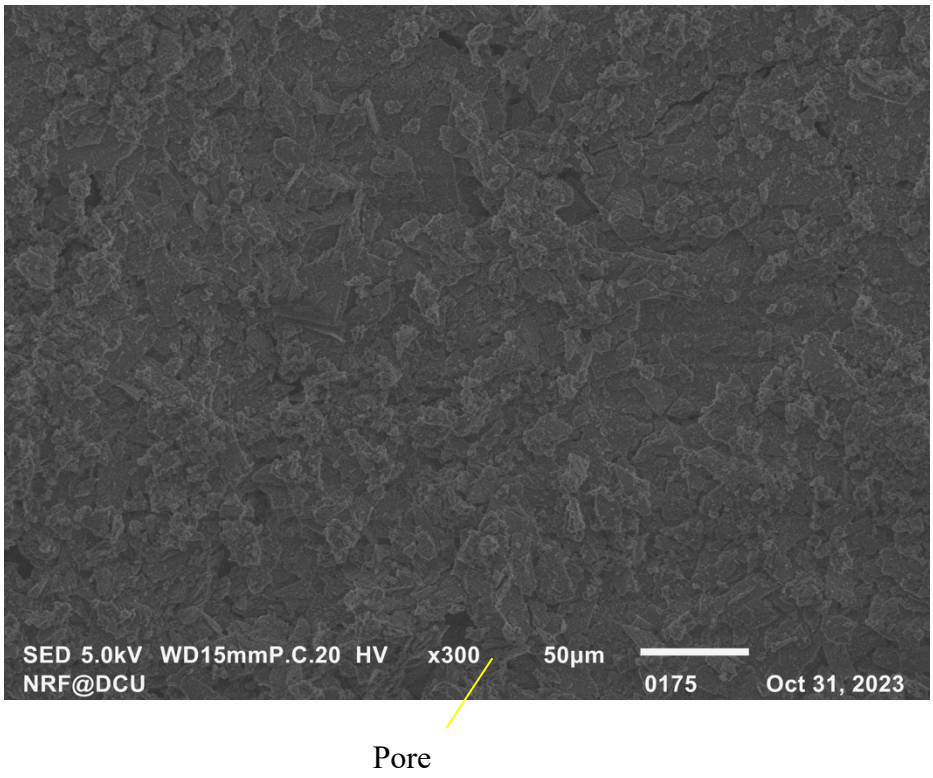

Figure 92, SEM image of Hydroxyapatite gel coating on the polished titanium substrate at 840 ºC heat treated in an argon atmosphere

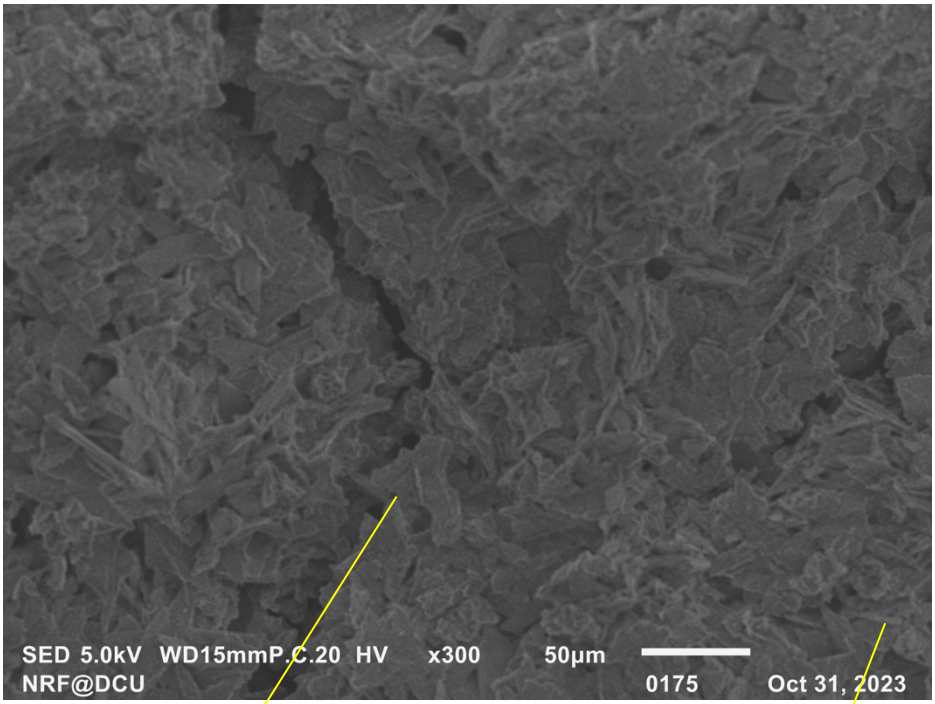

Figure 93, SEM image of Hydroxyapatite gel coating on mid-range titanium substrate at 840 ^{0}C heat treated in an argon atmosphere

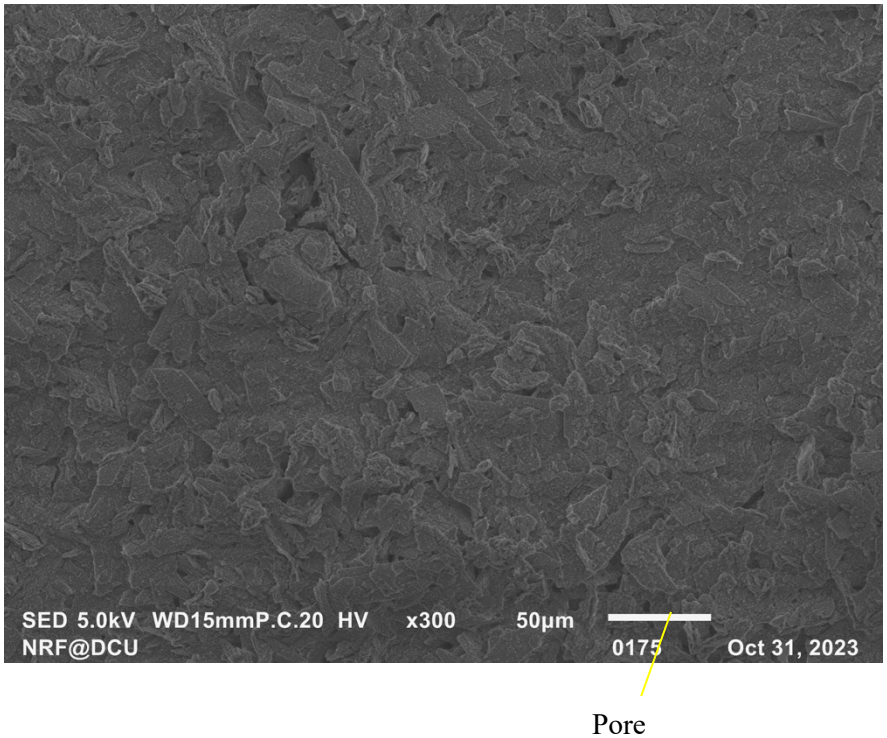

Figure 94, SEM image of Hydroxyapatite gel coating on grit-blasted titanium substrate at 840 ^{0}C heat treated in an argon atmosphere

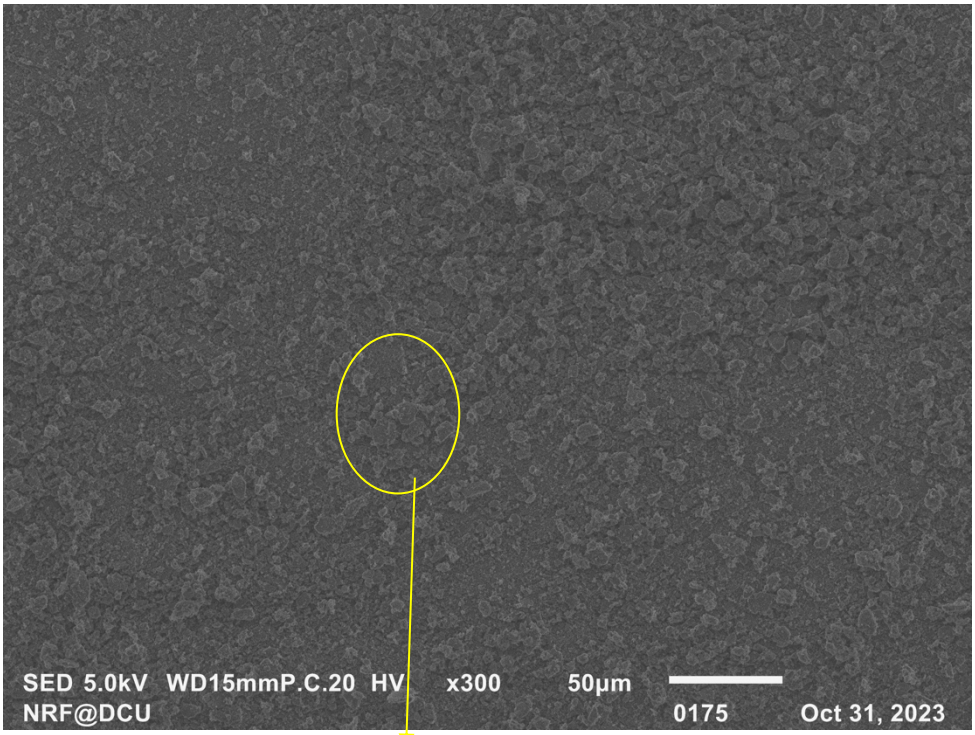

Smooth structure with less porosity and no crack

Figure 95, SEM image of Hydroxyapatite gel coating on polished titanium substrate at 650 ^{0}C heat treated in an argon atmosphere

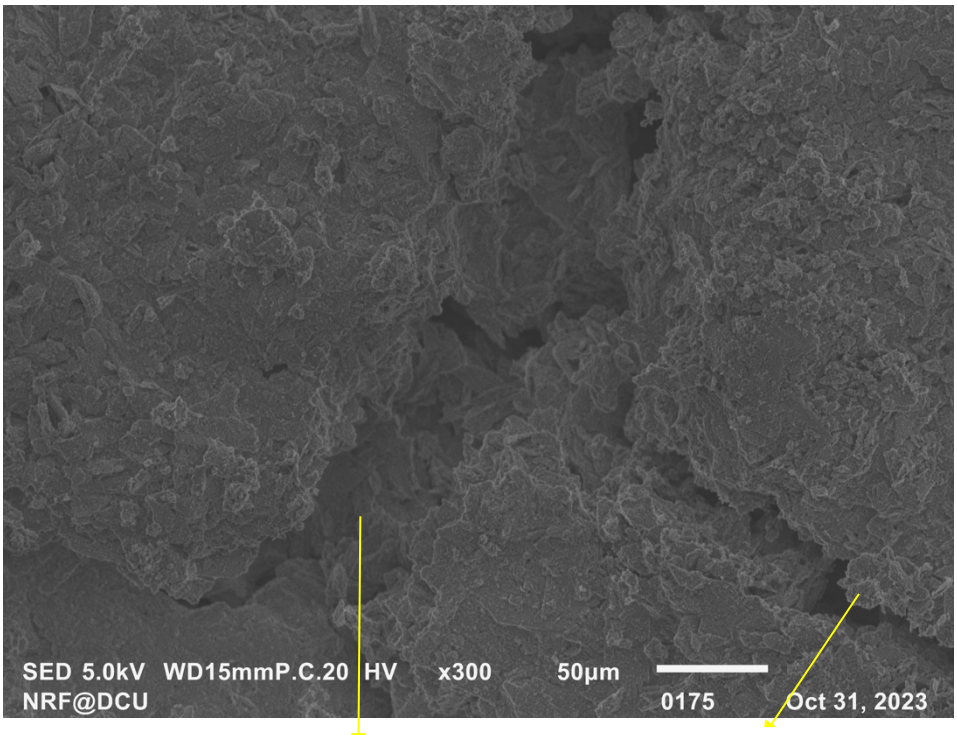

Crack

Pore

Figure 96, SEM image of Hydroxyapatite gel coating on mid-range titanium substrate at 650 ^{0}C heat treated in an argon atmosphere

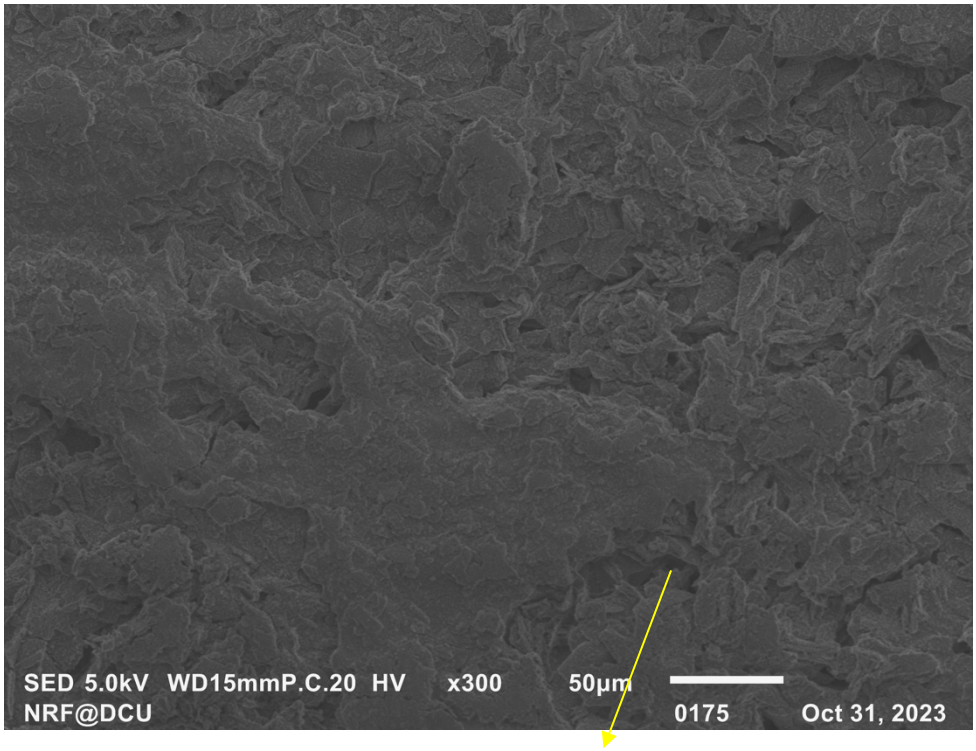

Figure 97, SEM image of Hydroxyapatite gel coating on grit-blasted titanium substrate at 650 ºC heat treated in an argon atmosphere

Almost all of the Hydroxyapatite coated samples demonstrated above had porosity, as supported by Jaafar et al. [250]. Most of the coatings shown above had cracks. The reason was mechanical constraints due to the difference in the coefficient of thermal expansion between Hydroxyapatite and titanium alloy [347]. Moreover, heat treatment of the titanium above 600 °C in an air atmosphere and could be undesirable due to the phase transformation in titanium alloys and the formation of a TiO_2 layer on the substrate, which could result in crack and delamination, as observed in **Figures 68** [250, 312]. Therefore, out of all the coatings observed by SEM, Hydroxyapatite coated on polished titanium sample heat treated at 650 °C in an argon environment (**Figure 95**) had better quality coating. Hydroxyapatite coated on the polished sample had fewer pores and negligible cracks. The reason could be attributed to the slow heating rate (1 °C/min), heat treatment at less than 800 °C, minimal formation of TiO_2 and an inert environment [250].

b) *FTIR spectroscopy of dip-coated Hydroxyapatite on titanium alloy*

In the FTIR spectroscopy, the background was initially checked to ensure no external element was present before scanning the Hydroxyapatite-coated titanium substrates. The

coating side to be characterised was placed against a $LiTaO_3$ with the application of force by a diamond indenter. The force applied in all three substrate types was 69 N. The device automatically calculated an average of four readings.

Figures 98, 99 and 100 show the FTIR spectroscopy with transmittance value in the wavelength range of 400 cm^{-1}- 4000 cm^{-1} for the Hydroxyapatite-coated titanium substrates heat treated at 840 ºC and 650 ºC and comparison with titanium alloy substrate with no HA coating, respectively.

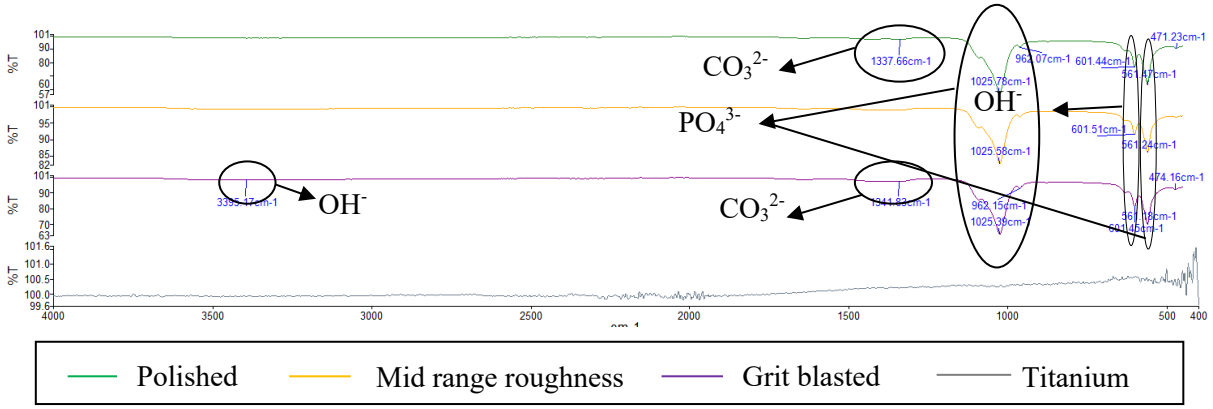

Figure 98, FTIR spectra of HA-coated titanium alloy substrate heat treated at 650 °C in an air atmosphere

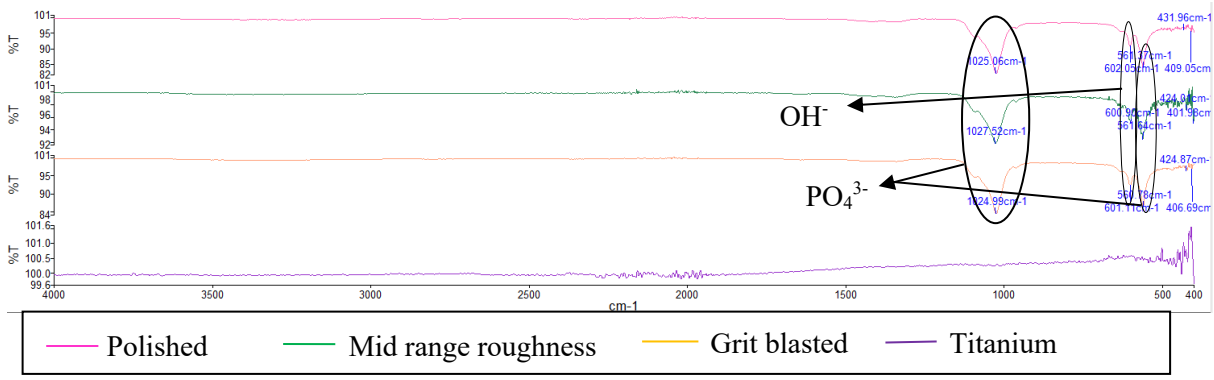

Figure 99, FTIR spectra of HA-coated titanium alloy substrate heat treated at 840 ºC in an argon atmosphere

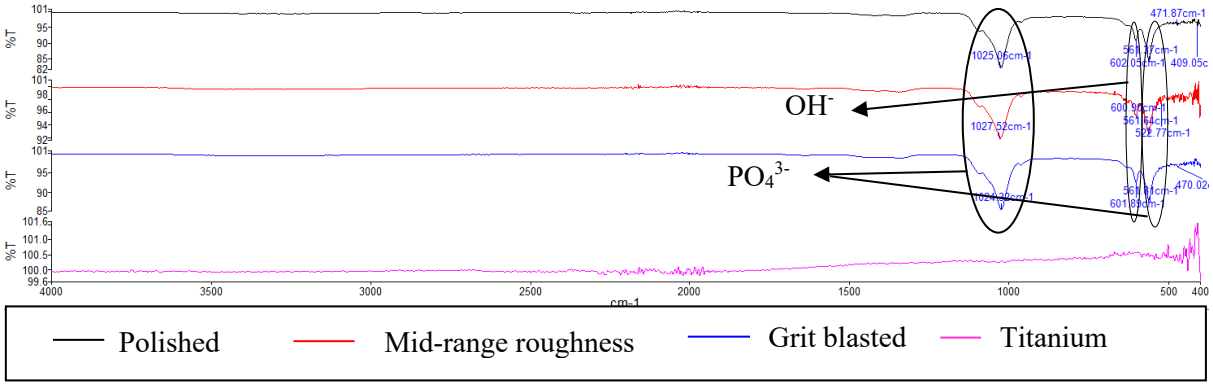

Figure 100, FTIR spectra of HA-coated titanium alloy substrate heat treated at 650 ºC in an argon atmosphere

Figure 98 shows the FTIR spectra of the Hydroxyapatite coated on polished titanium alloy substrate (average roughness: 0.08 µm), mid-range roughness titanium alloy substrate (average roughness: 1.85 µm) and grit blasted titanium substrate (average roughness: 4.01 µm) and titanium alloy substrate with no HA coating heat treated at 650 °C in an air atmosphere. **Figure 99** compared the FTIR spectra of Hydroxyapatite coated on polished (average roughness: 0.08 µm) titanium substrate, mid-range roughness (average roughness: 1.85 µm) titanium substrate, grit blasted titanium substrate (average roughness: 4.01 µm) and titanium alloy substrate with no HA coating post-heat treated at 840 °C in an argon atmosphere. **Figure 100** compared the FTIR spectra of HA coated on polished (average roughness: 0.08 µm) titanium substrate, mid-range roughness (average roughness: 1.85 µm) titanium substrate, grit blasted titanium substrate (average roughness: 4.01 µm) and titanium alloy substrate with no HA coating heat-treated at 650 °C in an argon atmosphere.

Four major broad bands were observed in all the samples. FTIR spectra in the wavelength range of 1350 cm^{-1} showed the presence of CO_3^{2-} [334]. FTIR spectra in the wavelength range of 1024 cm^{-1} and 560 cm^{-1} showed the presence of PO_4^{3-} [334]. FTIR spectra in the wavelength range of 600 cm^{-1} showed the presence of OH^- in apatite, showing the presence of Hydroxyapatite, [334]. The FTIR spectra of Hydroxyapatite-coated polished titanium substrate heat treated at 650 °C in air, respectively (**Figure 98**), had an OH^- band (of adsorbed water) near 3500 cm^{-1} in grit blasted samples. It was observed that the Hydroxyapatite coated on the titanium substrate heat-treated in an inert atmosphere (**Figures 99** and **100**) had sharper broad bands and more distinguishable FTIR patterns of OH^- group and PO_4^{3-} (particularly around 600 cm^{-1} and 560 cm^{-1}). The polished at all temperatures and environmental conditions had deeper transmittance, which might show more Hydroxyapatite deposition at a particular region. The FTIR spectra

around the wavelength was more pronounced around the region 570 cm^{-1} and 600 cm^{-1} (regions of PO_4^{3-}) due to heat treatment [348].The FTIR spectra shown above were very similar to the one suggested by Głąb et al. [334]. The FTIR spectra of the heat-treated titanium substrate presented a straight line with no major bands, similar to that of Ti-6Al-4V FTIR spectra, as described by Dzhurinskiy [349].

Regarding FTIR results, Hydroxyapatite coated on a polished substrate had deeper broad bands, observed at all environmental and temperature conditions. However, heat treatment of titanium at a temperature over 800 °C could result in phase transformation in titanium, as mentioned in the previous subsection. There were peaks of Hydroxyl group (OH^- group) and carbonate group (CO_3^{2-}) in the HA-coated substrate heat treated at 650 °C in air atmosphere , which may be due to incomplete evaporation and decarbonation of HA even at higher temperature [53]. Henceforth, Hydroxyapatite coated on polished titanium alloy substrate heat treated at 650 °C in an argon atmosphere was the most desired FTIR result because most of the peaks corresponded to the presence of Hydroxyapatite.

b) *XRD analysis of Hydroxyapatite-coated titanium substrate*

Four samples of Hydroxyapatite coated on polished titanium alloy substrates were considered for the study. XRD analysis was done on all Hydroxyapatite coated titanium alloy substrates following the procedure mentioned in **Section 3.3.7**. A polished titanium substrate was considered because it had better results regarding SEM and FTIR.

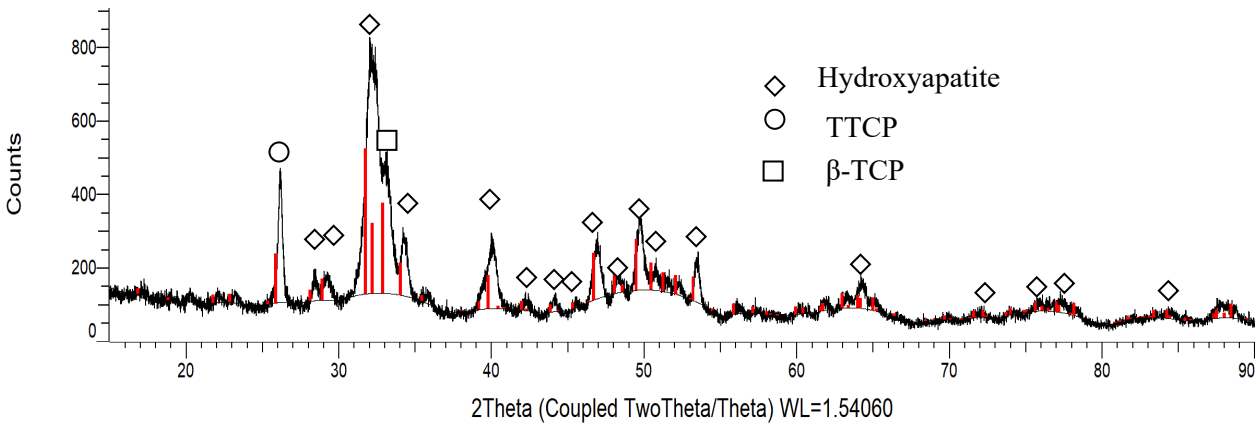

Figure 101, XRD analysis of Hydroxyapatite coated on polished titanium substrate heat treated at 650 °C in an air atmosphere

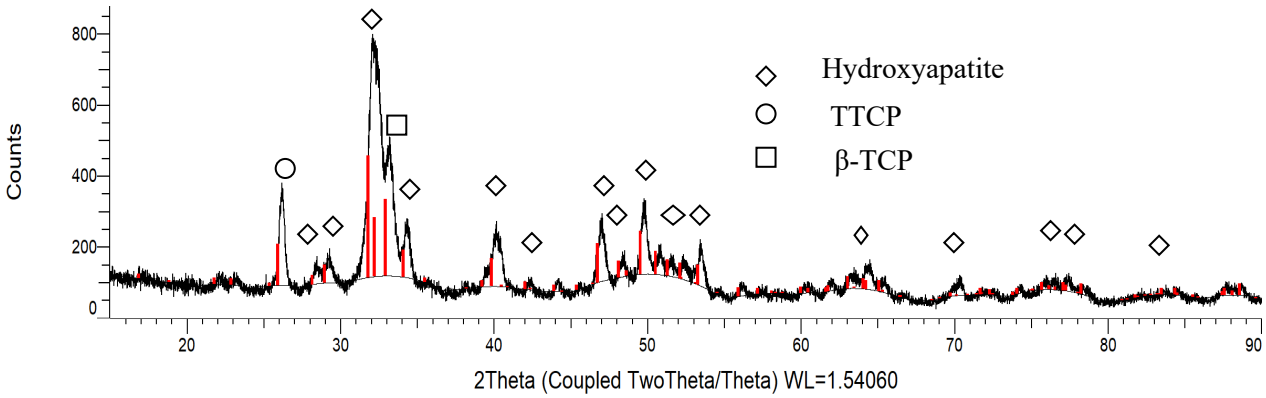

Figure 102, XRD analysis of Hydroxyapatite coated on polished titanium substrate heat treated at 840 °C in an argon atmosphere

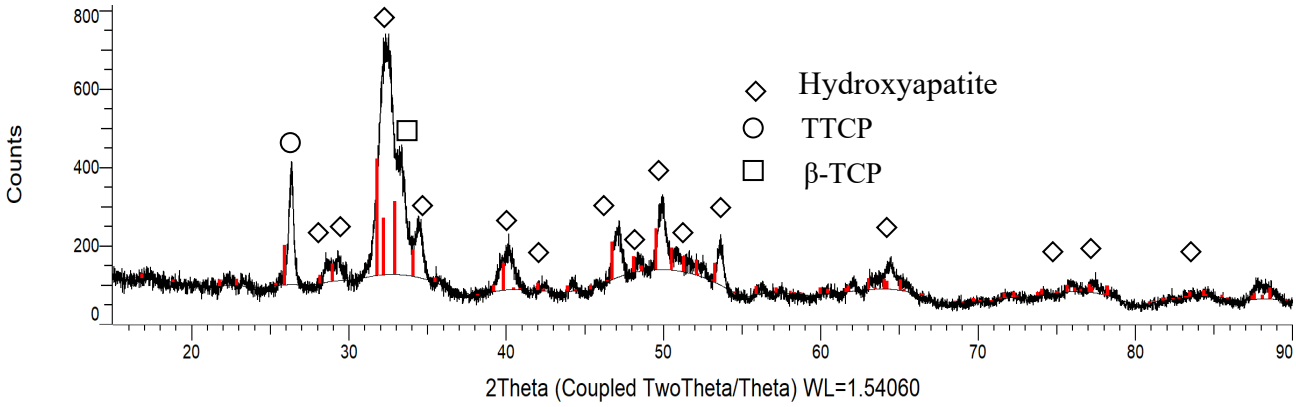

Figure 103, XRD analysis of Hydroxyapatite coated on polished titanium substrate heat treated at 650 °C in an argon atmosphere

Figure 101 shows the XRD analysis of the Hydroxyapatite-coated on a titanium substrate heat-treated at 650 °C in an air atmosphere; **Figure 102** shows the XRD analysis of the Hydroxyapatite-coated on a titanium substrate heat treated at 840 °C in an argon atmosphere and **Figure 103** shows the XRD analysis of the Hydroxyapatite-coated on a titanium substrate heat treated at 650 °C in an argon atmosphere.

The pattern observed in all the samples was similar, with no major difference in the coated titanium alloy substrate at different temperatures and atmosphere conditions. The only phase present was Hydroxyapatite, which red line displayed. More sharp phases were present in the diffraction angle range of 25-37° [350, 351]. There were minor phases of TTCP (Tetracalcium phosphate) at 2θ angle of 25 ° and a small impurity phase of β-TCP at an angle (2θ) of 31.5°, as also found in the studies conducted by Levingstone [4]. An amorphous phase of Hydroxyapatite was present at an angle (2θ) ranging from 30.5 ° and 33.5 ° [4]. No other compounds observed in XRD analysis showed the uniform and nearly pure deposition of the Hydroxyapatite coating onto a titanium surface. Any major change

in the chemical composition of Hydroxyapatite can occur at around 1350 °C, with no involvement of such high temperature in heat treatment or synthesis [79]. There was no presence of titanium nitride (TiN), titanium (Ti) or titanium dioxide (TiO_2) as observed by XRD analysis because the peaks around the angle (2θ) of 38°, 40° or 42° were not pronounced, which showed the uniform layer coating of Hydroxyapatite on a titanium substrate. The XRD pattern, shown in **Figure 102** had broader peaks with less counts but had major peaks observed at an angle (2θ) of 26°, 32°, 34° and diffraction peaks at an angle (2θ) of 40°, 47°, 50 and 54°, similar to XRD studies conducted by Manafi et al. [352].

4.8.2 Dip Coating of Wollastonite

To synthesise a Wollastonite gel, 5.68 ml tetraethyl orthosilicate (TEOS) dissolved in 25 ml ethanol, was added to 5.96 gm calcium nitrate tetrahydrate [$Ca(NO_3)_2.4H_2O$] dissolved in 25 ml ethanol at a pH of 3.5 [255]. Any pH deviation was controlled by adding nitric acid, which acted as a buffer [255], as there were certain issues initially regarding the regulation of the pH. Therefore, a study of pH versus time for both TEOS and [$Ca(NO_3)_2.4H_2O$] dissolved in either 25 ml or 50 ml ethanol was conducted in advance; moreover, studies were carried out on the pH of strong nitric acid and diluted nitric acid.

a) *TEOS in ethanol*

i. 5.68 ml TEOS in 25 ml ethanol

The average weight of two sets at 0 seconds and 1200 seconds (20 minutes) were noted to measure the difference caused by the volatile nature of alcohol. The average weight of the glass beaker was 24.15 grams at 0 seconds, whereas it reduced to 23.68 grams at the end of 20 minutes, with a percentage weight (wt.%) difference of 1.95 wt.%. The weight change was insignificant as the weight loss was less than 5 wt.%, considering the volatile nature of ethanol [353].

Table 37 shows the different parameters used for the formation of the TEOS/ethanol solution and the results found. The average solution temperature for the process ranged between 14.80 °C and 15.00 °C with a maximum temperature difference of 0.20 °C [354]. The average temperature value for the whole process was 14.89 °C. A standard temperature deviation of 0.05 °C was insignificant because no heat treatment was

involved, and the temperature was dependent on external factors such as room/surrounding temperature. **Figure 104** shows the graph of pH versus time.

Table 37, Different parameters for 5.68 ml TEOS dissolved in 25 ml ethanol solution

Time (sec)	Avg wt. (g)	Avg temperature (°C)	pH1	pH2	Avg pH
0	24.15	15.00	6.95	7.24	7.10
30		14.90	6.35	6.07	6.21
60		14.85	5.44	4.55	5.00
90		14.85	4.45	3.82	4.14
120		14.85	3.79	3.39	3.59
150		14.90	3.16	3.10	3.13
180		14.85	2.74	2.90	2.82
210		14.85	2.41	2.70	2.56
240		14.85	2.19	2.50	2.35
270		14.85	2.02	2.35	2.19
300		14.85	1.91	2.21	2.06
330		14.85	1.83	2.12	1.98
360		14.85	1.76	2.03	1.90
390		14.85	1.71	1.94	1.83
420		14.80	1.68	1.89	1.79
450		14.80	1.65	1.86	1.76
480		14.85	1.63	1.82	1.73
510		14.85	1.61	1.80	1.71
540		14.80	1.60	1.78	1.69
570		14.85	1.59	1.76	1.68
600		14.90	1.59	1.75	1.67
630		14.85	1.58	1.73	1.66
660		14.90	1.57	1.74	1.66
690		14.90	1.58	1.73	1.66
720		14.90	1.57	1.72	1.65
750		14.90	1.57	1.72	1.65
780		14.95	1.57	1.70	1.64
810		14.95	1.57	1.70	1.64
840		14.95	1.56	1.70	1.63
870		14.95	1.57	1.70	1.64
900		14.90	1.56	1.70	1.63
930		14.95	1.56	1.70	1.63
960		14.95	1.57	1.70	1.64
990		14.95	1.56	1.71	1.64
1020		14.85	1.56	1.70	1.63
1050		14.85	1.56	1.70	1.63
1080		14.90	1.57	1.71	1.64
1110		14.95	1.57	1.69	1.63

1140		14.95	1.57	1.70	1.64
1170		14.95	1.57	1.70	1.64
1200	23.68	14.95	1.58	1.70	1.64

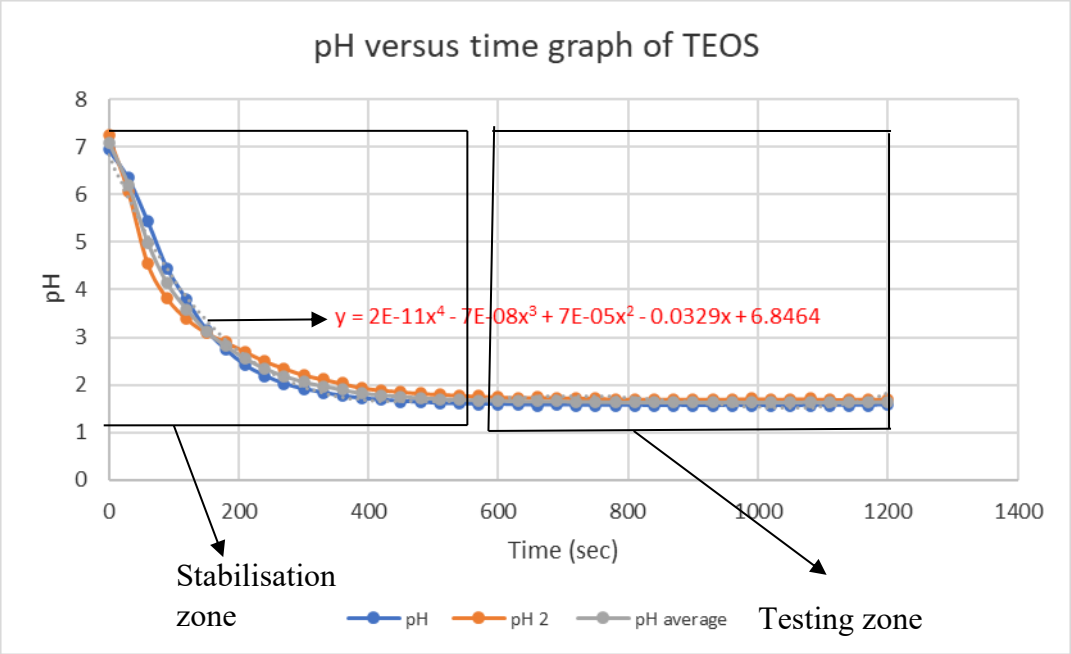

Figure 104, pH versus time graph for 5.68 ml TEOS dissolved in 25 ml ethanol solution.

The solution was continuously stirred to ensure the proper mixing of TEOS with ethanol. The average pH value decreased as the stirring period increased, decreasing from 7.10 at 0 seconds to 1.64 after 1200 seconds, with a pH difference of 5.46. The standard deviation in the pH value of TEOS was 1.27, which was higher than the temperature deviation. To understand the deviation in the average pH value, a deviation was observed after every 5 minutes. As per **Table 37**, the deviation in average pH value decreased as time increased. The average pH value was 7.10 at 0 seconds, which reduced to 2.06 after 300 seconds (5 minutes), showing a standard deviation of 1.70 [355]. The average pH value then reduced from 2.06 at 300 seconds (5 minutes) to 1.67 at 600 seconds (10 minutes) with a standard deviation of 0.10 [355]. The average pH value further reduced from 1.67 at 600 seconds to 1.63 at 900 seconds (15 minutes) with a standard deviation of 0.01. The average pH value increased slightly from 1.63 at 900 seconds (15 minutes) to 1.64 at 1200 seconds (20 minutes) with a standard deviation of 0.003. Therefore, **Figure 104** shows the

stabilisation zone of 0 to 600 seconds and the testing zone after 600 seconds (10 minutes), which can be observed with the nearly straight line after 10 minutes, which implies that the TEOS mixing in ethanol should continue for 10 minutes for the pH value to stabilise, before using the solution for Wollastonite synthesis; therefore, indicating the solution testing should be conducted after 600 seconds (10 minutes).

There were results in the case of 5.68 ml mixed in 25 ml ethanol, but three issues were encountered. Firstly, the beaker had to be tilted at an angle due to low volume occupied by the TEOS solution (5.68 ml TEOS in 25 ml ethanol solution) in the 250 ml beaker, resulting in improper mixing of TEOS and ethanol. Secondly, the weight of the probe tipped the beaker over when a smaller size beaker (50 ml volume) was used. Finally, a narrow beaker (capacity 100 ml) could not accommodate a pH meter probe, temperature probe, or stirring bead due to the volumetric size and shape of the beaker. Therefore, the volume of TEOS and ethanol was doubled to keep the mol/L concentration of TEOS constant [255].

ii. 11.36 ml TEOS in 50 ml ethanol

11.36 ml of TEOS was then added to 50 ml ethanol to address the issues presented above, and the solution was stirred for 20 minutes. The change in pH, weight, and temperature with the stabilisation zone and testing zone was noted. **Table 38** shows the different parameters of TEOS in 50 ml ethanol solution and the results found. **Figure 105** shows the graph of pH versus time of 11.36 ml TEOS in 50 ml ethanol solution.

Table 38, Different parameters for 11.36 ml TEOS in 50 ml ethanol solution

Time (sec)	Weight (g)	Temperature (°C)	pH
0	46.13	15.30	6.67
30		15.10	6.04
60		15.00	5.64
90		15.10	5.32
120		15.10	5.05
150		15.10	4.80
180		15.10	4.57
210		15.10	4.36
240		15.20	4.13
270		15.20	3.93
300		15.20	3.74

330		15.20	3.58
360		15.20	3.41
390		15.20	3.27
420		15.20	3.12
450		15.20	2.99
480		15.20	2.87
510		15.20	2.75
540		15.20	2.63
570		15.30	2.54
600		15.30	2.44
630		15.30	2.36
660		15.30	2.29
690		15.30	2.21
720		15.30	2.15
750		15.30	2.1
780		15.30	2.04
810		15.30	2.00
840		15.30	1.96
870		15.30	1.92
900		15.30	1.89
930		15.30	1.86
960		15.30	1.84
990		15.30	1.82
1020		15.30	1.79
1050		15.40	1.78
1080		15.40	1.76
1110		15.40	1.74
1140		15.40	1.73
1170		15.40	1.72
1200	45.42	15.50	1.71

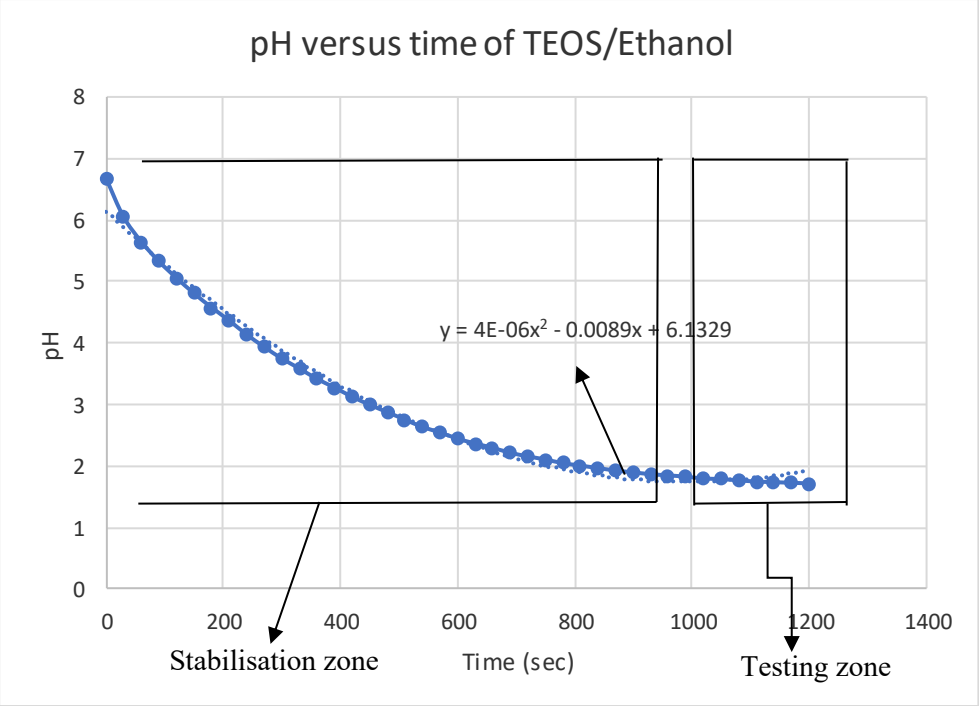

Figure 105, pH versus time for 11.36 ml TEOS dissolved in 50 ml ethanol

Again, the weight was measured at 0 seconds and 1200 seconds, similar to 5.68 ml TEOS in 25 ml ethanol solution. The weight measured was 46.13 grams at 0 seconds and 45.42 grams after 1200 seconds. The weight loss in this experiment was 1.54 wt.%, in fact, less than 5.68 ml TEOS/25 ml ethanol solution at 1.95 wt.%. The reason may be due to the higher stabilisation time observed in 11.36 ml TEOS/50 ml ethanol (15 minutes). TEOS was mixed in the ethanol by dissolution in the stabilisation zone, whereas in the testing zone, it formed a solution (TEOS/ethanol). The weight loss was insignificant (less than 5 wt.%), considering the volatile nature of ethanol [353].

The average temperature of the process was 15.25 °C, which was more than the 5.68 ml TEOS/25 ml ethanol solution (14.89 °C). The temperature reduced from 15.30 °C at 0 seconds to 15.00 °C at 60 seconds (1 minute). The temperature then increased from 15.00 °C at 60 seconds to 15.50 °C after 1200 seconds, with a standard deviation of 0.10 °C and a temperature difference of 0.5 °C [354]. The deviation in the temperature was more than 5.68 ml TEOS/ 25 ml ethanol solution (0.05 °C) but was still insignificant. The temperature value depended on external factors such as room/surrounding temperature. The temperature deviation was insignificant as the testing was done at the same time of the year and in the same location.

The pH value was 6.67 at 0 seconds and reduced to 1.71 after 1200 seconds (20 minutes). The standard deviation in pH value was 1.36, which was similar to the standard deviation of 1.26 found in 5.68 ml TEOS/ 25 ml ethanol solution. To understand this difference, the standard deviation was observed every 5 minutes. The pH value reduced from 6.67 at 0 seconds to 3.74 at 300 seconds with a standard deviation of 0.90 [355]. The standard deviation for the first 5 minutes was less than 5.68 ml/ 25 ml ethanol solution (1.70) due to a gradual decrease in pH value in 11.36 ml TEOS/ 50 ml ethanol solution. The pH value was then reduced to 2.44 at 600 seconds, with a standard deviation of 0.43, compared to a higher standard deviation (0.01) for 5.68 ml TEOS/ 25 ml ethanol solution [355]. The pH value further reduced between 600-900 seconds with a value of 1.89 at 900 seconds, with a standard deviation of 0.18, more than 5.68 ml TEOS/ 25 ml ethanol solution (0.01) [355]. The pH value continuously reduced to 1.71 at 1200 seconds (standard deviation of 0.06) [355]. The lowest/final pH value was 1.71 for the 11.36 ml TEOS/ 50 ml ethanol solution, whereas the lowest value was 1.64 for the 5.68 ml TEOS/ 25 ml ethanol solution. Whilst these two values were similar, considering the change in the concentration of TEOS and ethanol, there were no experimental challenges during the 11.36 ml TEOS/50 ml ethanol compared to the initial 5.68 ml/25 ml experiment. A stabilisation zone was observed after 15 minutes for the 11.36 ml TEOS/ 50 ml ethanol solution, unlike the 5.68 ml TEOS/ 25 ml ethanol solution, which had a stabilisation zone after 10 minutes. Also, there was a more sudden decrease in the pH value for the 5.68 ml TEOS/ 25 ml ethanol solution. In contrast, there was a gradual decrease in the pH value for the 11.36 ml TEOS/ 50 ml ethanol solution, which can be observed in **Figure 105**. Therefore, the testing zone, which is when TEOS solution should be added calcium nitrate solution, must be conducted after 15 minutes when using a 11.36 ml TEOS/ 50 ml ethanol solution. 11.36 ml TEOS/50 ml ethanol solution was required for peristaltic pump solution method as 5.68 ml/ 25 ml ethanol was not feasible. The comparison between all the methods with results were detailed in **Section c**).

b) *5.96 gm calcium nitrate tetrahydrate in 25 ml ethanol*

To analyse the calcium nitrate/ethanol solution, the average weight of two sets of the solution was 25.14 grams at 0 seconds, and this decreased to 24.75 grams after 1200 seconds (20 minutes), with a percentage weight difference of 1.57 wt.%. The weight loss of the solution after 1200 seconds (20 minutes) was insignificant (less than 5 wt.%),

considering the volatile nature of the ethanol [353]. **Table 39** shows the different parameters of calcium nitrate solution with results.

Table 39, Different parameters for 5.96 g of calcium nitrate tetrahydrate/25 ml ethanol solution

Time (sec)	Avg wt (g)	Avg temperature (°C)	pH1	pH2	Avg pH
0	25.14	16.10	7.00	6.90	6.95
30		15.70	5.66	5.73	5.70
60		15.45	5.71	5.68	5.70
90		15.25	5.74	5.61	5.68
120		15.15	5.80	5.64	5.72
150		15.05	5.81	5.65	5.73
180		14.90	5.79	5.64	5.72
210		14.90	5.78	5.62	5.70
240		14.85	5.77	5.60	5.69
270		14.80	5.75	5.53	5.64
300		14.75	5.73	5.49	5.61
330		14.75	5.69	5.49	5.59
360		14.75	5.65	5.49	5.57
390		14.75	5.61	5.45	5.53
420		14.75	5.59	5.48	5.54
450		14.70	5.57	5.41	5.49
480		14.75	5.55	5.39	5.47
510		14.75	5.54	5.36	5.45
540		14.70	5.51	5.35	5.43
570		14.75	5.49	5.34	5.42
600		14.75	5.47	5.31	5.39
630		14.75	5.45	5.29	5.37
660		14.70	5.42	5.27	5.35
690		14.75	5.39	5.26	5.33
720		14.80	5.37	5.24	5.31
750		14.80	5.35	5.22	5.29
780		14.80	5.34	5.20	5.27
810		14.85	5.31	5.18	5.25
840		14.85	5.3	5.16	5.23
870		14.85	5.29	5.15	5.22
900		14.90	5.28	5.13	5.21
930		14.95	5.26	5.12	5.19
960		14.95	5.24	5.10	5.17
990		14.95	5.23	5.08	5.16
1020		15.05	5.21	5.07	5.14
1050		15.00	5.19	5.06	5.13
1080		15.00	5.17	5.05	5.11

1110		15.05	5.16	5.03	5.10
1140		15.10	5.15	5.02	5.09
1170		15.10	5.13	5.01	5.07
1200	24.75	15.15	5.12	5.00	5.06

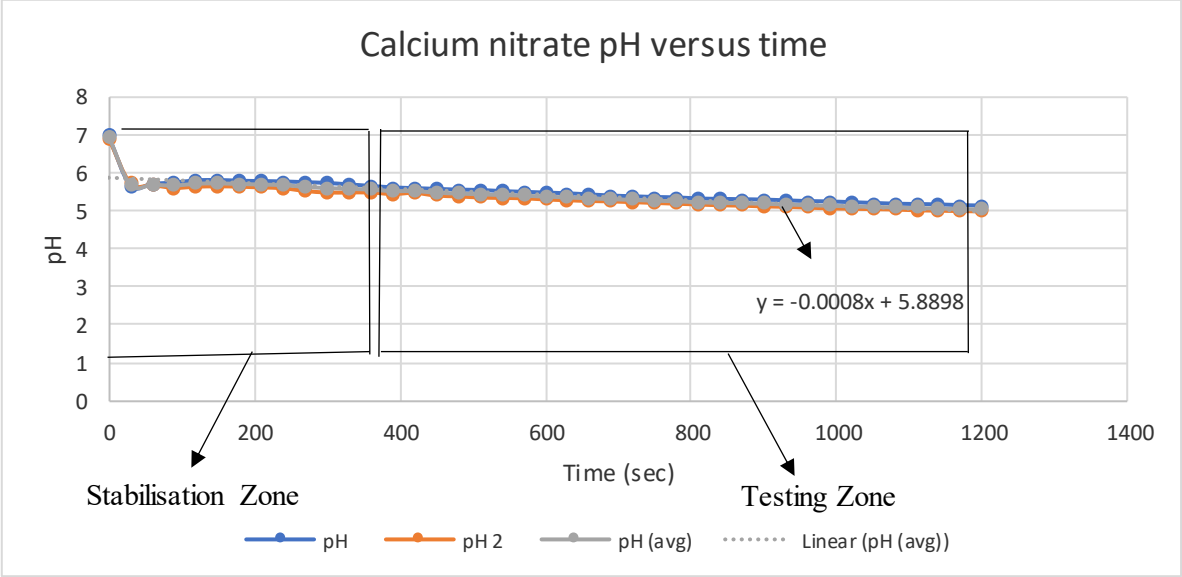

Figure 106, pH versus time graph for calcium nitrate tetrahydrate/ethanol solution

The largest temperature difference was 1.40 °C. The average temperature of the two sets was 16.10°C at 0 seconds and thus reduced to 14.70 °C at 450 seconds. The average temperature of the two sets changed from 14.70 °C at 450 seconds to 15.15 °C at 1200 seconds. The deviation in average temperature was 0.28, which may be due to a higher average temperature (16.10 °C) at 0 seconds, reduced to 14.70 °C at 450 seconds, and changed to 15.15 °C after 20 minutes (1200 seconds) [356]. The average temperature value decreased from 0 seconds to 450 seconds but did not vary significantly from 450 seconds to 1200 seconds. The average temperature may have dropped due to the addition of calcium nitrate tetrahydrate to the ethanol [356].

The average value of the pH for the whole process was 5.43. The pH difference of the solution was 1.89, with a standard deviation of 0.33. The average pH of the solution reduced from 6.95 at 0 seconds to 5.70 after 60 seconds [357]. There was a slight change in the average pH value from 30 seconds to 20 minutes, with a pH of finally at 5.06 after 1200 seconds (20 minutes) [357]. The average pH value only reduced slightly after every 30 seconds. The average pH value reduced from 6.95 to 5.61, with a standard deviation 0.38 between 0 and 30 seconds. The average pH value reduced from 5.61 to 5.39 with a

standard deviation of 0.07 between 300 and 600 seconds [357]. The average pH value further reduced from 5.39 to 5.21, with a standard deviation of 0.06 from 600 to 900 seconds [357]. Finally, the average was reduced to 5.06 after 1200 seconds (20 minutes) with a standard deviation of 0.05 [357]. **Figure 106** shows a pH versus time graph of calcium nitrate solution, indicating a stabilisation time of 5 minutes or testing time after 5 minutes.

c) *Solution for Wollastonite synthesis*

i. Wollastonite solution by a peristaltic pump

As per the previous section, only half of the total 61.36 ml solution (50 ml ethanol and 11.36 ml TEOS) was transferred via a peristaltic pump, thus the volume of mixtures were adjusted accordingly. To form a Wollastonite solution, 5.68 ml TEOS dissolved in 25 ml ethanol (1 mol/L) was added to 5.96 grams of calcium nitrate tetrahydrate dissolved in 25 ml ethanol (1 mol/L) [255]. Therefore, half the amount of TEOS dissolved in ethanol solution (30.68 ml solution) was added drop-by-drop to the calcium nitrate tetrahydrate dissolved in solution for 5 minutes at a pump flow rate of 6 ml/min. The peristaltic pump had a range of values for pump flow. This value varied from 0 to 4600 ml/hr, as per **Table 40,** which shows the scaled value relating to the pump flow rate.

Table 40, Scaled value for pump flow [307]

Scale	ml/hr
0	0
10	350
20	600
30	1000
35	1500
40	1900
45	3200
50	4600

According to the results obtained detailed in **Table 40**, 6 ml/min corresponded to a scale value of 10 (at scale value and the pump flow rate was 350 ml/hr, equal to 350 ml/60

minutes = 5.83 ml/minute). However, as this was not an exact value, the scaled values and corresponding pump flow rate values were plotted, given in **Figure 107**.

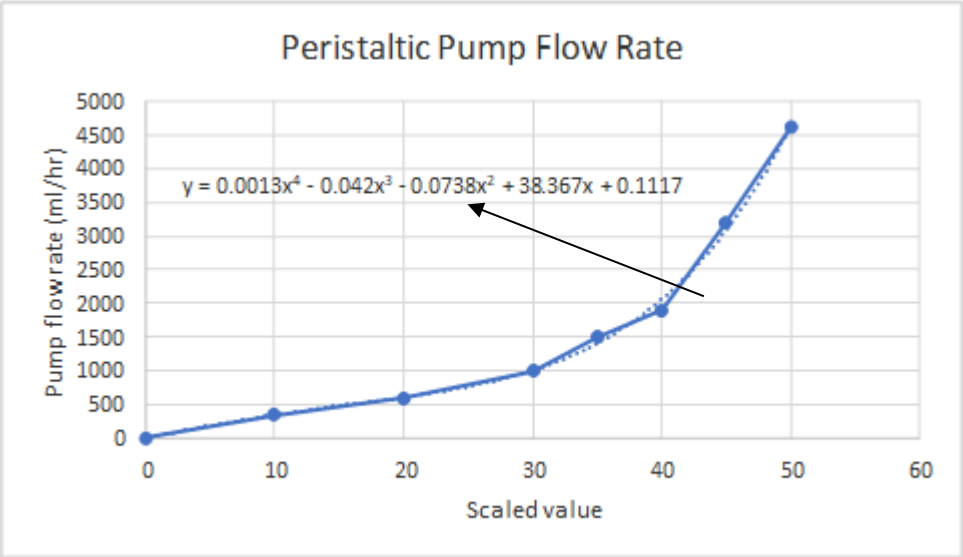

Figure 107, Pump flow rate of peristaltic pump versus scaled value

After calibration, a pump flow rate of 360 ml/hr (6 ml/min), yielded a scaled value of 10.45. However, as only whole numbers are displayed on the peristaltic pump, the scaled value taken was 10.

60 ml ethanol was passed through the peristaltic pump at the scale value of 10 to calculate the actual flow rate. The measuring beaker was placed on the other side with time calibration. It took 10 minutes for 60 ml of ethanol to transfer from the glass beaker to the measuring beaker. Generally, distilled water is passed through to check the actual flow rate, however, as water causes TEOS to degrade to silica and ethanol, this could not be achieved [358].

Two sets of experiments were performed to improve the repeatability. **Table 41** shows the temperature and pH values every 30 seconds with the addition of a TEOS/ethanol solution to a calcium nitrate tetrahydrate/ethanol solution produced via a peristaltic pump. **Figure 108** shows the graph of the set of experiments.

Table 41, 11.36 ml TEOS/50 ml ethanol addition to calcium nitrate tetrahydrate/ethanol via peristaltic pump

Time (sec)	Average temperature (°C)	pH3	pH4	Average pH
0	17.85	5.29	5.28	5.28
30	17.85	5.17	5.07	5.12
60	18.05	5.08	4.98	5.03
90	18.25	4.96	4.67	4.81
120	18.30	4.81	4.48	4.64
150	18.40	4.65	4.43	4.54
180	18.50	4.53	4.36	4.44
210	18.60	4.40	4.29	4.34
240	18.65	4.29	4.24	4.26
270	18.65	4.15	4.20	4.17
300	18.75	4.08	4.11	4.09

The average temperature increased by almost from 16.85 °C at 0 seconds to 18.75 °C after 300 seconds, with a gradual increase in the temperature after 60 seconds [354]. The average temperature increased steadily from 18.30 °C at 120 seconds to 18.75 °C after 300 seconds, with a temperature difference of 0.90 °C and a standard deviation of 0.32 °C. The addition of TEOS/ethanol solution, therefore, increased the temperature of the solution [354].

The pH decreased with the stirring time and the addition of TEOS/ethanol to the calcium nitrate tetrahydrate/ethanol solution. The average pH value was 5.29 at 0 seconds and reduced to 4.09 after 300 seconds for the first set. In the second set of experiments, the average pH value reduced from 5.28 at 0 seconds to 4.54 after 150 seconds. However, the pH value reduction was not much after 150 seconds. The reason may be due to the stabilisation of the solution. There was a gradual reduction in the pH value, with a pH difference of 1.19 and a standard deviation of 0.40. **Figure 107** shows the graph of the pH versus time of the Wollastonite synthesis by peristaltic pump for two experiment sets. The graph shows less difference between the values of each of the two sets at any particular time.

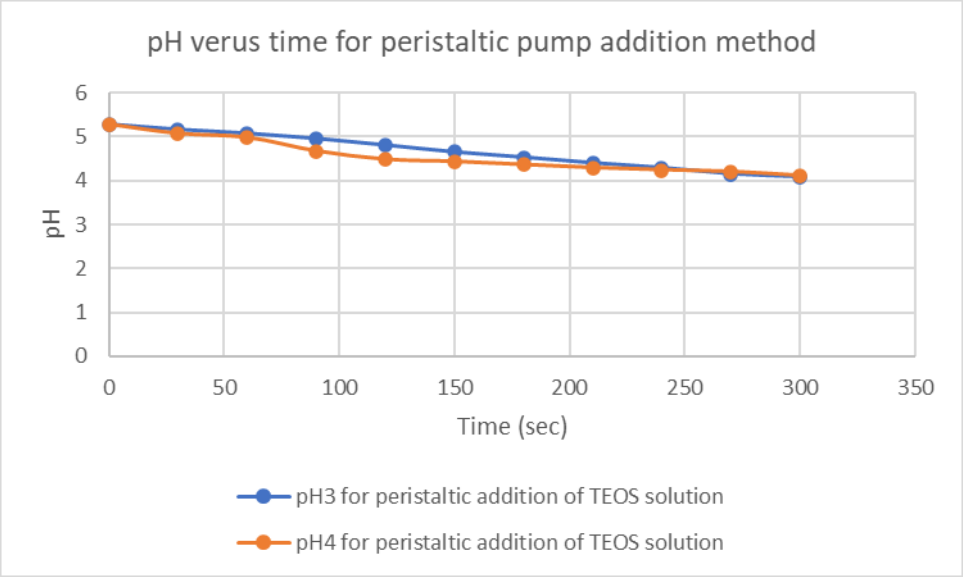

Figure 108, pH value for Wollastonite synthesis by peristaltic pump method

ii. Wollastonite synthesis by constant addition method with 11.36 ml TEOS/50 ml ethanol solution

In this method, approximately half the quantity prepared of TEOS/ethanol solution (30.68 ml) was added to calcium nitrate tetrahydrate/ethanol solution via a 10 ml syringe, as detailed in **Figure 41**, which equated to 7 ml of TEOS/ethanol solution each minute for 4 minutes (7 * 4 = 28 ml of TEOS solution) and 2.86 ml of TEOS/ethanol solution at the fifth minute. Two sets of experiments were performed to understand the change in pH with time after adding TEOS to calcium nitrate solution. **Table 42** shows the average pH and average temperature results of TEOS/ethanol solution addition to calcium nitrate tetrahydrate/ethanol solution in increments.

Table 42, TEOS/ethanol solution addition to calcium nitrate tetrahydrate /ethanol solution at a constant rate (by constant addition) with 11.36 ml TEOS/50 ml ethanol solution

Time (sec)	Average temperature (°C)	pH5	pH6	Average pH
0	16.15	5.24	5.27	5.25
30	16.30	5.02	5.04	5.03
60	16.50	4.81	4.82	4.81
90	16.60	4.57	4.60	4.58
120	16.80	4.30	4.36	4.33
150	16.90	4.24	4.26	4.25
180	17.00	4.14	4.17	4.15
210	17.05	4.09	4.13	4.11
240	17.15	4.04	4.08	4.06
270	17.20	4.03	4.07	4.05
300	17.20	4.02	4.05	4.03

The temperature of the solution increased by then 1 °C with the addition of TEOS/ethanol solution [354]. The temperature effect on the whole process was due to the addition of TEOS/ethanol solution, with a temperature difference of 1.05 °C and a standard deviation of 0.37 °C. The average temperature increased from 16.15 °C at 0 seconds to 17.2 °C after 300 seconds.

The pH decreased with the addition of TEOS/ethanol solution. The pattern observed in both sets was almost similar, as shown in **Figure 108** and **Table 42**. For the first set, the pH was 5.24 at 0 seconds and reduced to 4.02 after 300 seconds, whereas for the second set, the pH value reduced from 5.27 at 0 seconds to 4.05 after 300 seconds. The average pH reduced gradually from 5.25 at 0 seconds to 4.25 at 150 seconds. The reason may be the slow mixing of TEOS/ethanol solution with calcium nitrate tetrahydrate/ethanol solution. However, after 150 seconds, the pH reduction was not pronounced compared to the first 150 seconds. The reason may be due to a saturation point attained due to the addition of TEOS/ethanol solution to calcium nitrate tetrahydrate/ethanol after 150 seconds.

Figure 109 shows the graph of pH value versus time for the constant addition of TEOS/ethanol solution to calcium nitrate tetrahydrate/ethanol solution. The pattern for the change in the pH concerning the two sets was similar, with almost equal values. The difference in the average pH value was 1.22, with a standard deviation in pH of 0.44.

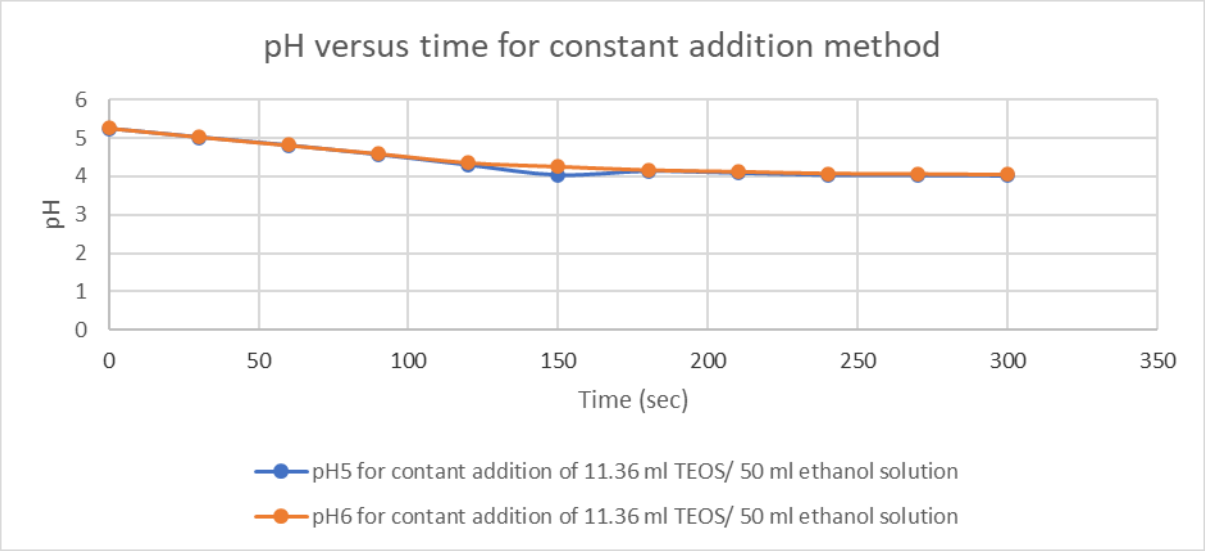

Figure 109, pH value versus the time for Wollastonite synthesis by constant addition method with 11.36 ml TEOS/50 ml ethanol solution

iii. Direct TEOS/ethanol solution addition with 11.36 ml TEOS/50 ml ethanol solution

Two sets of experiments were performed to reduce the deviation caused by temperature and pH values at different times. This method completely added 30.68 ml TEOS/ethanol solution to the calcium nitrate tetrahydrate/ethanol solution after the stabilisation time of TEOS/ethanol solution and calcium nitrate tetrahydrate/ethanol solution. The pH and temperature were noted every 30 seconds. **Table 43** shows the average pH and temperature value for direct TEOS/ethanol addition to calcium nitrate tetrahydrate/ethanol solution.

Table 43, Direct TEOS/ ethanol solution direct addition to calcium nitrate tetrahydrate/ethanol solution with 11.36 ml TEOS/50 ml ethanol solution

Time (sec)	Average temperature (°C)	pH7	pH8	Average pH
0	17.05	5.29	5.43	5.36
30	17.70	4.64	4.85	4.74
60	17.85	3.98	4.36	4.17
90	17.95	3.95	4.14	4.04
120	18.05	3.93	4.07	4.00
150	18.15	3.92	4.04	3.98
180	18.30	3.91	4.01	4.06
210	18.35	3.92	4.00	3.92
240	18.45	3.92	3.99	3.95
270	18.65	3.92	3.38	3.95
300	18.75	3.91	3.97	3.94

The temperature of the solution increased with the addition of TEOS/ethanol solution [354]. The temperature difference for the process was 1.70 °C, with a standard deviation of 0.48 °C. The average temperature was 17.05 °C at 0 seconds and increased to 17.85 °C after 60 seconds. The average temperature then increased to 18.75 °C after 300 seconds.

A drastic pH reduction was observed initially due to the complete addition of TEOS/ethanol solution. The first set had a pH value of 5.29 at 0 seconds and 3.91 after 300 seconds, whereas the second set had a pH value of 5.43 and was reduced to 3.91 after 300 seconds. The pH value was more or less equal to 4.00 after 120 seconds, with negligible difference observed in both sets. The pH value reduced significantly at the start, but the decrease in pH value was not so prominent after 120 seconds. The difference in the average pH value was 1.42, with a standard deviation of 0.45. **Figure 110** shows the pH value versus the time for both sets of experiments for Wollastonite synthesis by the direct addition method with 11.36 ml TEOS/50 ml ethanol solution.

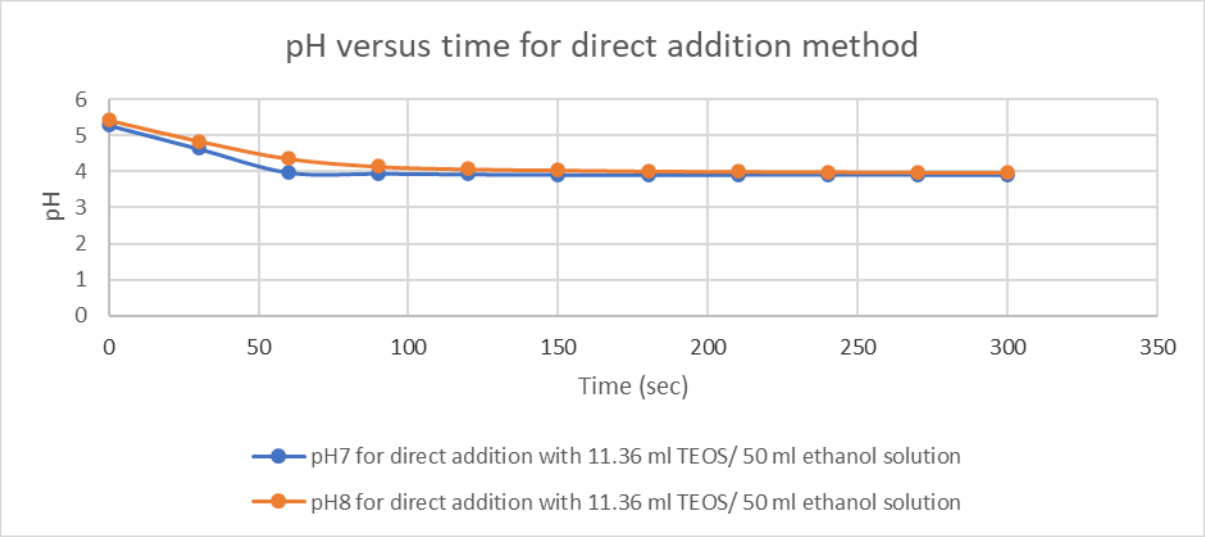

Figure 110, pH value versus the time for Wollastonite synthesis by direct addition method with 11.36 ml TEOS/50 ml ethanol solution

iv. TEOS/ethanol solution constant addition with 5.68 ml TEOS/25 ml ethanol solution

In this method, 30.68 ml of TEOS/ethanol solution was added to calcium nitrate tetrahydrate/ethanol solution via a 10 ml syringe, as detailed in **Figure 42**, which equates to 7 ml of TEOS/ethanol solution each minute for 4 minutes (7 * 4 = 28 ml of TEOS solution) and 2.86 ml of TEOS/ethanol solution at the fifth minute. Two sets of experiments were performed to understand the change in pH with time after adding TEOS/ethanol to calcium nitrate tetrahydrate/ethanol solution. **Table 44** shows the average pH and temperature results of TEOS/ethanol solution addition to calcium nitrate tetrahydrate/ethanol solution in increments with 5.68 ml TEOS/25 ml ethanol solution.

Again, the pH decreased with the addition of TEOS/ethanol solution. The pattern observed in both sets was similar to the constant addition method with 11.36 ml TEOS/50 ml ethanol solution. The average pH reduced gradually from 5.24 at 0 seconds to 4.15 at 150 seconds. The reason may be the slow mixing of TEOS/ethanol solution with calcium nitrate tetrahydrate/ethanol solution. However, after 150 seconds, the pH reduction was not pronounced compared to the first 150 seconds. The reason may be due to a saturation point attained due to the addition of TEOS/ethanol solution to calcium nitrate tetrahydrate/ethanol after 150 seconds.

Figure 111 shows the graph of pH value versus time for the constant addition of TEOS/ethanol solution to calcium nitrate tetrahydrate/ethanol solution. The pattern for the change in the pH concerning the two sets was similar, with almost equal values. The difference in the average pH value was 1.25, with a standard deviation in pH of 0.48. **Table 44** shows the pH value versus the time for both sets of experiments for Wollastonite synthesis by the constant addition method with 5.68 ml TEOS/25 ml ethanol solution.

Table 44, TEOS/ethanol solution addition to calcium nitrate tetrahydrate /ethanol solution at a constant rate with 5.68 ml TEOS/25 ml ethanol solution

Time (sec)	Average temperature (°C)	pH9	pH10	Average pH
0	18.00	5.25	5.23	5.24
30	18.50	5.12	5.17	5.14
60	18.50	4.80	4.73	4.76
90	18.60	4.48	4.43	4.45
120	18.75	4.22	4.19	4.20
150	18.80	4.15	4.1	4.12
180	18.95	4.08	4.03	4.05
210	19.15	4.01	4.01	4.01
240	19.20	4.00	3.99	3.99
270	19.40	4.00	3.98	3.99
300	19.50	4.00	3.97	3.98

The temperature of the solution increased with the addition of TEOS/ethanol solution [354]. The average temperature increased from 18.0 °C at 0 seconds to 19.5 °C after 300 seconds. The temperature effect on the whole process was due to the addition of TEOS/ethanol solution, with a temperature difference of 1.50 °C and a standard deviation of 0.45 °C.

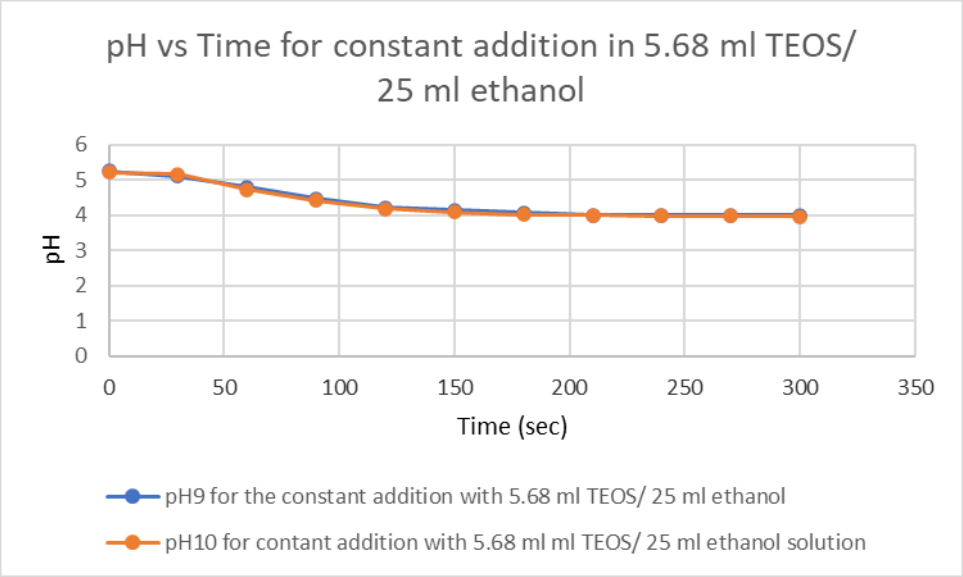

Figure 111, pH value versus the time for Wollastonite synthesis by constant addition method with 5.68 ml TEOS/25 ml ethanol solution

v. Direct TEOS/ethanol solution addition with 5.68 ml TEOS/25 ml ethanol solution

Two sets of experiments were performed to reduce the deviation caused by temperature and pH values at different times. This method completely added 30.68 ml TEOS/ethanol solution to the calcium nitrate tetrahydrate/ethanol solution after the stabilisation of TEOS/ethanol solution and calcium nitrate tetrahydrate/ethanol solution. Again, the pH and temperature were noted every 30 seconds. **Table 45** shows the average pH and temperature value for direct TEOS/ethanol addition to calcium nitrate tetrahydrate/ethanol solution with 5.68 ml TEOS/25 ml ethanol solution.

Table 45, Direct TEOS/ethanol solution addition to calcium nitrate tetrahydrate /ethanol solution with 5.68 ml TEOS/25 ml ethanol solution

Time (sec)	Average temperature (°C)	pH11	pH12	Average pH
0	19.10	5.25	5.23	5.24
30	19.15	5.12	5.17	5.14
60	19.25	4.80	4.73	4.76
90	19.35	4.48	4.43	4.45
120	19.55	4.22	4.19	4.20
150	19.75	4.15	4.10	4.12
180	19.85	4.08	4.03	4.05
210	20.05	4.01	4.01	4.01
240	20.20	4.00	3.99	3.99
270	20.35	4.00	3.98	3.99
300	20.50	4.00	3.97	3.98

The temperature of the solution increased with the addition of TEOS/ethanol solution [354]. The average temperature was 19.10 °C at 0 seconds and increased steadily to 20.50 °C (temperature difference of 1.4 °C) after 300 seconds, with a standard deviation of 0.49 °C.

Again, a significant pH reduction was observed initially due to the complete addition of TEOS/ethanol solution. The average pH value drastically reduced at the start from 5.24 at 0 seconds to 4.05 after 180 seconds. **Figure 112** shows the pH value versus the time for both sets of experiments for Wollastonite synthesis by the direct addition method with 5.68 ml TEOS/25 ml ethanol solution. The average pH value was nearly equal to 4.00 after 180 seconds, with negligible difference observed in both sets. The difference in the average pH value was 1.27, with a standard deviation of 0.39.

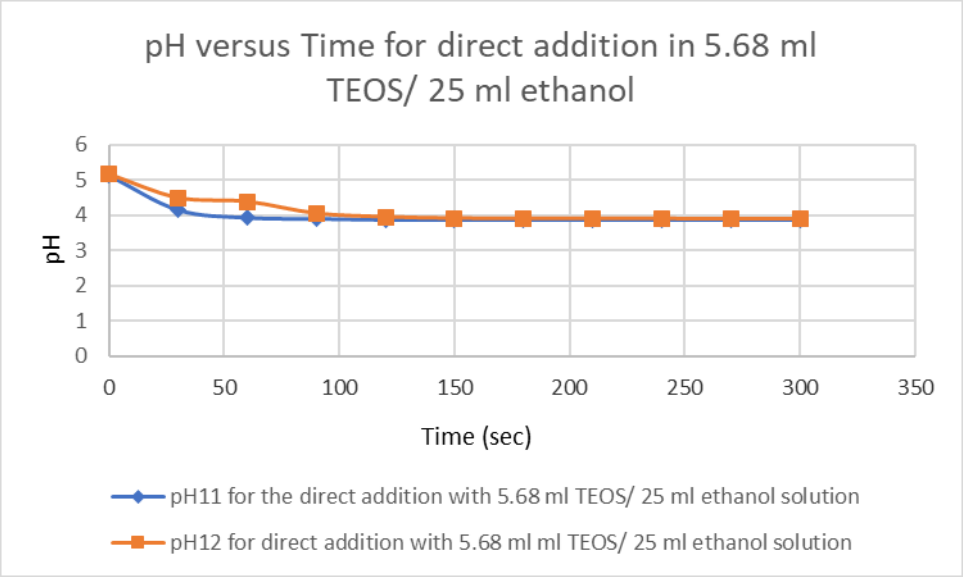

Figure 112, pH value versus the time for Wollastonite synthesis by direct addition method with 5.68 ml TEOS/25 ml ethanol solution

d) Comparison between all the methods

Approximately 30.68 ml TEOS/ethanol solution was added to a calcium nitrate tetrahydrate/ethanol solution containing 5.96 grams calcium nitrate tetrahydrate/ 25 ml ethanol solution by three methods. Firstly, by a peristaltic pump; secondly, by a constant rate of 7 ml/min for 4 minutes and 2.86 ml at the fifth minute; and finally, by the direct addition of TEOS/ethanol solution. The temperature difference and standard deviation were 0.9 °C and 0.32 °C, respectively for the peristaltic pump method. The temperature difference was 1.05 °C with a standard deviation of 0.37 °C for the 11.36 ml TEOS/50 ml ethanol solution and a temperature difference of 1.5 °C with a standard deviation of 0.45 °C for the 5.68 ml TEOS/25 ml ethanol solution using the constant addition method. The temperature difference was 1.70 °C with a standard deviation of 0.48 °C for the 11.36 ml TEOS/50 ml ethanol solution, and the temperature difference was 1.40 °C with a standard deviation of 0.49 °C for the 5.68 ml TEOS/25 ml ethanol solution using the direct addition method. Therefore, the addition of TEOS/ethanol solution increased the temperature of the solution in all cases [354]. The temperature increase was more pronounced in the constant addition method and direct addition method compared to the peristaltic pump method. The reason may be due to the higher quantity of TEOS/ethanol solution added at a particular time. However, notwithstanding the temperature effect was overall insignificant as there was no heat treatment involved, and the temperature of the experiment was dependent on other factors such as room/surrounding temperature.

In terms of average pH, the addition via a peristaltic pump showed a gradual reduction in the value of average pH from 5.29 at 0 seconds, to 4.09 after 300 seconds, with a pH difference of 1.19. **Figure 113** shows the average pH value versus time for all methods (**Tables 41-45** and **Figures 108-112**). The standard deviation of the average pH value in the peristaltic pump method was 0.4. However, in the case of constant addition and direct addition, there was a more sudden decrease in the average pH value up to 150 seconds because more TEOS/ethanol solution was added at a particular time. In the case of constant addition, the average pH value was 5.25 at 0 seconds, which reduced to 4.03 after 300 seconds, showing a difference of 1.22 and a standard deviation of 0.44 with 11.36 ml TEOS/50 ml ethanol solution and the average pH difference of 1.25 and standard deviation in average pH of 0.48 with 5.68 ml TEOS/25 ml ethanol solution. In the case of direct addition, the average pH value was 5.36 at 0 seconds, which reduced to 3.94 after 300 seconds, showing a difference of 1.42, and the standard deviation in average pH of 0.45 with 11.36 ml TEOS/50 ml ethanol solution and average pH difference of 1.27 and the standard deviation in average pH of 0.39 with 5.68 ml TEOS/25 ml ethanol solution.

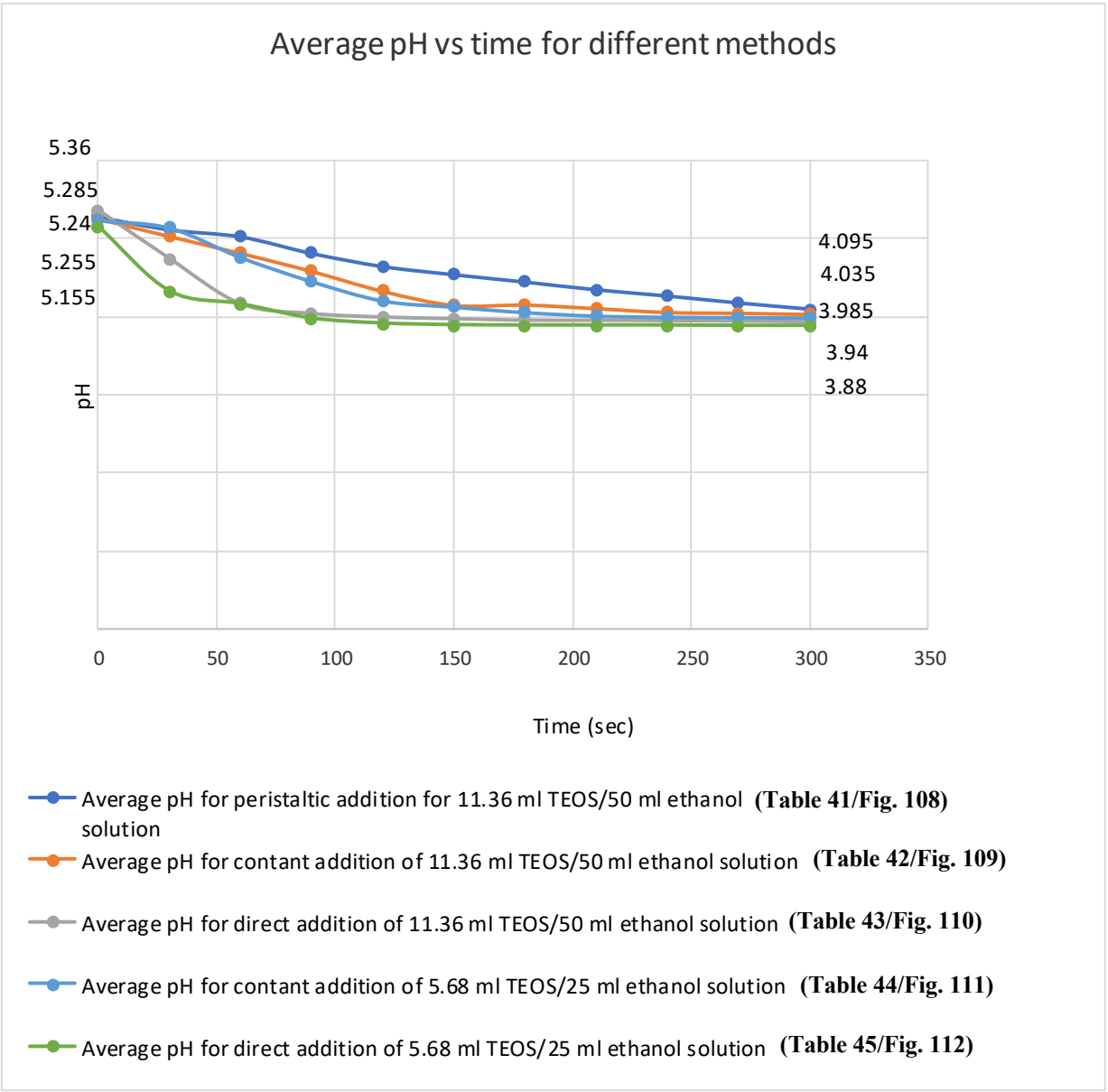

Figure 113, Average pH versus time for three addition methods

TEOS/ethanol solution was added to calcium nitrate tetrahydrate/ethanol solution to synthesise Wollastonite at pH 3.5 [255]. The addition of diluted nitric acid can easily regulate the pH. The pH of TEOS varied from 1.5 to 2, as shown in **Tables 37** and **38**, whereas the pH value of the calcium nitrate was between 5 and 5.5, as shown in **Table 39** [355, 357]. The average pH value, as observed in **Figure 113**, was 4.09 after 5 minutes in the case of the peristaltic pump, 4.03 after 5 minutes in the case of constant addition, and 3.94 in the case of direct addition. **Table 46** shows an observed matrix summary of the final pH values for all of the methods.

Table 46, pH after 300 seconds for all the methods for Wollastonite synthesis

Method	The final pH value of Wollastonite solution with 5.68 ml TEOS/ 25 ml ethanol solution after 300 seconds	The final pH value of Wollastonite solution with 11.36 ml TEOS/ 50 ml ethanol solution after 300 seconds
Peristaltic Pump Method	Could not be identified due to volumetric issues	4.09
Constant addition method	3.98	4.03
Direct addition method	3.88	3.94

The aim of this study was to synthesise Wollastonite at a pH of 3.5 [255]. However, in all three methods, the pH were greater than 3.5, as shown in **Table 46**, and a nitric acid buffer solution would have to be added to balance the pH of any solution to 3.5. However, it would be undesirable if the pH value was less than 3.5. Although any method could be used for the addition of TEOS/ethanol solution to a calcium nitrate tetrahydrate/ethanol solution for Wollastonite synthesis; to avoid wastage of material during an experiment, the constant addition or direct addition method using 5.68 ml TEOS/25 ml ethanol solution would be a more desirable method. However, as there would be less control over the pH and temperature with the direct addition method, moreover, the average pH value after 300 seconds in the case of direct addition was less, therefore, in the current study, the constant addition method with 5.68 ml TEOS/25 ml ethanol addition to calcium nitrate tetrahydrate/ethanol solution was further investigated for the synthesis of Wollastonite thus added timesaving during the experimentation.

e) *Nitric Acid Buffer Solution*

The Nitric acid (strong nitric acid and diluted nitric acid) was added to the Wollastonite solution formed by the constant addition method. A strong nitric acid solution was obtained from the DCU biomedical laboratory, with a pH of 0.86. A minor titration test was performed to prepare the diluted nitric acid solution. 1 ml each of strong nitric acid was added to separate beakers containing 100 ml, 200 ml, 300 ml, 400 ml and 500 ml deionised water, respectively in order to provide a varying level of nitric acid to act as a

buffer to bring the Wollastonite synthesised to a pH of 3.5, if the need arose. **Table 47** shows the pH values of each 1 ml strong nitric acid added to different quantities of deionised water.

Table 47, pH value of nitric acid added to different quantities of deionised water

Quantity of deionised water	pH when 1 ml strong nitric acid was added
100 ml	1.62
200 ml	2.41
300 ml	3.16
400 ml	3.75
500 ml	4.17

As mentioned above, given the Wollastonite solution forms at a pH of 3.5 [255], therefore, the pH of nitric acid dissolved in 400 ml and 500 ml deionised water were greater than 3.5 they were deemed undesirable. The pH of 1 ml nitric acid dissolved in 300 ml was 3.16. Therefore, two solutions, one strong acid with a pH of 0.86 and another diluted nitric acid with a pH of 3.16, were used as a buffer to maintain the pH at 3.5 for Wollastonite synthesis.

4.8.3 Wollastonite Coating on Titanium Alloy Substrate

Similar to Hydroxyapatite, now that Wollastonite has been synthesised, again titanium substrates with three different roughness (polished with average roughness: 0.08 µm, mid-range with average roughness: 1.8 µm and grit blasted substrate with average roughness: 4 µm) were preheated in the furnace at a temperature of 650 °C, detailed in the **Section 3.10.4** [300]. As detailed previously in **Chapter 3**, the prepared titanium substrates were immersed in a Wollastonite gel synthesised by the constant addition method. After dipping, the Wollastonite-coated titanium alloy substrates were heat treated at 650 °C in air, as explained in **Section 3.10.4**. The same procedure was followed for the titanium alloy substrate heat-treatment in an argon environment. It was not possible to heat-treat the Wollastonite-coated titanium substrate at 840 °C as suggested by Mavis and Taş [254], because Wollastonite flaked away after post heat-treatment at

840 °C; moreover, there was a formation of titanium nitride (Ti_4N_{3-x}) , could be detrimental to human health [359].

a) *SEM images of Wollastonite coatings on titanium alloy substrate*

For comparison purposes, most of the SEM images were taken at a magnification of 300X. **Figure 114** shows the SEM images of Wollastonite coating applied onto a polished (average roughness: 0.08 µm) titanium heat treated at 650 °C in an air environment; **Figure 115** shows the SEM image of Wollastonite coating applied onto a titanium substrate with mid-range roughness (average roughness: 1.85 µm) titanium substrate heat-treated at 650 °C in an air environment, and **Figure 116** shows the SEM image of Wollastonite coating applied onto a grit-blasted titanium substrate (average roughness: 4 µm) heat-treated at 650 °C in an air environment.

Figure 117 shows the SEM image of Wollastonite coating applied onto a polished (average roughness: 0.08 µm) titanium substrate heat treated at 650 °C in an argon environment; **Figure 118** shows the SEM image of Wollastonite coating applied onto a grit blasted titanium substrate with mid-range roughness (average roughness: 1.85 µm) heat treated at 650 °C in an argon environment, **Figure 119** shows the SEM image of Wollastonite coating applied onto a grit-blasted titanium substrate (average roughness: 4 µm) heat treated at 650 °C in an argon environment.

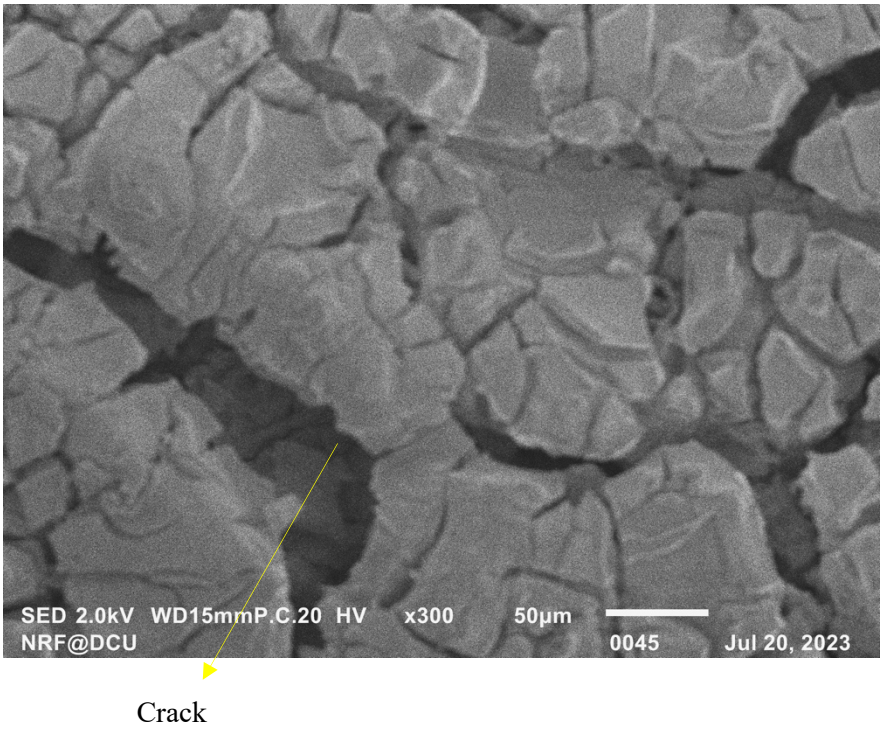

Figure 114, SEM image of Wollastonite gel coating on the polished titanium substrate heat-treated at 650 °C in an air environment.

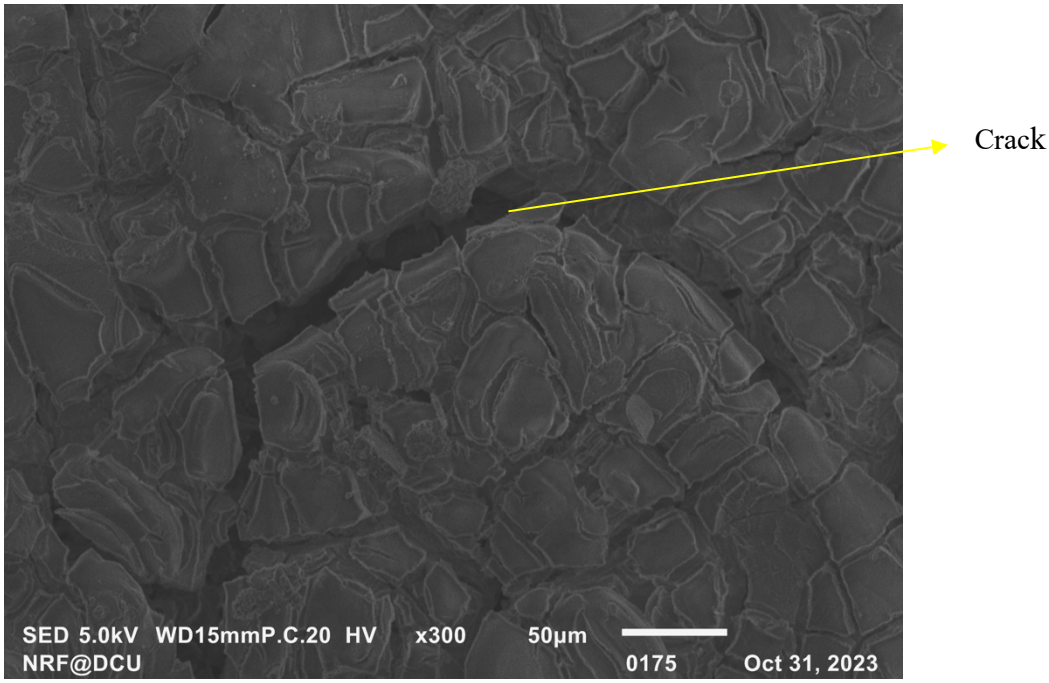

Figure 115, SEM image of Wollastonite gel coating on mid-range titanium substrate heat-treated at 650 °C in an air environment.

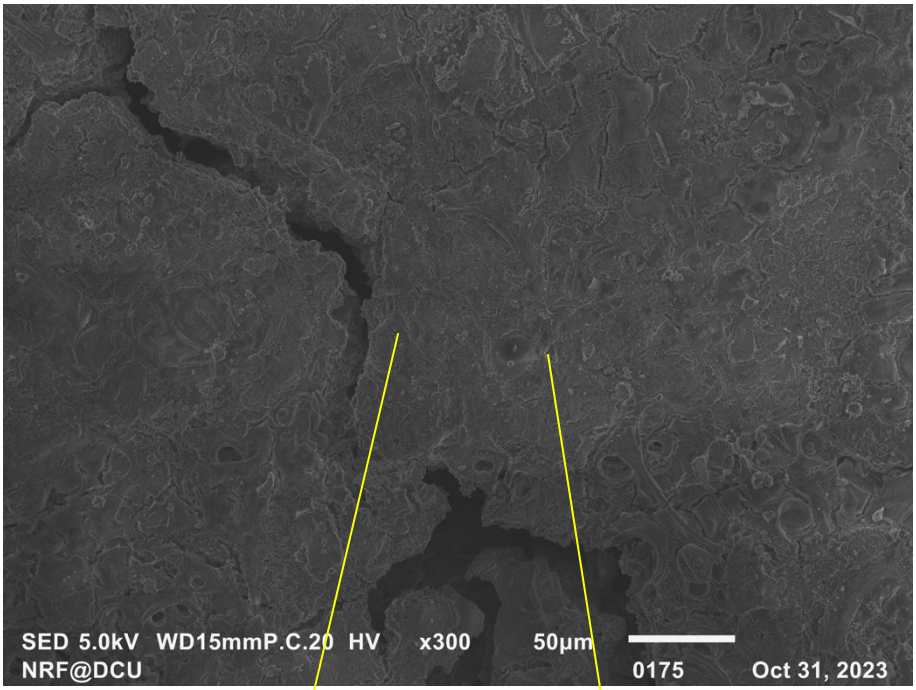

Figure 116, SEM image of Wollastonite gel coating on grit-blasted titanium substrate heat-treated at 650 °C in an air environment.

SEM images of the Wollastonite coated on heat-treated titanium alloy substrate heat treated at 650 °C in an air atmosphere are shown in **Figures 114, 115 and 116**, respectively.

Images showed the irregular structure of the Wollastonite coating [360]. In all the samples, cracks formed, which might be due to the evaporation of the gel, polymerisation and cross-linking of the polymer-gel and formation of tensile stress due to capillary forces [255]. The intensity of the cracks reduced as the substrate roughness increased. Few cracks were observed in the Wollastonite coating applied to a grit-blasted sample (**Figure 116**). There were more cracks observed in the Wollastonite coating applied to a mid-range roughness sample (**Figure 115**), and the cracks observed were large in number, with more intensity in the Wollastonite coating applied to a polished sample (**Figure 114**).

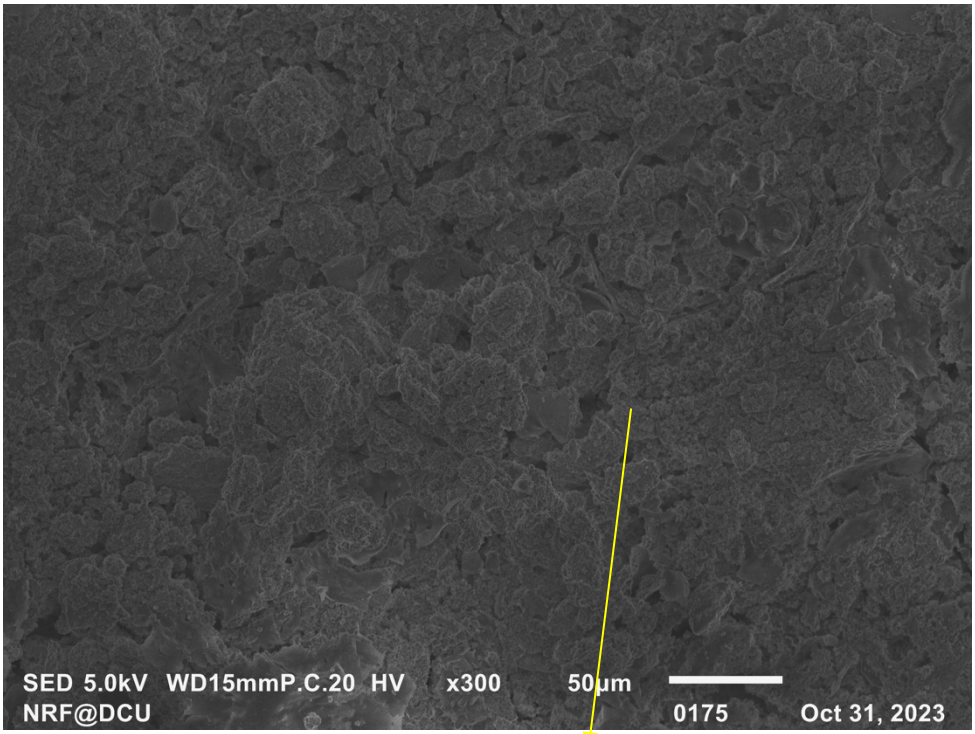

Figure 117, SEM image of Wollastonite gel coating on the polished titanium substrate heat treated at 650 °C in an argon environment

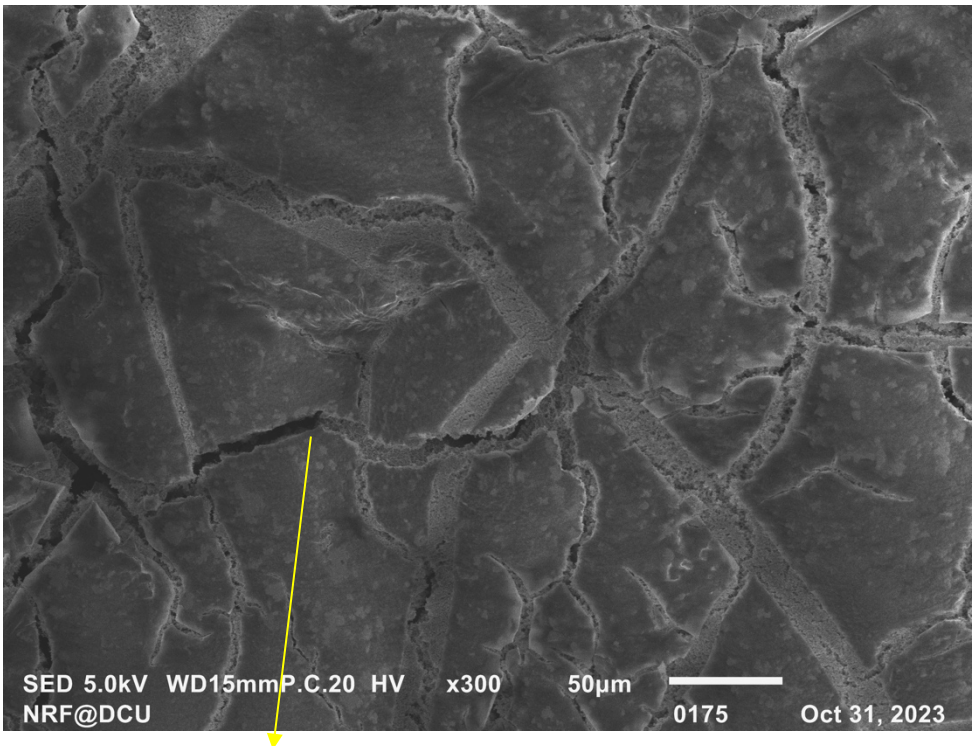

Figure 118, SEM image of Wollastonite gel coating on mid-range titanium substrate heat-treated at 650 °C in an argon environment

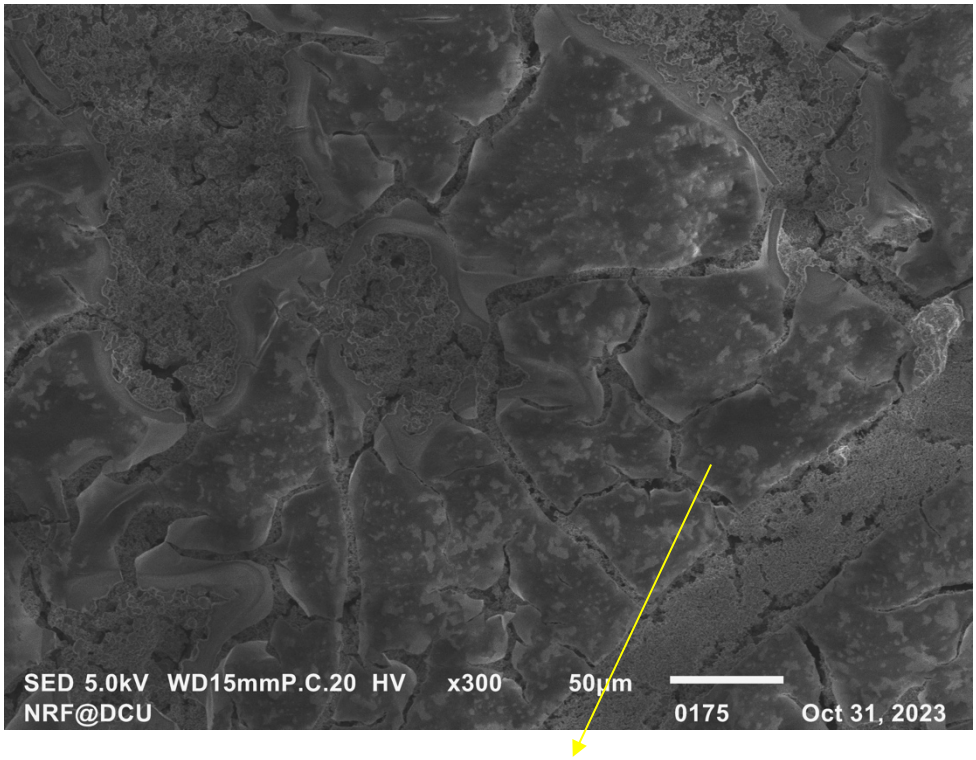

Figure 119, SEM image of Wollastonite gel coating on grit-blasted titanium substrate heat-treated at 650 °C in an argon environment

Figures 117, 118 and **119** show the Wollastonite coated onto a polished (average roughness: 0.08 µm), mid-range roughness (average roughness: 1.85 µm), and grit-blasted (average roughness: 4.01 µm) titanium alloy substrate heat treated at 650 °C in an argon atmosphere. Compared to the coatings obtained from sample heat treated in an air atmosphere, these samples had fewer cracks with less intensity. The Wollastonite-coated sample with polished substrate (**Figure 117**) had some pores and minimal cracks. The crack increase was observed in the Wollastonite coatings on mid-range roughness samples (**Figure 118**), as observed by Bao et al. [255]. Fewer cracks with lower intensity were observed in Wollastonite coatings on the grit-blasted sample (**Figure 119**) than in Wollastonite coatings on the mid-range roughness sample (**Figure 118)**.

Out of all the samples above, Wollastonite coated on the polished titanium substrate heat treated at 650 °C in an argon atmosphere (**Figure 117**) presented relatively no porosity and cracks within its coating structure.

b) *FTIR analysis of the dip-coated Wollastonite on titanium alloy substrates*

The Wollastonite coated titanium substrate samples were characterised by FTIR with the same device and working principle which was used for Hydroxyapatite-coated titanium substrate sample as mentioned in **Section 3.3.6**

Figure 120 shows the FTIR spectroscopy with transmittance value in the wavelength range of 400 cm^{-1}- 4000 cm^{-1} of the Wollastonite coated on the polished titanium substrate (average roughness: 0.08 µm), mid-range roughness titanium substrate (average roughness: 1.85 µm), grit blasted titanium substrate (average roughness: 4.01 µm) and titanium alloy substrate with no Wollastonite coating heat treated at 650 °C in an air atmosphere, respectively.

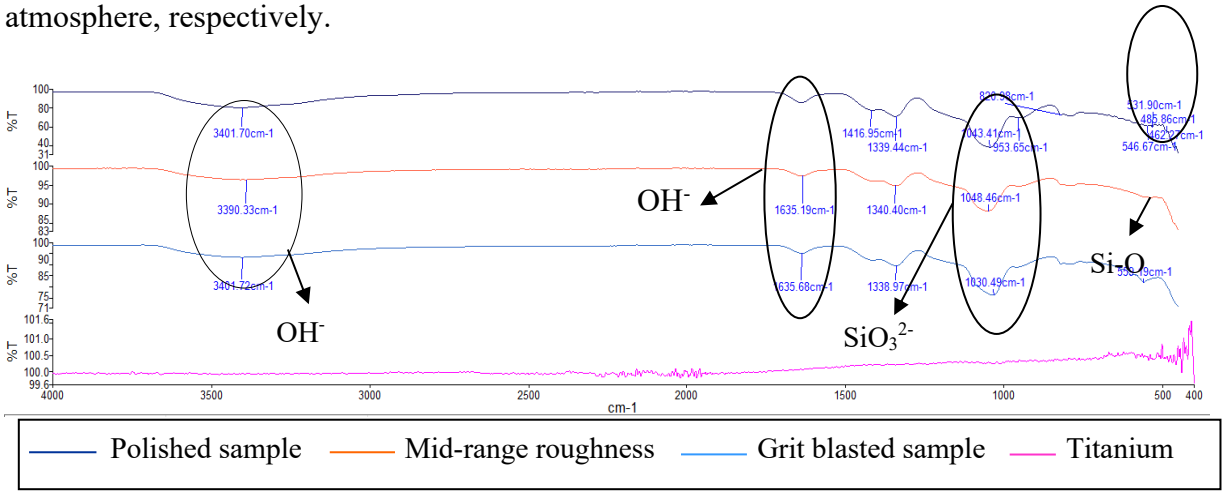

Figure 120, Comparison of FTIR spectra of Wollastonite-coated on titanium alloy substrates heat treated at 650 °C in air atmosphere.

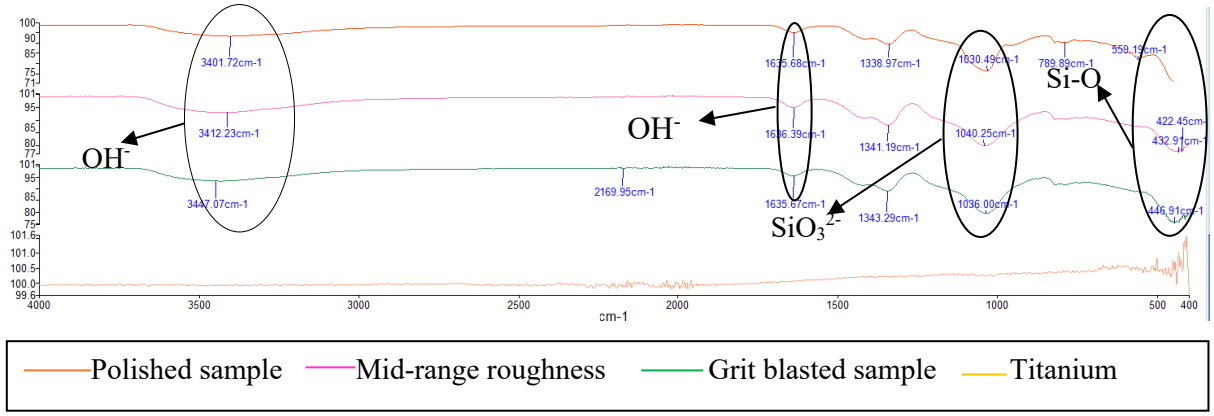

Figure 121, Comparison of FTIR spectra of Wollastonite coated on titanium alloy substrates heat treated at 650 °C in an argon atmosphere

Figure 121 compares the FTIR spectra of Wollastonite coatings on a polished titanium substrate (average roughness: 0.08 µm), mid-range roughness titanium substrate (average roughness: 1.85 µm), grit blasted titanium substrate (average roughness: 4.01 µm) and

titanium alloy substrate with no Wollastonite coating heat treated at 650 °C in an argon atmosphere.

FTIR spectra shown in **Figures 120** and **121** had four major bands. The first band corresponded to around 3400 cm^{-1}, which showed the presence of OH^-, which improved the bioactivity of material when immersed in SBF fluid [255]. The second band corresponding to 1634 cm^{-1} corresponded to the OH^- group in H_2O bending mode [361]. The FTIR spectra in the 967 cm^{-1} and 1063 cm^{-1} range corresponded to the SiO_3^{2-} group, which showed the presence of Wollastonite [255]. All the bands were centred around 963 cm^{-1} region corresponding to Si-O stretching bonds [361]. Moreover, the series of bands in the 400 cm^{-1} to 650 cm^{-1} range corresponded to Si-O linkage due to the deformation of SiO_4 tetrahedra [361]. The FTIR spectra of the heat-treated titanium had straight line with no major bands, similar to that of Ti-6Al-4V FTIR spectra, as mentioned by Dzhurinskiy [349].

Comparing the analysis shown in **Figures 120** and **121**, all three FTIR spectra could be easily verified in Wollastonite coated on all samples heat treated in an argon environment (**Figure 121**). There was less difference in the wavelength of the bands of all the samples heat treated in an argon atmosphere, whereas one could only identify all the bands in polished samples heat treated in an air atmosphere (**Figure 120**).

In the FTIR analysis shown in **Figures 120** and **121**, the polished titanium-coated samples had deeper wavelength bands than the Wollastonite-coated on the other prepared titanium samples. Considering the SEM images and FTIR results, Wollastonite coated onto a polished titanium alloy substrate heat-treated in an argon atmosphere had a better coating quality regarding cracks and pores.

c) *XRD analysis of the dip-coated Wollastonite on titanium alloy substrates*

Based on the FTIR and SEM results, the polished titanium samples heat treated at 650 °C in argon and air atmosphere were considered.

⬡ Wollastonite 2M ($Ca_3Si_3O_9$)

◇ Wollastonite ($Ca_{0.96}Mn_{0.04}SiO_3$)

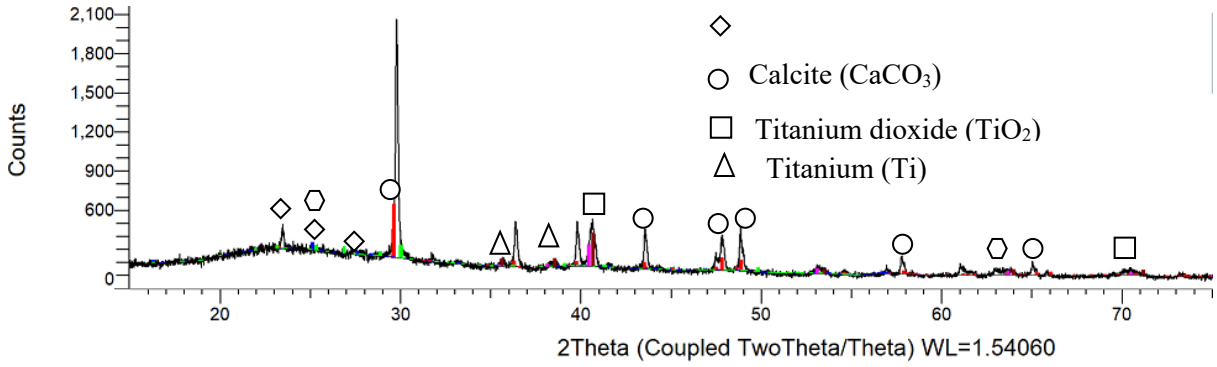

Figure 122, XRD pattern of Wollastonite coated on polished titanium substrate heated at 650 °C in air atmosphere

Figure 122 shows the XRD pattern of the Wollastonite coated onto a polished titanium substrate heat-treated at 650 °C in an air atmosphere. The red line showed a pattern with sharp calcite ($CaCO_3$) presence at an angle (2θ) of 30 ° with a minor presence at an angle (2θ) ranging from 43° to 65° with a total 1900 count. The presence of the calcite was due to the carbonation of Wollastonite in an aqueous environment [362]. There was the presence of Wollastonite ($Ca_{0.96}Mn_{0.04}SiO_3$) at an angle (2θ) of 22-30 ° [255]. There was the presence of Wollastonite 2M ($Ca_3Si_3O_9$) at an angle (2θ) of approximately 63°. There was some presence of titanium metal at an angle (2θ) of 35 ° and 38 °. Titanium dioxide was also present at an angle (2θ) of 42°, formed due to heat treatment of titanium alloy at a higher temperature (650 °C) in the air atmosphere, with exposure of titanium surface to air atmosphere possibly due to cracks in Wollastonite coatings [312]. The cracks were formed due to the evaporation of the solvent (in this case, ethanol) because of drying at 350 °C after each dip. The Wollastonite sol was a non-viscous, clear solution in which a titanium substrate, when dipped, formed a lower-thickness Wollastonite layer.

△ Calcite ($CaCO_3$)

◇ Wollastonite ($Ca_{0.96}Mn_{0.04}SiO_3$)

Titanium (Ti)

△

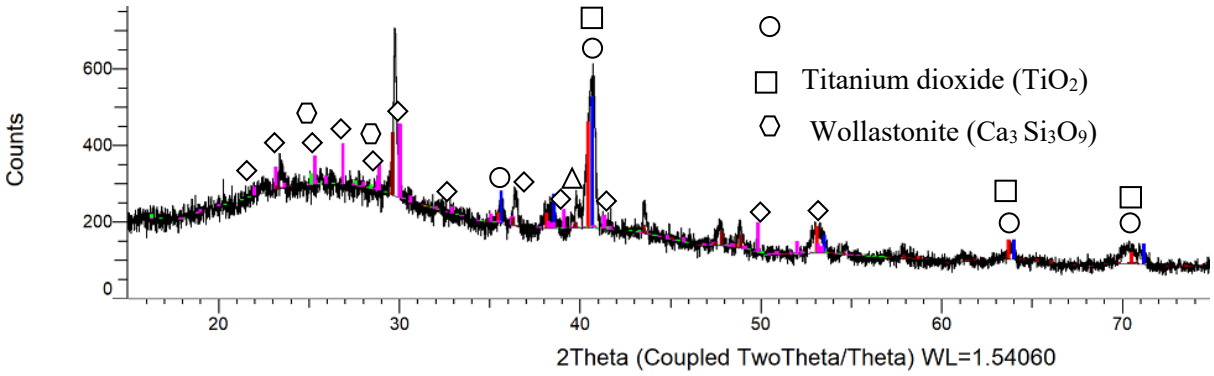

Figure 123, XRD pattern of Wollastonite coated on polished titanium substrate heated at 650 °C in argon atmosphere

Figure 123 shows the XRD pattern of the Wollastonite coated onto a polished titanium substrate heat-treated at 650 °C in an argon atmosphere. Compared to Wollastonite-coated titanium substrate heat treated in an air atmosphere, calcite ($CaCO_3$) was less at an angle (2θ) of 29° and 39°, respectively. There were more Wollastonite peaks (both $Ca_{0.96}Mn_{0.04}SiO_3$ and $Ca_3Si_3O_9$ present at an angle (2θ) ranging from 22-30 ° and up to an angle (2θ) of 55 °, as mentioned by Bao et al. [255]. There was some presence of titanium oxide (TiO_2) and titanium (Ti) with sharp peaks observed at an angle (2θ) of 40 ° and smaller peaks at an angle (2θ) of 65 ° and 70 °, respectively.

Overall, the Wollastonite coated onto a titanium substrate heat-treated in an argon atmosphere had fewer counts and more peaks, including that of Wollastonite ($Ca_{0.96}Mn_{0.04}SiO_3$), as shown in **Figure 123**. There was a more constant presence of Wollastonite coated in a polished sample heated-treated in an inert atmosphere (argon gas), with less calcite ($CaCO_3$) present due to the non-availability of an aqueous environment. Titanium dioxide was present (TiO_2) was present in both the XRD patterns shown in **Figures 122** and **123**. In the polished sample heat-treated in an air atmosphere, the presence of TiO_2 was due to heat treatment at 650 °C and in the polished sample heat-treated at an argon atmosphere, It was due to immersion of prepared substrate in precursors liquid during synthesise of Wollastonite coating. Larger peaks of non-oxidised titanium (Ti) were observed in the Wollastonite-coated sample heat-treated in an argon atmosphere due to the cracks observed in the Wollastonite-coated titanium substrate. The diffraction peaks observed in **Figure 123**, shows that the coating obtained was amorphous in nature [363]. Though Wollastonite is crystalline with a well-defined structure, the Wollastonite gel was obtained by burning ethanol from the Wollastonite sol

obtained from the precursor. The gel obtained usually has amorphous structure and lacks the crystalline order in their microstructure, which was observed by its XRD pattern [364].

4.8.4 Dip Coating of HA/Wollastonite Composite Powder

The procedure for dip coating of HA/Wollastonite composite powder is explained in detail in **Section 3.11.** The as-prepared substrates (polished in this case) were preheated in an argon environment at 650 °C at 1 °C/min with a dwell time of 5 hours and cooled to the room temperature at the same cooling rate. The substrates were dipped into the HA/Wollastonite sol and heat-treated at the same temperature and under the same environmental conditions. Polished substrates were only considered for the study as they had the best results observed in **Sections 4.8.1** and **4.8.3**, respectively.

Figures 124, 125 and 126 show the SEM image of dip-coated HA/ 10 wt.% Wollastonite on the polished sample, dip-coated HA/20 wt.% Wollastonite on the polished sample, dip-coated HA/30 wt.% Wollastonite on the polished sample. Prior to the coating, all polished substrates were heat treated at 650 °C in an argon atmosphere. As observed in **Figure 126**, the pores and intensity of the cracks were highest for the 30 wt.% Wollastonite. Moreover, the coating structure contained more acicular structure as the quantity of the Wollastonite was increased. The coating containing 10 wt.% Wollastonite was more uniform and contained less pores with fewer cracks. However, some minor cracks were observed in the 20 wt.% Wollastonite. Most of the Wollastonite, as shown in **Figures 124, 125** and **126**, remained on the layer surface. There was less mixing of the Wollastonite fibres with the Hydroxyapatite, unlike the studies conducted by Encinas-Romero et al. [160]. The reason may be due to the lack of high temperature (650 °C in the current study, as opposed to 1200 °C in the study conducted by Encinas-Romero et al. [160]). The addition of Wollastonite increased the porosity and cracks in the coatings [365, 366].

a) *SEM image of HA/ 10 wt.% Wollastonite on polished titanium substrate*

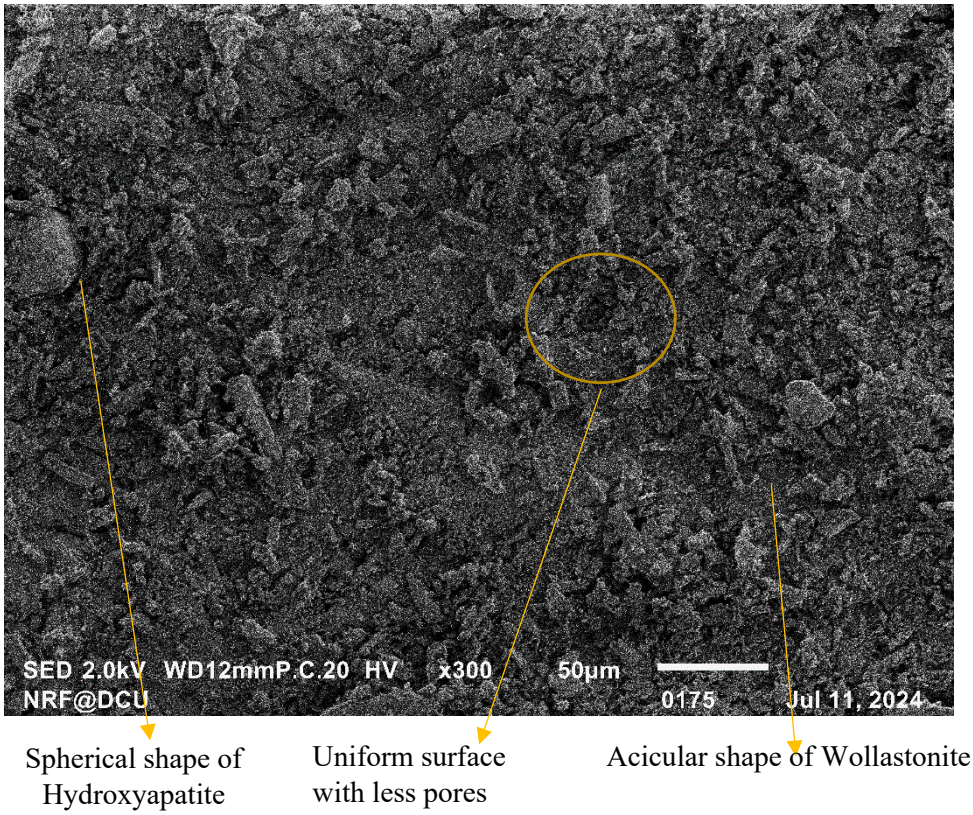

Figure 124, SEM image of HA/ 10 wt.% Wollastonite dip coated on polished sample substrate heat treated at 650 °C in an argon environment

b) *SEM image of HA/20 wt.% Wollastonite on polished titanium substrate*

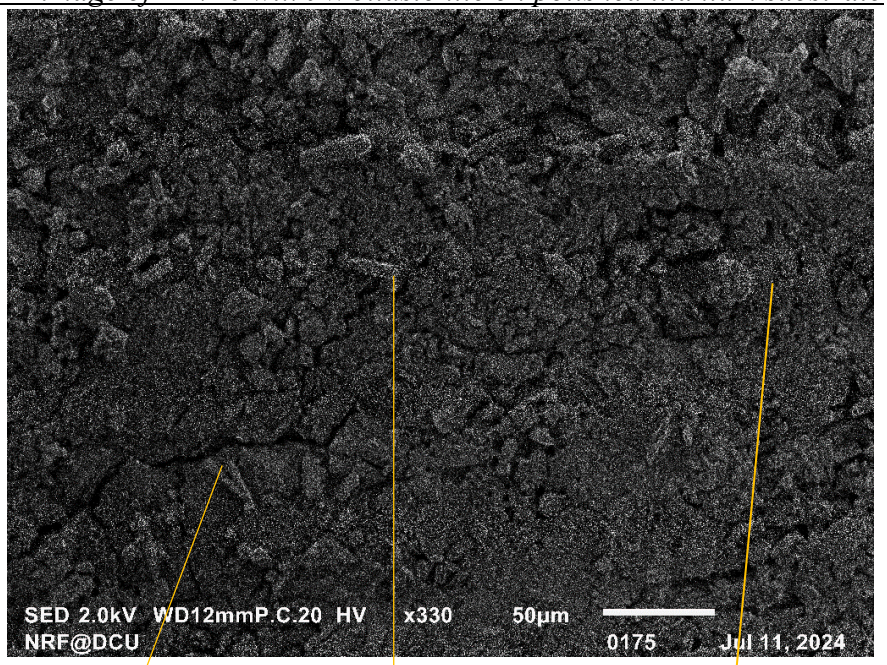

Figure 125, SEM image of HA/20 wt. % Wollastonite dip coated on polished sample substrate heat treated at 650 °C in an argon environment

c) *SEM image of HA/30 wt.% Wollastonite dip coated on polished titanium substrate*

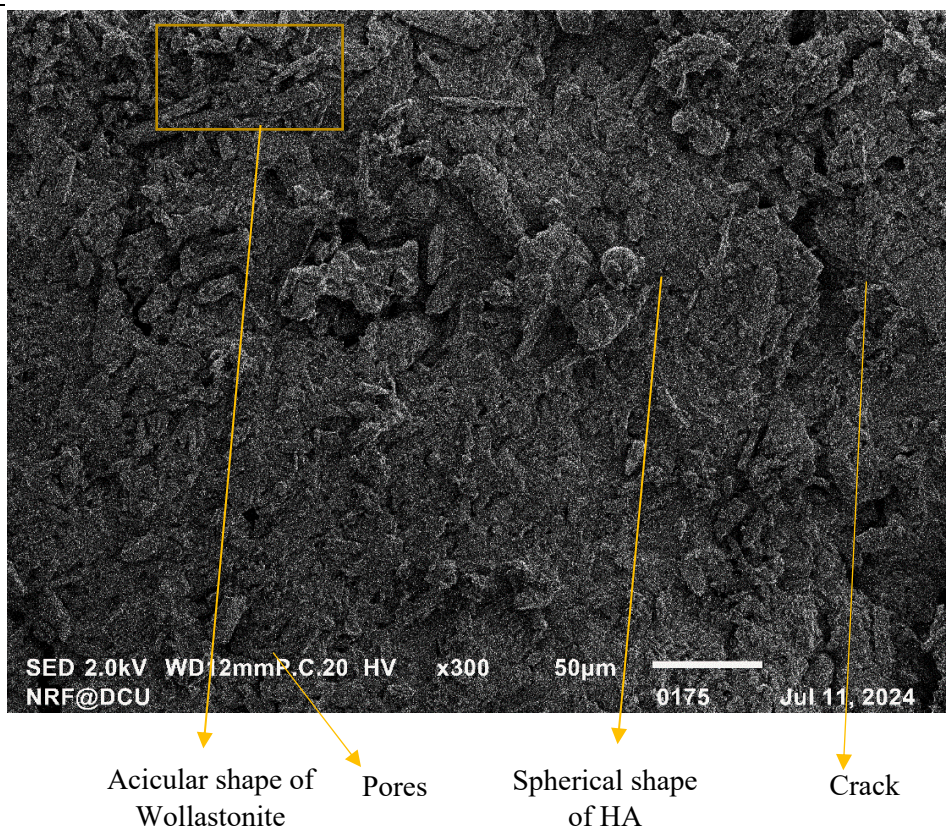

Figure 126, SEM image of HA/30 wt.% Wollastonite dip coated on polished sample heat treated at 650 °C in an argon environment.

Out of the coatings detailed above, the coatings containing 10 wt.% Wollastonite on a polished titanium substrate (**Figure 124**) was more desirable as it had fewer pores, almost no cracks, and a uniform structure.

d) *FTIR spectra of dip-coated HA/Wollastonite dried gel*

Similar to dip-coated samples of HA and Wollastonite, the polished titanium substrate was heat treated at 650 °C in an argon atmosphere prior to the coating. The preheated polished sample was dipped into a gel containing 10 wt.%, 20 wt.% and 30 wt.% Wollastonite, respectively. After dipping, the coated samples were heat-treated in the furnace in an argon atmosphere at 650 °C [300]. Three different HA/Wollastonite composites dip-coated on polished substrates comprised 10 wt.% Wollastonite/90 wt.% HA, 20 wt.% Wollastonite/ 80 wt.% HA and 30 wt. Wollastonite/70 wt.% HA were characterised using FTIR spectroscopy. **Figure 127** shows the FTIR spectra of dip-coated HA/Wollastonite coatings

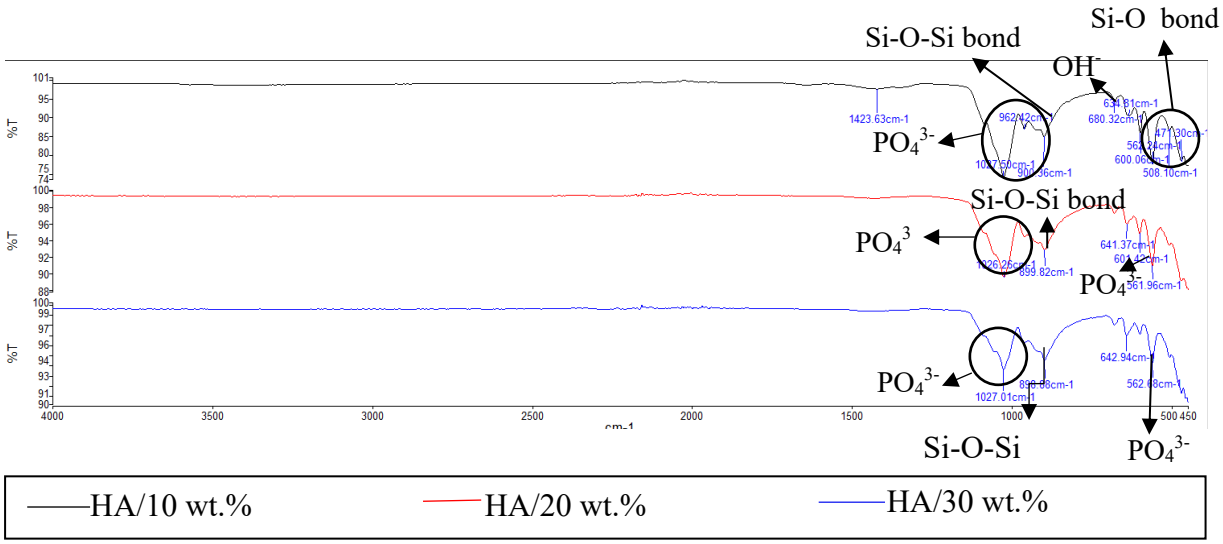

Figure 127, FTIR spectra of dip-coated HA/Wollastonite coatings heat treated at 650 °C in an argon environment

The FTIR spectra of the dip-coated dried HA/Wollastonite gels are shown in **Figure 127**. For HA/10 wt.% Wollastonite, 20 wt.% HA/Wollastonite and 30 wt.% HA/Wollastonite, the broad bands observed at the wavelength of approximately 1024 cm^{-1} and 963 cm^{-1} show the presence of the PO_4^{3-}, showing the presence of Hydroxyapatite and the band observed at a wavelength of approximately 900 cm^{-1} showed a Si-O-Si bond, indicating

the presence of Wollastonite [333, 334]. There were bands observed in the wavelength of approximately 563 cm^{-1} in 20 wt.% Wollastonite/Hydroxyapatite and 30 wt.% Wollastonite/HA, showing the presence of PO_4^{3-} (phosphate group), indicating Hydroxyapatite [334]. In the case of 10 wt.% Wollastonite/HA, additional bands were observed at the wavelength of 632 cm^{-1}, showing the OH^- bond in Hydroxyapatite. Moreover, additional bands were present at the wavelength of approximately 507 cm^{-1} and 472 cm^{-1}, showing Si-O bond in Wollastonite [333]. There was no OH^- group present (corresponding to the adsorbed water) because almost all the water evaporated due to high temperature (650 °C) [53].

Overall, again the 10 wt.% Wollastonite/HA had a better FTIR spectrum as it had more bands observed at various wavelengths, showing the presence of Wollastonite and Hydroxyapatite. Even though the Wollastonite quantity was less (10 wt.%), more Wollastonite remained on the top of the surface, so during implantation of hip implants in the body, this would be positive as the dissolution rate of Wollastonite is higher with superior mechanical properties [18]. Therefore, highly resorbable Wollastonite would dissolve quickly in the body, providing mechanical strength, which a more stable Hydroxyapatite layer would take over.

e) *XRD peaks of HA/Wollastonite biocomposite*

After heat treating the HA/Wollastonite coated titanium with different amounts of Wollastonite (10 wt.%, 20 wt.%, and 30 wt.%, respectively) in an argon atmosphere at 650 °C, the obtained coatings were characterised using XRD (X-ray diffraction). The HA/Wollastonite dip coated onto a polished substrate was considered for the study as it had better results for dip coating of Hydroxyapatite and Wollastonite in terms of SEM and FTIR analysis, explained in **Sections 4.8.1** and **4.8.3**, respectively. The XRD studies were conducted similar to spray-coated HA/Wollastonite onto a prepared titanium substrate.

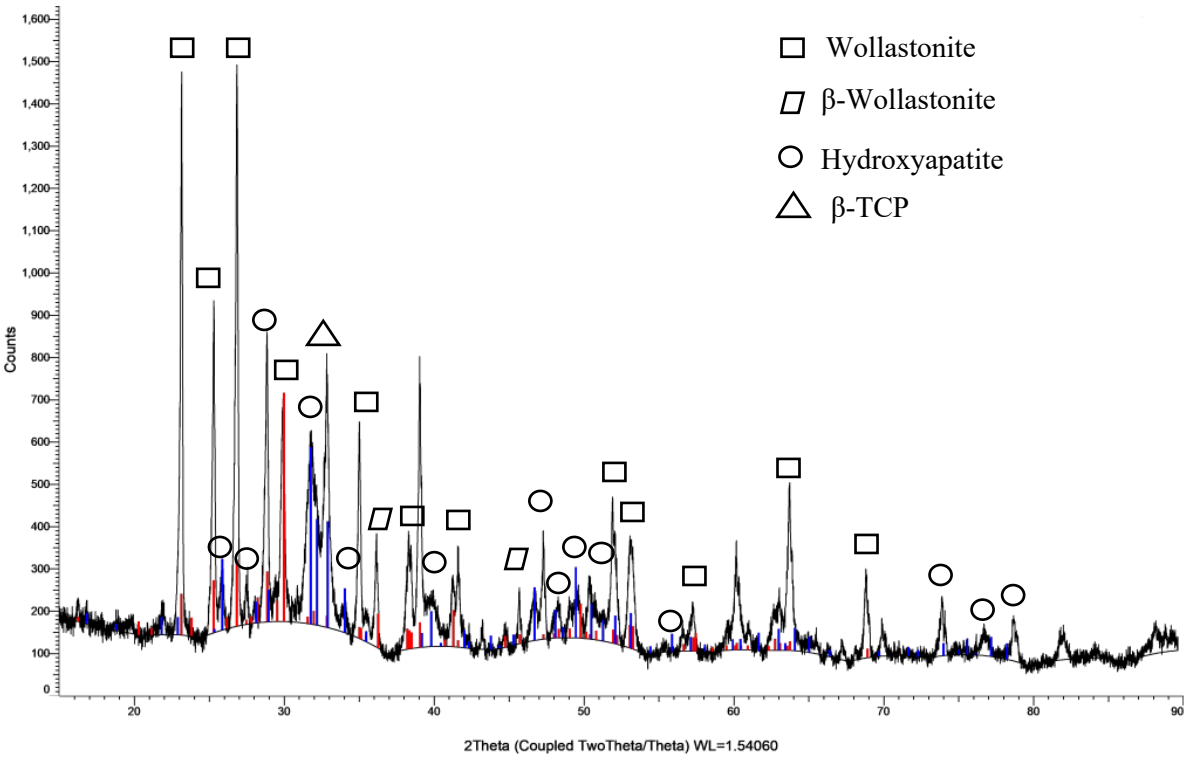

Figure 128, XRD pattern of 10 wt.% Wollastonite/HA-coated titanium substrate heat treated at 650 °C in an argon environment

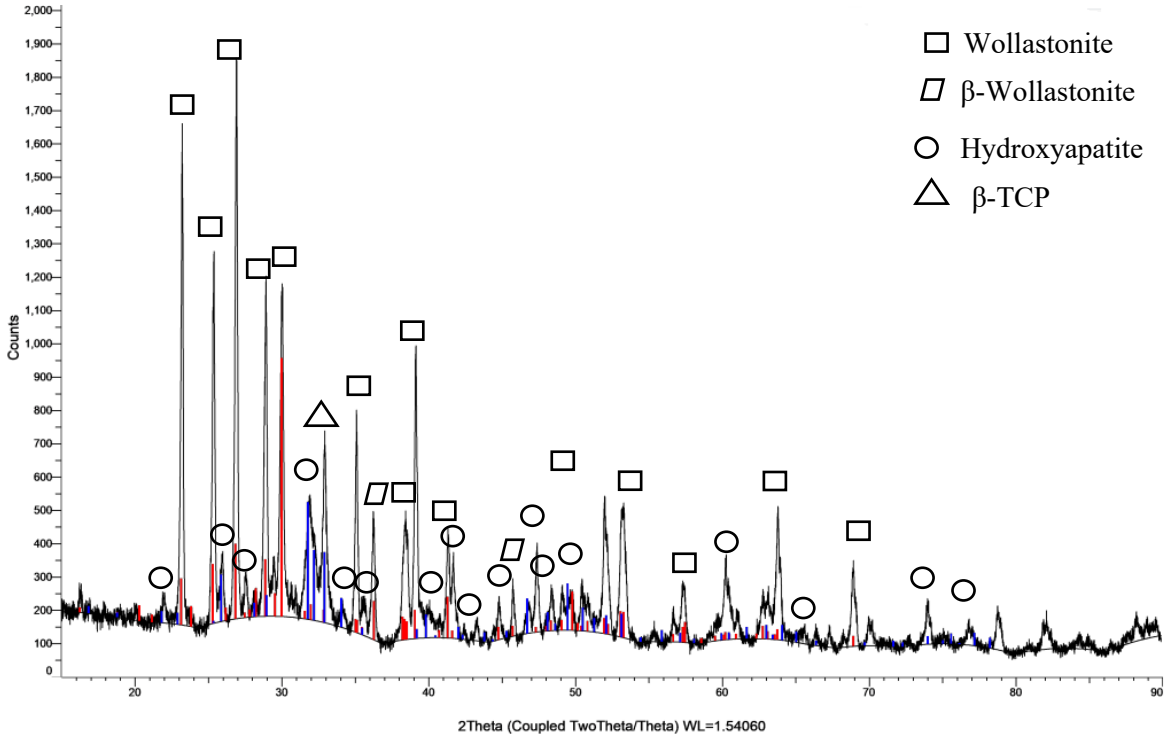

Figure 129, XRD pattern of 20 wt.% Wollastonite/HA-coated titanium substrate heat treated at 650 °C in an argon environment

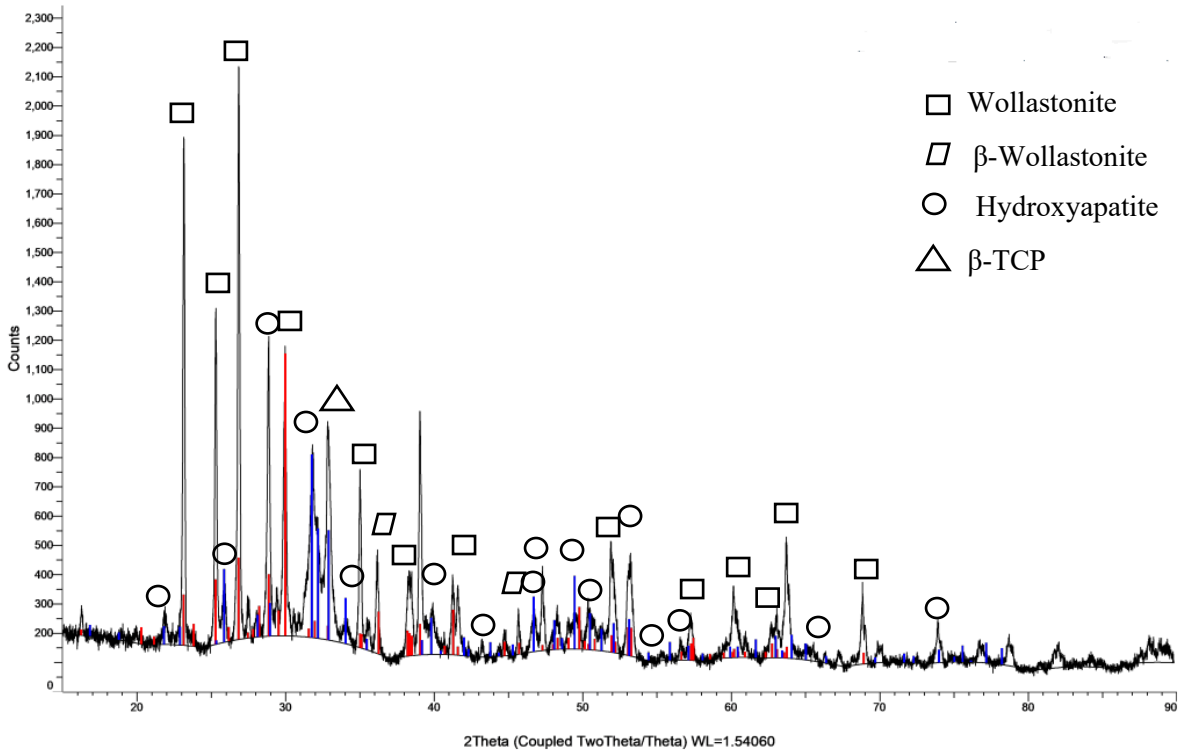

Figure 130, XRD pattern of 30 wt.% Wollastonite/HA-coated titanium substrate heat treated at 650 °C in an argon environment

Figures 128, 129 and **130** show the XRD peaks of the HA/Wollastonite biocomposite dip coated onto a polished titanium substrate. As seen in the figures, the diffraction peaks of Hydroxyapatite reduces as the Wollastonite quantity is increased [18]. In all the three XRD peaks observed, there was only peak of β-TCP observed at an angle (2θ) of 32° [4]. There was a small peak of Hydroxyapatite observed at a higher angle (2θ) at 74°, 76°, and 78°, which may be due to a higher presence of Hydroxyapatite (90 wt.%). The presence of Wollastonite was higher because most of the Wollastonite was present on the surface layer, and the Wollastonite was not intermixed with the semi-solid HA gel. The peak length relating to the presence of Wollastonite was higher at an angle (2θ) of 24°, 26°, 29° and 30°, respectively, which was due to crystalline Wollastonite present at these diffraction angles [337]. However, when the Wollastonite quantity increased to 20 wt.% and 30 wt.%, the presence of Hydroxyapatite reduced at a higher diffraction angle. Hydroxyapatite presence was prominent at a diffraction angle (2θ) of approximately 26°,31°, 40°, 46° and 50° [4]. The diffraction peaks of Hydroxyapatite were lower as compared to Wollastonite due to the presence of more Wollastonite on the surface layer [337], due to which there was a lower peak of Hydroxyapatite at a diffraction angle (2θ) in the range of 25-37°. Hydroxyapatite was synthesised using the sol-gel technique,

where the polished substrate was dipped into a Hydroxyapatite precipitate, whereas the as-received Wollastonite was crystalline [34].

The presence of Wollastonite became prominent as the quantity of Wollastonite increased. The number of counts for the diffraction peaks of Wollastonite was highest at 30 wt.% and reduced as the quantity of wollastonite reduced. The presence of Wollastonite was substantial at diffraction angle (2θ) of approximately 22°, 24°, 26°, 35°, 39°, 41°, 51° and 63°, similar to studies conducted by Ashraf et al. [344]. There was a minor presence of β-Wollastonite at an angle of 36° and 45° [23]. The presence of β-TCP and β-Wollastonite would increase biodegradability and have higher solubility in the physiological environment [343, 367]. There was no presence of α-TCP and α-Wollastonite due to heat treatment at lower temperatures (650 °C) [23, 53]. The presence of α-TCP leads to more amorphous formation and surface instabilities due to its higher dissolution rate, whereas, the α-Wollastonite has a higher dissolution rate when immersed in physiological environment, which may result in premature failure of the hip implant [23, 368].

4.9 Comparison of Spray-Coated and Dip-Coated Samples

4.9.1 Comparison of HA-Coated Samples

a) *Comparison in terms of morphology*

In the case of spray-coated samples, the HA-coated onto as-prepared grit-blasted samples post-heat treated at 1100 °C for 2 hours in an air atmosphere exhibited a more homogenous structure with increased agglomeration and a visible crystalline spherical structure. Due to the dihydroxylation of HA at a higher heat treatment temperature (1100 °C), the observed porosity could be beneficial for the bioactivity of the implants. These findings open up exciting possibilities for the application of such coatings in biomaterials research [221]. More studies are needed to be conducted for spray coated samples.

In the dip-coated samples, the HA-coated onto a polished sample heat treated at 650 °C in an argon atmosphere had a better microstructure in terms of porosity and cracks. However, no visible spherical morphology was observed, which may be due to the lower crystallinity of the coating than in spray-coated samples. The porosity was less as the heat temperature was less (650 °C) with no dihydroxylation observed; for any porosity to occur in the coating, the temperature must be a minimum of 800 °C [53]. Samples with lower porosity will have superior mechanical properties [369]. More studies are required

to understand dip-coated samples' mechanical behaviour. **Figures 131 (a) and (b)** show the best coatings of HA obtained on grit-blasted titanium substrate heat treated at 1100 °C for 2 hours in an air atmosphere from spray coating and HA coating obtained from dip coating techniques on a polished titanium substrate heat treated at 650 °C in an argon environment.

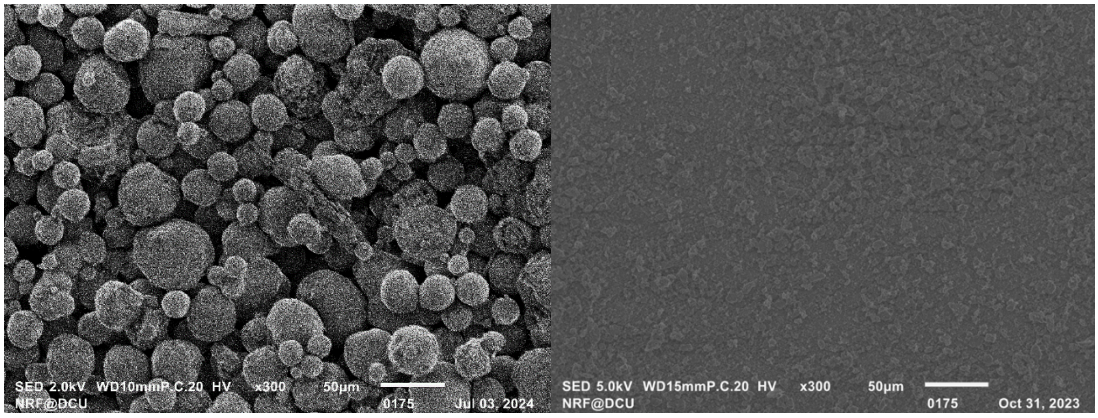

(a) ***(b)***

Figure 131, a) HA coatings on titanium substrate by spray coating technique heat treated at 1100 °C in an air environment at 300 X magnification and b) HA coatings obtained on titanium substrate by a dip coating technique heat treated at 650 °C in an argon environment at 300 X magnification

b) *Comparison in terms of FTIR spectra*

In the case of spray-coated HA samples, the as-sprayed powder post-heat-treated at 1100°C in an air atmosphere was considered for the study, as mentioned in **Section 4.7.1**. In the case of dip-coated samples, the pre-heated polished substrate at 650 °C in an argon atmosphere dip-coated into an HA gel and post-heat-treated at 650 °C in an argon atmosphere was considered for the study. **Figure 132** shows the FTIR spectra of dip-coated HA onto a prepared substrate and spray-coated HA powder, respectively.

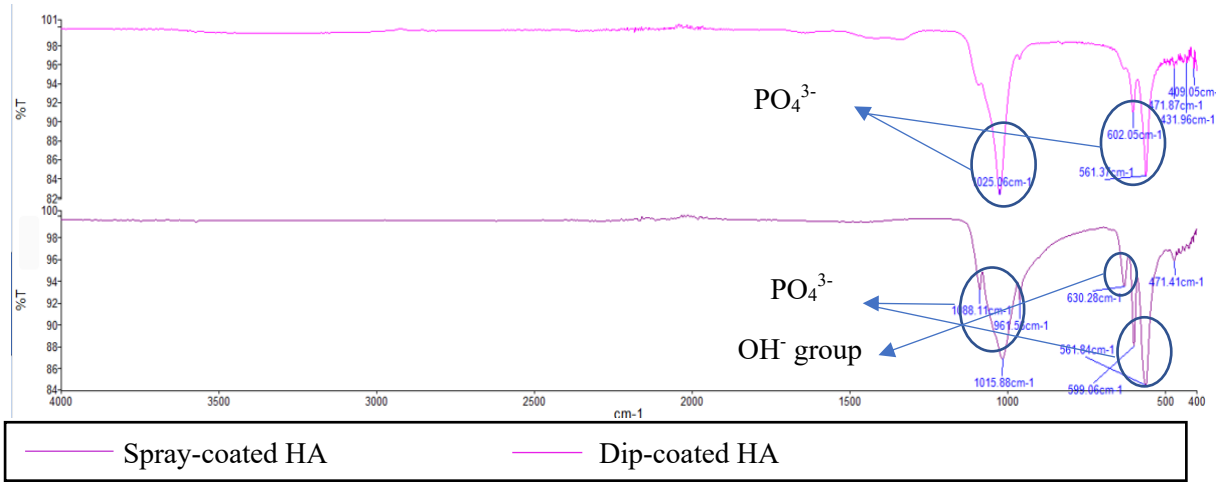

Figure 132, Comparison of spray-coated powder heat treated at 1100 °C in an air atmosphere and dip-coated HA samples heat treated at 650 °C in an argon atmosphere

Figure 132 shows the comparison of spray-coated HA and dip-coated HA. There were some common bands at a wavelength of approximately 1024 cm^{-1}, 599 cm^{-1} and 562 cm^{-1}, showing the presence of PO_4^{3-} [332, 334]. However, in the case of HA samples heat treated at 1100 °C, there were additional bands observed at 632 cm^{-1} (showing the presence of OH^- hydroxyl group) and 1088 cm^{-1} (showing the presence of PO_4^{3-} group) [332] in the HA samples spray-coated. Overall, HA samples that were spray-coated had more bands observed at different wavelengths. Out of this, spray-coated samples produced a better structure as it had a band at wavelength at 632 cm^{-1}, showing the presence of hydroxyl group (OH^-), confirming apatite structure and was indicative of good crystalline structure [332]. There were no peaks of OH^- group, which shows the presence of adsorbed water at a wavelength of approximately 3400 cm^{-1}, as dip-coated HA samples underwent heat treatment at 650 °C, which resulted in evaporation of water and spray-coated HA samples underwent heat treatment at 1100 °C, resulting in dihydroxylation of HA [53].

c) *Comparison in terms of XRD analysis and crystallinity*

The diffraction peaks and crystallinity of the coated HA were determined using XRD analysis. The crystallinity can be estimated by the XRD phase diagram, where the crystalline structure has sharp and longer peaks, whereas the amorphous structure has broader peaks [337]. **Figure 133** shows the XRD of the spray-coated HA onto an as-prepared titanium substrate (a grit-blasted sample, in this case) post-heat treated at 1100 °C and the preheated at 650 °C in an argon atmosphere dip-coated HA gel onto a prepared titanium substrate (a polished sample, in this case) a post-heat-treated at 650 °C in an

argon atmosphere. As-prepared grit blasted sample spray-coated with HA post-heat treated at 1100 °C in an air atmosphere was considered for the study as it had the better microstructure, shown in **Figure 75** and preheated polished titanium substrate dip coated with HA gel post-heat treated at 650 °C in an argon atmosphere shown in **Figure 95**, was considered for the study.

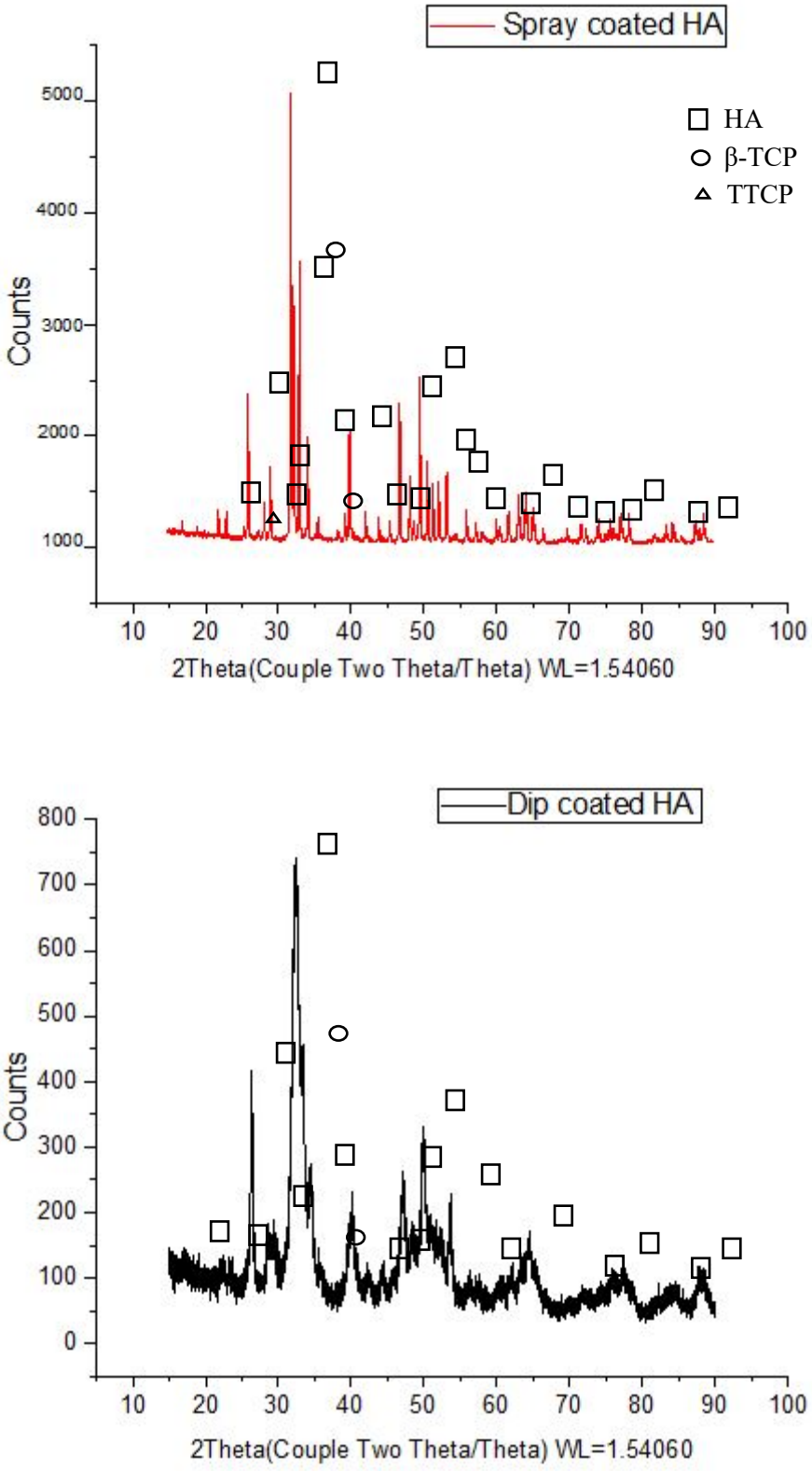

Figure 133, Comparison of XRD pattern of spray-coated Hydroxyapatite onto a grit-blasted sample heat treated at 1100 °C in an air atmosphere and dip-coated Hydroxyapatite samples onto a polished sample heat treated at 650 °C in an argon atmosphere.

The XRD pattern of spray-coated and dip-coated HA is explained in **Figures 83** and **109**, respectively. **Figure 133** compares HA dip-coated and spray-coated XRD patterns on a prepared titanium substrate. There was a clear difference in the peak length and breadth as the peak length of spray-coated samples was much higher, with a narrower width than that of dip-coated HA. The diffraction peaks of the spray-coated HA were much higher than dip-coated samples. HA is a stable, crystalline calcium phosphate with a Ca/P ratio of 1.67 to 1.76, whereas the presence of TTCP and β-TCP, which does not have a Ca/P ratio (1.67-1.76), would increase the amorphous nature of the coating [53, 343]. The amorphous nature of the coating would result in its failure when implanted inside the body [53]. The crystallinity of the dip-coated HA was 64.3%, whereas the crystallinity of the spray-coated HA was 90.4%. The crystallinity was calculated by DIFFRAC.EVA software installed with XRD instrument, where % crystallinity is calculated by the evaluation of the baseline to peak separation in an extended scan range [370]. The spray-coated and dip-coated HA samples followed the ISO standard ISO13779-3:2018 (50-70 %), which specifies the requirement for the use of HA in medical implant.

4.9.2 Comparison of Wollastonite-Coated Samples

a) Comparison in terms of morphology

In the case of spray-coated Wollastonite samples, the as-prepared grit-blasted sample coated with Wollastonite post-heat treated at 1100 °C in an air atmosphere had a porous structure but was more uniform as compared to other prepared samples (polished and mid-range roughness samples), as shown in **Figure 80**, whereas in the case of the pre-heated polished titanium substrate dip-coated with Wollastonite gel heat treated at 650 °C in an argon atmosphere had fewer pores and fewer cracks. The coating obtained from dip-coating had an amorphous structure as shown in **Figure 123**, whereas the coating obtained from spray coating was more crystalline. The porosity in both coatings was due to the presence of Wollastonite [211]. The coatings obtained from dip coating of Wollastonite onto a titanium substrate had more porosity than the coatings obtained from spray-coated samples. The porosity of the spray-coated sample was 13.89%. In contrast, the porosity of the dip-coated HA samples was 17.17%, calculated by the threshold function in ImageJ software, which uses pixels to measure the porosity. **Figure 134 (a) and (b)** shows the best Wollastonite coatings obtained from spray-coating and dip-coating. Overall, the Wollastonite spray coated onto a grit-blasted titanium substrate had a better microstructure.

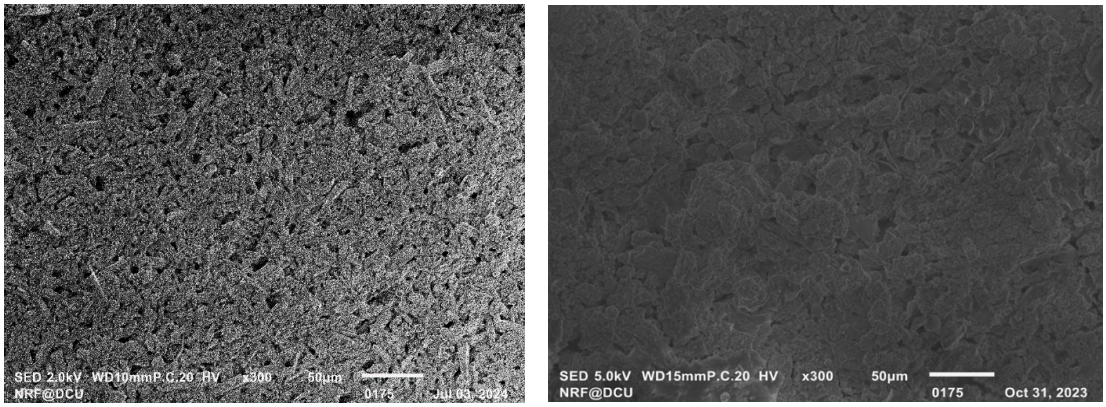

Figure 134, a) Wollastonite coatings obtained on titanium substrate by a spray-coating technique heat treated at 1100 °C in an air atmosphere and b) Wollastonite coatings obtained on titanium substrate by a dip-coating technique heat treated at 650 °C in an argon atmosphere

b) *Comparison in terms of FTIR spectra*

In the case of spray-coated Wollastonite samples, the powder post- heat-treated at 1100°C in an air atmosphere, as mentioned in **Section 4.7.2**, was considered for the study, whereas in the case of dip-coated samples, the pre-heated polished samples at 650 °C in an argon environment dip-coated with Wollastonite gel post-heat-treated at 650 °C in an argon atmosphere were considered for the study. Polished titanium substrate dip-coated with Wollastonite had a better microstructure, as shown in **Figure 117**. **Figure 135** shows the FTIR spectra of spray-coated Wollastonite powder and dip-coated Wollastonite onto a polished substrate, respectively.

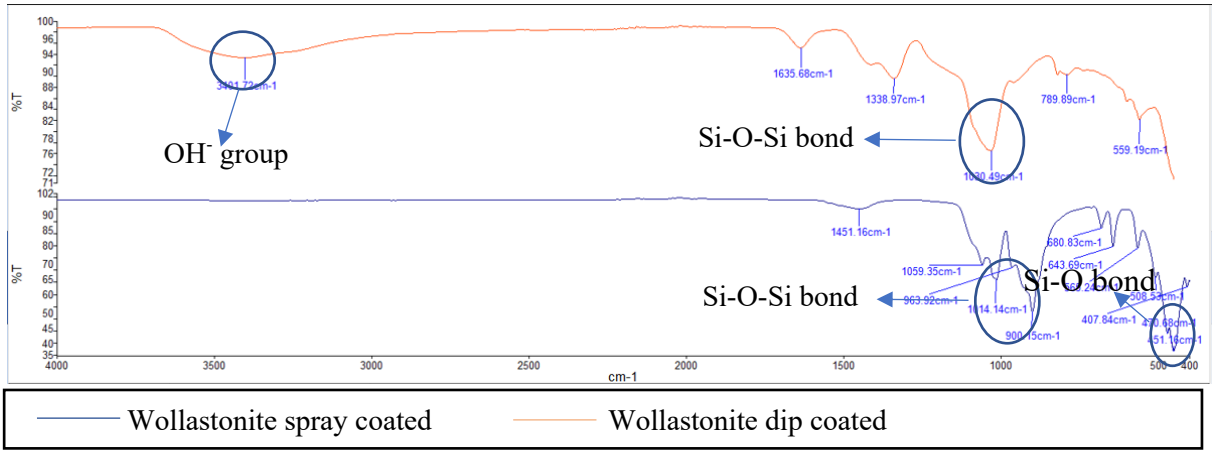

Figure 135, Comparison of FTIR spectra for spray-coated Wollastonite powder heat treated at 1100 °C in an air atmosphere and dip-coated Wollastonite on polished sample heat treated at 650 °C in an argon environment.

Figure 135 shows the comparison of spray-coated and dip-coated Wollastonite samples in terms of FTIR spectra. There were some common bands at a wavelength in the range of approximately 967-1063 $cm^{-1,}$ indicating the Si-O-Si bond, showing the presence of Wollastonite [255]. The dip-coated Wollastonite sample had a broad band at a wavelength of 3401 cm^{-1}, showing the presence of hydroxyl group (OH^- group) in adsorbed water, which was absent in Wollastonite spray-coated samples due to heat treatment at 1100 °C [255] In the case of spray-coated Wollastonite, spray-dried Wollastonite powder heat treated at 1100 °C, was considered. In spray-drying, as-received Wollastonite dissolved in deionised water in the form of suspension was spray-dried using optimised process parameters mentioned in **Section 4.4.** The peaks observed at 3400 cm^{-1} (corresponding to OH^- group in adsorbed water) in moist spray-dried Wollastonite powder after heat treatment at 1100 °C must have disappeared [332]. However, additional bands were observed at this range in the Wollastonite samples heat treated at 1100 °C. More bands in the region of 850-1100 cm^{-1}, indicating the Si-O-Si bond group (showing the presence of Wollastonite) and the bands in the region of 567, 509, 472 and 453 cm^{-1}, indicating the presence of Si-O bond were observed in FTIR spectra of spray-coated Wollastonite samples [255, 333]. Overall, the spray-coated sample had more bands of Wollastonite, which showed crystallinity and better FTIR spectra as compared to dip-coated Wollastonite samples because highly amorphous coatings dissolve quickly, leading to rapid weakening and disintegration of the coating [53]

c) *Comparison in terms of XRD analysis and crystallinity*

The comparison studies were carried out in a similar manner to that of Hydroxyapatite. **Figure 136** shows the comparison of XRD analysis of dip-coated Wollastonite onto a prepared titanium substrate (polished, in this case) and spray-coated Wollastonite onto a prepared titanium substrate (grit blasted, in this case). The Wollastonite was spray-coated onto as-prepared (grit blasted) samples post-heat treated at 1100 °C for 2 hours and was considered for the study due to its better microstructure, as shown in **Figure 80**. In the case of dip-coating, the preheated polished titanium substrate was heat treated at 650 °C in an argon atmosphere, dip-coated with Wollastonite gel, and post-heat treated at 650 °C in an argon atmosphere was considered for the study due to its better microstructure, as shown in **Figure 117**.

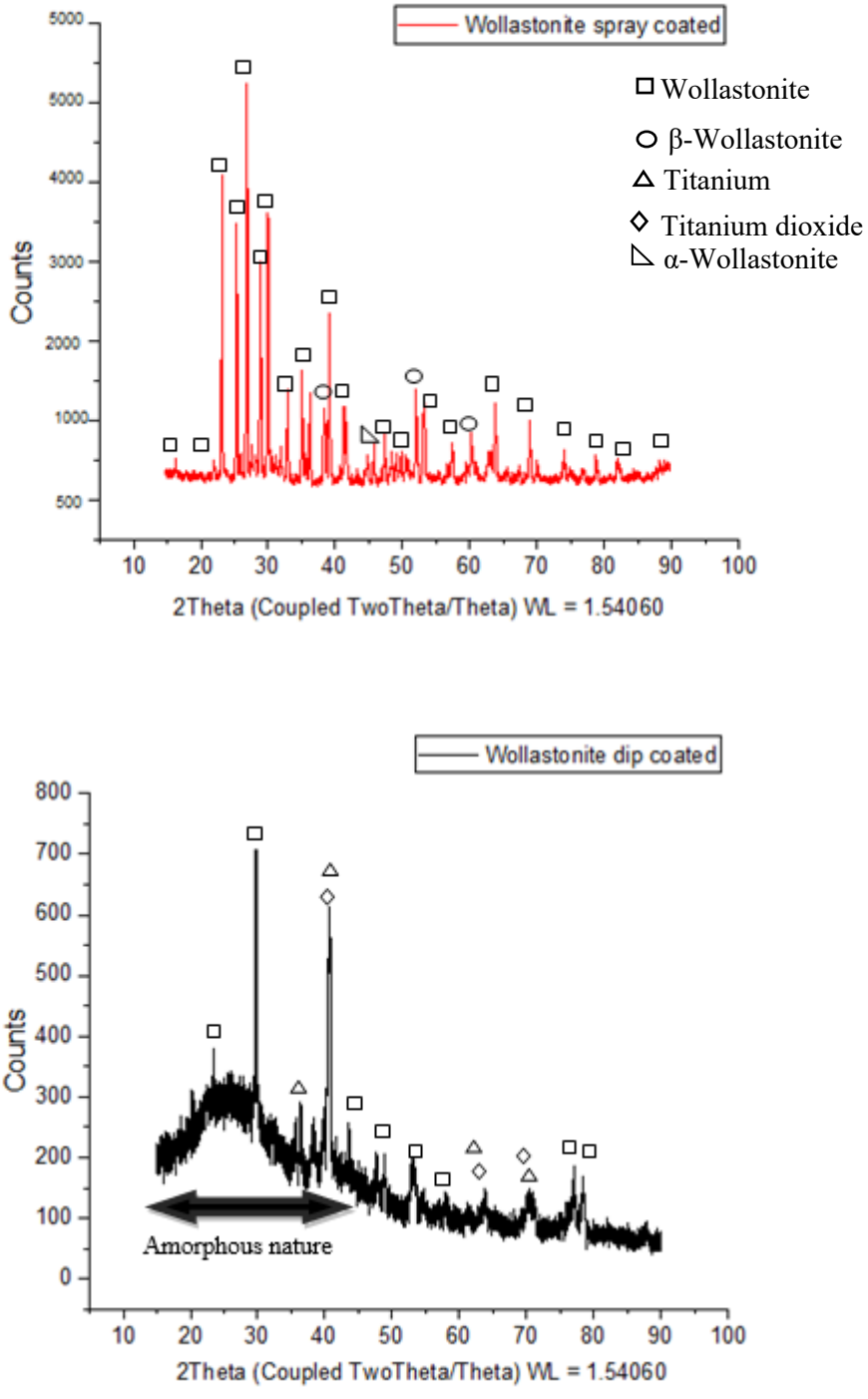

Figure 136, Comparison of XRD pattern of spray-coated Wollastonite on a grit blasted sample heat treated at 1100 °C in an air atmosphere and dip-coated Wollastonite onto a polished titanium substrate heat treated at 650 °C in an argon environment

Figure 136 compares spray-coated and dip-coated Wollastonite XRD patterns onto a titanium substrate. The XRD pattern was different for both the Wollastonite coated samples, with the spray-coated Wollastonite sample showing more crystallinity with high diffraction, whereas dip-coated samples were amorphous with shorter peaks and broad diffraction width [337, 363]. The XRD pattern of spray-coated Wollastonite onto a titanium substrate showed narrow and diffraction peaks showing the crystallinity of the Wollastonite. No titanium or titanium oxides presence phase showed that the Wollastonite layer completely covered the titanium substrate surface. There was minor presence of β-Wollastonite and α-Wollastonite, which may be due to heat treatment of the obtained coating at a higher temperature (1100 °C) [162]. The crystallinity of Wollastonite coating obtained by the spray-coating technique was 87.5%. This crystallinity % was calculated by the DIFFRAC.EVA software (installed with Bruker XRD equipment) which evaluates baseline to peak separation in a scan range, which aligns with the crystallinity range specified by ISO standard ISO 13779-3:2018 [370].

There was some titanium and titanium dioxide in the dip-coated Wollastonite substrate observed due to the pre-heat treatment of polished titanium substrate at 650 °C in an argon atmosphere. The reason may be due to the Wollastonite coating porous nature, as Bastan et al. [211] investigated. This porous nature exposed the titanium substrate layer, and heat treatment (650 °C) led to the formation of titanium dioxide. The XRD pattern showed that the Wollastonite formed by the dip-coating technique was amorphous and porous, as shown by the broader peaks in **Figure 136**. The amorphous nature was due to the synthesis of the Wollastonite by sol-gel method and the presence of Wollastonite increased the porosity in the coating [211, 364]. The crystallinity, as calibrated by the XRD for the dip-coated Wollastonite samples, was only 35.2%, calculated by the same software DIFFRAC.EVA mentioned above. Overall, the Wollastonite spray coated on titanium substrate had a better structure with more crystallinity and higher diffraction peaks. The amorphous nature of the Wollastonite was due to liquid state precipitation technique used to synthesis Wollastonite [34].

4.9.3 Comparison of HA/Wollastonite Composite Coated Samples

a) *Comparison in terms of morphology*

For spray-coated samples, the optimised samples consisted of 20 wt.% Wollastonite mixed with HA-coated onto a grit-blasted titanium substrate post-heat treated at 1100 °C

in an air atmosphere had a better morphology, as shown in **Figure 86**. Though heat treated at a higher temperature, the sample still retained its original structure (spherical for HA and acicular for Wollastonite) with clear boundaries [160]. The samples were more porous but agglomerated, whereas the Wollastonite fibrous structure mixed with the HA spherical structure, similar to studies conducted by Encinas-Romero [160]. The porosity observed in the HA/Wollastonite composite coating may benefit its bioactivity by ensuring the efficient integration of materials with bone tissues during implantation [160].

For the dip-coated samples, only pre-heat treated polished titanium substrate heat treated at 650 °C in argon atmosphere dip-coated with HA/Wollastonite gel post-heat treated at the same temperature and environment was considered as the polished substrate had a better structure mentioned in **Sections 4.8.1** and **4.8.3**. 10 wt.% Wollastonite added to HA gel dip coated onto a preheated (at 650 °C in an argon environment) polished titanium substrate post-heat treated at 650 °C in an argon atmosphere had a better morphology than other dip-coated samples (20 wt.% Wollastonite and 30 wt.% Wollastonite added to the HA gel) heat treated at same temperature and environmental conditions. The coating obtained from this composition produced fewer cracks and lower porosity. The porosity for dip-coated HA/Wollastonite containing 10 wt.% Wollastonite was 13.07%, whereas the porosity for dip-coated HA/Wollastonite biocomposite containing 20 wt. Wollastonite and 30 wt.% Wollastonite was 17.15% and 17.62%, respectively, as obtained by the threshold function in ImageJ software, which calculates the porosity based on the pixels of an SEM image. The acicular shape of the Wollastonite was visible, showing a less homogeneous mixing of Wollastonite with Hydroxyapatite with a concentration of Wollastonite on the surface of the coatings. **Figure 137 (a) and (b)** shows the HA/Wollastonite composite coatings onto a titanium substrate by both methods (dip-coating and spray-coating techniques).

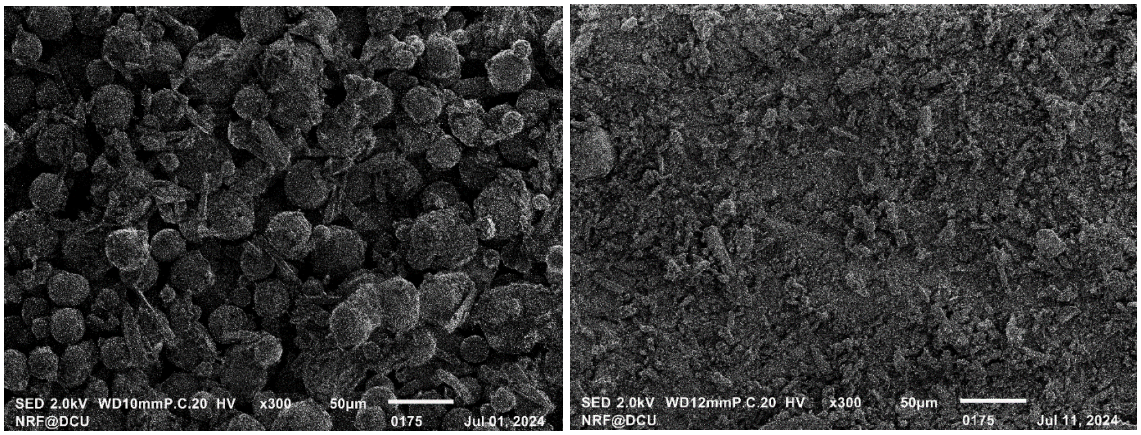

Figure 137, a) HA/Wollastonite composite coatings on grit-blasted titanium substrate by a spray-coating technique heat treated at 1100 °C in an air atmosphere and b) HA/Wollastonite composite coating on a polished titanium substrate by dip-coating technique heat treated at 650 °C in an argon atmosphere.

Overall, HA/Wollastonite composite spray-coated onto a grit blasted titanium substrate heat treated at 1100 °C had better crystallinity and porosity, which would be beneficial for the bioactivity and good crystallinity would ensure stability when implanted inside the body [53, 160].

b) *Comparison in terms of FTIR spectra*

In the case of spray-coated samples, optimised HA/Wollastonite with process parameters: pump flow rate of 19 (scaled value), airflow rate of 31 (scaled value) and Wollastonite wt. fraction of 0.2 spray spray-dried was considered for the study. The spray-dried powder obtained was post-heat-treated at 1100 °C for 2 hours and characterised using FTIR spectra for reasons mentioned in **Section 4.7.3**. In the case of the dip-coated sample, the polished titanium substrate pe-heat treated at 650 °C in an argon atmosphere, dip-coated in the gel containing 10 wt.% Wollastonite added to Hydroxyapatite and post-heat treated at 650 °C in an argon atmosphere was considered for the study due to its better morphology, shown in **Figure 124**. **Figure 138** compares FTIR spectra of spray-coated and dip-coated HA/Wollastonite samples.

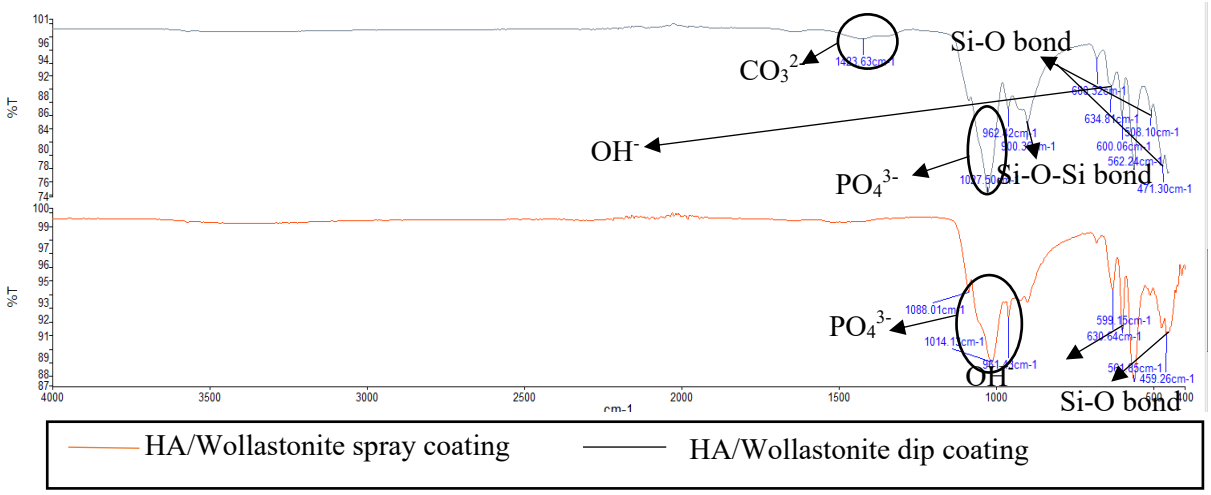

Figure 138, Comparison of FTIR spectra for spray-coated HA/Wollastonite powder heat treated at 1100 °C in an air atmosphere and dip-coated HA/Wollastonite on polished sample heat treated at 650 °C in an argon environment.

Figure 138 compares the FTIR spectra of HA/Wollastonite spray-coated and dip-coated onto a titanium substrate. In the case of the spray-coated HA/Wollastonite sample, the FTIR spectra observed were like those of Hydroxyapatite. This was because of the lower quantity of Wollastonite (20 wt.%) added and the intermixing of Wollastonite fibre and spherical HA particle, as observed in **Figure 138.** The bands were observed at the wavelength of 1088 cm^{-1}, 1015 cm^{-1} and 962 cm^{-1}, indicating the presence of PO_4^{3-} in Hydroxyapatite [333]. Moreover, there was a band observed at a wavelength of 632 cm^{-1}, showing the presence of OH^-. There was a minor band at the wavelength of 453 cm^{-1}, showing the presence of a Si-O bond, indicating Wollastonite [333].

In the case of HA/Wollastonite dip coated, the bands were observed in the wavelength of approximately 1423 cm^{-1}, which shows the presence of carbonate ions in Hydroxyapatite, respectively [332]. There was some presence of Si-O-Si bond at the wavelength 900 cm^{-1}, which shows the presence of Wollastonite [255]. There was a clear presence of Wollastonite in dip-coated HA/Wollastonite samples. There was also a presence of the OH^- group at a wavelength of approximately 630 cm^{-1}, showing the presence of hydroxyl group in Hydroxyapatite. Moreover, bands were observed at a wavelength of approximately 962 cm^{-1} and 1027 cm^{-1}, indicating the presence of phosphate ions (PO_4^{3-}) in Hydroxyapatite [334]. There was also a band observed at an approximate wavelength of 472 and 508 cm^{-1}, showing the presence of the Si-O bond in Wollastonite [333]. Though only 10 wt.% Wollastonite was added, but there bands of Wollastonite which showed most of the Wollastonite was coated on the surface layer.

There was a minor phase of Wollastonite observed in spray-coated HA/Wollastonite even with the higher quantities (20 wt.%) as compared to 10 wt.% Wollastonite present in dip-coated samples. The Wollastonite powder was uniformly mixed with HA in spray coated sample and in the case of dip-coated crystalline solid Wollastonite particles were added to semi-solid gel of HA, resulting in more Wollastonite present at the surface layer. Therefore, the peaks of Wollastonite were higher in dip-coated samples. Moreover, there was a presence of carbonate (CO_3^{2-} ions) for apatite in dip coated samples which disappeared in the case of spray-coated samples due to the heat treatment at higher temperatures (1100 °C) [332]. There were no OH^- peaks (showing the presence of adsorbed water) present at a wavelength of approximately 3400 cm^{-1}, because Wollastonite in a crystallised form and small quantities (20 wt. and 10 wt.%, respectively) was premixed with HA powder in the case of spray-coating technique and added to sol of HA in the case of dip coating technique. Post-heat treatment of the coating at 1100 °C (in the case of the spray coating technique) and 650 °C (in the case of the dip coating technique) may have resulted in dihydroxylation in the case of spray-coated samples and evaporation in the case of dip-coated samples [53].

c) *Comparison in terms of XRD analysis and crystallinity*

In the case of a spray-coated sample, the HA/Wollastonite with 20 wt.% Wollastonite and 80 wt.% HA was spray-coated onto the as-prepared substrate (grit blasted, in this case) with optimised parameters, and the coating was post-heat-treated at 1100 °C in an air atmosphere. HA/Wollastonite spray coated onto a grit blasted sample was considered as it had better microstructure, shown in **Figure 86**. In the case of dip-coating of HA/Wollastonite, the polished titanium substrate pre-heat treated in an argon atmosphere at 650 °C was dipped into the sol containing 10 wt.% Wollastonite and 90 wt.% Hydroxyapatite. The coated samples were post-heat-treated in an argon atmosphere at 650 °C. 10 wt.% Wollastonite dip-coated samples were chosen due to its better microstructure and more bands observed in **Figures 124 and 127**. **Figure 139** compares the XRD pattern of spray-coated and dip-coated HA/Wollastonite coatings onto a prepared substrate.

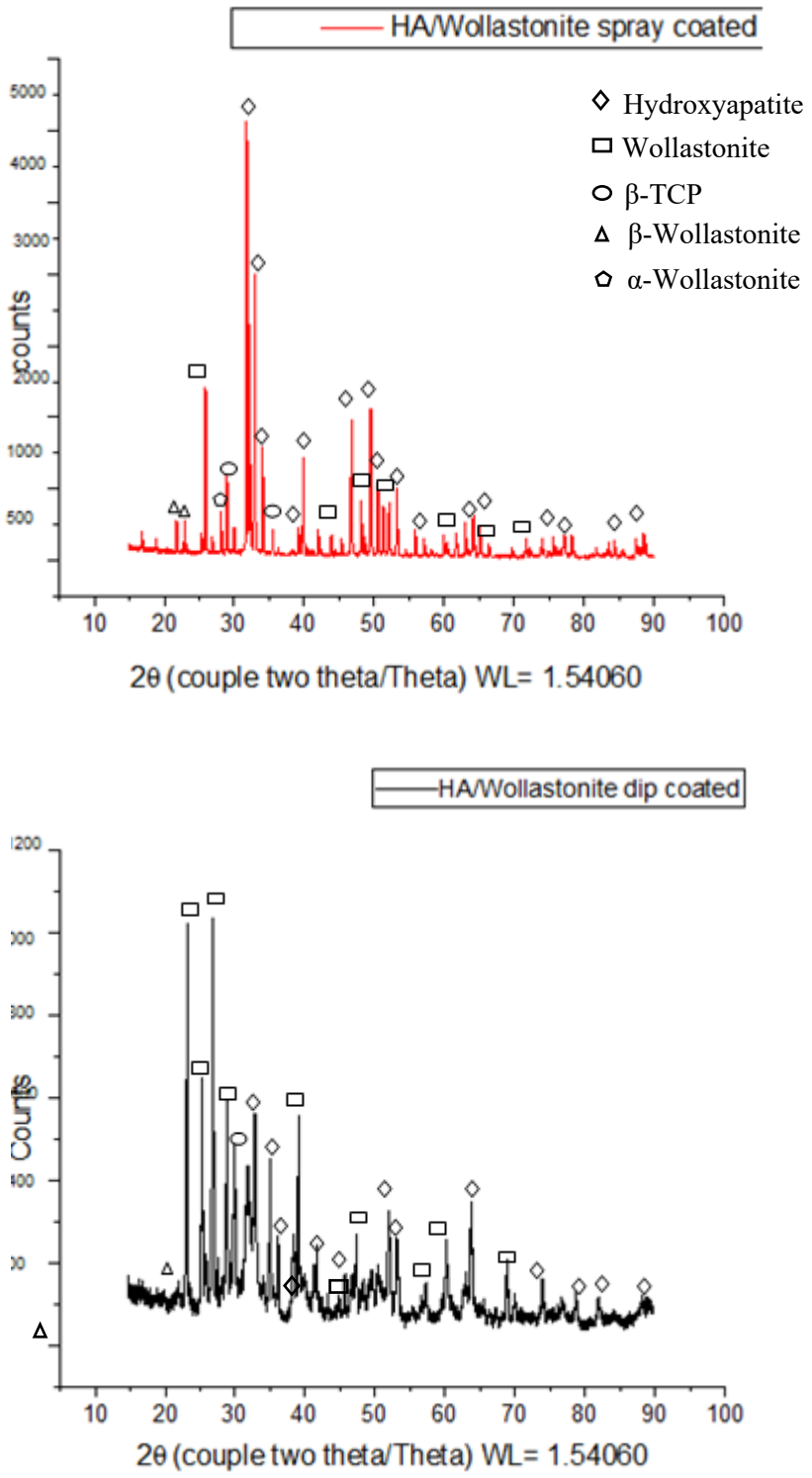

Figure 139, Comparison of XRD pattern of spray-coated HA/Wollastonite on a grit blasted sample heat treated at 1100 °C in an air atmosphere and dip-coated HA/Wollastonite onto a polished titanium substrate heat treated at 650 °C in an argon environment

Figure 139 compares the XRD pattern of dip-coated and spray-coated HA/Wollastonite onto a prepared titanium substrate. HA/Wollastonite spray coated onto a prepared

◇

titanium substrate had bigger diffraction peaks and a narrower region, which showed more crystallinity than dip-coated HA/Wollastonite coatings. The spray-coated samples contained phases of Hydroxyapatite, Wollastonite, α-TCP, β-TCP, α-Wollastonite and β-Wollastonite due to the heat treatment at higher temperature. However, the phases of HA and Wollastonite were minor and did not affect the crystallinity to that effect. The crystallinity of the spray-coated HA/Wollastonite was 87.3%, calculated by DIFFRAC.EVA software by evaluating the baseline to peak separation in a scan range [370], higher than that of the HA/Wollastonite composite coating obtained by the dip-coating technique and as per the specification of 50-70 % mentioned by ISO standard (ISO 13779-3:2018).

The dip-coated HA/Wollastonite coating was more crystalline as compared to the monolithic dip-coated HA and Wollastonite coatings. This may be due to the addition of crystalline Wollastonite particulate powder to the sol of the HA. Polished titanium substrate dip-coated in 10 wt.% Wollastonite/HA sol contained phases such Hydroxyapatite, Wollastonite, β-TCP and β-Wollastonite. The crystallinity of HA/Wollastonite composite with 10 wt.% Wollastonite was 74.1%, calculated by DIFFRAC.EVA software mentioned above. The dip-coated composites samples had more crystallinity and were in the range mentioned in ISO 13779-3:2018 (50-70%). **Table 48** shows an overview description of each coating technique and resulting morphology, FTIR spectra, XRD and crystallinity.

Table 48, Overall comparison of spray-coated and dip-coated samples and their output results

Coating technique	Morphology	FTIR spectroscopy	XRD analysis	Crystallinity	Rank
Titanium spray-coated with HA	Porous, spherical, and interconnected structure	Presence of OH^- and PO_4^{3-}	Phases of Hydroxyapatite, TTCP and β-TCP present	90.4%	#1
Titanium substrate dip-coated in HA gel	Granular structure with less porosity and no crack	Presence of OH^-, CO_3^{2-} and PO_4^{3-}	Phases of Hydroxyapatite, TTCP and β-TCP present	64.3%	#5
Titanium spray-coated with Wollastonite.	Porous with a uniform layer of acicular Wollastonite	Presence of O-Si-O bond, Si-O-Si bond and Si-O vibration bond	Presence of Wollastonite, α-Wollastonite and β-Wollastonite phases	87.7%	#2
Titanium dip coated with Wollastonite gel	Porous with the exposure of titanium layer	Presence of OH^-, H_2O, SiO_3^{2-} and Si-O vibrational bond	Presence of Wollastonite, titanium and titanium dioxide phases	35.2%	#6
HA/Wollastonite (80 wt.% HA and 20 wt.% Wollastonite) spray coated on titanium substrate	Porous coating with more interconnection and mixing of Wollastonite fibres into spherical HA	Presence of OH^-, PO_4^{3-} and Si-O vibration bond	Presence of Wollastonite, β-Wollastonite, α-Wollastonite Hydroxyapatite, TTCP and β-TCP phases	87.3%	#3
Titanium dip coated in	Uniform structure with the presence of	Presence of OH^-, CO_3^{2-}, PO_4^{3-}, Si-O-	Presence of Wollastonite, β-Wollastonite,	74.1%	#4

HA/Wollastonite (90 wt.% HA and 10 wt.% Wollastonite)	spherical HA and acicular Wollastonite particle	Si bond and Si-O vibration bond	Hydroxyapatite and β-TCP phases		

The ranking given above in **Table 48** was based on the crystallinity of the coating**.** The spray-coated samples had higher crystallinity than the dip-coated samples due to the use of crystallised as-received Hydroxyapatite and Wollastonite raw material. Hydroxyapatite-coated samples (spray-coated or dip-coated samples) had higher crystallinity than Wollastonite-coated samples using the same coating technique. The highest crystallinity was observed for the spray-coated HA sample (rank #1) at 90.4% and the lowest for Wollastonite dip-coated samples (#6) at 35.2%. The top 2 ranks were Hydroxyapatite spray-coated samples (rank #1) and Wollastonite spray-coated samples (rank #2), whereas the lowest rank containing the least crystallinity was dip-coated Hydroxyapatite (rank #5) with the crystallinity of 64.3% and dip-coated Wollastonite (rank #6) with the crystallinity of 35.2%. In the case of HA/Wollastonite composite coating, HA/Wollastonite biocomposite (80 wt.% HA and 20 wt.% Wollastonite) spray-coated samples had higher crystallinity of 87.3% (rank #3) than dip-coated HA/Wollastonite biocomposite (90 wt.% HA and 10 wt.% Wollastonite) with crystallinity of 74.1% (rank #4).

Overall, spray-coating was desirable for Hydroxyapatite, Wollastonite, and Hydroxyapatite/Wollastonite biocomposite powders. However, the dip-coating technique was also beneficial for HA/Wollastonite biocomposite with higher HA and lower quantities of Wollastonite (90 wt.% HA and 10 wt.% Wollastonite, in the current study).

4.10 Summary of Discussion

Before coating the substrate with Hydroxyapatite, Wollastonite, or Hydroxyapatite/Wollastonite, the titanium substrate had to be prepared. The two processes used to prepare the substrate in the current study were surface treatment and heat treatment (either polishing or surface roughening). The substrate was initially prepared with the surface treatment of three different roughness's. First the substrate was polished to get a mirror-like finish and obtain an average roughness of 0.08 μm. Second,

the substrate was prepared by grit blasting to obtain a roughness of 4.01 µm. Third, the substrate was prepared to obtain mid-range roughness of 1.85 µm. This surface preparation was done to understand the effect of the spray coating and dip-coating onto a roughness and which prepared substrate favoured which coating technique. For the spray coating technique, the prepared substrates were coated with Hydroxyapatite, Wollastonite or Hydroxyapatite/Wollastonite composite and then post-heat-treated at 1100 °C for 2 hours in an air atmosphere. 1100 °C temperature was selected as both Hydroxyapatite and Wollastonite remained stable up to 1100 °C [53, 162], and 2 hours was selected based on the studies conducted by Levingstone [4]. Heat treatment of the spray-coated sample was done to improve the adhesiveness of the coating and the post-heat treatment in an air atmosphere at 1100°C led to the formation of TiO_2 in non-coating side of the substrate. In the case of dip-coating, The prepared substrate were heat treated at 840 °C and 650 °C. In the case of 840 °C, the as-prepared substrate dip-coated with HA was post-heated in an argon atmosphere at 840 °C at a heating and cooling rate of 2 °C/min based on the studies conducted by Mavis and Taş [254]. Mavis and Taş [254] investigated dip-coated HA samples post-heat treated at 840 °C in a nitrogen atmosphere. In the current study, the as-prepared substrate heat treated at 840 °C in a nitrogen atmosphere resulted in the formation of TiN; therefore, an argon atmosphere was selected to create a vacuum environment. In the case of 650 °C, the as-prepared titanium substrates were pre-heated at 650 °C in an air and argon atmosphere at 1 °C/min with dwell time of 5 hours and cooled to room temperature at same cooling rate, based on the studies conducted by Usinskas et al. [300]. However, heat treatment of titanium substrate resulted in the formation of TiO_2, therefore substrate was also heat treated in an argon atmosphere to create a vacuum. Overall, substrate heat treated at 650 °C in an argon environment was selected for dip coating had less phase and oxide formation with more presence of titanium as observed by XRD analysis, as mentioned in **Figure 69.** Overall, for spray coating, HA, Wollastonite and HA/Wollastonite coated onto a grit blasted sample had better coating microstructure with more agglomerates of coating material and less dispersion whereas, for dip coating, HA, Wollastonite and HA/Wollastonite dip coated on polished sample had better microstructure with less cracks.

Various attempts have been made to synthesise the biocomposite of Hydroxyapatite (HA)/Wollastonite (W). The presence of Wollastonite does not affect the properties of

Hydroxyapatite [159]. The biocomposite (HA/W) phase evaluation synthesised by the co-precipitation method did not show any phase change at 800 ºC [256]. The acicular shape of Wollastonite can embed Hydroxyapatite particles well [162]. In the current study, HA and Wollastonite powder were spray-dried with process parameters such as pump flow rate, airflow rate, and inlet temperature, along with DOE results, explained in **Section 4.5**. Based on the best results obtained, HA and Wollastonite were blended to form a mixture of powder and spray-dried with DOE results. The morphological evaluation showed the spherical shape of Hydroxyapatite along with the acicular shape of Wollastonite, as shown in **Figure 53**. The DOE results obtained were further optimised, and the HA/Wollastonite were spray-coated with these optimised process parameters (yielding rank #1 and #2 in **Table 48**). The parameters would be pump flow rate (obtained from spray drying of HA and Wollastonite), airflow rate (obtained from spray drying of HA and Wollastonite), and HA/Wollastonite mixture composition (the inlet temperature was the same for the optimised results of Hydroxyapatite and Wollastonite). The maximum amount of Wollastonite used was 20 wt.% Wollastonite, based on the study conducted by Bastan et al. [211], as a higher percentage of Wollastonite would result in degradability of the coating within the body. The mixture powder was spray-coated onto a prepared titanium substrate and post-processed by heat treatment at 1100 °C for 2 hours to form a coating. The coating was characterised by its chemical properties. The results showed coatings onto the grit blasted showed better microstructure with more agglomerates, less dispersion of HA/Wollastonite due to a high surface area caused due to roughness of the surface [339,340]. The morphological structure of the spray-coatings was porous, which could have a positive impact on its bioactivity [160]. (ranked #3 according to **Table 48**)

Hydroxyapatite and Wollastonite were coated onto a titanium substrate by sol-gel dip coating technique. The coatings showed pores in Hydroxyapatite coating and cracks in Wollastonite coating. XRD pattern showed the complete covering of Hydroxyapatite coating onto a titanium substrate, shown in **Section 4.8.1**. In contrast, the substrate surface was exposed to the atmosphere due to cracks in Wollastonite coating resulting in XRD peak of titanium dioxide (TiO_2), as shown in **Section 4.8.3**. Therefore, Wollastonite in the particulate material was added to the gel of Hydroxyapatite to form a HA/Wollastonite biocomposite coating, similar to studies conducted by Encinas-Romero

et al. [160]. The Wollastonite powder was added 10 wt.%, 20 wt.% and 30 wt.%. These quantities were chosen to prevent early resorption when implanted in the body caused by the Wollastonite. Out of the three different biocomposite coatings, 10 wt.% Wollastonite/HA had a better microstructure with fewer cracks, more FTIR peaks and better crystallinity as compared to monolithic-coated HA and Wollastonite coatings. Most of the Wollastonite remained on the surface of the coating layer, which showed improper mixing due to different states of particulate Wollastonite and HA gel (it ranked #4 according to **Table 48**). Since the coating obtained, had fewer cracks and lower porosity, further studies must be conducted concerning its mechanical properties.

Spray-coated samples had better crystallinity than dip-coated samples (hence ranked higher according to **Table 48**). In the case of spray-coated samples, the Wollastonite particles were uniformly mixed with HA particles. There was no presence of a titanium or titanium dioxide layer, which showed a uniform coating of the coating onto a substrate in spray-coated samples. In the case of dip-coated HA/Wollastonite samples, the addition of the particulate Wollastonite increased the crystallinity of the dip-coated sample. Moreover, there was no exposure of substrate layer, observed in monolithic dip-coated Wollastonite samples. The dip coating results showed that Wollastonite could only be used as additive material and not as a monolithic coating due to pores and cracks.

5 Conclusion and Recommendation for Future Work

5.1 Conclusion

This project opens a wide range of possibilities for exploring Wollastonite and its compatibility with different types of processes. In combination with Hydroxyapatite, Wollastonite can improve the load-bearing capability of the implant.

- Spray drying technique was used for Hydroxyapatite and Wollastonite for the following reasons:
  - Hydroxyapatite was spray-dried with the process parameters obtained from the previous research. DOE analysis was performed on the spray-dried powder to understand the effect of process parameters on the response (45-75 μm). It was observed that a higher pump flow rate, lower airflow rate, and lower inlet air temperature favoured higher response in the case of Hydroxyapatite.
  - The same process parameters were used to spray dry Wollastonite with DOE analysis. Lower pump flow rate, higher airflow rate, and lower inlet temperature favoured higher response in the case of Wollastonite.
- Optimisation of spray-dried HA/Wollastonite powder
  - Spray-dried HA had the best results at process parameters: pump flow rate of 20 (scaled value), air flow rate of 22 (scaled value) and inlet temperature of 103 °C, whereas spray-dried Wollastonite had the best results at the pump flow rate of 15 (scaled value), air flow rate of 33 (scaled value) and inlet temperature of 103 °C. Therefore, HA/Wollastonite was spray dried with the process parameter: pump flow rate ranging from 15-20 (scaled value), airflow rate ranging from 22-33 (scaled value) and Wollastonite wt.fraction of 0.2-0.5. the results showed higher pump flow rate, airflow rate and Wollastonite wt.fraction favoured higher response in HA/Wollastonite composite powder.
  - The optimisation of the results for spray-dried HA/Wollastonite was attained at a pump flow rate of 19 (scaled value), the airflow rate of 30 (scaled value) and Wollastonite wt. fraction of 0.2.
- Spray coating of HA, Wollastonite and HA/Wollastonite onto a prepared substrate.

- Initially, the substrates were prepared with 3 different roughness: polished with an average roughness of 0.08 µm, mid-range roughness with an average roughness of 1.85 µm and grit-blasted with an average roughness of 4.01 µm.
- The prepared samples were spray coated with HA, Wollastonite, and HA/Wollastonite obtained from the best spray drying process parameters of the corresponding material. The obtained coatings were heat treated in an air atmosphere at 1100 °C for 2 hours.
- The results showed that grit-blasted samples have better microstructures with more agglomerated structures and porous structures, which could be tested for its bioactivity.
- The crystallinity of spray-coated HA was 90.4%, spray-coated Wollastonite was 87.7%, spray-coated HA/Wollastonite was 87.3%.

- Preparation and characterisation of the titanium substrate for the dip-coating technique
  - Initially, the titanium alloy substrates were prepared by polishing and grit blasting to attain three different roughness's: the first substrate with an average roughness of 0.08, the second substrate with an average roughness of 1.85 µm, and the third substrate with an average roughness of 4.01 µm. All substrates were heat-treated at different temperatures and environment conditions: 650 °C in an air environment in the first setup, 840 °C in an argon environment in the second setup, 650 °C in an argon environment in the third setup. The substrate heat treated at nitrogen was deducted, as studies from the XRD showed the presence of titanium nitride.
  - The substrates were then characterised by XRD analysis. It was observed that the polished substrate heat treated at 650 °C in an argon environment performed in terms of less phase change and less oxide formation. The substrate heat treated at this temperature and environmental condition was dip-coated with HA, Wollastonite and HA/Wollastonite to obtain their corresponding coatings.
- The sol-gel dip immersive technique was employed to coat Hydroxyapatite, Wollastonite and HA/Wollastonite onto a polished titanium substrate.
  - The precursors of Hydroxyapatite and Wollastonite were obtained to synthesise the sol-gel solution of Hydroxyapatite and Wollastonite separately. The prepared titanium alloy substrate mentioned above was dipped into the solution containing Hydroxyapatite and Wollastonite precipitate. In the case of HA/Wollastonite composite dip-coatings,

Wollastonite in the particulate form was added in 10 wt.%, 20wt.% and 30 wt.%, respectively was added to HA gel separately. The samples obtained through coating and heat treatment underwent chemical characterisation, which included SEM, FTIR, and XRD analysis.

- The chemical characterisation tests inferred that the Hydroxyapatite, Wollastonite and 10 wt.% Wollastonite/HA coating on polished sample heat treated at 650 °C in an argon atmosphere performed better. The coatings obtained from this temperature and environmental conditions had fewer cracks, more particle deposition and less phase change.
- The crystallinity of dip-coated HA was 64.3% (rank #5), dip-coated Wollastonite was 35.2% (rank #6) and dip-coated HA/Wollastonite was 74.1% (rank #4), as shown in **Table 48**.
- Overall, spray coated sample coated with HA (rank #1), Wollastonite (rank #2), HA/Wollastonite composite 20 wt.% Wollastonite (rank #3) had the better structure in terms of crystallinity and porosity, as shown in **Table 48**. However, more studies are needed to be conducted to investigate its mechanical and biological properties.

5.2 Objective Success

In **Chapter 1**, the objectives of the research were outlined, therefore below is a detail of which objectives were achieved and how they were satisfied as follows:

- Objective 1 success: - The Hydroxyapatite was spray-dried and had optimal response at process parameters: pump flow rate of 20 (scaled value), airflow rate of 22 (scaled value) and inlet temperature of 103 °C. The process parameters were obtained from 2-factor fractional factorial method. The Wollastonite was spray-dried and had optimal response at process parameters: pump flow rate of 15 (scaled value), airflow rate of 33 (scaled value) and inlet temperature of 103 °C. Based on the response obtained from the spray drying of Hydroxyapatite and Wollastonite, HA/Wollastonite was spray-dried with the process parameters and analysed using the Box-Behnken method. Further, optimisation of the obtained results was attained at process parameters: pump flow rate of 19 (scaled value), airflow rate of 30 (scaled value) and Wollastonite wt. a fraction of 0.2 (80 wt.% HA and 20 wt.% Wollastonite) and constant inlet temperature of 103 °C.
- Objective 2 was unsuccessful due to the lack of flowability of Wollastonite.

- Objective 3 success: - The prepared titanium substrate was dipped into the precursor of calcium and phosphorous to form Hydroxyapatite coating. It was observed that the polished titanium substrate preheated at 650 °C in an argon atmosphere coated in Hydroxyapatite gel and was post-heat treated at similar temperatures and environmental conditions presented the coating with minimal cracks and lower porosity. The same results were attained for dip coating of titanium substrate in the precursor of calcium and silicon to obtain a Wollastonite. Polished substrate heat treated at the same temperature and environmental conditions presented the best microstructure with minimal cracks. In the case of HA/Wollastonite biocomposite, polished titanium substrate dipped 10 wt.% Wollastonite added to the sol of HA heat treated at same temperature and environment conditions presented better microstructure and had better crystallinity than monolithic coatings of HA and Wollastonite obtained by dip-coating technique.

- Objective 4 success: - Hydroxyapatite spray-coated with the optimal process parameters obtained from Design of Experiment onto a grit-blasted sample presented porous, agglomerated but highly crystallised microstructure (rank #1 in **Table 48**). In the case of spray coating of Wollastonite, Wollastonite spray-coated with optimal process parameters obtained from Design of Experiment presented porous, uniform structure with higher crystallinity (rank #2 in **Table 48**). Simialr to spray coating of HA and Wollastonite, HA/Wollastonite spray-coated with optimised process parameters presented porous, agglomerated and well defined crystalline coating microstructure (rank #3).

5.3 Recommendations for Future Research

- In depth study of coating of the prepared substrates (polished, mid-range roughness and grit-blasted samples) by spray-coating and dip-coating techniques in terms of coating deposition and properties.
- Analysis of the prepared coated (both spray-coated and dip coated) samples through the cross-section of the coating to get in-depth analysis of the coating. Moreover, the impact of heat-treatment on the coated samples by analysis using techniques like SEM, FTIR and XRD.
- Mechanical characterisation, which includes an adhesion test and tensile strength test, should be conducted on the high ranked (**Table 48**) samples obtained from the dip-coating technique and spray-coating technique to understand its application in load-

bearing applications. These tests would also help to understand the effect on mechanical strength with the addition of Wollastonite. The mechanical characterisation test should be carried out on the sol-gel dip-coated samples as they had better adhesion than the spray-coated samples.

- Biological characterisation, especially on the spray-coated samples. The spray-coated samples were porous, which would promote osseointegration. Biological tests such as immersion in SBF fluid, MTT Assay and cytotoxicity tests would be help to understand the effect of the porosity and the addition of the Wollastonite onto a sample both *in vivo* and *in vitro*.
- Further mechanical characterisation techniques such as tensile strength tests, scratch tests, residual strength tests, bond strength tests or fatigue testing and comparison with the monolithic HA coating would help to understand the effect of Wollastonite on the overall mechanical properties of the coating.
- More studies are needed to improve the flowability of the Wollastonite. Techniques such as plasma spherodisation, which change the acicular shape of Wollastonite without affecting its properties, are needed, or one can also use Wollastonite in suspension plasma spray either as a monolithic coating or as composite coating with Hydroxyapatite. The comparison with the thermally sprayed Hydroxyapatite coating would open a wide area of research to understand Wollastonite as a substitute for bone.
- Further studies are required to synthesise a biocomposite of Hydroxyapatite/Wollastonite by sintering techniques, milling the obtained sintered material to the desired particle size and then conducting mechanical and biological studies onto a synthesised biocomposite.

6 References

[1] Navarro, M., Michiardi, A., Castaño, O., and Planell, J. A., 2008, "Biomaterials in Orthopaedics," J. R. Soc. Interface, **5**(27), pp. 1137–1158.

[2] Scheidt, R. B., Rosito, R., De Souza Macedo, C. A., and Galia, C. R., 2010, "Total Hip Arthroplasty With Biomec Prosthesis: 20-Year Follow-Up," Rev. Bras. Ortop. (English Ed., **45**(2), pp. 155–159.

[3] Feith, R., 1975, "Side-Effects of Acrylic Cement Implanted into Bone: A Histological, (Micro)Angiographic, Fluorescence-Microscopic and Autoradiographic Study in the Rabbit Femur," Acta Orthop. Scand., **46**(sup161), pp. 1–136.

[4] Levingstone, T., 2008, "Optimisation of Plasma Sprayed Hydroxyapatite Coatings," Thesis, PhD Thesis, p. 256, (Online), Available: http://doras.dcu.ie/579/, (Accessed: 04-Sep-2024).

[5] Kwon, J. Y., Naito, H., Matsumoto, T., and Tanaka, M., 2013, "Estimation of Change of Bone Structures after Total Hip Replacement Using Bone Remodeling Simulation," Clin. Biomech., **28**(5), pp. 514–518.

[6] Ohtsuki, C., Kamitakahara, M., and Miyazaki, T., 2009, "Bioactive Ceramic-Based Materials with Designed Reactivity for Bone Tissue Regeneration," J. R. Soc. interface, **6**(January), pp. 349–360.

[7] Huang, Y., Song, L., Liu, X., Xiao, Y., Wu, Y., Chen, J., Wu, F., and Gu, Z., 2010, "Hydroxyapatite Coatings Deposited by Liquid Precursor Plasma Spraying: Controlled Dense and Porous Microstructures and Osteoblastic Cell Responses," Biofabrication, **2**(4), pp. 1–10.

[8] Sun, L., Berndt, C. C., Khor, K. A., Cheang, H. N., and Gross, K. A., 2002, "Surface Characteristics and Dissolution Behavior of Plasma-Sprayed Hydroxyapatite Coating," J. Biomed. Mater. Res., **62**(2), pp. 228–236.

[9] Czupryński, A., 2019, "Flame Spraying of Aluminum Coatings Reinforced with Particles of Carbonaceous Materials as an Alternative for Laser Cladding Technologies," Materials, **12**(21), pp. 1–18.

[10] Moya, S., Dolores, M., and Vilches, Sánchez, Javier, Enrique, Rodrigo, Moreno. Emiie, Bannier, Monica, V., 2013, "Atmospheric Plasma Spraying Coatings from Alumina – Titania Feedstock Comprising Bimodal Particle Size Distributions.," J. Eur. Ceram. Soc., **33**(15), pp. 3313–3324.

[11] Tadic, D., Peters, F., and Epple, M., 2002, "Continuous Synthesis of Amorphous Carbonated Apatites," Biomaterials, **23**(12), pp. 2553–2559.

[12] Heimann, R., 2017, "Osseoconductive and Corrosion-Inhibiting Plasma-Sprayed Calcium Phosphate Coatings for Metallic Medical Implants," Metals, **7**(11), pp. 1–19.

[13] With, G., Dijk, H. J. A., Hattu, N., and Prijs, K., 1981, "Preparation, Microstructure and Mechanical Properties of Dense Polycrystalline Hydroxy Apatite," J. Mater. Sci., **16**(6), pp. 1592–1598.

[14] Cheang, P., and Khor, K. A., 1996, “Addressing Processing Problems Associated with Plasma Spraying of Hydroxyapatite Coatings,” Biomaterials, **17**(5), pp. 537–544.

[15] Yang, Y., Kim, K. H., and Ong, J. L., 2005, “A Review on Calcium Phosphate Coatings Produced Using a Sputtering Process - An Alternative to Plasma Spraying,” Biomaterials, **26**(3), pp. 327–337.

[16] Nimb, L., Gotfredsen, K., and Steen Jensen, J., 1993, “Mechanical Failure of Hydroxyapatite-Coated Titanium and Cobalt-Chromium-Molybdenum Alloy Implants. An Animal Study.,” Acta Orthop. Belg., **59**(4), pp. 333–338.

[17] Xue, W., Liu, X., Zheng, X. Bin, and Ding, C., 2005, “In Vivo Evaluation of Plasma-Sprayed Wollastonite Coating,” Biomaterials, **26**(17), pp. 3455–3460.

[18] Lin, K., Zhang, M., Zhai, W., Qu, H., and Chang, J., 2011, “Fabrication and Characterization of Hydroxyapatite/Wollastonite Composite Bioceramics with Controllable Properties for Hard Tissue Repair,” J. Am. Ceram. Soc., **94**(1), pp. 99–105.

[19] Zenebe, C. G., 2022, “A Review on the Role of Wollastonite Biomaterial in Bone Tissue Engineering,” Biomed Res. Int., pp. 1–15.

[20] Brunette, D., Tengvall, P., and Textor, M., 2001, “Titanium in Medicine: Material Science, Surface Science, Engineering, Biological Responses and Medical Applications,” Springer, New York, Berlin. ISBN: 978-3-642-63119-1.

[21] Nelea, V., Morosanu, C., Iliescu, M., and Mihailescu, I. N., 2004, “Hydroxyapatite Thin Films Grown by Pulsed Laser Deposition and Radio-Frequency Magnetron Sputtering: Comparative Study,” Appl. Surf. Sci., **228**(1–4), pp. 346–356.

[22] Almasri, K. A., Sidek, H. A. A., Matori, K. A., and Zaid, M. H. M., 2017, “Effect of Sintering Temperature on Physical, Structural and Optical Properties of Wollastonite Based Glass-Ceramic Derived from Waste Soda Lime Silica Glasses,” Results Phys., **7**, pp. 2242–2247.

[23] Núñez-Rodríguez, L. A., Encinas-Romero, M. A., Gómez-Álvarez, A., Valenzuela-García, J. L., and Tiburcio-Munive, G. C., 2018, “Evaluation of Bioactive Properties of α and β Wollastonite Bioceramics Soaked in a Simulated Body Fluid,” J. Biomater. Nanobiotechnol., **09**(03), pp. 263–276.

[24] Arboleda, J. A., Serna, C. M., Cadavid, E., Barrios, A. C., Vargas, F., and Toro, A., 2018, “Effect of Flame Spray Deposition Parameters on the Microstructure of Al2O3 - 13 %TiO2 Coatings Applied onto 7075 Aluminum Alloy,” Mater. Res., **21**(5), pp. 3–14.

[25] Sakka, S., 1994, “The Current State of Sol-Gel Technology,” J. Sol-Gel Sci. Technol., **3**(2), pp. 69–81.

[26] Guglielmi, M., 1997, “Sol-Gel Coatings on Metals,” J. Sol-Gel Sci. Technol., **8**(1–3), pp. 443–449.

[27] Regan, J., VanPutte, C., and Russo, A., 2016, “Seeley’s Essential of Anatomy

and Physiology," New York, ISBN: 9780078097324.

[28] Lerner, U. H., 2012, "Osteoblasts, Osteoclasts, and Osteocytes: Unveiling Their Intimate-Associated Responses to Applied Orthodontic Forces," Semin. Orthod., **18**(4), pp. 237–248.

[29] Gray, H., 2013, "Grays Anatomy," Arcturus Publishing, London, ISBN: 9781782124269.

[30] Tarik, 2016, "Anatomy and Physiology," (Online), Available: https://socratic.org/questions/what-does-bone-structure-mean, (Accessed: 04-Sep-2024).

[31] Hadjidakis, D. J., and Androulakis, I. I., 2006, "Bone Remodeling," Ann. N. Y. Acad. Sci., **1092**, pp. 385–396.

[32] Levingstone, T., Hingston, J., 2008, "Issue 4: Guide to Hip Replacements for Engineers: Design, Material and Stress Issues," Dublin City University, Dublin, ISBN: 1-87232-779-6.

[33] Kehoe, S., 2008, "Optimisation of Hydroxyapatite (HAp) for Orthopaedic Application via the Chemical Precipitation Technique," (September), PhD Thesis, p. 393, (Online), Available: http://doras.dcu.ie/583/, (Accessed: 04-Sep-2024).

[34] Kehoe, S., 2008, "Issue 4: Calcium Phosphates for Medical Applications," Dublin City University, Dublin, ISBN: 1-87232-776-1.

[35] Hughes, J. M., Cameron, M., and Crowley, K. D., 1989, "Structural Variations in Natural F, OH, and Cl Apatites," Am. Mineral., **74**(7–8), pp. 870–876.

[36] Santavirta, S., 1998, "Materials in Total Joint Replacement," Curr. Orthop., **12**(1), pp. 51–57.

[37] Merola, M., and Affatato, S., 2019, "Materials for Hip Prostheses: A Review of Wear and Loading Considerations," Materials, **12**(3), pp. 1–24.

[38] Wang, M., 2003, "Developing Bioactive Composite Materials for Tissue Replacement," Biomaterials, **24**(13), pp. 2133–2151.

[39] Hench, L. L., and Cao, W., 1996, "Bioactive Materials," Ceram. Int. 22, **8842**(95), pp. 493–507.

[40] Wang, W., and Yeung, K. W. K., 2017, "Bone Grafts and Biomaterials Substitutes for Bone Defect Repair: A Review," Bioact. Mater., **2**(4), pp. 224–247.

[41] Kamaly, N., Yameen, B., Wu, J., and Farokhzad, O. C., 2016, "Nanoparticles: Mechanisms of Controlling Drug Release," Chem Rev., **116**(4), pp. 2602–2663.

[42] Asadi, N., Del Bakhshayesh, A. R., Davaran, S., and Akbarzadeh, A., 2020, "Common Biocompatible Polymeric Materials for Tissue Engineering and Regenerative Medicine," Mater. Chem. Phys., **242**(122528), pp. 1–11.

[43] Langer, R., 2000, "Biomaterials in Drug Delivery and Tissue Engineering: One Laboratory's Experience," Acc. Chem. Res., **33**(2), pp. 94–101.

[44] Singh, R., and Lillard, J. W., 2009, “Nanoparticle-Based Targeted Drug Delivery,” Exp. Mol. Pathol., **86**(3), pp. 215–223.

[45] Soleymani Eil Bakhtiari, S., Bakhsheshi-Rad, H. R., Karbasi, S., Tavakoli, M., Hassanzadeh Tabrizi, S. A., Ismail, A. F., Seifalian, A., RamaKrishna, S., and Berto, F., 2021, “Poly(Methyl Methacrylate) Bone Cement, Its Rise, Growth, Downfall and Future,” Polym. Int., **70**(9), pp. 1182–1201.

[46] Huiskes, R., 1993, “Mechanical Failure in Total Hip Arthroplasty with Cement,” Curr. Orthop., **7**(4), pp. 239–247.

[47] Dunne, N. J., and Orr, J. F., 2002, “Curing Characteristics of Acrylic Bone Cement,” J. Mater. Sci. Mater. Med., **13**(1), pp. 17–22.

[48] Hench, L. L., and Wilson, J., 2013, “Introduction,” An Introduction to Bioceramics, L.L. Hench, ed., Florida, pp. 1–26, ISBN: 978-1-908977-15-1.

[49] Vallet-Regí, M., and González-Calbet, J. M., 2004, “Calcium Phosphates as Substitution of Bone Tissues,” Prog. Solid State Chem., **32**(1–2), pp. 1–31.

[50] Shekhawat, D., Singh, A., Bhardwaj, A., and Patnaik, A., 2021, “A Short Review on Polymer, Metal and Ceramic Based Implant Materials,” IOP Conf. Ser. Mater. Sci. Eng., **1017**(1), pp. 1–12.

[51] Thamaraiselvi, T., and Rajeswari, S., 2004, “Biological Evaluation of Bioceramic Materials - A Review,” Trends Biomater. Artif. Organs, **18**(1), pp. 9–17.

[52] Licuilli, A., 2005, “An Introduction to Bioceramics,” p. 78, (Online), Available: https://www.scribd.com/document/484394864/bioceramics-pdf, (Accessed: 04-Sep-2024).

[53] Levingstone, T. J., 2008, "Issue 1 : Ceramics for Medical Applications," Dublin City University, Dublin, ISBN: 1-87232-752-4.

[54] Böke, F., Schickle, K., and Fischer, H., 2014, “Biological Activation of Inert Ceramics: Recent Advances Using Tailored Self-Assembled Monolayers on Implant Ceramic Surfaces,” Materials, **7**(6), pp. 4473–4492.

[55] Maccauro, G., Rossi, P., Raffaelli, L., and Francesco, P., 2011, “Alumina and Zirconia Ceramic for Orthopaedic and Dental Devices,” Biomaterials Applications for Nanomedicine, Prof. Rosario Pignatello, ed., Intech, London, pp. 299-308, ISBN: 978-953-307-661-4.

[56] Hulbert, S. F., 2013, “The Use of Alumina and Zirconia in Surgical Implants,” An Introduction to Bioceramics, L.L. Hench, ed., Florida, pp. 27–47, ISBN: 981-02-1400-6.

[57] Lemons, J. E., 1996, “Ceramics: Past, Present, and Future,” Bone, **19**(1 SUPPL.), pp. S121–S128.

[58] Mohseni, E., Zalnezhad, E., and Bushroa, A. R., 2014, “Comparative Investigation on the Adhesion of Hydroxyapatite Coating on Ti-6Al-4V Implant: A Review Paper,” Int. J. Adhes. Adhes., **48**, pp. 238–257.

[59] Hench, L. L., and Andersson, O., 2013, “Bioactive Glasses,” An Introduction to Bioceramics, L.L. Hench, ed., Florida, pp. 49–70, ISBN: 978-953-307-661-4.

[60] Yoshimura, Masahiro, Suchanek, W., 1998, “Processing and Properties of Hydroxyapatite- Based Biomaterials for Use as Hard Tissue Replacement Implants,” J. Mater. Res., **13**(1), pp. 94–117.

[61] Gomes, D. S., Santos, A. M. C., Neves, G. A., Menezes, R. R., Grande, C., and Grande, C., 2019, “A Brief Review on Hydroxyapatite Production and Use in Biomedicine (Uma Breve Revisão Sobre a Obtenção de Hidroxiapatita e Aplicação Na Biomedicina),” Cerâmica, **65**, pp. 282–302.

[62] Mobasherpour, I., Heshajin, M. S., Kazemzadeh, A., and Zakeri, M., 2007, “Synthesis of Nanocrystalline Hydroxyapatite by Using Precipitation Method,” J. Alloys Compd., **430**(1–2), pp. 330–333.

[63] Hu, J., Russell, J. J., Ben-Nissan, B., and Vago, R., 2001, “Production and Analysis of Hydroxyapatite from Australian Corals via Hydrothermal Process,” J. Mater. Sci. Lett., **20**(1), pp. 85–87.

[64] Lee, S. J., and Oh, S. H., 2003, “Fabrication of Calcium Phosphate Bioceramics by Using Eggshell and Phosphoric Acid,” Mater. Lett., **57**(29), pp. 4570–4574.

[65] Ben-Nissan, B., Milev, A., and Vago, R., 2004, “Morphology of Sol-Gel Derived Nano-Coated Coralline Hydroxyapatite,” Biomaterials, **25**(20), pp. 4971–4975.

[66] Liu, D. M., Troczynski, T., and Tseng, W. J., 2001, “Water-Based Sol-Gel Synthesis of Hydroxyapatite: Process Development,” Biomaterials, **22**(13), pp. 1721–1730.

[67] Bogdanoviciene, I., Beganskiene, A., Tõnsuaadu, K., Glaser, J., Meyer, H. J., and Kareiva, A., 2006, “Calcium Hydroxyapatite, Ca10(PO4)6(OH)2 Ceramics Prepared by Aqueous Sol-Gel Processing,” Mater. Res. Bull., **41**(9), pp. 1754–1762.

[68] Weng, W., and Baptista, J. L., 1997, “A New Synthesis of Hydroxyapatite,” J. Eur. Ceram. Soc., **17**(9), pp. 1151–1156.

[69] Kim, I. S., and Kumta, P. N., 2004, “Sol-Gel Synthesis and Characterization of Nanostructured Hydroxyapatite Powder,” Mater. Sci. Eng. B Solid-State Mater. Adv. Technol., **111**(2–3), pp. 232–236.

[70] Zhang, S, Gonsalves, K. E., 1997, “Preparation and Characterization of Thermally Stable Nanohydroxyapatite,” J. Mater. Sci. Mater. Med., **8**, pp. 25–28.

[71] Chen, C. W., Oakes, C. S., Byrappa, K., Riman, R. E., Brown, K., TenHuisen, K. S., and Janas, V. F., 2004, “Synthesis, Characterization, and Dispersion Properties of Hydroxyapatite Prepared by Mechanochemical-Hydrothermal Methods,” J. Mater. Chem., **14**(15), pp. 2425–2432.

[72] Rhee, S. H., 2002, “Synthesis of Hydroxyapatite via Mechanochemical Treatment,” Biomaterials, **23**(4), pp. 1147–1152.

[73] Bernard, L., Freche, M., Lacout, J. L., and Biscans, B., 1999, “Preparation of Hydroxyapatite by Neutralization at Low Temperature - Influence of Purity of

the Raw Material," Powder Technol., **103**(1), pp. 19–25.

[74] Yoon, S. Y., Park, Y. M., Park, S. S., Stevens, R., and Park, H. C., 2005, "Synthesis of Hydroxyapatite Whiskers by Hydrolysis of α-Tricalcium Phosphate Using Microwave Heating," Mater. Chem. Phys., **91**(1), pp. 48–53.

[75] Sopyan, I., Mel, M., Ramesh, S., and Khalid, K. A., 2007, "Porous Hydroxyapatite for Artificial Bone Applications," Sci. Technol. Adv. Mater., **8**(1–2), pp. 116–123.

[76] Chow, L. C., and Hockey, Bernard, Sun, L., 2004, "Properties of Nanostructured Hydroxyapatite Prepared by a Spray Drying Technique," J. Res. Natl. Inst. Stand. Technol., **109**(6), pp. 543–551.

[77] Hongquan, Z., Yuhua, Y., Youfa, W., and Shipu, L., 2003, "Morphology and Formation Mechanism of Hydroxyapatite Whiskers from Moderately Acid Solution," Mater. Res., **6**(1), pp. 111–115.

[78] Bulina, N. V., Makarova, S. V., Baev, S. G., Matvienko, A. A., Gerasimov, K. B., Logutenko, O. A., and Bystrov, V. S., 2021, "A Study of Thermal Stability of Hydroxyapatite," Minerals, **11**(12), pp. 1–15.

[79] Liao, C. J., Lin, F. H., Chen, K. S., and Sun, J. S., 1999, "Thermal Decomposition and Reconstruction of Hydroxyapatite in Air Atmosphere," Biomed. Sci. Instrum., **20**, pp. 1807–1813.

[80] Widiyanti, S., Faradisa, E., Mubarok, A. M., Fauziyyah, N., Triadi, H. A., Nawawi, M. R., and Nandiyanto, A. B. D., 2020, "Review: Synthesis of Nano Bioactive Glass or Bioglass," Rhazes Green Appl. Chem., **10**(0), pp. 01–32.

[81] Krishnan, V., and Lakshmi, T., 2013, "Bioglass: A Novel Biocompatible Innovation," J. Adv. Pharm. Technol. Res., **4**(2), pp. 78–83.

[82] Rahaman, M. N., Xiao, W., Fu, Q., and Huang, W., 2017, "Review - Bioactive Glass Implants for Potential Application in Structural Bone Repair," Biomed. Glas., **3**(1), pp. 56–66.

[83] Nawang, R., Hussein, M. Z., Matori, K. A., Che Abdullah, C. A., and Hashim, M., 2019, "Physicochemical Properties of Hydroxyapatite/Montmorillonite Nanocomposite Prepared by Powder Sintering," Results Phys., **15**(102540), pp. 1–19.

[84] Ielo, I., Calabrese, G., De Luca, G., and Conoci, S., 2022, "Recent Advances in Hydroxyapatite-Based Biocomposites for Bone Tissue Regeneration in Orthopedics," Int. J. Mol. Sci., **23**(17), pp. 1–25.

[85] Mabrouk, A., Bachar, A., Atbir, A., Follet, C., Mercier, C., Tricoteaux, A., Leriche, A., and Hampshire, S., 2018, "Mechanical Properties, Structure, Bioactivity and Cytotoxicity of Bioactive Na-Ca-Si-P-O-(N) Glasses," J. Mech. Behav. Biomed. Mater., **86**, pp. 284–293.

[86] Kaur, G., Pickrell, G., Sriranganathan, N., Kumar, V., and Homa, D., 2016, "Review and the State of the Art: Sol–Gel and Melt Quenched Bioactive Glasses for Tissue Engineering," J. Biomed. Mater. Res. - Part B Appl. Biomater.,

104(6), pp. 1248–1275.

[87] Dey, P., Pal, S. K., Banerjee, I., and Sarkar, R., 2020, "Effect of Addition of B2O3 to the Sol-Gel Synthesized 45S5 Bioglass," J. Aust. Ceram. Soc., **56**(4), pp. 1309–1322.

[88] Deshmukh, K., Kovářík, T., Křenek, T., Docheva, D., Stich, T., and Pola, J., 2020, "Recent Advances and Future Perspectives of Sol-Gel Derived Porous Bioactive Glasses: A Review," RSC Adv., **10**(56), pp. 33782–33835.

[89] Sarkar, S. K., and Lee, B. T., 2011, "Synthesis of Bioactive Glass by Microwave Energy Irradiation and Its In-Vitro Biocompatibility," Bioceram. Dev. Appl., **1**, pp. 1–3.

[90] Essien, E. R., Atasie, V. N., and Udobang, E. U., 2016, "Microwave Energy-Assisted Formation of Bioactive CaO-MgO-SiO2ternary Glass from Bio-Wastes," Bull. Mater. Sci., **39**(4), pp. 989–995.

[91] Cacciotti, I., Lombardi, M., Bianco, A., Ravaglioli, A., and Montanaro, L., 2012, "Sol-Gel Derived 45S5 Bioglass: Synthesis, Microstructural Evolution and Thermal Behaviour," J. Mater. Sci. Mater. Med., **23**(8), pp. 1849–1866.

[92] Lefebvre, L., Chevalier, J., Gremillard, L., Zenati, R., Thollet, G., Bernache-Assolant, D., and Govin, A., 2007, "Structural Transformations of Bioactive Glass 45S5 with Thermal Treatments," Acta Mater., **55**(10), pp. 3305–3313.

[93] He, Z., Shen, A., Lyu, Z., Li, Y., Wu, H., and Wang, W., 2020, "Effect of Wollastonite Microfibers as Cement Replacement on the Properties of Cementitious Composites: A Review," Constr. Build. Mater., **261**(119920), pp. 1–13.

[94] Saxena, S. K., Kumar, M., Chundawat, D. S., and Singh, N. B., 2019, "Utilization of Wollastonite in Cement Manufacturing," Mater. Today Proc., **29**, pp. 733–737.

[95] Imerys, 2023, "Wollastonite," (Online), Available: https://www.imerys.com/minerals/wollastonite, (Accessed: 04-Sep-2024).

[96] Zheng, Y., Wang, C., Zhou, S., and Luo, C., 2021, "The Self-Gelation Properties of Calcined Wollastonite Powder," Constr. Build. Mater., **290**(123061), pp. 1–8.

[97] Carrodegaus, RG, De Aza, AH, DE Aza PN, Baudin C, Jimenez, J, Lopez-Bravo, A, Pena, P, De Aza, S., 2007, "Assessment of Natural and Synthetic Wollastonite Source for Bioceramic Preparation.Pdf," J. Biomed. Mater. Res. Part A, pp. 484–495.

[98] Abd Rashid, R., Shamsudin, R., Abdul Hamid, M. A., and Jalar, A., 2014, "Low Temperature Production of Wollastonite from Limestone and Silica Sand through Solid-State Reaction," J. Asian Ceram. Soc., **2**(1), pp. 77–81.

[99] Shamsudin, R., 'Atiqah Abdul Azam, F., Abdul Hamid, M. A., and Ismail, H., 2017, "Bioactivity and Cell Compatibility of β-Wollastonite Derived from Rice Husk Ash and Limestone," Materials, **10**(10), pp. 1–15.

[100] Al-Noaman, A., Rawlinson, S. C. F., and Hill, R. G., 2013, "Bioactive Glass-

Stoichimetric Wollastonite Glass Alloys to Reduce TEC of Bioactive Glass Coatings for Dental Implants," Mater. Lett., **94**, pp. 69–71.

[101] Domingues, J. A., Motisuke, M., Bertran, C. A., Hausen, M. A., De Rezende Duek, E. A., and Camilli, J. A., 2017, "Addition of Wollastonite Fibers to Calcium Phosphate Cement Increases Cell Viability and Stimulates Differentiation of Osteoblast-Like Cells," Sci. World J., **2017**, pp. 1–6.

[102] Liu, X., Chuan-Xian, D., and Chu, P. K., 2004, "Mechanism of Apatite Formation on Wollastonite Coatings in Simulated Body Fluids," Biomaterials, **25**, pp. 1755–1761.

[103] Park, J., 2008, "Development of a Glass-Ceramic for Biomedical Applications," (February), PhD thesis, p. 179, Middle East Technical University, (Online), Available: https://citeseerx.ist.psu.edu/document?repid=rep1&type=pdf&doi=c98943e2c66dfce5f78f9fe035b5bcc77de4f675, (Accessed: 04-Sep-2024).

[104] Pattanayak, D. K., 2009, "Apatite Wollastonite-Poly Methyl Methacrylate Bio-Composites," Mater. Sci. Eng. C, **29**(5), pp. 1709–1714.

[105] Workie, A. B., and Shih, S. J., 2022, "A Study of Bioactive Glass-Ceramic's Mechanical Properties, Apatite Formation, and Medical Applications," RSC Adv., **12**(36), pp. 23143–23152.

[106] Kawanabe, K., Iida, H., Matsusue, Y., Nishimatsu, H., Kasai, R., and Nakamura, T., 1998, "A-W Glass Ceramic as a Bone Substitute in Cemented Hip Arthroplasty: 15 Hips Followed 2-10 Years," Acta Orthop. Scand., **69**(3), pp. 237–242.

[107] Vakifahmetoglu, C., Park, J., Korkusuz, F., Ozturk, A., and Timucin, M., 2009, "Production and Properties of Apatite-Wollastonite Ceramics for Biomedical Applications," InterCeram Int. Ceram. Rev., **58**(2–3), pp. 86–90.

[108] Suwanprateeb, J., Sanngam, R., Suvannapruk, W., and Panyathanmaporn, T., 2009, "Mechanical and in Vitro Performance of Apatite-Wollastonite Glass Ceramic Reinforced Hydroxyapatite Composite Fabricated by 3D-Printing," J. Mater. Sci. Mater. Med., **20**(6), pp. 1281–1289.

[109] Faeghi-Nia, A., 2013, "Preparation of Apatite-Wollastonite-Phlogopite Glass-Ceramic Composites by Powder Sintering Method," Sci. Sinter., **45**(3), pp. 331–339.

[110] Zhang, H., Ye, X. J., and Li, J. S., 2009, "Preparation and Biocompatibility Evaluation of Apatite/Wollastonite-Derived Porous Bioactive Glass Ceramic Scaffolds," Biomed. Mater., **4**(4), pp. 1–7.

[111] Xiang, Z., Jianwen, G., Yue, Z., Ynafei, T., Jiabei, Z., and Dali, Z., 2009, "Immobilization of RGD Peptide onto the Surface of Apatite-Wollastonite Ceramic for Enhanced Osteoblast Adhesion and Bone Regeneration," J. Wuhan Univ. Technol., **29**(3), pp. 626–634.

[112] Fujita, H., Iida, H., Ido, K., and Matsuda, Y., 2000, "Porous Apatite-Wollastonite Glass- Ceramic as an Intramedullary Plug," J. Bone Jt. Surg.,

82B(4), pp. 614–618.

[113] Kokubo, T., Shigematsu, M., Nagashima, Y., Tashiro, M., Nakamura, T., Yamamuro, T., and Higashi, S., 1982, "Apatite- and Wollastonite-Containg Glass-Ceramics for Prosthetic Application," Bull. Inst. chemcial Res. Kyoto Univ., **60**(3–4), pp. 260–268.

[114] Eliaz, N., and Metoki, N., 2017, "Calcium Phosphate Bioceramics: A Review of Their History, Structure, Properties, Coating Technologies and Biomedical Applications," Materials, **10**(4), p. 104.

[115] Raynaud, S., Champion, E., Bernache-Assollant, D., and Thomas, P., 2002, "Calcium Phosphate Apatites with Variable Ca/P Atomic Ratio I. Synthesis, Characterisation and Thermal Stability of Powders," Biomaterials, **23**(4), pp. 1065–1072.

[116] Yousefi, A. M., 2019, "A Review of Calcium Phosphate Cements and Acrylic Bone Cements as Injectable Materials for Bone Repair and Implant Fixation," J. Appl. Biomater. Funct. Mater., **17**(4), pp. 1–21.

[117] Ooms, E. M., Wolke, J. G. C., Van de Heuvel, M. T., Jeschke, B., and Jansen, J. A., 2003, "Histological Evaluation of the Bone Response to Calcium Phosphate Cement Implanted in Cortical Bone," Biomaterials, **24**(6), pp. 989–1000.

[118] Saleh, A. T., Ling, L. S., and Hussain, R., 2016, "Injectable Magnesium-Doped Brushite Cement for Controlled Drug Release Application," J. Mater. Sci., **51**(16), pp. 7427–7439.

[119] Hench, L. L., 1998, "Bioceramics," J. Am. Ceram. Soc., **81**(7), pp. 1705–1728.

[120] Barakat, N. A. M., Khil, M. S., Omran, A. M., Sheikh, F. A., and Kim, H. Y., 2009, "Extraction of Pure Natural Hydroxyapatite from the Bovine Bones Bio Waste by Three Different Methods," J. Mater. Process. Technol., **209**(7), pp. 3408–3415.

[121] Ofudje, E. A., Rajendran, A., Adeogun, A. I., Idowu, M. A., Kareem, S. O., and Pattanayak, D. K., 2017, "Synthesis of Organic Derived Hydroxyapatite Scaffold from Pig Bone Waste for Tissue Engineering Applications," Adv. Powder Technol., **29**(1), pp. 1–8.

[122] Taha, A., Akram, M., Jawad, Z., Alshemary, A. Z., and Hussain, R., 2017, "Strontium Doped Injectable Bone Cement for Potential Drug Delivery Applications," Mater. Sci. Eng. C, **80**, pp. 93–101.

[123] Wach, T., and Kozakiewicz, M., 2020, "Fast-versus Slow-Resorbable Calcium Phosphate Bone Substitute Materials-Texture Analysis after 12 Months of Observation," Materials, **13**(17), pp. 1–11.

[124] Tronco, M. C., Cassel, J. B., and dos Santos, L. A., 2022, "α-TCP-Based Calcium Phosphate Cements: A Critical Review," Acta Biomater., **151**, pp. 70–87.

[125] Zakaria, M. N., Cahyanto, A., and El-Ghannam, A., 2018, "Calcium Release and Physical Properties of Modified Carbonate Apatite Cement as Pulp Capping

Agent in Dental Application," Biomater. Res., **22**(1), pp. 1–6.

[126] Pajor, K., and Pajchel, L., 2019, "Hydroxyapatite and Fluorapatite in Conservative," Materials, **12**(2683), pp. 1–16.

[127] Canillas, M., Pena, P., De Aza, A. H., and Rodríguez, M. A., 2017, "Calcium Phosphates for Biomedical Applications," Bol. la Soc. Esp. Ceram. y Vidr., **56**(3), pp. 91–112.

[128] Xu, H. H. K., Wang, P., Wang, L., Bao, C., Chen, Q., Weir, M. D., Chow, L. C., Zhao, L., Zhou, X., and Reynolds, M. A., 2017, "Calcium Phosphate Cements for Bone Engineering and Their Biological Properties," Bone Res., **5**(August), pp. 1–19.

[129] Dorozhkin, S., 2015, "Calcium Orthophosphate-Containing Biocomposites and Hybrid Biomaterials for Biomedical Applications," J. Funct. Biomater., **6**(3), pp. 708–832.

[130] Roether, J. A., Gough, J. E., Boccaccini, A. R., Hench, L. L., Maquet, V., and Jérôme, R., 2002, "Novel Bioresorbable and Bioactive Composites Based on Bioactive Glass and Polylactide Foams for Bone Tissue Engineering," J. Mater. Sci. Mater. Med., **13**(12), pp. 1207–1214.

[131] Ramesh, N., Moratti, S. C., and Dias, G. J., 2018, "Hydroxyapatite–Polymer Biocomposites for Bone Regeneration: A Review of Current Trends," J. Biomed. Mater. Res. - Part B Appl. Biomater., **106**(5), pp. 2046–2057.

[132] Rajula, B., M.Prem, N., Vivek, V. G. D., Chandra Mani, R., and Sujana, A., 2021, "Nano-Hydroxyapatite: A Driving Force for Bone Tissue Engineering," J. Pharm. Bioallied Sci., **13**(1), pp. 11–14.

[133] Safavi, M.S., Walsh, F.C., Surmeneva, M.A., Surmenev, R.A., Khalil-Allafi, J., 2021, "Electrodeposited Hydroxyapatite-Based Biocoatings : Recent Progress and Future Challenges," coatings, **11**(110), pp. 1–62.

[134] Yan, W. Q., Nakamura, T., Kawanabe, K., Nishigochi, S., Oka, M., and Kokubo, T., 1997, "Apatite Layer-Coated Titanium for Use as Bone Bonding Implants," Biomaterials, **18**(17), pp. 1185–1190.

[135] Ning, C. Q., and Zhou, Y., 2004, "On the Microstructure of Biocomposites Sintered from Ti, HA and Bioactive Glass," Biomaterials, **25**(17), pp. 3379–3387.

[136] Chalisgaonkar, V., Das, M., and Balla, V. K., 2018, "Laser Processing of Ti Composite Coatings Reinforced with Hydroxyapatite and Bioglass," Addit. Manuf., **20**(October 2016), pp. 134–143.

[137] Prasad, S., Vyas, V. K., Mani, K. D., Ershad, M., and Pyare, R., 2017, "Preparation, in-Vitro Bioactivity and Mechanical Properties of Reinforced 45S5 Bioglass Composite with HA-ZrO2powders," Orient. J. Chem., **33**(3), pp. 1286–1296.

[138] Bakar, M. S. A., Cheang, P., and Khor, K. A., 2003, "Tensile Properties and Microstructural Analysis of Spheroidized Hydroxyapatite-Poly

(Ehteretherketone) Biocomposites," Mater. Sci. Eng. A, **345**, pp. 55–63.

[139] Kim, H. W., Knowles, J. C., and Kim, H. E., 2004, "Hydroxyapatite/Poly(ε-Caprolactone) Composite Coatings on Hydroxyapatite Porous Bone Scaffold for Drug Delivery," Biomaterials, **25**(7–8), pp. 1279–1287.

[140] Xiao, X., Liu, R., Huang, Q., and Ding, X., 2009, "Preparation and Characterization of Hydroxyapatite/Polycaprolactone- Chitosan Composites," J. Mater. Sci. Mater. Med., **20**(12), pp. 2375–2383.

[141] Yamaguchi, I., Iizuka, S., Osaka, A., Monma, H., and Tanaka, J., 2003, "The Effect of Citric Acid Addition on Chitosan/Hydroxyapatite Composites," Colloids Surfaces A Physicochem. Eng. Asp., **214**(1–3), pp. 111–118.

[142] Çalişkan, F., 2016, "Apatite Wollastonite-Reinforced Hydroxyapatite Biocomposites," Acta Phys. Pol. A, **129**(4), pp. 665–668.

[143] Sabree, I. K., and Mahdi, O. S., 2016, "Characterization , Mechanical , and In Vitro Bioactivity Properties of Hydroxyapatite / Bioactive Glass Composite," J. Babylon Univ., **24**(4), pp. 1–12.

[144] Cholewa-Kowalska, K., Kokoszka, J., Łczka, M., Niedźwiedzki, Ł., Madej, W., and Osyczka, A. M., 2009, "Gel-Derived Bioglass as a Compound of Hydroxyapatite Composites," Biomed. Mater., **4**(5), pp. 1–11.

[145] Amaral, M., Silva, R.F., Lopes, M.A, Santos, J. ., 2002, "Densification Route and Mechanical Properties of Si3N4-Bioglass Biocomposites," Biomaterials, **23**, pp. 857–862.

[146] Himanshu, T., Singh, S., Sampath, K., Prerna, M., and Ashish, J., 2016, "Preparation and Characterisation of 45S5 Bioactive Glass Doped with (TiO2 +ZrO2) as Bioactive Ceramic Material," Bioceram. Dev. Appl., **6**(1), pp. 1–6.

[147] Hench, L. L., and Wilson, J., 1984, "Surface-Active Biomaterials," Am. Assoc. Adv. Sci., **226**(4675), pp. 630–636.

[148] Misra, S. K., Mohn, D., Brunner, T. J., Stark, W. J., Philip, S. E., Roy, I., Salih, V., Knowles, J. C., and Boccaccini, A. R., 2008, "Comparison of Nanoscale and Microscale Bioactive Glass on the Properties of P(3HB)/Bioglass Composites," Biomaterials, **29**(12), pp. 1750–1761.

[149] Bellucci, D., Sola, A., and Cannillo, V., 2014, "Bioactive Glass/ZrO2composites for Orthopaedic Applications," Biomed. Mater., **9**(1), pp. 1–12.

[150] Szesz, Eduardo Mioduski, Lepienski, C. M., 2017, "Anodic Bonding of Titanium Alloy with Bioactive Glass," J. Non. Cryst. Solids, **471**, pp. 19–27.

[151] Drnovšek, N., Novak, S., Dragin, U., Ĉeh, M., Gorenšek, M., and Gradišar, M., 2012, "Bioactive Glass Enhances Bone Ingrowth into the Porous Titanium Coating on Orthopaedic Implants," Int. Orthop., **36**(8), pp. 1739–1745.

[152] Tancred, D. C., Carr, A. J., and McCormack, B. A. O., 2001, "The Sintering and Mechanical Behavior of Hydroxyapatite with Bioglass Additions," J. Mater. Sci. Mater. Med., **12**(1), pp. 81–93.

[153] Carvalho, F. L. S., Borges, C. S., Branco, J. R. T., and Pereira, M. M., 1999, "Structural Analysis of Hydroxyapatite/Bioactive Glass Composite Coatings Obtained by Plasma Spray Processing," J. Non. Cryst. Solids, **247**(1–3), pp. 64–68.

[154] Ragel, C. V., Vallet-Regí, M., and Rodríguez-Lorenzo, L. M., 2002, "Preparation and in Vitro Bioactivity of Hydroxyapatite/Solgel Glass Biphasic Material," Biomaterials, **23**(8), pp. 1865–1872.

[155] Yakout, M., Elbestawi, M. A., and Veldhuis, S. C., 2020, "A Study of the Relationship between Thermal Expansion and Residual Stresses in Selective Laser Melting of Ti-6Al-4V," J. Manuf. Process., **52**, pp. 181–192.

[156] Miyazaki, H., Ushiroda, I., Itomura, D., Hirashita, T., Adachi, N., and Ota, T., 2009, "Thermal Expansion of Hydroxyapatite between - 100 °C and 50 °C," Mater. Sci. Eng. C, **29**(4), pp. 1463–1466.

[157] Gomez-Vega, J. M., Saiz, E., Tomsia, A. P., Marshall, G. W., and Marshall, S. J., 2000, "Bioactive Glass Coatings with Hydroxyapatite and Bioglass® Particles on Ti-Based Implants. 1. Processing," Biomaterials, **21**(2), pp. 105–111.

[158] Bheemaneni, G., Saravana, S., and Kandaswamy, R., 2018, "Processing and Characterization of Poly (Butylene Adipate-Co-Terephthalate) / Wollastonite Biocomposites for Medical Applications," Mater. Today Proc., **5**(1), pp. 1807–1816.

[159] Encinas-Romero, M. A., and Aguayo-Salinas, S., 2008, "Synthesis and Characterization of Hydroxyapatite Wollastonite Composite Powder by Sol-Gel Processing," Int. J. Appl. Ceram. Technol., **5**(4), pp. 401–411.

[160] Encinas-Romero, M. A., Peralta-Haley, J., and Valenzuela-García, J. L., 2013, "Synthesis and Structural Characterization of Hydroxyapatite-Wollastonite Produced by an Alternative Sol-Gel Route," Sci. Res., **4**, pp. 327–333.

[161] Edrees, S. J., Shukur, M. M., and Mahde, O. S., 2015, "Effect of Hydroxyapatite on the Properties of Wollastonite Bioceramics," Int. J. Eng. Technol., **5**(6), pp. 322–328.

[162] Padmanabhan, S. K., Gervaso, F., Carrozzo, M., Scalera, F., Sannino, A., and Licciulli, A., 2013, "Wollastonite/Hydroxyapatite Scaffolds with Improved Mechanical, Bioactive and Biodegradable Properties for Bone Tissue Engineering," Ceram. Int., **39**(1), pp. 619–627.

[163] Wei, J., Chen, F., Shin, J. W., Hong, H., Dai, C., Su, J., and Liu, C., 2009, "Preparation and Characterization of Bioactive Mesoporous Wollastonite - Polycaprolactone Composite Scaffold," Biomaterials, **30**(6), pp. 1080–1088.

[164] Li, H., Zhai, W., and Chang, J., 2009, "Effects of Wollastonite on Proliferation and Differentiation of Human Bone Marrow-Derived Stromal Cells in PHBV/Wollastonite Composite Scaffolds," J. Biomater. Appl., **24**(3), pp. 231–246.

[165] Li, X., and Chang, J., 2005, "Preparation and Characterization of Bioactive Collagen/Wollastonite Composite Scaffolds," J. Mater. Sci. Mater. Med., **16**(4),

pp. 361–365.

[166] Goswami, J., Bhatnagar, N., Mohanty, S., and Ghosh, A. K., 2013, “Processing and Characterization of Poly(Lactic Acid) Based Bioactive Composites for Biomedical Scaffold Application,” Express Polym. Lett., **7**(9), pp. 767–777.

[167] Sopcak, T., Medvecky, L., Giretova, M., Stulajterova, R., and Durisin, J., 2018, “Hydrolysis, Setting Properties and in Vitro Characterization of Wollastonite/Newberyite Bone Cement Mixtures,” J. Biomater. Appl., **32**(7), pp. 871–885.

[168] Guo, H., Wei, J., Song, W., Zhang, S., Yan, Y., Liu, C., and Xiao, T., 2012, “Wollastonite Nanofiber-Doped Self-Setting Calcium Phosphate Bioactive Cement for Bone Tissue Regeneration,” Int. J. Nanomedicine, **7**, pp. 3613–3624.

[169] Abdolahpour, Z., Saneipour, Z., and Azarhoosh, M. J., 2017, “Application of Biomaterials in Dentistry,” Curr. trends Biomed. Eng. Biosci., **2**(3), pp. 44–47.

[170] Girón, J., Kerstner, E., Medeiros, T., Oliveeira, L., Machado, G. ., Malfatti, C. ., and Pranke, P., 2021, “Biomaterials for Bone Regeneration : An Orthopedic and Dentistry Overview,” Brazilian J. Med. Biol. Res., **54**(9), pp. 1–15.

[171] Banigo, A. T., Iwuji, S. C., and Iheaturu, N. C., 2019, “Application of Biomaterials in Tissue Engineering : A Review,” J. Chem. Pharm. Res., **11**(4), pp. 1–16.

[172] Morales-Flórez, V., and Domínguez-Rodríguez, A., 2022, “Mechanical Properties of Ceramics Reinforced with Allotropic Forms of Carbon,” Prog. Mater. Sci., **128**(10966), pp. 1–78.

[173] Xidaki, D., Agrafioti, P., Diomatari, D., Kaminari, A., Tsalavoutas-Psarras, E., Alexiou, P., Psycharis, V., Tsilibary, E. C., Silvestros, S., and Sagnou, M., 2018, “Synthesis of Hydroxyapatite, β-Tricalcium Phosphate and Biphasic Calcium Phosphate Particles to Act as Local Delivery Carriers of Curcumin: Loading, Release and In Vitro Studies,” Materials, **11**(595), pp. 1–13.

[174] Szczes, A., Holysz, L., and Chibowski, E., 2017, “Synthesis of Hydroxyapatite Fir Biomedical Applications.Pdf,” Adv. Colloid Interface Sci., **249**, pp. 321–330.

[175] Epinette, J. A., and Manley, M. T., 2008, “Uncemented Stems in Hip Replacement - Hydroxyapatite or Plain Porous: Does It Matter? Based on a Prospective Study of HA Omnifit Stems at 15-Years Minimum Follow-Up,” HIP Int., **18**(2), pp. 69–74.

[176] Cannio, M., Bellucci, D., Roether, J. A., Boccaccini, D. N., and Cannillo, V., 2021, “Bioactive Glass Applications: A Literature Review of Human Clinical Trials,” Materials, **14**(18), pp. 1–26.

[177] Ng, J. F., Weil, T., and Jaenicke, S., 2011, “Cationized Bovine Serum Albumin with Pendant RGD Groups Forms Efficient Biocoatings for Cell Adhesion,” J. Biomed. Mater. Res. - Part B Appl. Biomater., **99 B**(2), pp. 282–290.

[178] Salinas, A. J., and Vallet-Regí, M., 2013, “Bioactive Ceramics: From Bone Grafts to Tissue Engineering,” RSC Adv., **3**(28), pp. 11116–11131.

[179] Shi, H., Zhou, P., Li, J., Liu, C., and Wang, L., 2021, "Functional Gradient Metallic Biomaterials: Techniques, Current Scenery, and Future Prospects in the Biomedical Field," Front. Bioeng. Biotechnol., **8**, pp. 1–26.

[180] Demirkiran, A. S., Çelik, E., Yargan, M., and Avci, E., 2001, "Oxidation Behaviour of Functionally Gradient Coatings Including Different Composition of Cerments," Surf. Coatings Technol., **142**–**144**, pp. 551–556.

[181] Sathish, M., Radhika, N., and Saleh, B., 2021, "A Critical Review on Functionally Graded Coatings: Methods, Properties, and Challenges," Compos. Part B Eng., **225**(August), pp. 1–31.

[182] Prasad, K., Bazaka, O., Chua, M., Rochford, M., Fedrick, L., Spoor, J., Symes, R., Tieppo, M., Collins, C., Cao, A., Markwell, D., Ostrikov, K., and Bazaka, K., 2017, "Metallic Biomaterials: Current Challenges and Opportunities," Materials, **10**(8), pp. 1–33.

[183] Ji, H., Ponton, C. B., and Marquis, P. M., 1992, "Microstructural Characterization of Hydroxyapatite Coating on Titanium," J. Mater. Sci. Mater. Med., **3**(4), pp. 283–287.

[184] Yang, Y. C., and Chou, B. Y., 2007, "Bonding Strength Investigation of Plasma-Sprayed HA Coatings on Alumina Substrate with Porcelain Intermediate Layer," Mater. Chem. Phys., **104**(2–3), pp. 312–319.

[185] Chen, C.-C., Huang, T.-H., Kao, C.-T., and Ding, S.-J., 2006, "Characterization of Functionally Graded Hydroxyapatite/Titanium Composite Coatings Plasma-Sprayed on Ti Alloys," J. Biomed. Mater. Res. Part B Appl. Biomater., **78B**, pp. 146–152.

[186] Fabris, D., Fredel, M. C., Souza, J. C. M., Silva, F. S., and Henriques, B., 2021, "Biomechanical Behavior of Functionally Graded S53P4 Bioglass-Zirconia Dental Implants: Experimental and Finite Element Analyses," J. Mech. Behav. Biomed. Mater., **120**(April), pp. 1–11.

[187] Luginina, M., Angioni, D., Montinaro, S., Orrù, R., Cao, G., Sergi, R., Bellucci, D., and Cannillo, V., 2020, "Hydroxyapatite/Bioactive Glass Functionally Graded Materials (FGM) for Bone Tissue Engineering," J. Eur. Ceram. Soc., **40**(13), pp. 4623–4634.

[188] Goller, G., 2004, "The Effect of Bond Coat on Mechanical Properties of Plasma Sprayed Bioglass-Titanium Coatings," Ceram. Int., **30**(3), pp. 351–355.

[189] Cattini, A., Bellucci, D., Sola, A., Pawłowski, L., and Cannillo, V., 2013, "Microstructural Design of Functionally Graded Coatings Composed of Suspension Plasma Sprayed Hydroxyapatite and Bioactive Glass," J. Biomed. Mater. Res. - Part B Appl. Biomater., **102**(3), pp. 551–560.

[190] Muslim, N. B., Hamzah, A. F., and Al-kawaz, A. E., 2018, "Study of Mechanical Properties of Wollastonite Filled Epoxy Functionally Graded Composite," Int. J. Mech. Eng. Technol., **9**(8), pp. 669–677.

[191] Vangolu, Y., and Yurtcan, M. T., 2021, "Wear and Corrosion Properties of Wollastonite and Boron Nitride Doped, Hydroxyapatite-Based HAp-Wo-BN

Composite Coatings Prepared by Pulsed Laser Deposition," Ceram. Int., **47**(23), pp. 32969–32978.

[192] Singh, J., Chatha, S. S., and Singh, H., 2022, "Microstructural and In-Vitro Characteristics of Functional Calcium Silicate Topcoat on Hydroxyapatite Coating for Bio-Implant Applications," Prog. Biomater., **11**(1), pp. 95–108.

[193] Chu, P. K., 2013, "Surface Engineering and Modification of Biomaterials," Thin Solid Films, **528**, pp. 93–105.

[194] Boyan, B. D., Hummert, T. W., Dean, D. D., and Schwartz, Z., 1996, "Role of Material Surfaces in Regulating Bone and Cartilage Cell Response," Biomaterials, **17**(2), pp. 137–146.

[195] Ducheyne, P., and Qiu, Q., 1999, "Bioactive Ceramics: The Effect of Surface Reactivity on Bone Formation and Bone Cell Function," Biomaterials, **20**(23–24), pp. 2287–2303.

[196] Vernè, E., Ferraris, S., Cassinelli, C., and Boccaccini, A. R., 2015, "Surface Functionalization of Bioglass® with Alkaline Phosphatase," Surf. Coatings Technol., **264**, pp. 132–139.

[197] Cattini, A., Bellucci, D., Sola, A., Pawłowski, L., and Cannillo, V., 2014, "Functional Bioactive Glass Topcoats on Hydroxyapatite Coatings: Analysis of Microstructure and in-Vitro Bioactivity," Surf. Coatings Technol., **240**, pp. 110–117.

[198] Uchida, M., Kim, H. M., Kokubo, T., Fujibayashi, S., and Nakamura, T., 2002, "Effect of Water Treatment on the Apatite-Forming Ability of NaOH-Treated Titanium Metal," J. Biomed. Mater. Res., **63**(5), pp. 522–530.

[199] Ismail, H., and Mohamad, H., 2021, "Bioactivity and Biocompatibility Properties of Sustainable Wollastonite Bioceramics from Rice Husk Ash/Rice Straw Ash: A Review," Materials, **14**(18), pp. 1–27.

[200] Santos, D., Maurício, A. C., Sencadas, V., Santos, J. D., Fernandes, M. H., and Gomes, P. S., 2018, "Spray Drying: An Overview," Biomaterials - Physics and Chemistry - New Edition, R. Pignatello, and T. Musumeci, eds., IntechOpen, pp. 10–35, ISBN: 978-1-78923-065-9.

[201] Schutyser, M. A. I., Both, E. M., Siemons, I., Vaessen, E. M. J., and Zhang, L., 2019, "Gaining Insight on Spray Drying Behavior of Foods via Single Droplet Drying Analyses," Dry. Technol., **37**(5), pp. 525–534.

[202] Parikh, D. M., 2008, "Advances in Spray Drying Technology: New Applications for a Proven Process," Am. Pharm. Rev., **11**(1), pp. 1–5.

[203] Cal, Krzysztof, Sollohub, K., 2010, "Spray Drying Technique. I: Hardware and Process Parameters," J. Pharm. Sci., **99**(2), pp. 575–585.

[204] Panos, I., Acosta, N., and Heras, A., 2008, "New Drug Delivery Systems Based on Chitosan," Curr. Drug Discov. Technol., **5**(4), pp. 333–341.

[205] Harun, N. H., Abdul-Aziz, A., Wan-Zamri, W. M., Rahman, R. A., and Aziz, R., 2015, "Optimization of Process Parameters for Spray Drying of Tongkat Ali

Extract," J. Eng. Sci. Technol., **10**(Spec.issue6), pp. 31–41.

[206] Tee, L. H., Luqman Chuah, A., Pin, K. Y., Abdul Rashih, A., and Yusof, Y. A., 2012, "Optimization of Spray Drying Process Parameters of Piper Betle L. (Sirih) Leaves Extract Coated with Maltodextrin," J. Chem. Pharm. Res., **4**(3), pp. 1833–1841.

[207] Sosnik, A., and Seremeta, K. P., 2015, "Advantages and Challenges of the Spray-Drying Technology for the Production of Pure Drug Particles and Drug-Loaded Polymeric Carriers," Adv. Colloid Interface Sci., **223**, pp. 40–54.

[208] Cao, X. Q., Vassen, R., Schwartz, S., Jungen, W., Tietz, F., and Stöever, D., 2000, "Spray-Drying of Ceramics for Plasma-Spray Coating," J. Eur. Ceram. Soc., **20**(14–15), pp. 2433–2439.

[209] Bastan, F. E., Erdogan, G., Moskalewicz, T., and Ustel, F., 2017, "Spray Drying of Hydroxyapatite Powders: The Effect of Spray Drying Parameters and Heat Treatment on the Particle Size and Morphology," J. Alloys Compd., **724**, pp. 586–596.

[210] Murtaza, Q., 2006, "A Critical Investigation into the Spray-Drying of Hydroxyapatite Powder for Thermal Spray Applications," PhD Thesis, p. 262, (Online), Available: https://doras.dcu.ie/17586/, (Accessed: 04-Sep-2024).

[211] Bastan, F. E., Karaarslan, O., Erdogan, G., and Ustel, F., 2016, "Investigation of Bond Strenght of Spray Dried Hydroxyapatite-Wollastonite Composite Powder after Plasma Spray," **61**, pp. 79–86.

[212] Smith, R. W., and Knight, R., 1995, "Thermal Spraying I: Powder Consolidation-From Coating to Forming," JOM, **47**(8), pp. 32–39.

[213] Li, C. J., Yang, G. J., and Li, C. X., 2013, "Development of Particle Interface Bonding in Thermal Spray Coatings: A Review," J. Therm. Spray Technol., **22**(2–3), pp. 192–206.

[214] Erne, M., and Kolar, D., 2012, "Thermal Spraying of Oxide Ceramic and Ceramic Metallic Coatings," Ceramic Coatings - Applications in Engineering, F. Shi, ed., IntechOpen, pp. 167–194, ISBN: 978-953-51-6124-0.

[215] Antonini, J. M., Mckinney, W. G., Lee, E. G., Afshari, A. A., and Effects, H., 2021, "Review of the Physicochemical Properties and Associated Health Effects of Aerosols Generated during Thermal Spray Coating Processes," Toxical Ind Heal., **37**(1), pp. 47–58.

[216] Herman, H., Sampath, S., and McCune, R., 2000, "Thermal Spray: Current Status and Future Trends," MRS Bull., **25**(7), pp. 17–25.

[217] Davis, J. R., 2004, "Handbook of Thermal Spray Technology," ASM International, Ohio, ISBN: 0-87170-795-0.

[218] Stokes, J., 2008, "The Theory and Application of the Sulzer Metco HVOF Thermal Spray Process," Dublin, ISBN: 1-87232-753-2.

[219] Gerald, O. J., Wenge, L., Yuan Tao, Z., Cheng Long, L., and Qiang, L., 2021, "Influence of Plasma Spraying Current on the Microstructural Characteristics

and Tribological Behaviour of Plasma Sprayed Cr2O3 Coating," Bol. la Soc. Esp. Ceram. y Vidr., **60**(6), pp. 338–346.

[220] Weng, J., Wang, M., and Chen, J., 2002, "Plasma-Sprayed Calcium Phosphate Particles with High Bioactivity and Their Use in Bioactive Scaffolds," Biomaterials, **23**(13), pp. 2623–2629.

[221] Kweh, S. W. K., Khor, K. A., and Cheang, P., 2000, "Plasma-Sprayed Hydroxyapatite (HA) Coatings with Flame-Spheroidized Feedstock: Microstructure and Mechanical Properties," Biomaterials, **21**(12), pp. 1223–1234.

[222] Khor, K. A., Cheang, P, Wang, Y., 1997, "The Thermal Spray Processing of HA Powders and Coatings," J. Miner. Met. Mater. Soc., **49**, pp. 51–57.

[223] Chang, C., Huang, J., Xia, J., and Ding, C., 1999, "Study on Crystallization Kinetics of Plasma Sprayed Hydroxyapatite Coating," Ceram. Int., **25**(5), pp. 479–483.

[224] Kweh, S. W. K., Khor, K. A., and Cheang, P., 2002, "An in Vitro Investigation of Plasma Sprayed Hydroxyapatite (HA) Coatings Produced with Flame-Spheroidized Feedstock," Biomaterials, **23**(3), pp. 775–785.

[225] Yang, Y. C., and Chang, E., 2003, "The Bonding of Plasma-Sprayed Hydroxyapatite Coatings to Titanium: Effect of Processing, Porosity and Residual Stress," Thin Solid Films, **444**(1–2), pp. 260–275.

[226] Dyshlovenko, S., Pawlowski, L., Roussel, P., Murano, D., and Le Maguer, A., 2006, "Relationship between Plasma Spray Operational Parameters and Microstructure of Hydroxyapatite Coatings and Powder Particles Sprayed into Water," Surf. Coatings Technol., **200**(12–13), pp. 3845–3855.

[227] Cao, H., and Liu, X., 2013, "Plasma-Sprayed Ceramic Coatings for Osseointegration," Int. J. Appl. Ceram. Technol., **10**(1), pp. 1–10.

[228] Chou, B. Y., and Chang, E., 1999, "Microstructural Characterization of Plasma-Sprayed Hydroxyapatite-10wt% ZrO2composite Coating on Titanium," Biomaterials, **20**(19), pp. 1823–1832.

[229] Ding, S. J., Ju, C. P., and Chern Lin, J. H., 2000, "Morphology and Immersion Behavior of Plasma-Sprayed Hydroxyapatite/Bioactive Glass Coatings," J. Mater. Sci. Mater. Med., **11**(3), pp. 183–190.

[230] Monsalve, M., Lopez, E., Ageorges, H., and Vargas, F., 2015, "Bioactivity and Mechanical Properties of Bioactive Glass Coatings Fabricated by Flame Spraying," Surf. Coatings Technol., **268**, pp. 142–146.

[231] Monsalve, M., Ageorges, H., Lopez, E., Vargas, F., and Bolivar, F., 2013, "Bioactivity and Mechanical Properties of Plasma-Sprayed Coatings of Bioglass Powders," Surf. Coatings Technol., **220**, pp. 60–66.

[232] Cañas, E., Vicent, M., Bannier, E., Carpio, P., Orts, M. J., and Sánchez, E., 2016, "Effect of Particle Size on Processing of Bioactive Glass Powder for Atmospheric Plasma Spraying," J. Eur. Ceram. Soc., **36**(3), pp. 837–845.

[233] Dobrádi, A., Enisz-Bódogh, M., and Kovács, K., 2017, “Plasma Spraying of Bioactive Glass-Ceramics Containing Bovine Bone,” Process. Appl. Ceram., **11**(2), pp. 113–119.

[234] Liu, Xuanyong, Chuan-Xian, D., 2005, “Study on Plasma Sprayed Bioactive Wollastonite Coating,” J. Grad. Sch. chinese Acad. Sci., **22**(4), pp. 518–523.

[235] Liu, X., and Ding, C., 2002, “Characterization of Plasma Sprayed Wollastonite Powder and Coatings,” Surf. Coatings Technol., **153**(2–3), pp. 173–177.

[236] Xue, W., Liu, X., Zheng, X., and Ding, C., 2005, “Dissolution and Mineralization of Plasma-Sprayed Wollastonite Coatings with Different Crystallinity,” Surf. Coatings Technol., **200**(7), pp. 2420–2427.

[237] Liu, X., and Ding, C., 2002, “Plasma Sprayed Wollastonite/TiO2 Composite Coatings on Titanium Alloys,” Biomaterials, **23**(20), pp. 4065–4077.

[238] Li, Baoe, Liu Xuanyong, Cao, Cong, Dong, Yuqi, D. C., 2009, “Biological and Antibacterial Properties of Plasma Sprayed Wollastonite Silver Coatings,” J. Biomed. Mater. Res. Part B Appl. Biomater., **91**, pp. 596–603.

[239] Tejero-Martin, D., Rezvani Rad, M., McDonald, A., and Hussain, T., 2019, “Beyond Traditional Coatings: A Review on Thermal-Sprayed Functional and Smart Coatings,” J. Therm. Spray Technol., **28**(4), pp. 598–644.

[240] Fauchais, P. L., Herberlein, J. V. R., and Boulos, M. I., 2014, “Overview of Thermal Spray,” Thermal Spray Fundamentals: From Powder to Part, Springer, New York, pp. 17–72, ISBN: 978-0-387-68991-3.

[241] Tucker. Jr., R., 2013, "Thermal Spray Technology," ASM International, ISBN: 978-1-61503-996-8.

[242] Habib, K. A., Saura, J. J., Ferrer, C., Damra, M. S., Giménez, E., and Cabedo, L., 2006, “Comparison of Flame Sprayed Al2O3/TiO2 Coatings: Their Microstructure, Mechanical Properties and Tribology Behavior,” Surf. Coatings Technol., **201**(3–4), pp. 1436–1443.

[243] Herman, H., 1991, “Powders for Thermal Spray Technology,” KONA Powder Part. J., **9**(9), pp. 187–199.

[244] Shamim, T., Xia, C., and Mohanty, P., 2007, “Modeling and Analysis of Combustion Assisted Thermal Spray Processes,” Int. J. Therm. Sci., **46**(8), pp. 755–767.

[245] Garcia, E., Miranzo, P., and Sainz, M. A., 2018, “Thermally Sprayed Wollastonite and Wollastonite-Diopside Compositions as New Modulated Bioactive Coatings for Metal Implants,” Ceram. Int., **44**(11), pp. 12896–12904.

[246] Chebbi, A., 2011, “Thermal Spray of a Drug Delivery System onto Femoral Orthopaedic Implant,” PhD Thesis, p. 272, (Online), Available: http://doras.dcu.ie/16638/, (Accessed: 04-Sep-2024).

[247] Periyasamy, A. P., Venkataraman, M., Kremenakova, D., Militky, J., and Zhou, Y., 2020, “Progress in Sol-Gel Technology for the Coatings of Fabrics,” Materials, **13**(8), pp. 1–34.

[248] Danks, A. E., Hall, S. R., and Schnepp, Z., 2016, "The Evolution of 'sol-Gel' Chemistry as a Technique for Materials Synthesis," Mater. Horizons, **3**(2), pp. 91–112.

[249] Brinker, C. J., Frye, G. C., Hurd, A. J., Ashley, C. S., Laboratories, S. N., and Introduction, I., 1991, "Fundaments of Sol-Gel Coating," Thin Solid Films, **201**, pp. 97–108.

[250] Jaafar, A., Hecker, C., Árki, P., and Joseph, Y., 2020, "Sol-Gel Derived Hydroxyapatite Coatings for Titanium Implants: A Review," Bioengineering, **7**(4), pp. 1–23.

[251] Ün, S., and Durucan, C., 2009, "Preparation of Hydroxyapatite-Titania Hybrid Coatings on Titanium Alloy," J. Biomed. Mater. Res. - Part B Appl. Biomater., **90 B**(2), pp. 574–583.

[252] Ballarre, J., Seltzer, R., Mendoza, E., Orellano, J. C., Mai, Y. W., García, C., and Ceré, S. M., 2011, "Morphologic and Nanomechanical Characterization of Bone Tissue Growth around Bioactive Sol-Gel Coatings Containing Wollastonite Particles Applied on Stainless Steel Implants," Mater. Sci. Eng. C, **31**(3), pp. 545–552.

[253] Li, T., Lee, J., Kobayashi, T., and Aoki, H., 1996, "Hydroxyapatite Coating by Dipping Method, and Bone Bonding Strength," J. Mater. Sci. Mater. Med., **7**(6), pp. 355–357.

[254] Mavis, B., and Taş, A. C., 2000, "Dip Coating of Calcium Hydroxyapatite on Ti-6Al-4V Substrates," J. Am. Ceram. Soc., **83**(4), pp. 989–991.

[255] Bao, Q., Zhao, K., and Liu, J., 2012, "Characterization of Wollastonite Coatings Prepared by Sol-Gel on Ti Substrate," J. Coatings Technol. Res., **9**(2), pp. 189–193.

[256] Morsy, R., Abuelkhair, R., and Elnimr, T., 2017, "A Facile Route to the Synthesis of Hydroxyapatite/ Wollastonite Composite Powders by a Two-Step Coprecipitation Method," Springer, **9**(4), pp. 637–641.

[257] Benayahu, D., 2022, "Mesenchymal Stem Cell Differentiation and Usage for Biotechnology Applications: Tissue Engineering and Food Manufacturing," Biomater. Transl., **3**(1), pp. 17–23.

[258] Imbriglio, S. I., Munagala, V. N. V., Schmitt, T., Gauvin, R., Klemberg-Sapieha, J. E., and Chromik, R. R., 2019, "Failure Dynamics of Spherical and Irregular Shaped Ti Splats Deposited on Sapphire by Cold Spray," Surf. Topogr. Metrol. Prop., **7**(4), pp. 1–30.

[259] Yang, Y. C., Chang, E., Hwang, B. H., and Lee, S. Y., 2000, "Biaxial Residual Stress States of Plasma-Sprayed Hydroxyapatite Coatings on Titanium Alloy Substrate," Biomaterials, **21**(13), pp. 1327–1337.

[260] Hashemi, R., 2020, "Failure Analysis of Biometals," Metals, **10**(662), pp. 1–4.

[261] Huiskes, R., Weinans, H., and Dalstra, M., 1989, "Adaptive Bone Remodeling and Biomechanical Design Considerations for Noncemented Total Hip

Arthroplasty," Orthopedics, **12**(9), pp. 1255–1267.

[262] Teoh, S. H., 2000, "Fatigue of Biomaterials: A Review," Int. J. Fatigue, **22**(10), pp. 825–837.

[263] Dowson, D, Neville, A., 2014, "Tribology and Corrosion in Hip Joint Replacements: Materials and Engineering," Joint Replacement Technology, P. Revell, ed., Elsevier, Leeds, pp. 401–442, ISBN: 978-0-387-68991-3.

[264] Karachalios, T., Komnos, G., and Koutalos, A., 2018, "Total Hip Arthroplasty: Survival and Modes of Failure," EFORT Open Rev., **3**(5), pp. 232–239.

[265] Kim, H. W., Kong, Y. M., Bae, C. J., Noh, Y. J., and Kim, H. E., 2004, "Sol-Gel Derived Fluor-Hydroxyapatite Biocoatings on Zirconia Substrate," Biomaterials, **25**(15), pp. 2919–2926.

[266] Ducheyen, P., and Hench, L. L., 1982, "The Processing and Static Mechanical Properties of Metal Fibre Reinforced Bioglass," J. Mater. Sci., **17**(2), pp. 595–606.

[267] Yang, Y. C., and Chang, E., 2005, "Measurements of Residual Stresses in Plasma-Sprayed Hydroxyapatite Coatings on Titanium Alloy," Surf. Coatings Technol., **190**(1), pp. 122–131.

[268] Tsui, Y. C., Doyle, C., and Clyne, T. W., 1998, "Plasma Sprayed Hydroxyapatite Coatings on Titanium Substrates. Part 1: Mechanical Properties and Residual Stress Levels," Biomaterials, **19**(22), pp. 2015–2029.

[269] Sergo, V., Sbaizero, O., and Clarke, D. R., 1997, "Mechanical and Chemical Consequences of the Residual Stresses in Plasma Sprayed Hydroxyapatite Coatings," Biomaterials, **18**(6), pp. 477–482.

[270] Lee, M. J., Lee, B. C., Lim, J. G., and Kim, M. K., 2014, "Residual Stress Analysis of the Thermal Barrier Coating System by Considering the Plasma Spraying Process," J. Mech. Sci. Technol., **28**(6), pp. 2161–2168.

[271] Oh, Yoon-Suk, Kim, Seong-Won, Lee, Sung-Min, Kim Hyung-Tae, Kim Min-Sik, M. H.-S., 1998, "Effect of the Raw Material and Coating Process Conditions on the Densification of 8 Wt% Y2O3-ZrO2 Thermal Barrier Coating by Atmospheric Plasma Spray," **5803**(98), pp. 55–67.

[272] Jiju, A., 2014, "Design of Experiment for Engineer and Scientists," Elsiever, ISBN: 9780080994192.

[273] University, V., 2023, "Design of Experiments," Villanova Univ, (Online), Available: https://www.villanovau.com/articles/six-sigma/design-of-experiments/#:~:text=Factor – This is an independent, can be discrete or numeric, (Accessed: 04-Sep-2024).

[274] ACS, 2024, "Main Effects and Interactions," ACS Green Chem. Inst, (Online), Available: https://learning.acsgcipr.org/process-design/design-of-experiments/main-effects-and-interactions/#:~:text=Interactions occur where the impact, temperature, (Figure 2), (Accessed: 04-Sep-2024).

[275] Hayes, A., 2023, "Two-Way ANOVA: What It Is, What It Tells You, vs. One-

Way ANOVA," Investopedia, (Online), Available: https://www.investopedia.com/terms/t/two-way-anova.asp#:~:text=A one-way ANOVA evaluates, statistically significant differences between groups, (Accessed: 04-Sep-2024).

[276] Durakovic, B., 2017, "Design of Experiments Application, Concepts, Examples: State of the Art," Period. Eng. Nat. Sci., **5**(3), pp. 421–439.

[277] Pierlot, C., Pawlowski, L., Bigan, M., and Chagnon, P., 2008, "Design of Experiments in Thermal Spraying: A Review," Surf. Coatings Technol., **202**(18), pp. 4483–4490.

[278] Bradley, N., 2007, "The Response Surface Methodology,", Master's Thesis, p. 84, (Online), Available: https://clas.iusb.edu/math-compsci/_prior-thesis/NBradley_thesis.pdf, (Accessed: 04-Sep-2024).

[279] Montgomery, D. C., 2019, "Design and Analysis of Experiments," John Wiley and sons, New York, ISBN: 978-1-119-49244-3.

[280] Support, M., 2024, "What Are Response Surface Designs, Central Composite Designs, and Box-Behnken Designs?," Minitab Support, (Online), Available: https://support.minitab.com/en-us/minitab/help-and-how-to/statistical-modeling/doe/supporting-topics/response-surface-designs/response-surface-central-composite-and-box-behnken-designs/, (Accessed: 04-Sep-2024).

[281] Box, G. E. P., and Behnken, D. W., 1960, "American Society for Quality Some New Three Level Designs for the Study of Quantitative Variables Society for Quality Stable," Technometrics, **2**(4), pp. 455–475.

[282] NIST, "Box-Behnken Designs", (Online), Available: https://www.itl.nist.gov/div898/handbook/pri/section3/pri3362.htm, (Accessed: 07-Jan-2024).

[283] Ross, A., and Willson, V. L., 2018, "Basic and Advanced Statistical Tests: Writing Results Sections and Creating Tables and Figures.", Rotterdam, ISBN: 9789463510868.

[284] Chatterjee, S., and Hadi, A. S., 2013, "Regression Analysis by Example," Wiley, ISBN: 978-1-118-45624-8.

[285] Benyounis, K., 2006, "Prediction and Optimization of Residual Stresses, Weld-Bead Profile and Mechanical Properties of Laser Welded Components,", PhD Thesis, p. 276, (Online), Available: http://doras.dcu.ie/16941/, (Accessed: 04-Sep-2024).

[286] Biotal, P., 2017, "Technical Data Sheet", (Online), Available: http://www.plasma-biotal.com/wp-content/uploads/2019/08/Sintered-Captal-HA-Technical-Data-Sheet-v2.2.pdf, (Accessed: 04-Sep-2024).

[287] VWR, 2024, "VWR Venti-Line, Drying Ovens with Forced Convection", (Online), Available: https://ie.vwr.com/store/product/16844011/drying-ovens-with-forced-convection-venti-line-prime, (Accessed: 04-Sep-2024).

[288] Carson, J. W., Pittenger, B. H., and Jenike & Johanson, 1998, "Bulk Properties

of Powders," ASM Handbook, P.W. Lee, ed., pp. 287–301, ISBN: 978-0-87170-387-3.

[289] Fisher, T., 2021, "Safety Data Sheets," Thermo Fish. Sci., p. 10, (Online), Available: https://www.fishersci.com/store/msds?partNumber=AA3584314&productDescription=calcium-silicate-meta--metals-basis-alfa-aesar&vendorId=VN00024248&keyword=true&countryCode=US&language=en, (Accessed: 04-Sep-2024).

[290] Seppälä, K., Heinämäki, J., Hatara, J., Seppälä, L., and Yliruusi, J., 2010, "Development of a New Method to Get a Reliable Powder Flow Characteristics Using Only 1 to 2 g of Powder," AAPS PharmSciTech, **11**(1), pp. 402–408.

[291] Fritsch, "Analysette 3 Pro," (Online), Available: https://www.fritsch-international.com/sample-preparation/sieving/vibratory-sieve-shakers/details/product/analysette-3-pro/, (Accessed: 04-Sep-2024).

[292] Nabertherm, "Economy Muffle Furnace Upto 1100 °C," (Online), Available: https://nabertherm.com/en/products/laboratory/muffle-furnaces/economy-muffle-furnaces-1100-degc, (Accessed: 04-Sep-2024).

[293] Wolflabs, 2020, "Installation and Operation Instructions- 1200 C Tube Furnace-TF1/3 450 Mm 60 Mm," Carbolite, pp. 1–70, (Online), Available: https://www.wolflabs.co.uk/document/Carbolite_furnaces_STF1400_STF1500_STF1600_manual.pdf, (Accessed: 04-Sep-2024).

[294] Zeiss, 2024, "EVO LS Scanning Electron Microscope for Life Science Research from Carl Zeiss", (Online), Available: https://www.news-medical.net/EVO-LS-Scanning-Electron-Microscope-for-Life-Science-Research-from-Carl-Zeiss, (Accessed: 04-Sep-2024).

[295] Zeiss, 2017, "ZEISS EVO SOP," Univ. Louisev., p. 13, (Online), Available: https://www.scribd.com/document/403705773/EVO-SEM-SOP, (Accessed: 04-Sep-2024).

[296] Mathias, J., 2018, "A Beginner's Guide to FTIR Analysis: Interpreting & Analyzing Results," innovaTECH, (Online), Available: https://www.innovatechlabs.com/newsroom/1882/interpreting-analyzing-ftir-results/, (Accessed: 04-Sep-2024).

[297] Taha, M., Hassan, M., Essa, S., and Tartor, Y., 2013, "Use of Fourier Transform Infrared Spectroscopy (FTIR) Spectroscopy for Rapid and Accurate Identification of Yeasts Isolated from Human and Animals," Int. J. Vet. Sci. Med., **1**(1), pp. 15–20.

[298] Perkin Elmer, 2024, "Spectrum Two FT-IR Spectrometer", (Online), Available: https://www.perkinelmer.com/product/spectrum-two-ft-ir-sp10-software-l1160000a, (Accessed: 11-Jan-2024).

[299] Bruker, 2023, "D2 Phaser: X-Ray Diffraction," (Online), Available: https://www.bruker.com/en/products-and-solutions/diffractometers-and-x-ray-microscopes/x-ray-diffractometers/d2-phaser.html, (Accessed: 04-Sep-2024).

[300] Usinskas, P., Stankeviciute, Z., Beganskiene, A., and Kareiva, A., 2016, "Sol-Gel Derived Porous and Hydrophilic Calcium Hydroxyapatite Coating on Modified Titanium Substrate," Surf. Coatings Technol., **307**, pp. 935–940.

[301] Bruker, 2024, "CounterX-500", (Online), Available: https://www.bruker.com/en/products-and-solutions/test-and-measurement/3d-optical-profilers/contourx-500.html, (Accessed: 04-Sep-2024).

[302] Nwaogu, U. C., Tiedje, N. S., and Hansen, H. N., 2013, "A Non-Contact 3D Method to Characterize the Surface Roughness of Castings," J. Mater. Process. Technol., **213**(1), pp. 59–68.

[303] Riley Surf. World, "Guyson International Mamouth 690/40 With Type 40 Extractor," p. 2, (Online), Available: https://www.rileysurfaceworld.co.uk/machines/23105.htm, (Accessed: 09-Jan-2024).

[304] Guyson, 2020, "Safety Data Sheet According to Regulation (EC) No 1907/2006," p. 7, (Online), Available: https://s3-eu-west-1.amazonaws.com/resources.guyson.co.uk/product-downloads/GHSM001-HS12-A-Saftigrit-White-Premium_Issue2.pdf?mtime=20201111160116, (Accessed: 04-Sep-2024).

[305] Marinosci, V. M., Grouve, W. J. B., de Rooij, M. B., Wijskamp, S., and Akkerman, R., 2021, "Effect of Grit-Blasting on the Fracture Toughness of Hybrid Titanium-Thermoplastic Composite Joints," Int. J. Adhes. Adhes., **109**(102893), pp. 1–11.

[306] Labplant, "SD-05 Laboratory Scale Spray Dryer", (Online), Available: http://www.keison.co.uk/products/labplant/SD05.pdf, (Accessed: 04-Sep-2024).

[307] Labplant, 2002, "Assembly & Operating Instructions," p. 12, (Online), Available: http://www.keison.co.uk/products/labplant/SD05Manual.pdf, (Accessed: 04-Sep-2024).

[308] Ferreira, S. L. C., Bruns, R. E., Ferreira, H. S., Matos, G. D., David, J. M., Brandão, G. C., da Silva, E. G. P., Portugal, L. A., dos Reis, P. S., Souza, A. S., and dos Santos, W. N. L., 2007, "Box-Behnken Design: An Alternative for the Optimization of Analytical Methods," Anal. Chim. Acta, **597**(2), pp. 179–186.

[309] Faustini, M., Ceratti, D. R., Louis, B., Boudot, M., Albouy, P. A., Boissière, C., and Grosso, D., 2014, "Engineering Functionality Gradients by Dip Coating Process in Acceleration Mode," ACS Appl. Mater. Interfaces, **6**(19), pp. 17102–17110.

[310] Sanderson, T., 2021, "Mixology: A Tool for Calculating Required Masses and Volumes for Laboratory Solutions," Wellcome Open Res., **6**(May), pp. 1–9.

[311] Edrisy, A., and Farokhzadeh, K., 2016, "Plasma Nitriding of Titanium Alloys," Plasma Science and Technology - Progress in Physical States and Chemical Reactions, T. Mieno, ed., p. 548, ISBN: 978-953-51-5067-1.

[312] Casadebaigt, A., Monceau, D., and Hugues, J., 2020, "High Temperature Oxidation of Ti-6Al-4V Alloy Fabricated By Additive Manufacturing. Influence

on Mechanical Properties," MATEC Web Conf., **321**(03006), pp. 1–4.

[313] Luo, S. D., Liu, B., Tian, J., and Qian, M., 2020, "Sintering of Titanium in Argon and Vacuum: Pore Evolution and Mechanical Properties," Int. J. Refract. Met. Hard Mater., **90**(105226), pp. 1–6.

[314] Renishaw, 2024, "Inert Atmosphere Generation", (Online), Available: https://www.renishaw.com/en/inert-atmosphere-generation--31885, (Accessed: 04-Sep-2024).

[315] Eltawahni, H. ., 2006, "Characterization and Finite Element Analysis for Soft Magnetic Materials Used in Automotive Applications," Dublin City University, Master's Thesis, p.156, (Online), Available: https://doras.dcu.ie/17299/1/hayat_a._eltawahni_20120702105017.pdf, (Accessed: 04-Sep-2024).

[316] Ademiluyi, F. T., and Mepba, H. D., 2013, "Yield and Properties of Ethanol Biofuel Produced from Different Whole Cassava Flours," ISRN Biotechnol., **2013**(40), pp. 1–6.

[317] Oberbek, P., Bolek, T., Chlanda, A., Hirano, S., Kusnieruk, S., Rogowska-Tylman, J., Nechyporenko, G., Zinchenko, V., Swieszkowski, W., and Puzyn, T., 2018, "Characterization and Influence of Hydroxyapatite Nanopowders on Living Cells," Beilstein J. Nanotechnol., **9**(1), pp. 3079–3094.

[318] Hossain, S. S., and Roy, P. K., 2018, "Study of Physical and Dielectric Properties of Bio-Waste-Derived Synthetic Wollastonite," J. Asian Ceram. Soc., **6**(3), pp. 289–298.

[319] Zhang, C., Cai, J., Xu, H., Cheng, X., and Guo, X., 2020, "Mechanical Properties and Mechanism of Wollastonite Fibers Reinforced Oil Well Cement," Constr. Build. Mater., **260**(120461), pp. 1–11.

[320] Baker, A., 2013, "Design of Experiment Analysis of the Spray Drying of the Powders," Dublin City University, Master's Thesis, p.82.

[321] Bmj, 2024, "2. Mean and Standard Deviation," bmj publising Gr, (Online), Available: https://www.bmj.com/about-bmj/resources-readers/publications/statistics-square-one/2-mean-and-standard-deviation, (Accessed: 04-Sep-2024).

[322] Chen, Q., and Qi, J., 2023, "How Much Should We Trust R 2 and Adjusted R 2: Evidence from Regressions in Top Economics Journals and Monte Carlo Simulations," J. Appl. Econ., **26**(1), pp. 1–16.

[323] Mugendiran, V., Gnanavelbabu, A., and Ramadoss, R., 2014, "Parameter Optimization for Surface Roughness and Wall Thickness on AA5052 Aluminium Alloy by Incremental Forming Using Response Surface Methodology," Procedia Eng., **97**, pp. 1991–2000.

[324] Vera Candioti, L., De Zan, M. M., Cámara, M. S., and Goicoechea, H. C., 2014, "Experimental Design and Multiple Response Optimization. Using the Desirability Function in Analytical Methods Development," Talanta, **124**, pp. 123–138.

[325] Lou, S., Zhu, Z., Zeng, W., Majewski, C., Scott, P. J., and Jiang, X., 2021, "Material Ratio Curve of 3D Surface Topography of Additively Manufactured Parts: An Attempt to Characterise Open Surface Pores," Surf. Topogr. Metrol. Prop., **9**(1), pp. 1–12.

[326] Sneddon, S., Xu, Y., Dixon, M., Rugg, D., Li, P., and Mulvihill, D. M., 2021, "Sensitivity of Material Failure to Surface Roughness: A Study on Titanium Alloys Ti64 and Ti407," Mater. Des., **200**(109438), pp. 1–14.

[327] Bahbou, M. F., Nylén, P., and Wigren, J., 2004, "Effect of Grit Blasting and Spraying Angle on the Adhesion Strength of a Plasma-Sprayed Coating," J. Therm. Spray Technol., **13**(4), pp. 508–514.

[328] Bhowmik, A., Wei-Yee Tan, A., Sun, W., Wei, Z., Marinescu, I., and Liu, E., 2020, "On the Heat-Treatment Induced Evolution of Residual Stress and Remarkable Enhancement of Adhesion Strength of Cold Sprayed Ti–6Al–4V Coatings," Results Mater., **7**(100119), pp. 1–9.

[329] Kaschel, F. R., Vijayaraghavan, R. K., Shmeliov, A., McCarthy, E. K., Canavan, M., McNally, P. J., Dowling, D. P., Nicolosi, V., and Celikin, M., 2020, "Mechanism of Stress Relaxation and Phase Transformation in Additively Manufactured Ti-6Al-4V via in Situ High Temperature XRD and TEM Analyses," Acta Mater., **188**(June), pp. 720–732.

[330] Zhang, J., Li, Y., Bao, F., Rui, X., Duan, Z., Yan, W., Shi, Q., Wang, W., Shan, Y., and Yang, K., 2021, "Study on the Formation Mechanism of Y-Ti-O Oxides during Mechanical Milling and Annealing Treatment," Adv. Powder Technol., **32**(2), pp. 582–590.

[331] Skocaj, M., Filipic, M., Petkovic, J., and Novak, S., 2011, "Titanium Dioxide in Our Everyday Life; Is It Safe?," Radiol. Oncol., **45**(4), pp. 227–247.

[332] Ahmed, Y. M. Z., El-Sheikh, S. M., and Zaki, Z. I., 2015, "Changes in Hydroxyapatite Powder Properties via Heat Treatment," Bull. Mater. Sci., **38**(7), pp. 1807–1819.

[333] Chen, W., Liang, Y., Hou, X., Zhang, J., Ding, H., Sun, S., and Cao, H., 2018, "Mechanical Grinding Preparation and Characterization of TiO2-Coated Wollastonite Composite Pigments," Materials, **11**(4), pp. 1–11.

[334] Głab, M., Kudłacik-Kramarczyk, S., Drabczyk, A., Walter, J., Kordyka, A., Godzierz, M., Bogucki, R., Tyliszczak, B., and Sobczak-Kupiec, A., 2021, "Hydroxyapatite Obtained via the Wet Precipitation Method and PVP/PVA Matrix as Components of Polymer-Ceramic Composites for Biomedical Applications," Molecules, **26**(14), pp. 1–18.

[335] Ma, X., Yang, J., Ma, H., and Liu, C., 2016, "Hydrothermal Extraction of Potassium from Potassic Quartz Syenite and Preparation of Aluminum Hydroxide," Int. J. Miner. Process., **147**(January), pp. 10–17.

[336] Vichaphund, S., Kitiwan, M, Atong, D., Thavorniti, P., 2011, "Microwave Synthesis of Wollastonite Powder from Eggshells," J. Eur. Ceram. Soc., **31**, pp. 2435–2440.

[337] Nasiri, S., Rabiei, M., Palevicius, A., Janusas, G., Vilkauskas, A., Nutalapati, V., and Monshi, A., 2023, "Modified Scherrer Equation to Calculate Crystal Size by XRD with High Accuracy, Examples Fe2O3, TiO2 and V2O5," Nano Trends, **3**(August), pp. 1–12.

[338] Baştan, F. E., Karaarslan, O., and Üstel, F., 2021, "Production and Characterization of Wollastonite Particles Reinforced Hydroxyapatite Composite Granules for Biomedical Applications," Deu Muhendis. Fak. Fen ve Muhendis., **23**(67), pp. 1–9.

[339] Yazdanpanah, Z., Bahrololoom, M. E., and Hashemi, B., 2015, "Evaluating Morphology and Mechanical Properties of Glass-Reinforced Natural Hydroxyapatite Composites," J. Mech. Behav. Biomed. Mater., **41**, pp. 36–42.

[340] Croll, S. G., 2020, "Surface Roughness Profile and Its Effect on Coating Adhesion and Corrosion Protection: A Review," Prog. Org. Coatings, **148**(April), pp. 1–14.

[341] Y, L., Yao, X., Liu, Y. W., and Wang, Y., 2014, "A Fourier Transform Infrared Spectroscopy Analysis of Carious Dentin from Transparent Zone to Normal Zone.," Caries Res., **48**(4), pp. 320–329.

[342] Shahabi, S., Najafi, F., Majdabadi, A., Hooshmand, T., Haghbin Nazarpak, M., Karimi, B., and Fatemi, S. M., 2014, "Effect of Gamma Irradiation on Structural and Biological Properties of a PLGA-PEG-Hydroxyapatite Composite," Sci. World J., **2014**, pp. 1–9.

[343] Hou, X., Zhang, L., Zhou, Z., Luo, X., Wang, T., Zhao, X., Lu, B., Chen, F., and Zheng, L., 2022, "Calcium Phosphate-Based Biomaterials for Bone Repair," J. Funct. Biomater., **13**(4), pp. 1–39.

[344] Ashraf, W., Olek, J., and Tian, N., 2016, "Multiscale Characterization of Carbonated Wollastonite Paste and Application of Homogenization Schemes to Predict Its Effective Elastic Modulus," Cem. Concr. Compos., **72**, pp. 284–298.

[345] Obeid, M. M., 2014, "Crystallization of Synthetic Wollastonite Prepared from Local Raw Materials," Int. J. Mater. Chem., **4**(4), pp. 79–87.

[346] Ryu, H. S., Lee, J. K., Kim, H., and Hong, K. S., 2005, "New Type of Bioactive Materials: Hydroxyapatite/α-Wollastonite Composites," J. Mater. Res., **20**(5), pp. 1154–1163.

[347] Jaafar, A., Schimpf, C., Mandel, M., Hecker, C., Rafaja, D., Krüger, L., Arki, P., and Joseph, Y., 2022, "Sol–Gel Derived Hydroxyapatite Coating on Titanium Implants: Optimization of Sol–Gel Process and Engineering the Interface," J. Mater. Res., **37**(16), pp. 2558–2570.

[348] Abifarin, J. K., Obada, D. O., Dauda, E. T., and Dodoo-Arhin, D., 2019, "Experimental Data on the Characterization of Hydroxyapatite Synthesized from Biowastes," Data Br., **26**(104485), pp. 1–8.

[349] Dzhurinskiy, D., 2018, "Bioactive Antimicrobial Coatings for Implantable Medical Devices Formed by Plasma Electrolytic Oxidation," Met. Form., **29**(1), pp. 65–76.

[350] Rabiei, M., Palevicius, A., Monshi, A., Nasiri, S., Vilkauskas, A., and Janusas, G., 2020, "Comparing Methods for Calculating Nano Crystal Size of Natural Hydroxyapatite Using X-Ray Diffraction," Nanomaterials, **10**(9), pp. 1–21.

[351] Rapacz-Kmita, A., Paluszkiewicz, C., Ślósarczyk, A., and Paszkiewicz, Z., 2005, "FTIR and XRD Investigations on the Thermal Stability of Hydroxyapatite during Hot Pressing and Pressureless Sintering Processes," J. Mol. Struct., **744**–**747**(SPEC. ISS.), pp. 653–656.

[352] Manafi, S. A., Yazdani, B., Rahimiopour, M. R., Sadrnezhaad, S. K., Amin, M. H., and Razavi, M., 2008, "Synthesis of Nano-Hydroxyapatite under a Sonochemical/Hydrothermal Condition," Biomed. Mater., **3**(2), pp. 1–6.

[353] Liu, S., Laaksonen, O., Marsol-Vall, A., Zhu, B., and Yang, B., 2020, "Comparison of Volatile Composition between Alcoholic Bilberry Beverages Fermented with Non- Saccharomyces Yeasts and Dynamic Changes in Volatile Compounds during Fermentation," J. Agric. Food Chem., **68**(11), pp. 3626–3637.

[354] Klein, L. C., Al-Marzoki, K., Jitianu, A., and Rodriguez, G., 2020, "Effect of Tetraethoxysilane (TEOS) on Melting Gel Behavior," J. Am. Ceram. Soc., **103**(8), pp. 4140–4149.

[355] Marino, I. G., Lottici, P. P., Bersani, D., Raschellà, R., Lorenzi, A., and Montenero, A., 2005, "Micro-Raman Monitoring of Solvent-Free TEOS Hydrolysis," J. Non. Cryst. Solids, **351**(6–7), pp. 495–498.

[356] Kičaite, A., Skripkiunas, G., and Pundiene, I., 2020, "The Effect of Calcium Nitrate on the Properties of Portland Cement Pastes and Concrete Hardening at Low Temperatures," Ceram. - Silikaty, **64**(3), pp. 263–270.

[357] Scientific, F., 2024, "Calcium Nitrate Tetrahydrate, 99%, for Analysis, Thermo Scientific Chemicals," Thermo Fish. Sci, (Online), Available: https://www.fishersci.fi/shop/products/calcium-nitrate-tetrahydrate-99-analysis-thermo-scientific/10733221, (Accessed: 04-Sep-2024).

[358] Kaur, H., Chaudhary, S., Kaur, H., Chaudhary, M., and Jena, K. C., 2022, "Hydrolysis and Condensation of Tetraethyl Orthosilicate at the Air–Aqueous Interface: Implications for Silica Nanoparticle Formation," ACS Appl. Nano Mater., **5**(1), pp. 411–422.

[359] Kim, Y. S., Cho, E. S., Park, C. H., and Cha, H. G., 2023, "The Effects of 4-Week Inhalation Exposure to Titanium Nitride on Lungs of Sprague–Dawley Rats," Toxicol. Res., **39**(1), pp. 157–167.

[360] Miu, D. M., Jinga, S. I., Voicu, G., and Iordache, F., 2021, "Characteristics of Wollastonite Ceramic Coatings Obtained by Pulsed Laser Deposition," J. Inorg. Organomet. Polym. Mater., **31**(4), pp. 1601–1607.

[361] Bouatrous, M., Bouzerara, F., Bhakta, A. K., Delobel, F., Delhalle, J., and Mekhalif, Z., 2020, "A Modified Wet Chemical Synthesis of Wollastonite Ceramic Nanopowders and Their Characterizations," Ceram. Int., **46**(8), pp. 12618–12625.

[362] Svensson, K., Neumann, A., Feitosa Menezes, F., Lempp, C., and Pöllmann, H., 2019, "Carbonation of Natural Pure and Impure Wollastonite," SN Appl. Sci., **1**(4), pp. 1–12.

[363] Rowe, M. C., and Brewer, B. J., 2018, "AMORPH: A Statistical Program for Characterizing Amorphous Materials by X-Ray Diffraction," Comput. Geosci., **120**(September 2017), pp. 21–31.

[364] Bokov, D., Turki Jalil, A., Chupradit, S., Suksatan, W., Javed Ansari, M., Shewael, I. H., Valiev, G. H., and Kianfar, E., 2021, "Nanomaterial by Sol-Gel Method: Synthesis and Application," Adv. Mater. Sci. Eng., **2021**.

[365] Cucuruz, A., Ghițulică, C. D., Voicu, G., Bogdan, C. A., Dochiu, V., and Popescu, R. C., 2023, "Investigation of Porous Ceramic Structures Based on Hydroxyapatite and Wollastonite with Potential Applications in the Field of Tissue Engineering," Ceramics, **6**(4), pp. 2333–2351.

[366] Liu, X., and Ding, C., 2001, "Phase Compositions and Microstructure of Plasma Sprayed Wollastonite Coating," Surf. Coatings Technol., **141**(2–3), pp. 269–274.

[367] Solonenko, A. P., Blesman, A. I., and Polonyankin, D. A., 2018, "Preparation and in Vitro Apatite-Forming Ability of Hydroxyapatite and β-Wollastonite Composite Materials," Ceram. Int., **44**(15), pp. 17824–17834.

[368] Martinez, T., Espanol, M., Charvillat, C., Marsan, O., Ginebra, M. P., Rey, C., and Sarda, S., 2021, "A-Tricalcium Phosphate Synthesis From Amorphous Calcium Phosphate: Structural Characterization and Hydraulic Reactivity," J. Mater. Sci., **56**(24), pp. 13509–13523.

[369] Iqbal, A. A., and Lim, M. J., 2023, "A Relationship of Porosity and Mechanical Properties of Spark Plasma Sintered Scandia Stabilized Zirconia Thermal Barrier Coating," Results Eng., **19**(June), p. 101263.

[370] Bruker, 2024, "DIFFRAC.EVA", (Online), Available: https://www.bruker.com/en/products-and-solutions/diffractometers-and-x-ray-microscopes/x-ray-diffractometers/diffrac-suite-software/diffrac-eva.html, (Accessed: 04-Sep-2024).